A Thesis for the Degree of Ph.D. in Engineering

Synthesis and Transport Properties of van der Waals-type Quasi-Two-Dimensional Pnictide, $EuSn_2As_2$

August 2021

Graduate School of Science and Technology
Keio University

Ryosuke Sakagami

Acknowledgements

本研究は神原陽一教授 (慶應義塾大学理工学部物理情報工学科) の御指導のもと行われました. 神原教授には, 研究面から生活面に至るまで多くのご教示をいただきました. 大変感謝しております. 的場正憲教授 (慶應義塾大学理工学部物理情報工学科) からは, 研究に対する助言を頂くのみならず, 他愛のない世間話をお話ししていただき, 研究を進める活力となりました. 太田英二名誉教授, 海住英生准教授 (慶應義塾大学理工学部物理情報工学科) には, お忙しいところ, 副査として多くのご助言を頂きました. 厚く御礼申し上げます. Simon R. Hall 教授 (Complex Functional Materials Group, School of Chemistry, University of Bristol, 英国) の研究グループへの 5 か月間の留学は, 得難い貴重な経験で, 忘れることはありません. 李哲虎研究グループ長, 木方邦宏博士, 西当弘隆様, 村田正行博士, 長瀬和夫様, 高島泰子様 (産業技術総合研究所) には, 熱電変換材料の合成とその輸送測定について大変お世話になり, また, つくばでの新生活に関してもご配慮をいただきました. 水口佳一准教授, 後藤陽介助教 (東京都立大学) には, ホットプレス装置と熱特性評価装置を使わせていただいただけでなく, 熱電の原著論文の共著者としてディスカッションをしていただきました. 北尾真司准教授, 瀬戸誠教授 (京都大学複合原子力科学研究所) には, Mössbauer 分光の測定および結果の解釈に関するディスカッションをしていただきました. 藤岡正弥助教 (北海道大学電子科学研究所) からは, 高温熱電変換性能の測定条件に関する重要なヒントをご教示いただきました. 末國晃一郎准教授 (九州大学), 橋國克明助教 (山口東京理科大学), 森仁志博士 (理化学研究所) には, 熱電変換材料の輸送測定結果, 電子状態やフォノン状態について, ディスカッションをしていただきました. 櫻木俊輔博士 (東京大学物性研究所), 近藤猛准教授 (東京大学物性研究所), 黒田健太助教 (東京大学物性研究所), 山下穣准教授 (東京大学物性研究所), 和達大樹教授 (兵庫県立大学), 福井宏之助教 (兵庫県立大学), 小濱芳允准教授 (東京大学物性研究所), 平田昂輝様 (慶應義塾大学理工学部物理情報工学科) , Wonjong Lee 様 (慶應義塾大学理工学部物理情報工学科) , 山田悠太朗様 (慶應義塾大学理工学部物理情報工学科) には, トポロジカル物質についてご教示をいただきました. 飯原潤様, 岩崎秀博士 (慶應義塾大学理工学部物理情報工学科) からは, 試料合成技術のノウハウを学ばせて頂きました. Imad Chelali 様, 金安航大様, 高橋慧様, 劉子豪様 (慶應義

塾大学理工学部物理情報工学科) とは, 試料合成を共に行いました. 松本裕介様, 金安航大様, 村田陽様, 山口道太郎様 (慶應義塾大学理工学部物理情報工学科) からは, 超伝導体に関する知識とノウハウを共有していただきました. 河野佳世子博士と林洋子様 (慶應義塾大学理工学部中央試験所) には, 無茶な要望に応えていただき, 大変お世話になりました. 三谷智明様, 李在鐵様 (慶應義塾大学理工学部中央試験所) には, 実験装置のノウハウをご教示いただきました. 木下拓郎様, 中西愛様, 北脇樹様 (慶應義塾大学理工学部物理情報工学科) からは, 電子状態計算の基礎とノウハウをご教示いただきました. 大学院修士課程の同期であった中野翔太様, 谷中慎太郎様, 大塚貴史様, 加藤達輝様, 山本和賜様 (慶應義塾大学理工学部物理情報工学科) には, 日常生活を送る上で良き話し相手になって頂きました. 狩俣春成様, 東伸彦様, 山口道太郎様 (慶應義塾大学理工学部物理情報工学科) には, 高温熱電変換測定でご協力をいただきました. Jason Potticary 博士 (Complex Functional Materials Group, School of Chemistry, University of Bristol, 英国), 國岡春乃博士 (産業技術総合研究所), 小野圭吾様 (産業技術総合研究所, 東京理科大学) には, Rietveld 解析を教わりました. Walid Malaeb 博士 (Beirut Arab University) とは, 磁化測定をご一緒しました. 小林幸弘様, 小堤渉平様, 藤田航様 (慶應義塾大学理工学部物理情報工学科) には, 低温電気抵抗測定関連でご協力いただきました. 高野義彦グループリーダー (物質・材料研究機構), 田中将嗣助教 (九州工業大学), 山下愛智特任助教 (東京都立大学), 長尾雅則准教授 (山梨大学), 平井慈人准教授 (北見工業大学), 荻野拓博士 (産業技術総合研究所), 平松秀典教授 (東京工業大学), 為ヶ井強准教授 (東京大学), 亀谷文健博士 (フロリダ州立大学), 永崎洋博士 (産業技術総合研究所), 伊豫彰博士 (産業技術総合研究所), 石田茂之博士 (産業技術総合研究所), 二宮博樹博士 (産業技術総合研究所) には学会や見学でお世話になりました.

神原研究室に所属し, 充実した時間を過ごすことができました. 出会った全ての皆様に心から感謝申し上げます.

Table of contents

Symbols and acronyms

List of symbols

a	A lattice constant
A	area
a_{B}	Bohr radius
B	thermoelectric quality factor
c	A lattice constant
c_{p}	specific heat capacity at constant pressure
c_{v}	specific heat capacity at constant volume
C_{inter}	coupling constant for intervalley scattering
C_{sct}	scattering-related constant
D	electronic density of states near Fermi level
d	distance
d_{calc}	ideally calculated density
d_{meas}	measured apparent density
e	elementary charge
E_{c}	default maximum cut-off energy of each pseudopotential
E_{F}	Fermi level
E_{tot}	total free energy of the ion-electron system
f_{FD}	Fermi–Dirac distrubution function
$F_{\mathrm{W}j}$	window functions that determines electric transports
$\hbar\omega$	energy of the acoustic phonon
I	electrical current
I_{14}	electric current flows through the electrodes 1 and 4
I_{h}	electric current through the heater
J	heat flux

J_{os}	on-site exchange interaction parameter
$\boldsymbol{k}$	wave vector
k_{B}	Boltzmann constant
K	absolute permittivity
L	Lorenz number
L_0	Sommerfeld value as the Lorenz number
M	magnetization per fromula unit
M_{m}	molar mass
M_{g}	magnetization per gram
m_{i}^*	inertial effective mass
m^*	effective electron mass
m_{b}^*	density of states effective mass of a single valley
m_{e}	free electron mass
n	charge carrier density
p	pressure
P	power factor
P_{rad}	radiation heat
$\mathbf{P}_{\parallel}$	parallel to the pressing direction in a hot-pressing process
$\mathbf{P}_{\perp}$	perpendicular to the pressing direction in a hot-pressing process
Q	quality factor
R	electrical resistance of the specimen
R_{gas}	molar gas constant
R_{sp}	specular reflectivity
R_{tot}	total reflectivity
S	Seebeck coefficient
$\mathscr{S}$	entropy
s_{c}	spectral conductivity
T	temperature
t	thickness
U_{os}	on-site Coulomb interaction parameter
v	magnitude of group velocity of carriers
V	lattice volume
V_{23}	voltage between voltage terminals on the specimen in the four-terminal sensing
$\mathscr{V}$	volume

V_0	offset voltage
V_{HP}	cell volume of the hot-pressed sample
V_{ul}	voltage between the electrodes u and l
V_{23}	voltage between the electrodes 2 and 3
w	width
Z	material's figure of merit
ZT	dimensionless figure of merit
Z_{uc}	number of molecules in the unit cell
α	thermal diffusivity
γ	electronic specific heat coefficient
$\Delta\sigma_{ch}$	charge density difference
Θ_D	Debye temperature
2θ	diffraction angle
ϵ_{Sp}	emissivity of the specimen
ε	energy
η	chemiclal potential
κ	thermal conductivity
κ_{el}	electronic thermal conductivity
κ_{ph}	phonon thermal conductivity
${}^{LF}\kappa$	LASER flash thermal conductivity
${}^{LF}\kappa_{ph}$	LASER flash phonon thermal conductivity
${}^{SS}\kappa$	steady-state thermal conductivity
${}^{SS}\kappa_{ph}$	steady-state phonon thermal conductivity
λ	wavelength
μ	mobility
ρ	electrical resistivity
σ	electrical conductivity
σ_{ch}	charge density
σ_{SB}	Stefan–Boltzmann constant
τ	relaxation time
ϕ	porosity

List of acronyms

ARPES	angle-resolved photoemission spectroscopy
BSE	backscattered electron
CDD	charge density difference
DFT	density functional theory
EDX	energy-dispersive X-ray spectroscopy
GB	glove box
HP	hot-pressed
IS	Isomer shift
LASER	Light Amplification by Stimulated Emission of Radiation
LF	LASER flash
LW	line width
PAW	projector-augmented wave
PBE	Perdew–Burke–Ernzerhof
PGEC	a phonon glass and an electron single crystal
RA	relative amplitude
RT	room temperature
SEM	scanning electron microscope
SG	space group
SOC	spin orbit coupling
TE	thermoelectric
VASP	Vienna *Ab-initio* Package Simulation
VESTA	Visualization for Electronic and STructural Analysis
vdW	van der Waals
XRD	X-ray diffraction

1

General introduction

1.1 Chapter outlines

Quasi-two-dimensional pnictides are layered compounds that exhibit various functional properties including high thermoelectricity, superconductivity, and topological features. The present study aims application of van der Waals-type quasi-two-dimensional pnictide, $EuSn_2As_2$ to thermoelectric (TE) materials to reveal its transport properties. Furthernore, the present study examines its chemical bonding states by Mössbauer spectroscopy, magnetization measurements, and electronic state calculations to discuss relations between its chemical bonding states and transport properties.

Chapter 1 describes backgrounds of the present study. This chapter gives descriptions on crystallographic structures and chemical bonding states of quasi-two-dimensional pnictides as functional materials. Moreover, the chapter summarizes previous studies on functional properties of hexagonal layered compound $EuSn_2As_2$ and related materials and then states the significance of the present study. $EuSn_2As_2$ crystal is characterized by alternate stacking of Eu cation layers and SnAs anionic layers and has van der Waals (vdW) bonding between closely situated Sn-Sn, so $EuSn_2As_2$ thin film can be fabricated by cleavage exfoliation of its single crystal. Owing to the crystallographic structure, $EuSn_2As_2$ is a candidate for a TE material. Chpater 2 describes development of syntehsis procedeures of $EuSn_2As_2$ in order to obtain its polycrystalline samples with high purity for transport property measurements. In the first syntehsis procedure, a sample was prepared from Eu ingot, Sn and As powders in an alumina tube. In the second procedure, another sample was prepared from Eu ingot and Sn-As pellet in an carbon crucible. The purerest sample is obtained by the second procedure. Chapter 3 and Appendix B provides a detailed description on experimental for transport

property measurements. The chapter and appendix show Laboratory Virtual Instrumentation Engineering Workbench (LabVIEW) programs for control of electronic test equipments and temperature controllers to automate the measurements. The chapter and appendix publish Python code for obtaining measurement values of physical quantities from measurement raw data. Chapter 4 elucidates TE transport properties of a densified polycrystalline sample, which was obtained by hot pressing of samples prepared by the second procedure described in Chapter 2. The dimensionless figure of merit, ZT, is 0.092(17) at 673(3) K perpendicular to the pressing direction of hot pressing. Its temperature dependence of electrical resistivity increases with increasing temperature and has a component of temperature to the second power. Its electrical resistivity and Seebeck coefficient as functions of temperature were resulted from multi carriers. Chapter 5 directly observes its chemical bonding states by using Mössbauer spectroscopy and magnetization measurements for further discussion on the transport properties. ^{151}Eu Mössbauer spectra show both components of Eu^{2+} and Eu^{3+}. This is consistent with observed values of saturation magnetization of $EuSn_2As_2$. ^{119}Sn Mössbauer spectra demonstrate magnetic splitting caused by internal magnetic field of Eu. Eu atoms in $EuSn_2As_2$ are not isolated as cations but rather supply charge carriers to SnAs anionic layers. Chapter 6 describes chemical bonding states of $EuSn_2As_2$ obtained by electronic state calculations based on density functional theory. Chapter 7 describes summary and concluding remark. In conclusion, $EuSn_2As_2$-based compounds are promising as TE materials.

The present study seems to take a classical approach because materials development was supported by valency obtained by Mössbauer spectroscopy and results of magnetization measurements.

1.2 Background

1.2.1 Layered pnictides

Some pnictides crystallize in the layered structure with unique chemical bonding due to electronic configuration of pnictogen (*Pn*) (Fig. 1.2.1). Their features are transferred and shared electrons (Fig. 1.2.2). Judging from positions of TE materials and superconductors in Fig. 1.2.2, superconductors and thermoelectric materials have similar electronic states.

Generally, quasi-two-dimensional compounds exhibit high electronic density of states (DOSs) near the Fermi level (ε_F). Materials with high DOS near ε_F are expected to be a stage of successful search for new superconductors [1, 2].

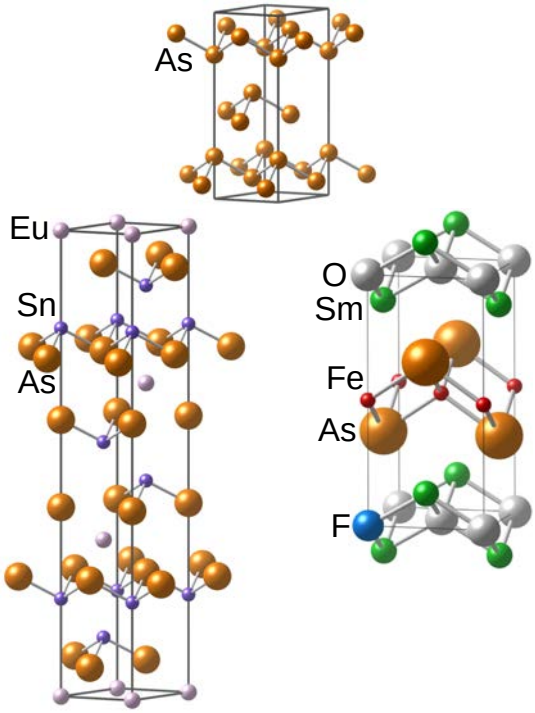

Fig. 1.2.1 Crystallographic structures of layered pnictides, gray arsenic (α-As) [6], $EuSn_2As_2$ [7], and $SmFeAsO_{0.9375}F_{0.0625}$ [8]. Crystallographic structures were drawn using VESTA [9].

Materials with low dimensionality potentially enhance TE performance [4] (Fig. 1.2.3).

1.2.2 Electronic and topological properties of $A Sn_2As_2$ (A = Na, Li, Sr, Eu)

SnAs-based layered compounds with a Bi_2Te_3-type structure have a wide variety of exotic electronic features and topological characters [7, 11–19]. $NaSn_2As_2$ is a superconductor with an onset superconducting transition temperature (T_c) of 1.2–1.6 K [13–16]. Seebeck coefficient (S) measurements of single crystals of $NaSn_2As_2$ have shown that they have n-type carrier polarity along an a-b plane direction in the hexagonal coordinate system and p-type carrier polarity along the c axis direction [17]. $Li_{1-x}Sn_{2+x}As_2$ has anisotropic electrical properties [18]. Specifically, the electrical resistivity (ρ) of $Li_{0.65}Sn_{2.35}As_2$ is 0.20 mΩ cm along the a-b plane direction in the hexagonal coordinate system and 1.08 mΩ cm along the c axis direction at room temperature (RT) [18].

Angle-resolved photoemission spectroscopy (ARPES) measurements imply that $SrSn_2As_2$ is a strong topological insulator, whereas density functional theory (DFT) calculations suggested that it is near the topological critical point between a trivial insulator and a strong

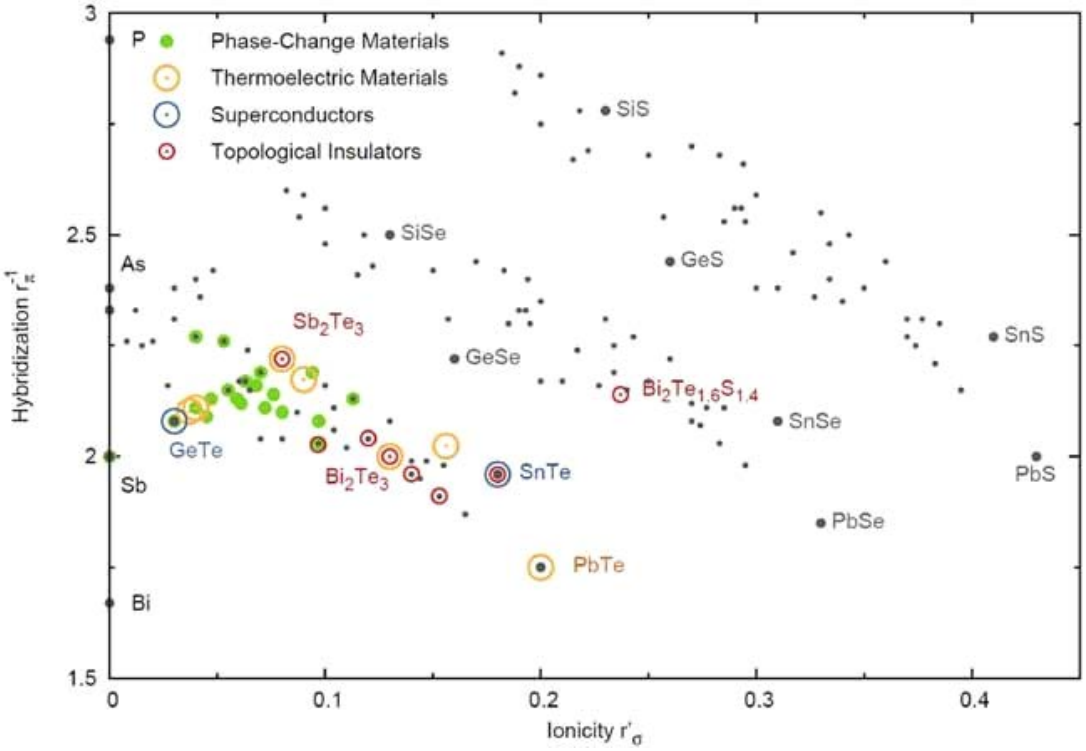

Fig. 1.2.2 Map for numerous compounds with an average number of three *p*-electrons per site. A wide variety of materials is shown which differ in their tendency towards hybridization ('covalency') and ionicity. Bands of sulphides, selenides and tellurides are clearly discernible. Phase-change materials, marked by green circles, are all localized in the lower left corner of the map. In their close vicinity, other classes with interesting physical properties can be found, which include Thermoelectric Materials (orange circles), Superconductors (blue circles) and Topological Insulators (red circles). This is evidence that tellurides possess very interesting and technologically important electronic properties. This figure is reprinted from Wuttig [3].

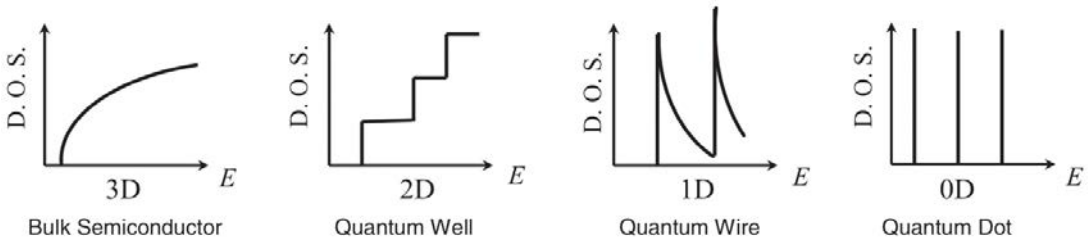

Fig. 1.2.3 Electronic density of states (DOSs) for a) a bulk 3D crystalline semiconductor, b) a 2D quantum well, c) a 1D nanowire or nanotube, and d) a 0D quantum dot. Materials systems with low dimensionality also exhibit physical phenomena, other than a high density of electronic states (DOS), that may be useful for enhancing thermoelectric (TE) performance. This figure is reprinted from Dresselhaus *et al.* [4].

topological insulator [19]. Arguilla *et al.* shows that $SrSn_2As_2$ is semimetallic in antiferromagnetic phase [7] (Fig. 1.2.4). Li *et al.* reported theoretical predictions showing that $EuSn_2As_2$ was a strong topological insulator in the paramagnetic phase [11]. Their time-resolved ARPES spectrum showed that a sample of $EuSn_2As_2$ exhibited Dirac-like electronic band dispersion of its surface states at ~0.4 eV above Fermi energy (ε_F), indicating that the sample was hole-doped [11]. Measurements of ρ of single crystal $EuSn_2As_2$ using four-terminal method by Sakuragi *et al.* demonstrated superconductivity with an onset T_c of 4.8 K and a zero T_c of 0.8 K along the a-b plane direction for the hexagonal coordinate system, whereas ρ increased with decreasing T below the onset T_c along the c axis direction [12]. Sakuragi *et al.* also discussed the effects of the antiferromagnetic order of europium (Eu) layers in the c axis direction on the superconducting current [12].

1.2.3 Crystallgraphic structure, magnetic, electronic and topological properties of $EuSn_2As_2$

A recently discovered van der Waals-type quasi-two-dimensional rhombohedral compound, $EuSn_2As_2$, undergoes a para-antiferromagnetic phase transition at temperature (T) of ~24 K due to a magnetic sublattice of Eu cation with an unfilled $4f$ shell [7]. The crystal of $EuSn_2As_2$ is characterized by a stack of Sn-As-Eu-As-Sn layers (Fig. 1.2.5 (a)). For the hexagonal coordinate system, the layer are stacked to the c-axis direction with shift to a direction in the a-b plane (Fig. 1.2.5 (b-i)–(b-iii)). As shown in Fig. 1.2.5 (a), the two-dimensional triangular sublattices of Eu cations, which mainly contributes to the spontaneous magnetic moments, are sandwiched between the anionic Sn-As layers. The Sn cations are located both in the edges of the Sn-As-Eu-As-Sn layers and in the starting points of the vdW bonding. The As anions meditate the binding of the Eu and Sn cations. $EuSn_2As_2$ is semimetallic in antiferromagnetic ground state in DFT calculations (Fig. 1.2.4) [7]. The anionic Sn-As layers might flow possible quantized spin-polarized current. The quantized spin-polarized current is an assumed phenomenon. Several interesting approaches has been introduced to describe the relations among electronic structures and topologically invariant conductance in low-dimensional materials. However, quantitative effects of the randomness of the crystal on the topologically invariant conductance remain controversial for $EuSn_2As_2$. Indeed, Chen *et al.* reported the absence of the quantum anomalous Hall effect (QAHE) for $EuSn_2As_2$ at T = 2–200 K under magnetic flux density (B) of 0–9 T [20]. The report discussed a relation between the absence of the QAHE and hybridization of the $4f$ orbital in Eu^{2+} cations and the topological electronic states [20]. We expect that the absence of the QAHE was probably derived from the randomness of the crystal, i.e. mixed valence and crystallographic defect.

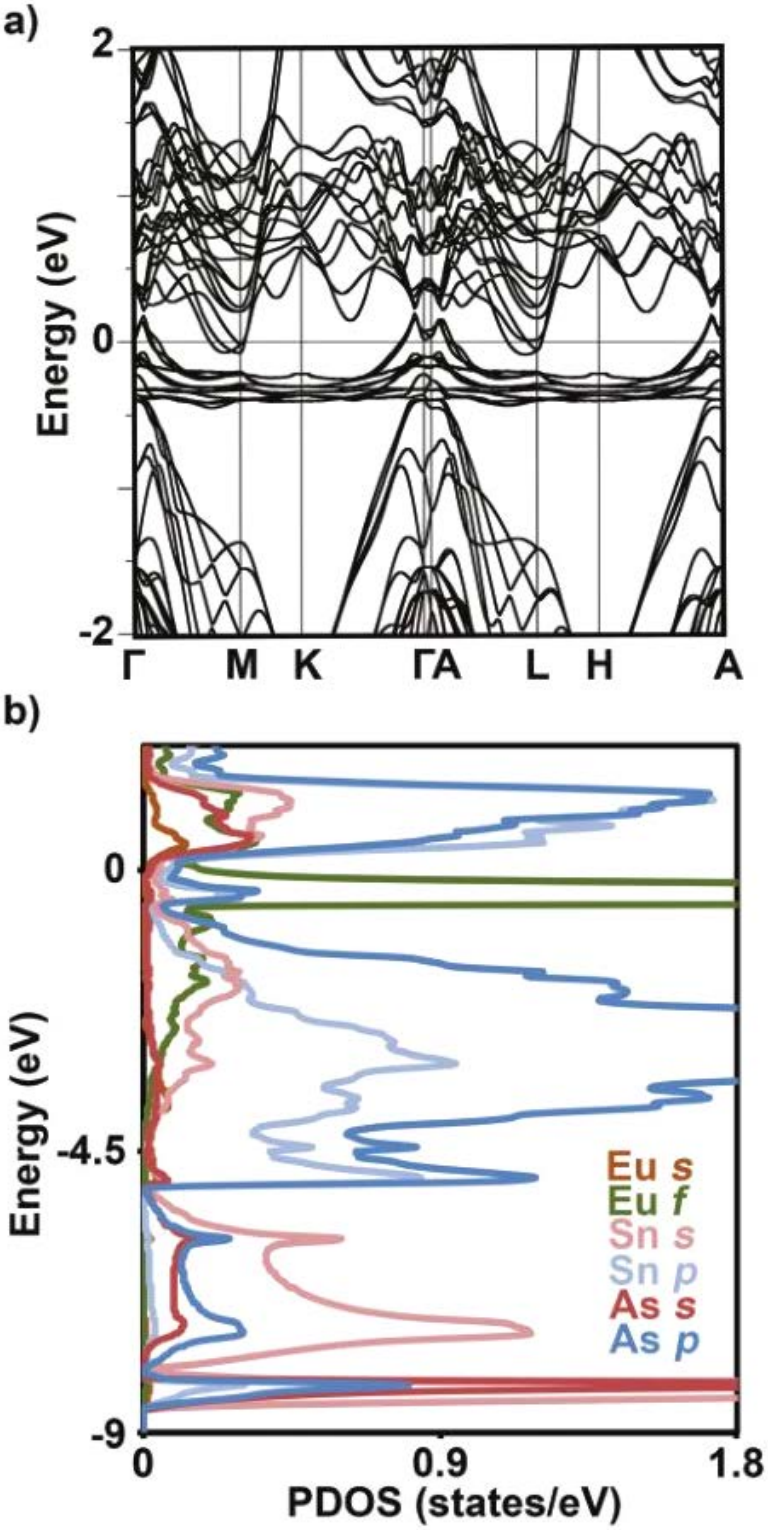

Fig. 1.2.4 (a) Electronic band structure of the antiferromagnetic magnetic ground state of $EuSn_2As_2$ highlighting its semi-metallic nature. (b) Partial density of states (DOSs) of the bands near the Fermi level. These figures are reprinted from Arguilla *et al.* [7].

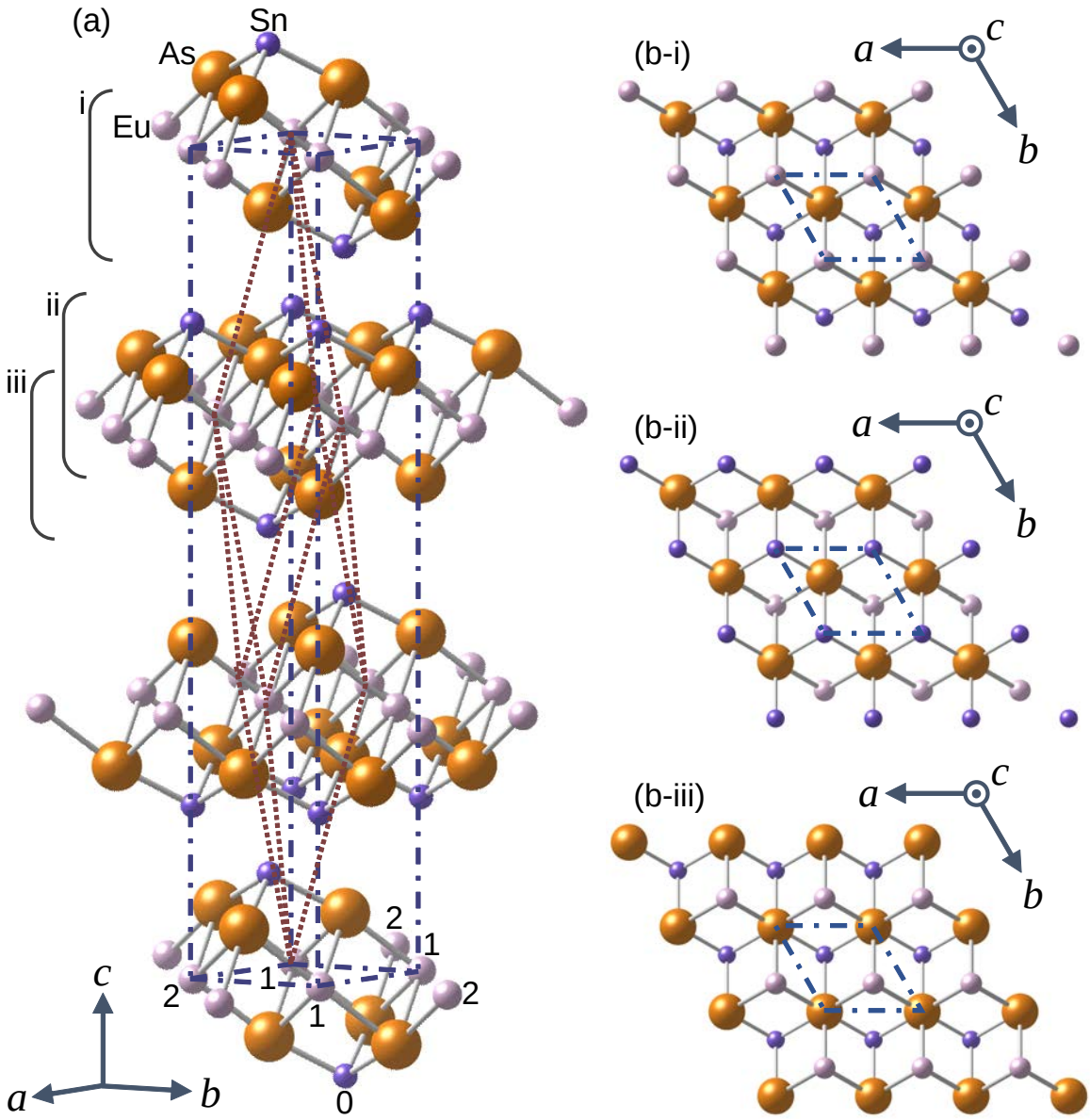

Fig. 1.2.5 Crystallographic structures of $EuSn_2As_2$. (a) was with hexagonal coordinates and with rhombohedral coordinates. (b-i), (b-ii), and (b-iii) show hexagonal lattice, looking down the *c*-axis in the crystallographic structure. Crystallographic structures were drawn using VESTA [9].

2

Syntheses of $EuSn_2As_2$

Parts of this chapter were translated from Sakagami *et al.* [21]

SnAs-based layered compound $EuSn_2As_2$ is a candidate for a TE material due to its "so-called Zintl-phase-like" crystallographic structure. Its crystallographic structure consists of cations of Eu and anionic bilayers of $[Sn_2As_2]^{2-}$. Polycrysalline samples of $EuSn_2As_2$ were parepared by two synthesis procedures. In a procedure, a polycrystalline sample was prepared from a europium (Eu) ingot and tin (Sn) and arsenic (As) powders in an alumina tube. In the other procedure, a polycrystalline sample was prepared from a Eu ingot and a Sn-As pellet in a carbon crucible. $EuSn_2As_2$ was obtained as a dominant phase by both of the procedures, although the purest sample was obtained by the latter procedure.

2.1 Introduction

The study of TE conversion technology has begun with a report on the Seebeck effect, where a temperature difference produces a voltage [22]. Since the development of Bi_2Te_3-based materials by Goldsmid and Douglas [23], studies on TE conversion for practical use has focused on integration of device and modularization of materials for about 30 years [24]. On the other hand, new materials were developed by a relatively small number of research groups [24]. However, since the 1990s, researchers have proposed candidates for materials with new crystallographic structures such as filled skutterudite $CeFe_4Sb_{12}$ [25], intermetallic compound Zn_4Sb_3 [26], and clathrate compound $Sr_6Ga_{16}Ge_{30}$ [27]. These new materials were found with the aid of a concept of a phonon glass and an electron single crystal (PGEC) [24, 28].

As to $EuSn_2As_2$, Arguilla *et al.* reported temperature (T) dependence of electrical resistiv-

Table 2.1.1 Electrical resistivity (ρ), Seebeck coefficient (S), thermal conductivity (κ) and dimensionless figure of merit (ZT) at near room temperature (RT) of $Bi_{0.5}Sb_{1.5}Te_3$ [29,30], $EuZn_{1.8}Cd_{0.2}Sb_2$ [31], $Ca_{0.25}Yb_{0.75}Zn_2Sb_2$ [32], $Ba_{0.98}K_{0.02}Zn_2As_2$ [33], $EuSn_2As_2$ [7] and $NaSn_2As_2$ [34].

Chemical composition	ρ (mΩ cm)	S (μV K^{-1})	κ (W m^{-1} K^{-1})	T (K)	ZT
$Bi_{0.5}Sb_{1.5}Te_3$	1.23(7)	217(10)	0.86(8)	300(3)	1.10(13)
$EuZn_{1.8}Cd_{0.2}Sb_2$	1.0	125	2.29	300	0.2
$Ca_{0.25}Yb_{0.75}Zn_2Sb_2$	0.974	58	1.64	300	0.11
$Ba_{0.98}K_{0.02}Zn_2As_2$	0.68	73	3.0	302	0.08
$EuSn_2As_2$	0.73	-	-	300	-
$NaSn_2As_2$	0.254	-	-	337	-
$NaSn_2As_2$	-	-	3.16	297	-

ity of its single crystal and magnetic susceptibility of its oriented crystal [7]. The temperature dependence of its dimensionless figure of merit ($ZT = S^2T\,\rho^{-1}\kappa^{-1)}$) above RT is unknown as of April 2021 (Table 2.1.1).

The crystallographic structure of $EuSn_2As_2$ belongs to the hexagonal crystal family, the trigonal crystal system, and the rhombohedral lattice system, and its space group is $R\bar{3}m$ under an ordinary temperature and pressure.

Figure 1.2.5 shows cyrstallographic structure of $EuSn_2As_2$ [9]. $EuSn_2As_2$ crystal are similar to Bi_2Te_3 crystal in that they both have a layered structure, a space group of $R\bar{3}m$, and vdW bonding.

$EuSn_2As_2$ crystals were synthesized by a liquid-phase reaction using Eu, Sn, and As as starting materials in an alumina crucible, whose inner and outer diameters are not given in the paper by Arguilla *et al.* [7]. The $EuSn_2As_2$ crystal obtained by Arguilla *et al.* was in the form of pellets with a length and width of 3–5 mm and a thickness of 1–3 mm [7]. It is difficult to measure the TE performance of such a small crystal as a bulk. For TE performance measurement, it is necessary to prepare about 5–10 g of polycrystalline powder.

The study in this chapter establishes a procedure to synthesize polycrystalline sample of $EuSn_2As_2$ close to the single phase. The syntheses of polycrystalline samples are important in materials science, where the accumulation of experiments is essential, and is indispensable for the application to TE power generation modules.

2.2 Experimental

$EuSn_2As_2$ bulk polycrystalline samples were synthesized via liquid-phase reactions by two different methods. The raw materials were Eu mass (Nippon Yttrium; >99.9 wt.%), Sn powder (Kojundo Chemical Lab.; >99.9 wt.%), and As grain (Kojundo Chemical Lab.; >99.999 wt.%).

Eu ingots (10–20 mm mass) were oil-packed when purchased. Several Eu ingots were ultrasonically cleaned with acetone, their surfaces wiped with Kim wipes, and quickly moved into an argon (Ar) atmosphere glove box (GB, MIWA Mfg; O_2, H_2O < 1 ppm).

2.2.1 Method 1: use of an alumina tube

An alumina tube (Nikkato; SSA-S 6B; 99.6 % Al_2O_3; 6 mm of inner diameter; 10 mm of outer diameter) was cut at 40 mm from the bottom of the tube. To dehydrate the alumina tube, it was heated to 850°C for 12 h, then cooled down to 80°C in the furnace, and then quickly transferred into the GB. As shown in Fig. 2.2.1 (a), Eu ingot, As powder, and Sn powder were put into the alumina tube. They were in a stoichiometric ratio of 1 : 2 : 2 and their total mass was 1.0 g. The Eu ingot was obtained by shaving down a Eu mass with a metal file (BAHCO; Homeowners Metal File 8in). The As powder was obtained by grinding As grains with an agate mortar and pestle. These processes were carried out in the GB. The alumina tube containing the mixture was heated in a evacuated silica tube under the conditions shown in Fig. 2.2.2 (a). It was visually confirmed that the silica tube was not broken between Step 1 and Step 2, between Step 2 and Step 3, and after Step 3. As shown in Fig. 2.2.3 (a)–(d), after the heat treatment in Step 3, the alumina tube was taken out by breaking the silica tube. The sample was removed by cutting the alumina tube using a low speed diamond wheel saw (South Bay Technology; MODEL 650) equipped with a diamond cutting wheel (Buehler; 11-4254) with the aid of IsoCut Fluid (Buehlar; 11-1193-128; petroleum distillates, hydrotreated light 60–90 %, olive oil 30–40 %) as a lubricant.

Parts of the sample was powderized using an agate mortar and pestle and then packed in a reflection free sample holder of Si (window diameter: 5 mm) for powder X-ray diffraction (XRD). Identification of the crystallographic phase was performed using an X-ray diffractometer (Rigaku; RINT2500Ultra; Cu Kα source). Si powder (NIST; SRM 640d) was used as an standard reference material to calibrate diffraction angle (2θ) of XRD measurement.

2.2.2 Method 2: use of a carbon crucible

Sn and As powders were mixed with an agate mortar and pestle. They were in a stoichiometric ratio of 1 : 1 and their total mass was 0.7182 g. The As powder was obtained by grinding As grains with an agate mortar and pestle. A Sn-As pellet were obtained by uniaxial pressing at 20 MPa using a foot-operated hydraulic pump (Riken Seiki; P-6).

A Eu ingot was obtained by shaving down a Eu mass with the metal file. The Eu ingot and the Sn-As pellet were in a stoichiometric ratio of 1 : 2. They are placed in a carbon crucible (Niraco; C-070658; 99.99 % carbon; 9 mm of inner diameter; 10 mm of outer diameter) as shown in Fig. 2.2.1 (b). These processes were conducted in the GB. The carbon crucible containing the Eu ingot and the Sn-As pellet was heated in a evacuated silica tube under the conditions shown in Fig. 2.2.2 (b).

After the heat treatment as shown in Fig. 2.2.3 (e)–(h), the carbon crucible was taken out by breaking the silica tube. The carbon crucible was wrapped in aluminum foil and broken with a hammer to collect the sample. The obtained sample was then cut out by rubbing a diamond cutting wheel against them with no lubricant. Fig. 2.2.3 (h) shows an optical microscope (Olympus; SZ60) image of parts of the sample. Powder XRD measurement was performed to examine the powderized sample.

2.3 Results and discussion

The powder XRD patterns of the obtained samples are shown in Fig. 2.3.1. In Method 1, $EuSn_2As_2$ was obtained as the main phase, and Eu_3As_4, Sn, and an unknown phase were obtained as secondary phases. On the other hand, in Method 2, $EuSn_2As_2$ was obtained as the main phase, and only Sn was obtained as a secondary phase. In other words, the $EuSn_2As_2$ sample closest to the single phase in our experiments was obtained by Method 2. The sample obtained by Method 2 shows any secondary phase other than Sn. The reason for this is that Method 2 suppressed the solid-state reaction for Eu and As. Indeed, the maximum heating temperature of both of method 1 and 2 (850°C) was higher than melting points of elemental Eu and any Sn-As binary compounds while it was lower than those of some Eu-Sn and Eu-As compounds (Figs. 2.3.2, 2.3.3, and 2.3.4).

Figure 2.3.5 shows the dependence of the lattice parameter of $EuSn_2As_2$ on the synthesis procedure. The lattice parameter a of the sample prepared by Method 1 is smaller than that

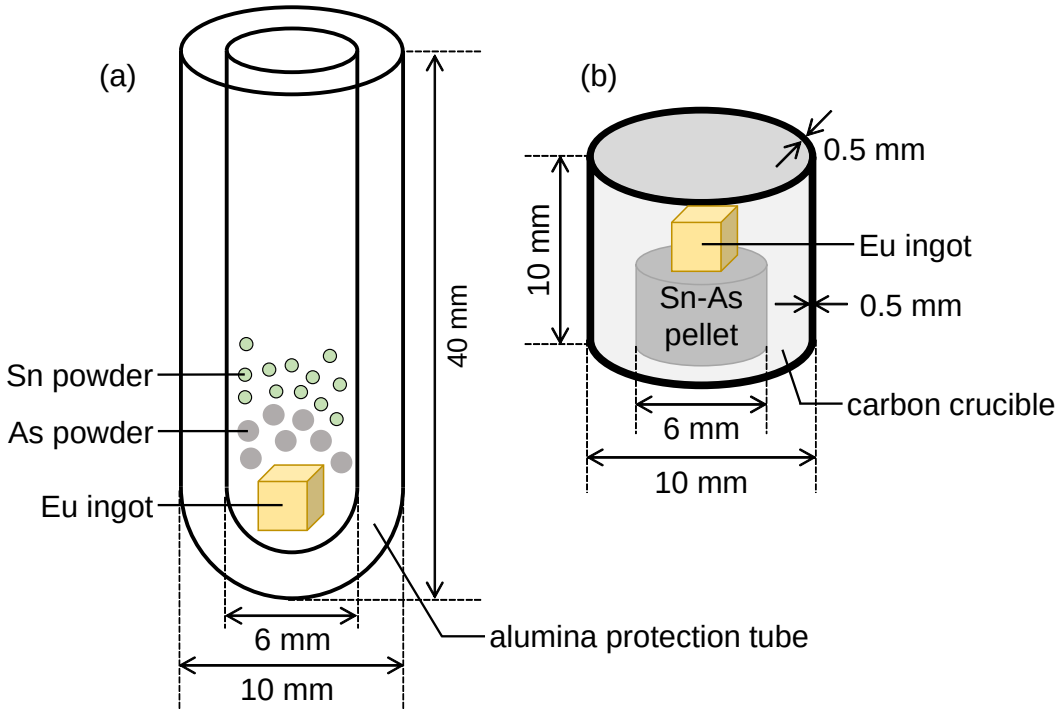

Fig. 2.2.1 Starting materials of polycrystalline samples of as-grown $EuSn_2As_2$ and their containers, which highlights the difference of two sysnthesis procedures. (a) The first sysnthesis procedure in which a sample was prepared from europium (Eu) ingot and tin (Sn) and arsenic (As) powder in an an alumina protection tube. (b) The second sysnthesis procedure in which a sample was prepared from Eu ingot and Sn-As pellet in a carbon crucibe.

of Method 2, while c of the sample prepared by Method 2 is larger than that of Method 1. It is considered that $EuSn_2As_2$ has an indeterminate ratio and the chemical composition differs among the samples. The lattice constants of the samples of Method 1 and Method 2 were inconsistent with those of Arguilla *et al.* [7] within the experimental standard deviation, which may be due to the deviation from the stoichiometric ratio or difference in the standard sample used for calibration of the optical axis of XRD.

In Method 1, the sample was hard to collect because it adhered to the alumina tube which was too hard and thick to be broken with a hammer, although the sample did not react with the alumina tube obviously. This problem may be solved by using alumina tube whose thickness of 0.5–1.5 mm. Cut surface of the sample by Method 2 showed a glossy appearance (Fig. 2.2.3 (h)).

The powderized sample is black, and the luster is considered to be a metallic luster caused by the plasma oscillation of electrons. It is consistent with the conclusion by Arguilla *et*

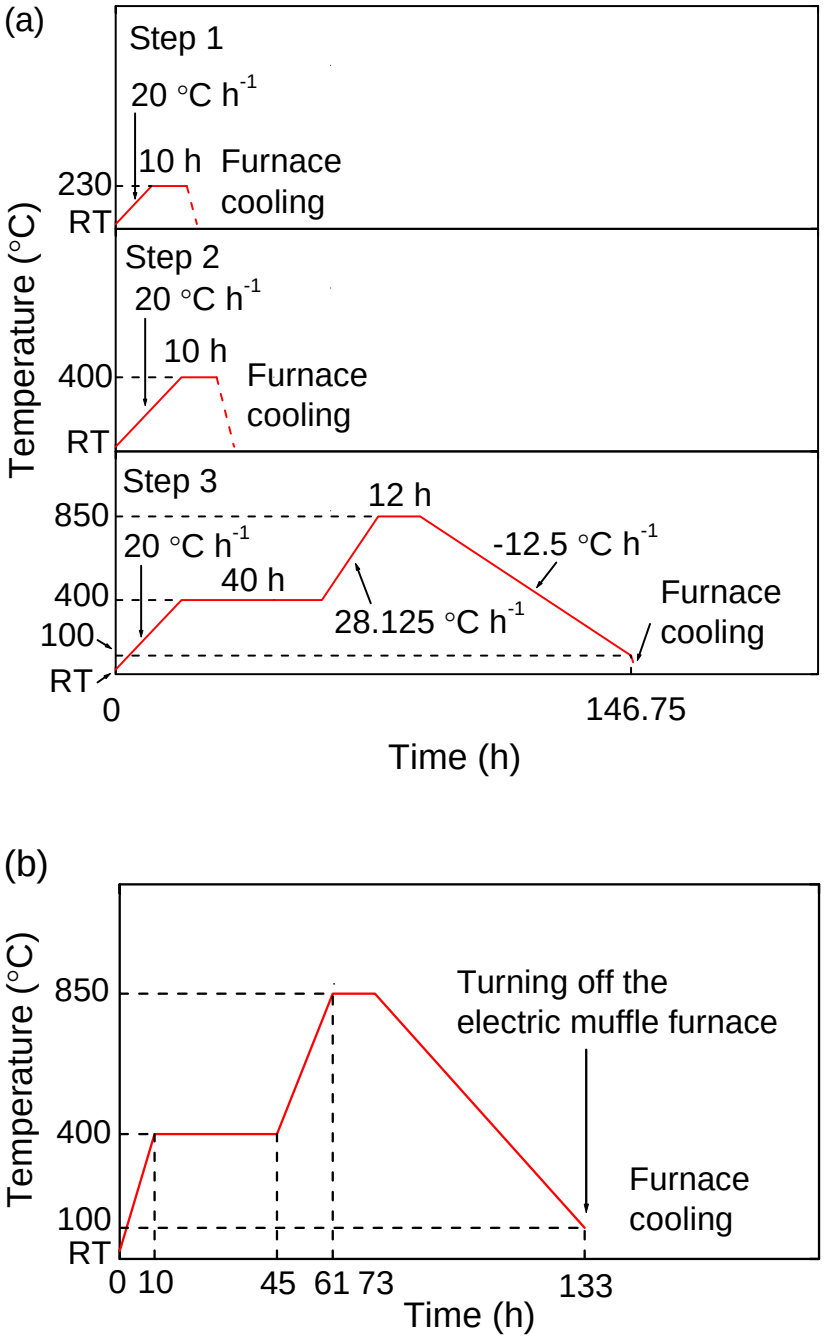

Fig. 2.2.2 Heat treatment conditions of preparation of polycrystalline samples of as-grown $EuSn_2As_2$ (a) prepared from Eu ingot and Sn and As powders in an alumina protection tube and (b) prepared from Eu ingot and Sn-As pellet in a carbon crucible.

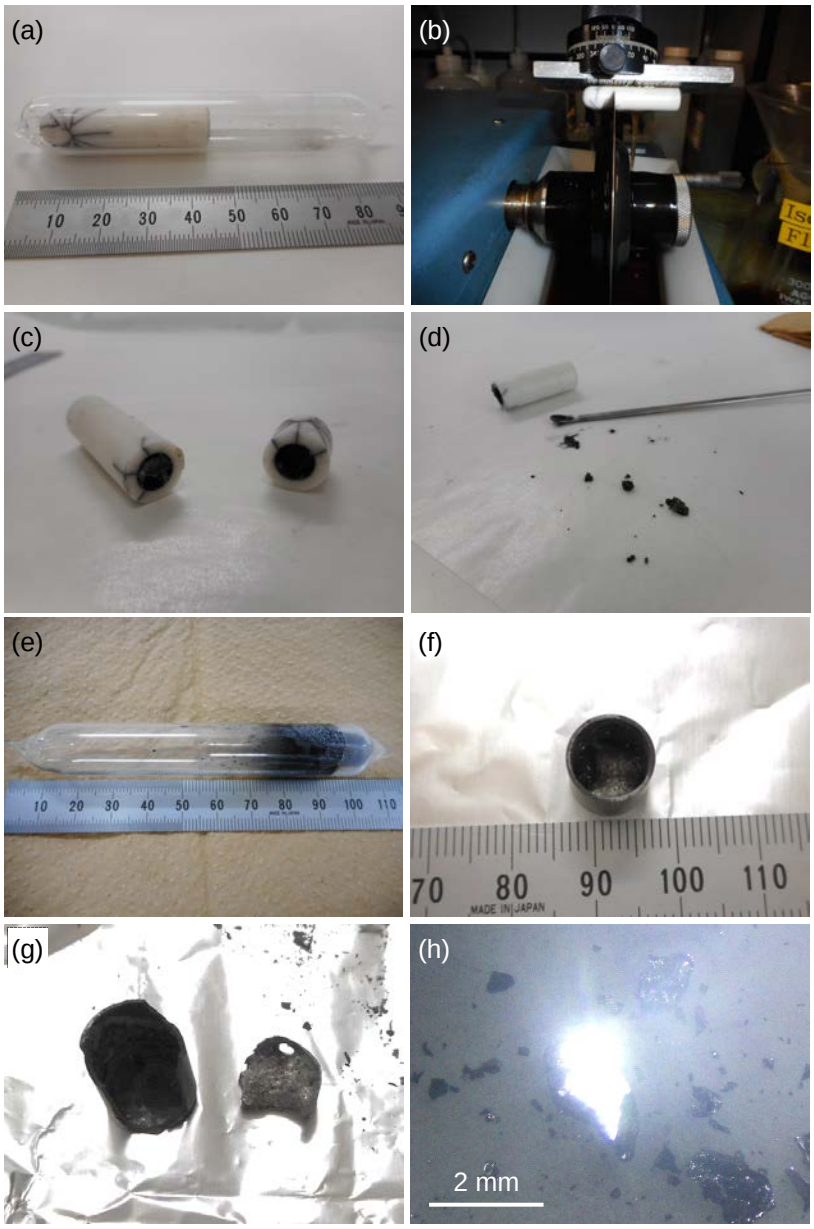

Fig. 2.2.3 Photographs in procedures taking out polycrystalline samples of as-grown $EuSn_2As_2$ after heat treatment (a)–(d) when an alumina protection tube was used and (e)–(h) when a carbon crucible was used. (a) The alumina protection tube including the sample in the silica tube. (b) The alumina protection tube including the sample cut off by low speed diamond wheel saw using the IsoCut Fluid. (c) The alumina protection tube shown in (b) after cutting. (d) The sample with the IsoCut Fluid scooped out before pulverization. (e) The carbon crucible including the sample in the silica tube, where its inner face was attached black matters. (f) The carbon crucible indluding the sample. (g) The carbon crucible (left) and the sample (right) after smashing the carbon crucible shown in (f) in aluminum foil with a hammer. (h) Optical microscope image of the sample cut off by diamond wafering blade for low speed diamond wheel saw before pulverization when exposed to light.

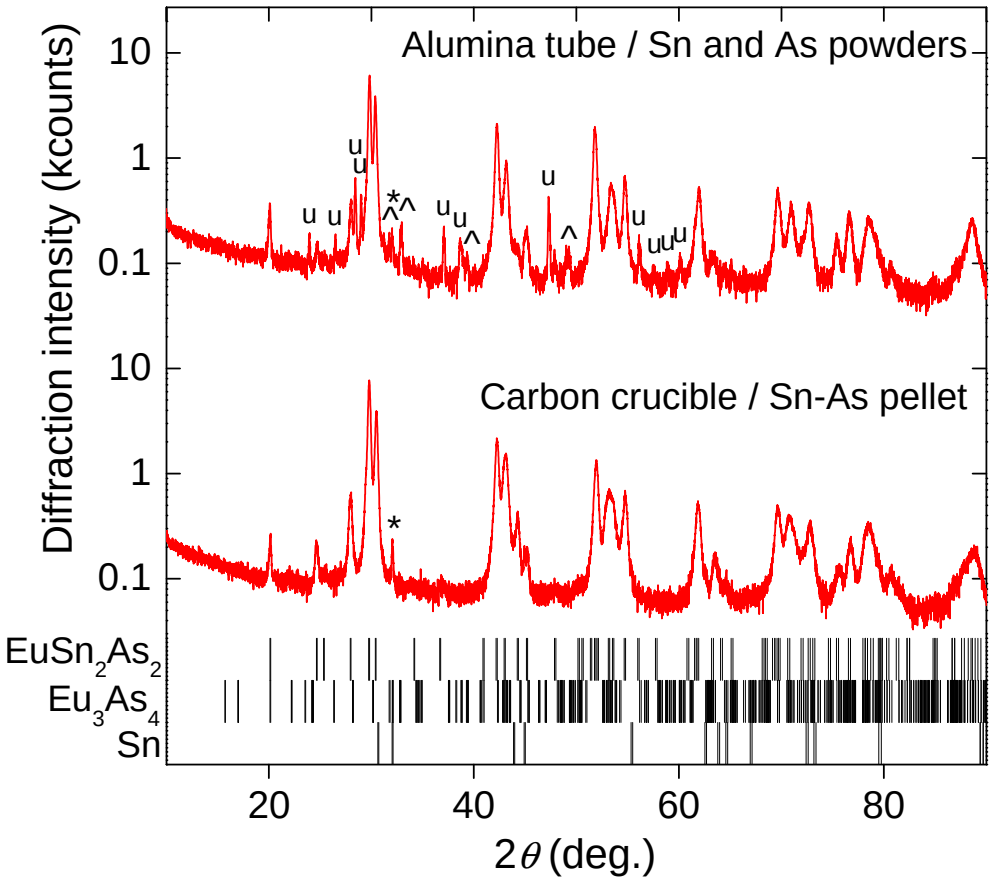

Fig. 2.3.1 Synthesis procedure dependence of X-ray diffraction (XRD) patterns of $EuSn_2As_2$ samples (one prepared from a Eu ingot and Sn and As powders in an alumina tube and one prepared from a Eu ingot and a Sn-As pellet in a carbon crucible) at RT. The vertical bars at the bottom represent calculated [9] positions of Bragg diffractions of $EuSn_2As_2$ [7], Eu_3As_4 [36] and Sn [38] from above. The circumflex accent (ˆ), the asterisk ($*$) and the letter called "u" denote Bragg diffractions due to Eu_3As_4, Sn and unknown phases, respectively.

al. that $EuSn_2As_2$ is semi-metallic. The weight of the sample recovered by Method 2 was 0.8050 g.

2.4 Short summary

In order to obtain near-single-phase polycrystalline samples of SnAs-based layered compound $EuSn_2As_2$ as a candidate for TE materials, we have established a method of synthesis

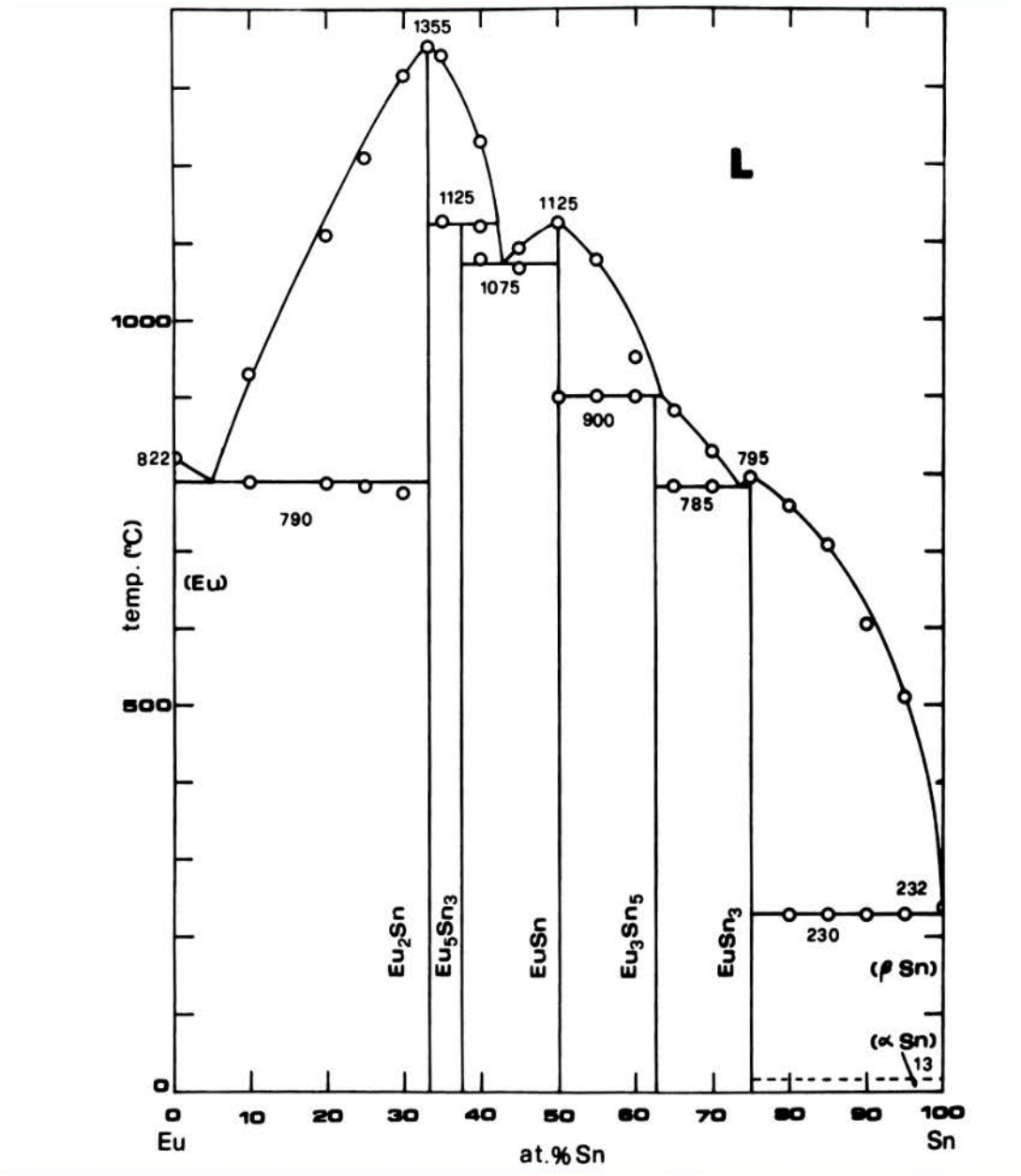

Fig. 2.3.2 Eu-Sn binary phase diagram 0–100 at.%Sn. This figure is reprinted from Palenzona *et al.* [35].

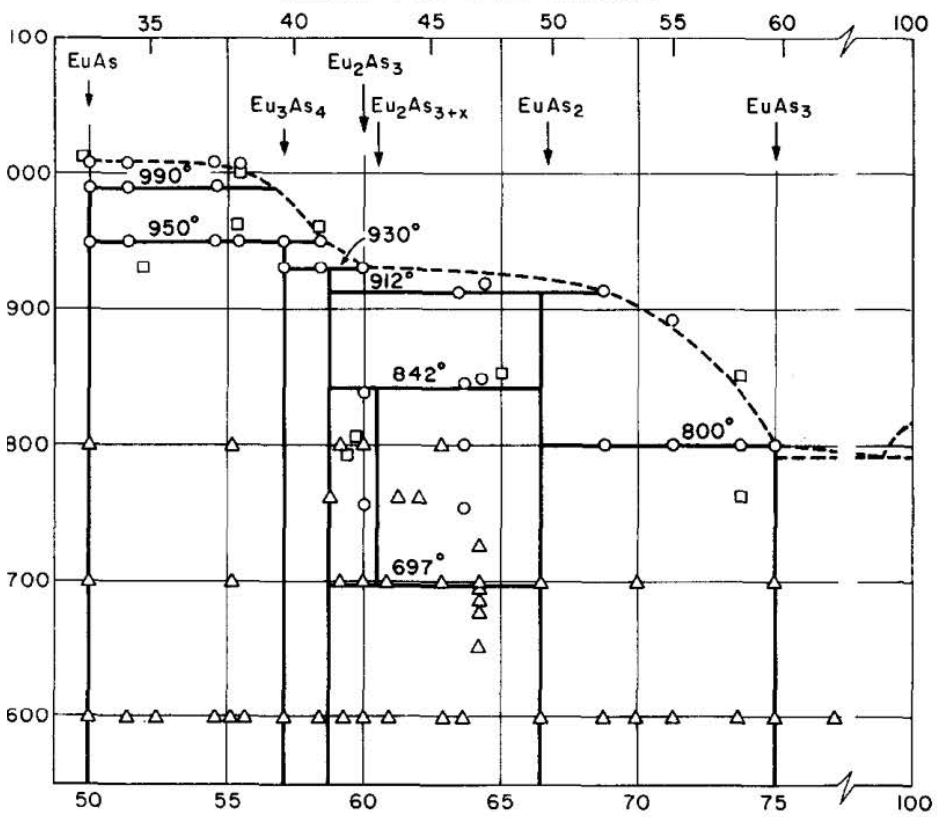

Fig. 2.3.3 Eu-As partial binary phase diagram at.%As. Rising thermal effects (○); fast quench in Ta capsules (□); anneal in fused silica ampoules (△). This figure is reprinted from Ono *et al.* [36].

procedure in which a sample was prepared from Eu ingot and Sn-As pellet in a carbon crucible. As far as our trials were concerned, this synthesis method produced polycrystalline samples free from second phases other than Sn, unlike another syntehsis method in which a sample was prepared from Eu ingot, Sn powder, and As powder in alumina tube. In the method using carbon crucible, 0.8050 g of the 0.9812 g of raw material was recovered. Several trial of this synthesis method will yield an adequate amounts of samples of $EuSn_2As_2$ for TE transport measurements.

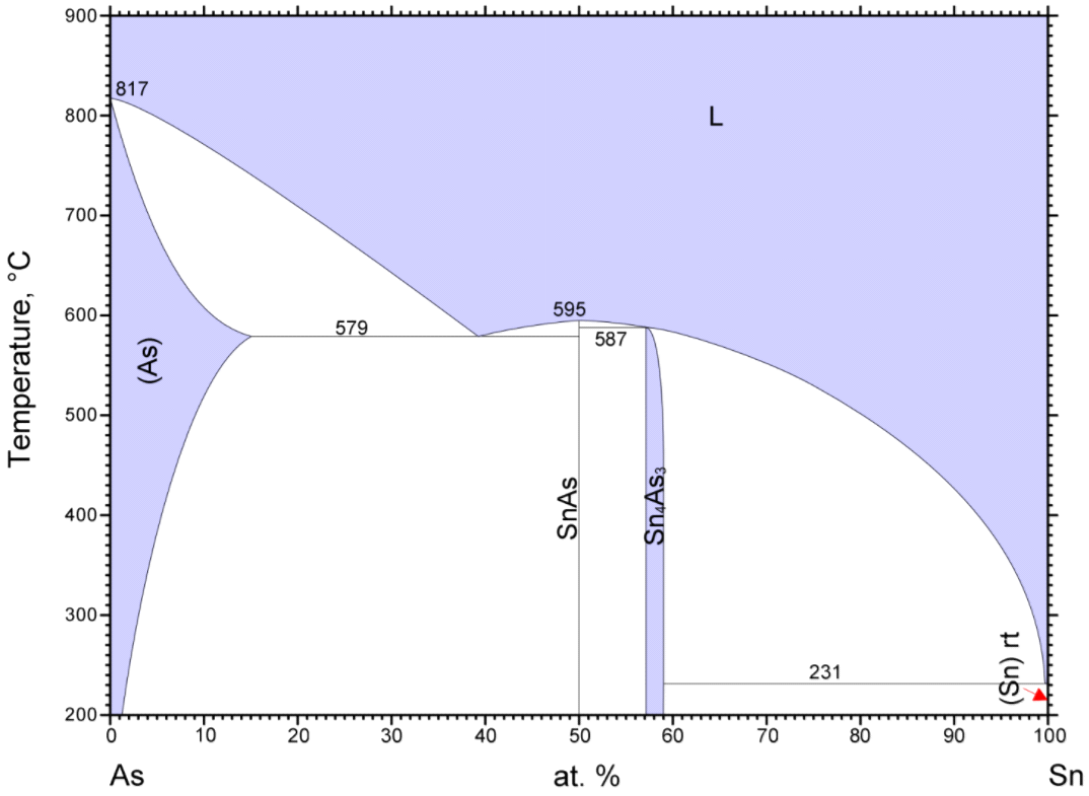

Fig. 2.3.4 As-Sn binary phase diagram 0–100 at.%Sn. This figure is reprinted from Springer Materials, which is based on Gokcen [37].

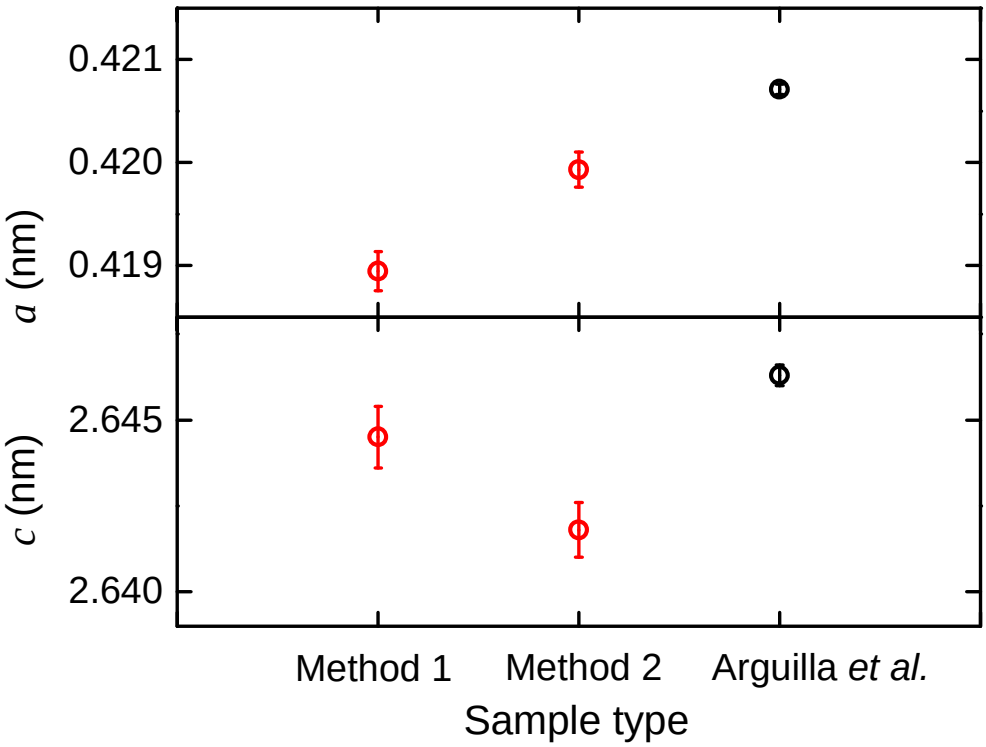

Fig. 2.3.5 Lattice constants of samples of $EuSn_2As_2$. Parts of data are collected from Arguilla *et al.* [7].

3

Experimental for transport property measurements

3.1 Electrical resistivity (ρ) measurement

Temperature (T) dependence of the electrical resisitivity (ρ) for superconductors below RT was measured using a current source (Yokogawa 7651 Programmable DC source), an ammeter (Keithley 2001 Multimeter) and a voltmeter (Keithley 2182 Nanovoltmeter) with the aid of temperature controller (Lakeshore 331) in a hand-made Gifford–McMahon (GM) cooler.

Temperature dependence of the ρ as one of the TE properties above RT was measured using a current source, an ammeter, and a voltmeter. In the measurements, T was controlled by a commercially supplied program for an infrared lamp heating system (Advance Riko MILA-5000). The infrared lamp heating system is illustrated in Fig. 3.1.1.

The measurement programs are written in Laboratory Virtual Instrumentation Engineering Workbench (LabVIEW). The details of the programs for the low-temperature measurements are shown in section B.1.

ρ of specimen was obtained using equations below:

$$V_{23} = RI + V_0, \tag{3.1}$$

$$\rho = \frac{wt}{d}R, \tag{3.2}$$

where V_{23} is voltage between voltage terminals on the specimen, R is electrical resistance of the specimen, I is electrical current thorough the specimen, V_0 is offset voltage, w is width of

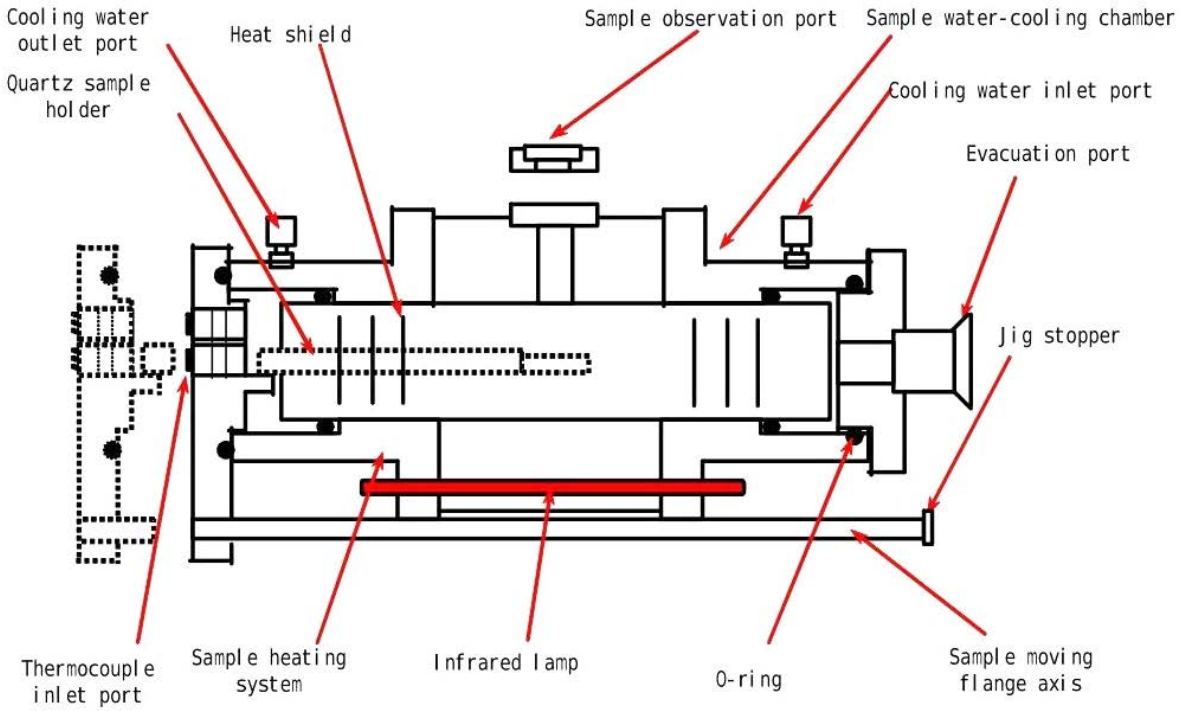

Fig. 3.1.1 Schematic diagram of infrared lamp heating system, MILA-5000. This figure is reprinted from Advance Riko (its former company name: ULVAC-RIKO) [39].

the specimen, t is thickness of the specimen, d is the distance between the electrical current terminals on the specimen[*1]. Raw data obtained by measurements were post-processed with the aid of Python programs shown in section B.2. Measurement temperatures were calibrated using a specimen of $GdFeAsO_{0.943}F_{0.057}$ as a standard reference specimen (Gd1111stn).

3.2 Seebeck coefficient (S) measurement

Measurement value of S was calculated as the the difference between the reported value of platinum (Pt) [40, 41] and experimentally observations ($S_{\mathrm{Pt}} - S_{\mathrm{obs}}$). S_{obs} was obtained from the slope of several plots of themoelectromotive force (V_{ul}) versus temperature difference ($T_{\mathrm{l}} - T_{\mathrm{u}}$) in the Seebeck effect.

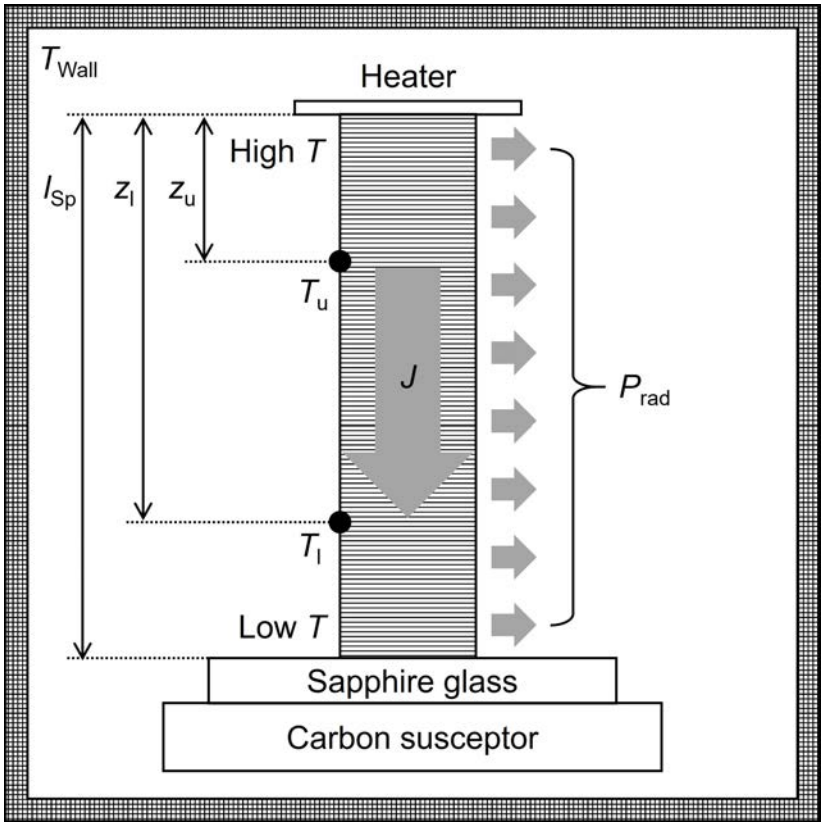

Fig. 3.3.1 Schematic diagram of inside of MILA-5000. It is noted that thermocouples are omitted in this diagram to avoid complexity.

3.3 Steady-state thermal conductivity ($^{SS}\kappa$) measurement

The basic equation of thermal conduction, Fourier's law is as follows [42, 43]:

$$J = -{}^{SS}\kappa \frac{T_u - T_l}{z_u - z_l}. \tag{3.3}$$

The steady-state method evaluates heat flux (J) through the specimen and steady-state temperature gradient ($-(T_u - T_l)/(z_u - z_l)$). This situation is adequate for practical TE power generation. The $^{SS}\kappa$ was obtained from slopes in several plots of $-(T_u - T_l)/(z_u - z_l)$ versus J.

In the present study, we demonstrate direct measurement of $^{SS}\kappa$ and estimate the effects of leakage of radiation heat (P_{rad}) in the measurement of $^{SS}\kappa$ (Fig. 3.3.1). The J was mainly calculated as Joule heat in the heater and was partly affected by both loss of thermal conduction

[*1] Electrode settings of specimens for high-temperature measurement are shown in Fig. 4.2.2. Those for low-temperature measurement are shown in Fig. C.2.4.

from the specimen to the thermocouples and loss of thermal radiation from the specimen and the thermocouples to the furnace wall. The P_{rad} for the specimen was calculated using the following equations:

$$P_{\mathrm{rad}} = \iint_A F \mathrm{d}A \tag{3.4}$$

$$F = \varepsilon_{\mathrm{Sp}} \sigma_{\mathrm{SB}} ({T_{\mathrm{Sp}}}^4 - {T_{\mathrm{Wall}}}^4) \tag{3.5}$$

$$\sigma_{\mathrm{SB}} = \frac{2\pi^5 {k_{\mathrm{B}}}^4}{15 h^3 c^2} \tag{3.6}$$

$$T_{\mathrm{Wall}} = \frac{T_{\mathrm{l}} - T_{\mathrm{u}}}{z_{\mathrm{l}} - z_{\mathrm{u}}} (l_{\mathrm{Sp}} - z_{\mathrm{u}}) + T_{\mathrm{u}} \tag{3.7}$$

where A is a surface area of the specimen, $\varepsilon_{\mathrm{Sp}}$ is an emissivity of the specimen, l_{Sp} is a length of the specimen, z_{u} is a distance between the top of the specimen and the upper terminal, z_{l} is a distance between the top of the specimen and the lower terminal, T_{Sp} is temperature of specimen, T_{l} is temperature of the upper terminal, T_{u} is temperature of lower terminal, T_{Wall} is temperature of inner wall of MILA-5000. The T_{Sp} was obtained by interpolation or extrapolation from measurement values of T_{u} and T_{l}. The T_{Wall} is an extrapolation value, as indicated in Eq. 3.7. The σ_{SB} represents the Stefan–Boltzmann constant.

3.4 Short summary

Automation of measurements were necessary for experimental competitive development research of TE materials and superconductors. Automated measurements in our laboratory of electrical resistivity (ρ) above and below RT, Seebeck coefficient (S) above RT, and steady-state thermal conductivity (${}^{\mathrm{SS}}\kappa$) at RT were realized using the Laboratory Virtual Instrument Engineering Workbench (LabVIEW) programs for controlling electronic test equipments and temperature controllers. Obtained measurement raw data were processed using Python code to obtain physical quantities. Particularly, we established calculation processes for obtaining ${}^{\mathrm{SS}}\kappa$ considering loss of thermal radiation. The above-mentioned work will achieve reduction in working hours and also will prevent careless mistakes.

4

Thermoelectric (TE) transport properties of $EuSn_2As_2$

Parts of this chapter were reproduced from Sakagami *et al.* [44].

The TE transport properties of the van der Waals-type layered rhombohedral SnAs-based compound, $EuSn_2As_2$, have been investigated. A densified polycrystalline sample of $EuSn_2As_2$ with porosity (ϕ) of 2.4(9) vol.% exhibited a weak orientation to the c-axis for hexagonal coordination system; the weak orientation is parallel ($\mathbf{P}_{\parallel}$) to the pressing direction of hot pressing. Measurements of electrical resistivity (ρ), Seebeck coefficient (S), and thermal conductivity (κ) were conducted perpendicular ($\mathbf{P}_{\perp}$) to the pressing direction. The experimental values of ρ and S exhibit metallic temperature dependence and p-type carrier polarity. The power factor (P) was 0.51(8) mW m^{-1} K^{-2} at 673(4) K. Using the Wiedemann–Franz–Lorenz law, the phonon thermal conductivity (κ_{ph}) was estimated to be 0.4(6) W m^{-1} K^{-1} at 673(6) K. The dimensionless figure of merit, ZT, was 0.092(17) at 673(3) K.

4.1 Introduction

TE materials are important for energy harvesting research [45, 46], which focuses on producing Gibbs free energy (G) from variations in the absolute temperature (T), pressure (p), and chemical potential of the ith component (η_i) in a heterogeneous system, as follows:

$$\mathrm{d}G = -\mathscr{S}\mathrm{d}T + \mathscr{V}\mathrm{d}p + \sum_i \eta_i \mathrm{d}N_i \tag{4.1}$$

where $\mathscr{S}$ is entropy, $\mathscr{V}$ is volume, and N_i is the number of particles, including carriers, atoms, and molecules of the ith component in the system [47–51]. One of the primary purposes of energy harvesting is to improve the efficiency of TE generators. TE conversion performance is characterized by a dimensionless figure of merit, ZT, which is based on the figure of merit of the material (Z) [52].

TE materials, which directly convert heat to electricity, could play an important part in research and development on energy harvesting from waste heat [53]. TE conversion performance of TE materials is governed by a dimensionless figure of merit, ZT, which is defined as follows:

$$ZT = \frac{S^2 T}{\rho\kappa} \tag{4.2}$$

where S, T, ρ, and κ are the Seebeck coefficient, absolute temperature, electrical resistivity, and thermal conductivity, respectively.

κ is calculated as follows:

$$\kappa = \kappa_{\mathrm{el}} + \kappa_{\mathrm{ph}} \tag{4.3}$$

where κ_{el} and κ_{ph} are the electronic and phonon thermal conductivities.

Lower values of ρ and κ are crucial for higher ZT values. TE materials with high ZT is required for high-efficiency TE devices.

Various TE materials have been investigated since a proposal of the concept of PGEC in 1995 [28]. Among them, one of attractive system for TE materials are compounds with a 1 : 2 : 2 compositional ratio (so-called "122 compounds") [54–56]. Promising TE properties of 122 compounds have been reported on AZn_2Sb_2 (A = Ca, Sr, Eu, Yb) [32, 57], (Ca,Yb)Cd_2Sb_2 [58], Eu(Zn,Cd)$_2Sb_2$ [31], Yb(Zn,Cd)$_2Sb_2$ [59], $YbZn_{2-x}Mn_xSb_2$ [60], Yb(Cd,Mn)$_2Sb_2$ [61], Mg_3Sb_2 [62], $Mg_{3-x}M_xSb_2$ (M = Zn, Mn, Na) [63–65], $Mg_3Sb_{2-x}Bi_x$ [66], $Mg_3Sb_{2-x}Pb_x$ [67], $Mg_{3+\delta}Sb_{2-x}Bi_{x-y}Te_y$ [68, 69], and (Ca,Yb,Eu)Mg_2Bi_2 [70–72] with the $CaAl_2Si_2$ [73] structure-type (hexagonal $P\bar{3}m1$ space group) as well as $BaZn_2Sb_2$ [74] with the α-$BaCu_2S_2$ [75] structure-type (orthorhombic *Pnma* SG). In particular, $Mg_3Sb_{1.48}Bi_{0.48}Te_{0.04}$ exhibits ZT = 1.65 at 725 K [69]. These studies employed antimony (Sb) and bismuth (Bi) as its constituent pnictogen (*Pn*); until a few years ago, rare investigations have been reported on TE properties of 122 compounds of lighter *Pn*, such as arsenic (As) and phosphorus (P). Recent studies demonstrate potential TE performances of As-based 122 compounds, namely, $Ba_{1-x}K_xCd_2As_2$ [76], $Ba_{1-x}K_xZn_2As_2$ [33, 77], and $NaSn_2As_2$ [34]. Their crystals are categorized into the $CaAl_2Si_2$ structure-type [76], α-$BaCu_2S_2$ structure-type [33, 77], $ThCr_2Si_2$ [78] structure-type (tetragonal $I4/mmm$

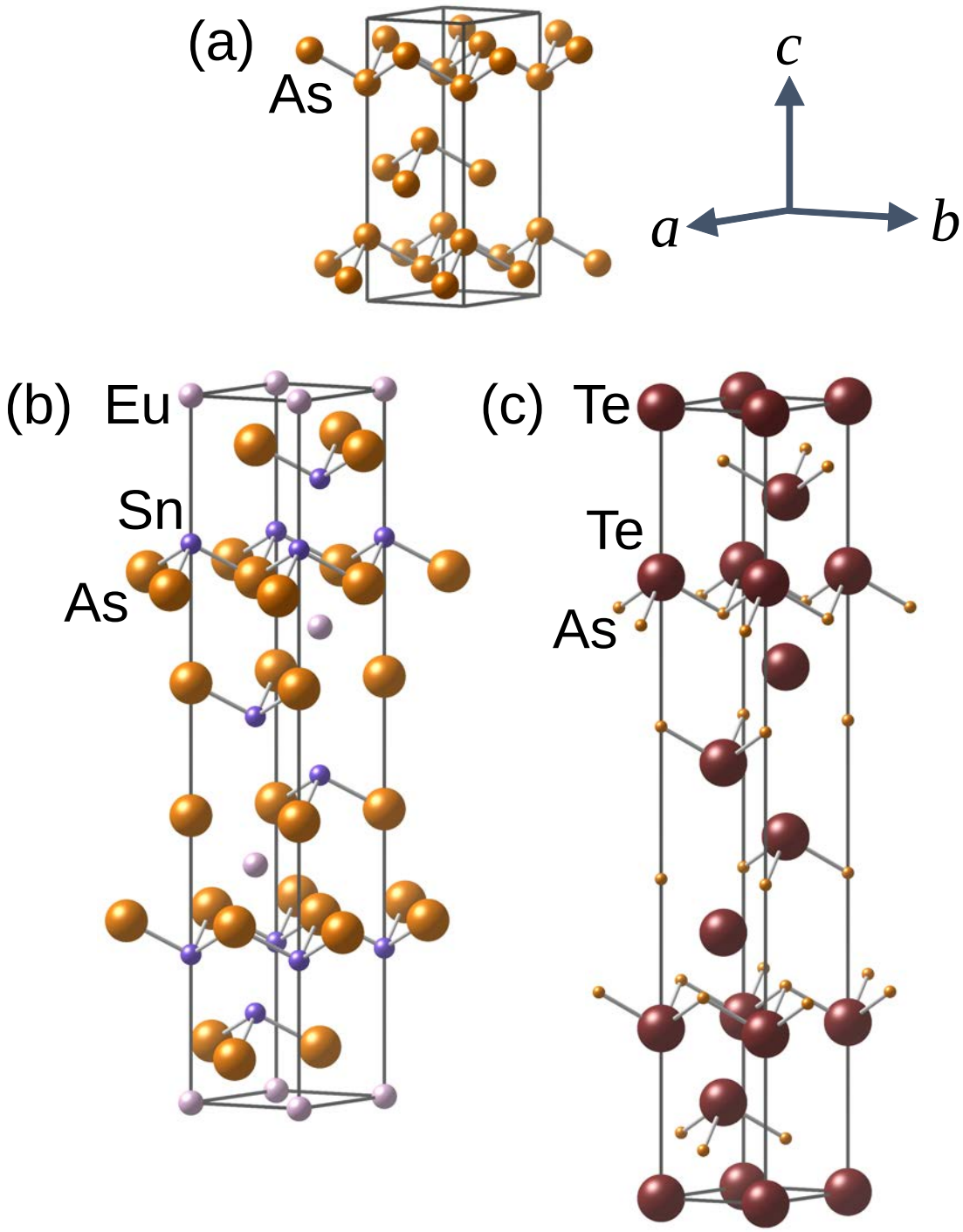

Fig. 4.1.1 Crystallographic structures of layered rhombohedral $R\bar{3}m$ materials, (a) gray arsenic (α-As) [6], (b) $EuSn_2As_2$ [7], and (c) β-As_2Te_3 [82] in the hexagonal coordinate system. Crystallographic structures were drawn using VESTA [9].

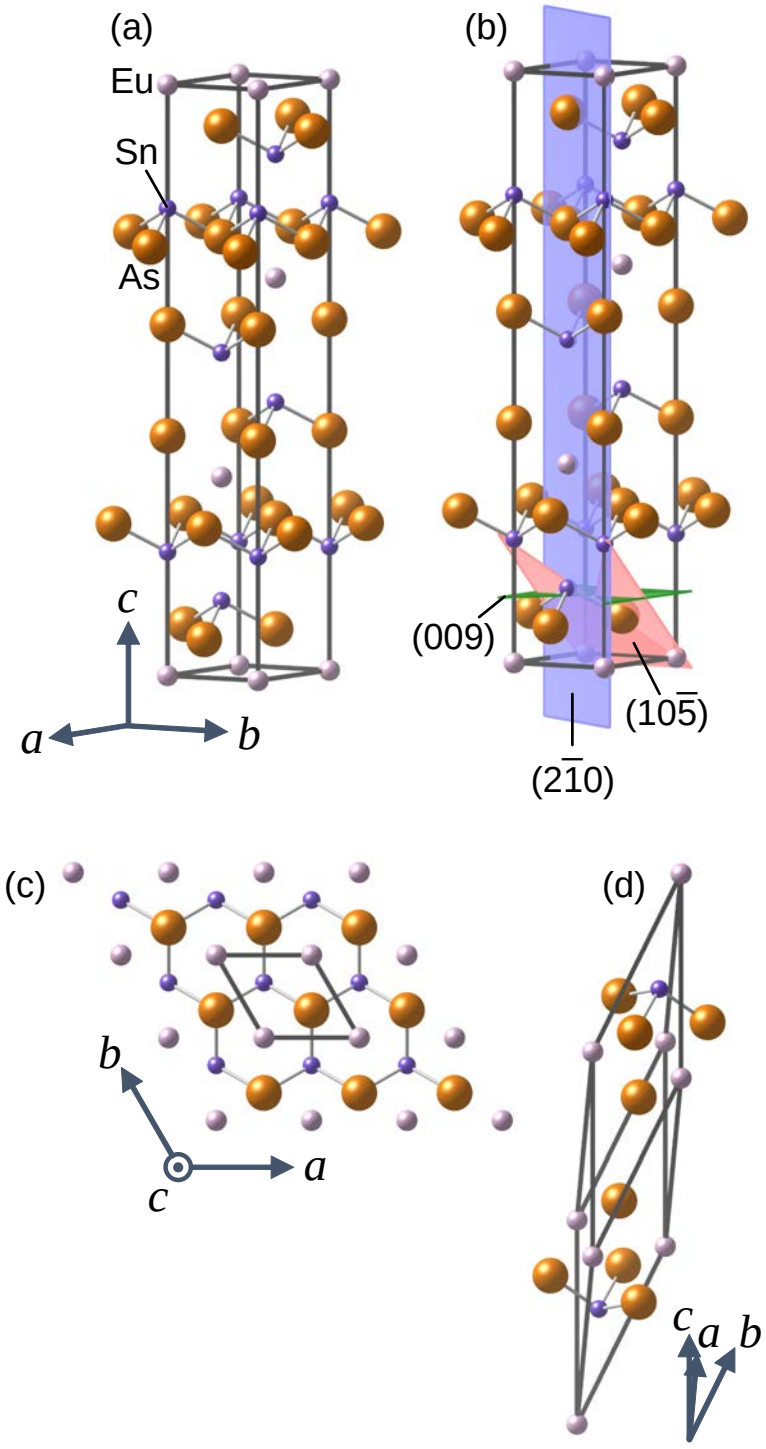

Fig. 4.1.2 Crystallographic structures of $EuSn_2As_2$ [7] with the Bi_2Te_2S [79] structure-type [80] (rhombohedral $R\bar{3}m$ space group). (a)–(c) were with hexagonal coordinates. (b) shows representative 009, 10$\bar{5}$, and 2$\bar{1}$0 lattice planes. (c) exhibits hexagonal lattice looking down the c-axis in the crystallographic structure. (d) was with rhombohedral coordinates. Crystallographic structures and lattice planes were drawn using VESTA [9].

SG) [33, 77], or Bi_2Te_2S [79] structure-type [80] (rhombohedral $R\bar{3}m$ SG) [34]. It is worth investigating TE properties of As-based 122 compounds with different crystallographic structures. However, there is only one report on TE properties of the Bi_2Te_2S structure-type As-based 122 compounds. The report describes $NaSn_2As_2$ with ρ of 0.254 mΩ cm at 337 K and κ of 3.16 W m^{-1} K^{-1} at 297 K but provides no infromation about its S [34].

In the present study, we demonstrate the TE properties of As-based 122 compound, $EuSn_2As_2$. $EuSn_2As_2$ has layered crystallographic structure like other As-based materials (Fig. 4.1.1). The crystal of $EuSn_2As_2$ has the Bi_2Te_2S structure-type (Fig. 4.1.1) and is characterized by alternate stacking of europium (Eu) cation layers and honeycomb-like SnAs anionic bilayers (Fig. 4.1.2 (c)), which are bound by vdW forces between tin (Sn) cations [7]. Since the vdW bonding is relatively weak, $EuSn_2As_2$ is capable of producing nanometer-scale thickness sheets by exfoliation [7]. Recently, $EuSn_2As_2$ is also attained attention from the viewpoint of topological materials [11, 12, 20]. Furthermore, its related compounds with the same structure-type, such as $Na_{1+x}Sn_{2-x}As_2$ [13–16] and $Na_{1-x}Sn_2P_2$ [81], are found to show superconductivity at low temperature. Thus, investigations regarding detailed transport properties of $EuSn_2As_2$ are required to obtain insights in physical properties of Sn*Pn*-based layered compounds. Here, we present high-temperature TE transport properties of polycrystalline $EuSn_2As_2$. The obtained properties are compared with those of other TE materials.

4.2 Experimental

Polycrystalline samples of $EuSn_2As_2$ were synthesized from Eu ingots and Sn-As pellets via a liquid phase reaction in graphite crucibles within evacuated silica tubes according to our previous report [21]. Sn-As pellets were fabricated from mixtures of Sn and As powders [21]. These polycrystalline samples, defined as "as-grown $EuSn_2As_2$" and two precursors, were prepared using different heat treatment conditions as shown in Figs. 4.2.1 (a) and 4.2.1 (b-1). We defined "as-grown $EuSn_2As_2$" as a representative polycrystalline sample of $EuSn_2As_2$. For obtaining a polycrystalline powder used for a hot pressing process, 0.681(1) g of the first precursor (named "precursor I") and 0.826(1) g of the second precursor (named "precursor II") were mixed. 1.41(2) g of the mixed powder was wrapped in graphite sheets and loaded into graphite dies. The outside of these graphite sheets was dusted with a BN powder before loading. During the hot pressing process, the dies were heated to 600°C for 30 min as shown in Fig. 4.2.1 (b-2) under a uniaxial pressure of 50 MPa and an Argon (Ar) at-

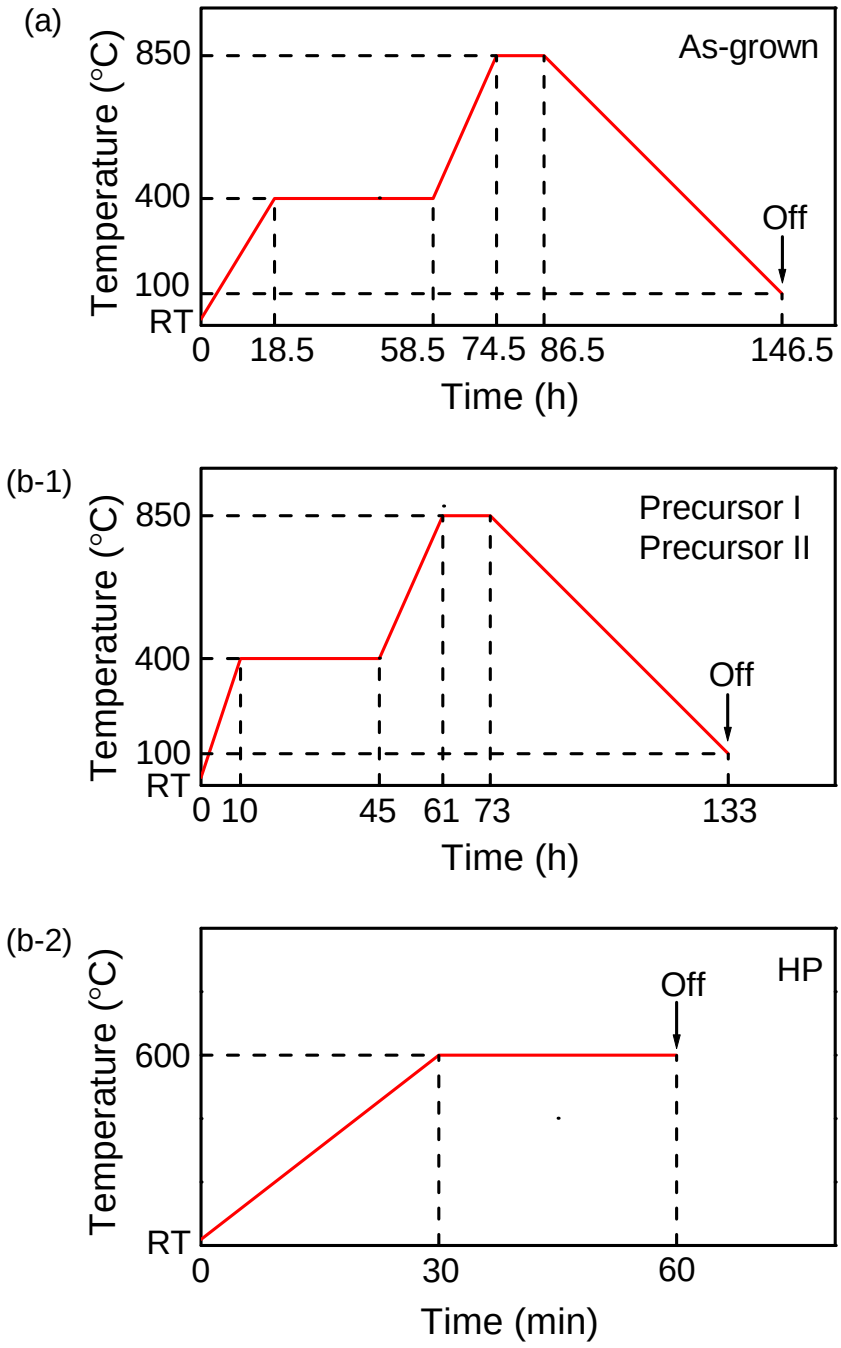

Fig. 4.2.1 Heat treatment conditions in the preparation of (a) polycrystalline samples of as-grown $EuSn_2As_2$, (b-1) two precursors "precursor I" and "precursor II"), and (b-2) hot-pressed polycrystalline sample of $EuSn_2As_2$ ("HP-$EuSn_2As_2$"). Heat treatment began at RT and concluded with furnace cooling after the furnace was turned off.

mosphere (S S Alloy Plasman KIT CSP-KIT-02121). The hot-pressed sample of $EuSn_2As_2$ ("HP-$EuSn_2As_2$") was polished using waterproof abrasive paper (Riken Corundum C34P P800; the abrasive is SiC) and lapping film sheet (3M #8000). The porosity (ϕ) of the HP-$EuSn_2As_2$ in vol.% was calculated as follows:

$$\phi = \left(1 - \frac{d_{\mathrm{meas}}}{d_{\mathrm{calc}}}\right) \times 100, \tag{4.4}$$

where d_{meas} is the measured density of HP-$EuSn_2As_2$ and d_{calc} is the ideally calculated density of defect-free, single-phase $EuSn_2As_2$ with the lattice parameters shown in Fig. 4.3.3. The thermal diffusivity (α) of HP-$EuSn_2As_2$ was measured by the LASER flash method. Thereafter, the HP-$EuSn_2As_2$ sample was cut using a low speed diamond wheel saw (South Bay Technology Model 650) without lubricant into four rectangular specimens for further measurements.

X-ray diffraction measurements at RT were performed in order to characterize the crystallographic phases of the powdered sample of as-grown $EuSn_2As_2$ and the crystallographic orientation of a specimen of the HP-$EuSn_2As_2$ sample. The porosity (ϕ) of HP-$EuSn_2As_2$ was obtained from the measured density (d_{meas}) and ideally calculated density (d_{calc}) of defect-free, single-phase $EuSn_2As_2$ with the lattice parameters.

Low-vacuum scanning electron microscopy (SEM) and energy-dispersive X-ray spectroscopy (EDX) analyses of a specimen of the HP-$EuSn_2As_2$ sample were undertaken parallel ($\mathbf{P}_{\parallel}$) to the pressing direction of hot pressing in order to examine the morphology and chemical composition.

Figure 4.2.2 shows schematic diagrams and photographs of specimens for measurements as described below. The T dependence of ρ for another specimen of the HP-$EuSn_2As_2$ sample was measured by a four-probe method perpendicular ($\mathbf{P}_{\perp}$) to the pressing direction of hot pressing. Measurements of ${}^{\mathrm{SS}}\kappa$ and S for another specimen of the HP-$EuSn_2As_2$ sample were also conducted in the $\mathbf{P}_{\perp}$ direction using a heater and two type R thermocouples under the steady-state conditions in a lamp heating unit (Ulvac MILA-5000) under 10^{-3} Pa with a vacuum pump (PFEIFFER Vacuum TSU 071 E). ${}^{\mathrm{SS}}\kappa$ was obtained in the way described in Chap. 3. The emissivity of the specimen ($\varepsilon_{\mathrm{Sp}}$) was 0.7(3) (Figure 4.4.3 was obtained for $\varepsilon_{\mathrm{Sp}}$ = 0.7(3) and 0). It is noted that in this paper uncertainty was expressed using parentheses, "( )" [83].

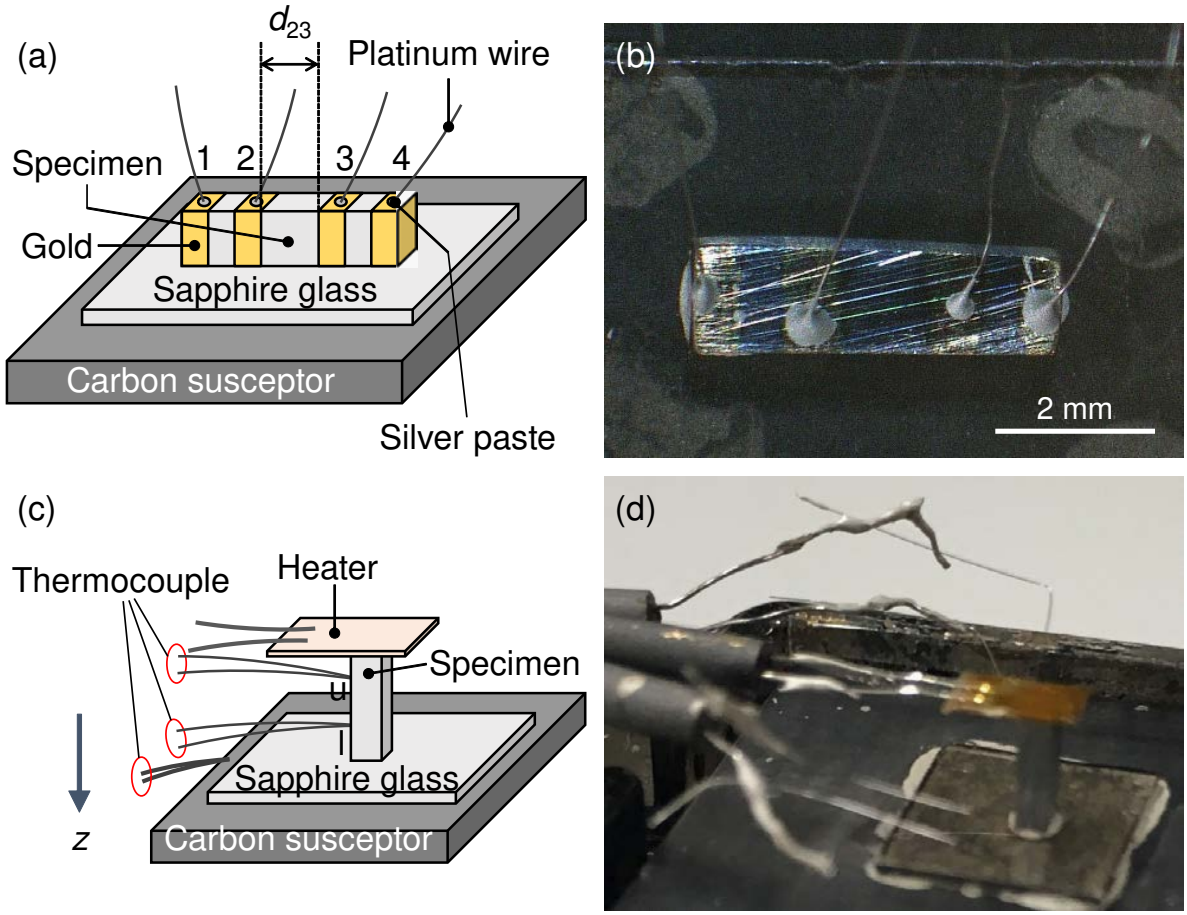

Fig. 4.2.2 Schematic diagrams and photographs of electrode settings for specimens, together with measurements of their electrical resistivity (ρ), steady-state thermal conductivity ($^{SS}\kappa$), and Seebeck coefficient (S). (a) Schematic diagram of ρ measurement by a four-probe method for a specimen of the HP-$EuSn_2As_2$ sample partly coated with gold (Au). The voltage between electrodes 2 and 3 (V_{23}) was measured while an electric current (I_{14}) flowed through electrodes 1 and 4. (b) Photograph of a specimen from the HP-$EuSn_2As_2$ sample showing ρ measured perpendicular ($\mathbf{P}_\perp$) to the pressing direction of hot pressing. (c) Schematic diagram showing measurements of $^{SS}\kappa$ and S using heater and type R thermocouples. The electric current through the heater (I_h) determines the heat flux (J) through the specimen. J generates the temperature gradient of the specimen in the direction of the z-axis ($(T_u - T_l) / d_T$), where d_T is the distance between terminals u and l. Thermocouples were used to sense the temperatures at junctions u and l, namely, T_u and T_l, respectively. Then the thermoelectromotive force between the electrodes u and l (V_{ul}) is measured. (d) Photograph showing another specimen of the HP-$EuSn_2As_2$ sample used for measurements of $^{SS}\kappa$ and S in the $\mathbf{P}_\perp$ direction.

4.3 Results

4.3.1 X-ray diffraction (XRD) measurements

Figure 4.3.1 (a) shows the XRD patterns of a pulverized sample of as-grown $EuSn_2As_2$ [21]; the vertical bars (|) at the bottom represent diffractions due to $EuSn_2As_2$ [7]. The dominant phase in the sample of "as-grown $EuSn_2As_2$" was $EuSn_2As_2$. A weak peak at $2\theta \sim 32.1°$ is ascribed due to Sn [38], which is a minor impurity.

$EuSn_2As_2$ was also the dominant phase in HP-$EuSn_2As_2$ sample (Fig. 4.3.2). The lattice constant a was 0.41843(6) nm and the value of c was 2.6496(5) nm for hexagonal coordination sytem in HP-$EuSn_2As_2$ having $\phi = 2.4(9)$ vol.%.

Figure 4.3.1 (b) shows the XRD patterns of a specimen of the HP-$EuSn_2As_2$ sample. The 009, $10\bar{5}$, and $2\bar{1}0$ peaks correspond to each lattice plane, as visualized in Fig. 4.1.2 (b). The pattern measured in the $\mathbf{P}_{\parallel}$ direction exhibited the 009 peak. However, the 009 peak was too weak to be detected in the pattern in the $\mathbf{P}_{\perp}$ direction due to interference from the stronger $10\bar{5}$ peak in the same region of the pattern. Moreover, the intensity of the $2\bar{1}0$ peak in the pattern in the $\mathbf{P}_{\parallel}$ direction was lower than that in the $\mathbf{P}_{\perp}$ direction, whereas the intensities of the $10\bar{5}$ peaks were almost the same. These findings indicate that the c-axis orientation of the HP-$EuSn_2As_2$ is in the $\mathbf{P}_{\parallel}$ direction.

For a further investigation of the crystallographic orientation of the HP-$EuSn_2As_2$, the Lotgering factor (f) [84] in the $\mathbf{P}_{\parallel}$ and $\mathbf{P}_{\perp}$ direction were calculated from the XRD patterns in $20° \leq 2\theta \leq 90°$. The f is defined as follows:

$$f = \frac{p_1 - p_0}{1 - p_0} \tag{4.5}$$

where

$$p_n = \frac{\sum I(00l)}{\sum [I(hkl) + I(00l)]} \tag{4.6}$$

for the non-oriented material ($n = 0$) and for an oriented sample ($n = 1$). $I(00l)$ and $I(hkl)$ indicate integral intensities of the $00l$ and hkl peaks, respectively. The XRD pattern of the non-oriented sample of $EuSn_2As_2$ was obtained based on reported crystallographic data [7] using VESTA [9]. f was 0.07764 in the $\mathbf{P}_{\parallel}$ direction and -0.00012 in the $\mathbf{P}_{\perp}$ direction. The difference in these values show the significant crystallographic orientation of the HP-$EuSn_2As_2$.

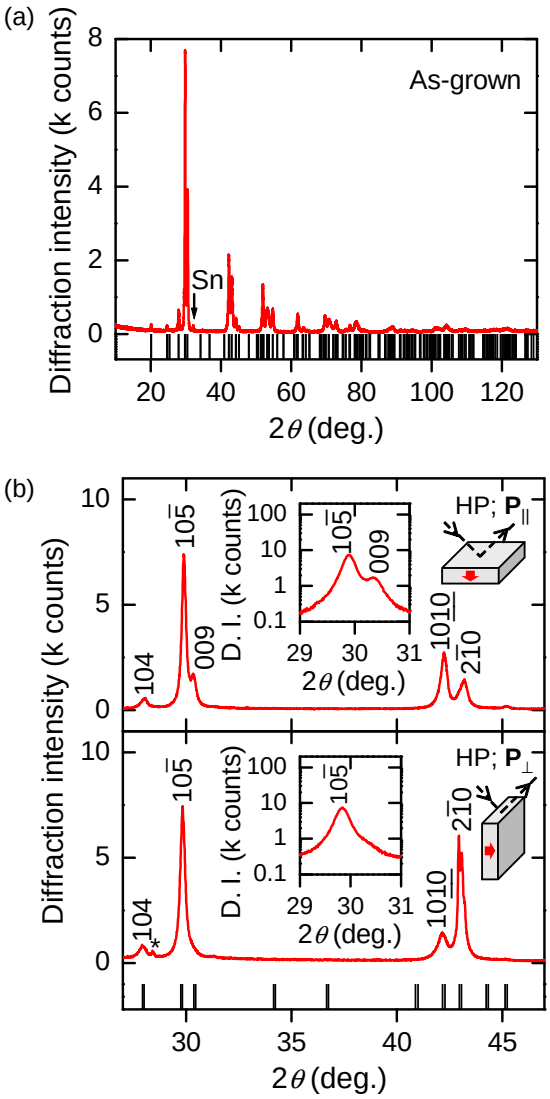

Fig. 4.3.1 XRD patterns of $EuSn_2As_2$ samples. Vertical bars (|) at the bottom of each figure denote diffractions due to $EuSn_2As_2$ [7] calculated by VESTA. [9] (a) XRD pattern at RT of a pulverized sample of as-grown $EuSn_2As_2$. Downward arrows (↓) denote peaks due to the tin (Sn) [38] phase. XRD pattern is reproduced from Sakagami *et al.* [21] (b) XRD patterns of a specimen of the hot-pressed polycrystalline sample of $EuSn_2As_2$ ("HP-$EuSn_2As_2$") measured parallel ($\mathbf{P}_{\parallel}$) and perpendicular ($\mathbf{P}_{\perp}$) to the pressing direction of hot pressing. Miller indices for the hexagonal coordinate system have been added. The asterisk (*) denotes a peak arising from an unknown phase. The upper right image of each pattern shows a schematic of the definition of the $\mathbf{P}_{\parallel}$ and $\mathbf{P}_{\perp}$ directions. The directions of arrows with thick solid lines and thin broken lines denote the pressing direction and the direction of incoming and outgoing X-rays at a diffraction angle (2θ) of ~90° in the XRD measurement, respectively.

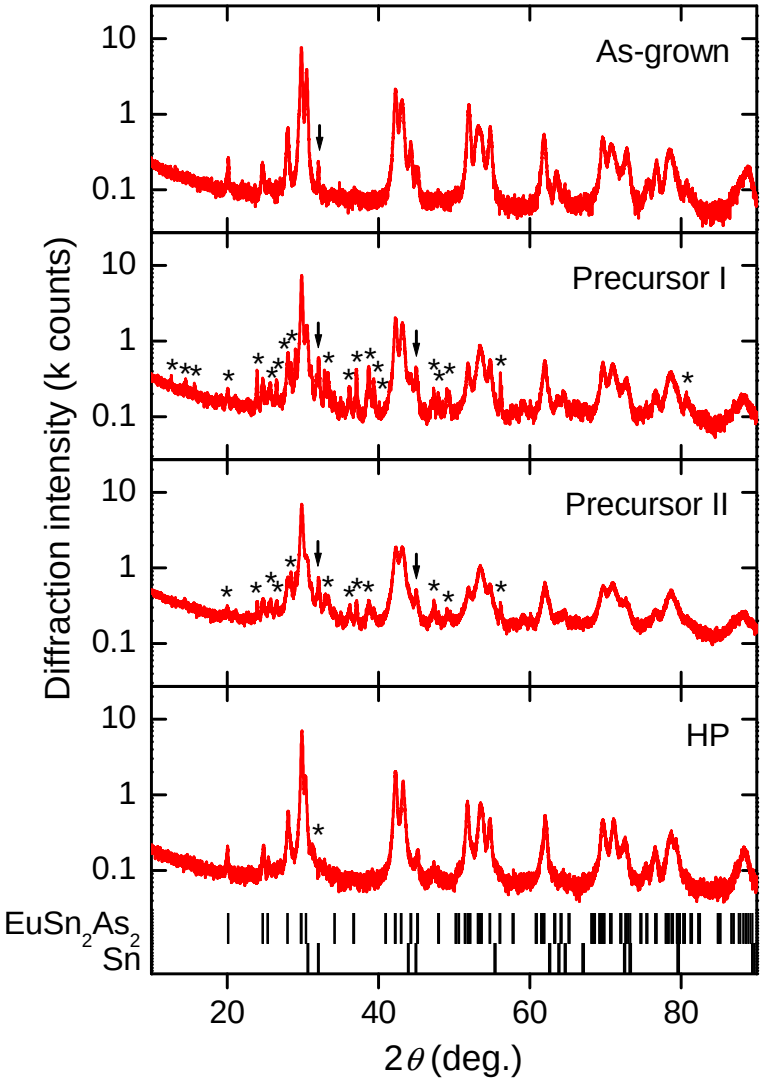

Fig. 4.3.2 XRD patterns at RT for pulverized sample of as-grown $EuSn_2As_2$, the two precursors ("precursor I" and "precursor II"), and the HP-$EuSn_2As_2$ samples. Vertical bars (|) at the bottom represent diffraction due to $EuSn_2As_2$ and tin (Sn) calculated by VESTA [9]. Downward-pointing arrows (↓) and asterisks (*) denote peaks due to Sn and unknown phases, respectiviely.

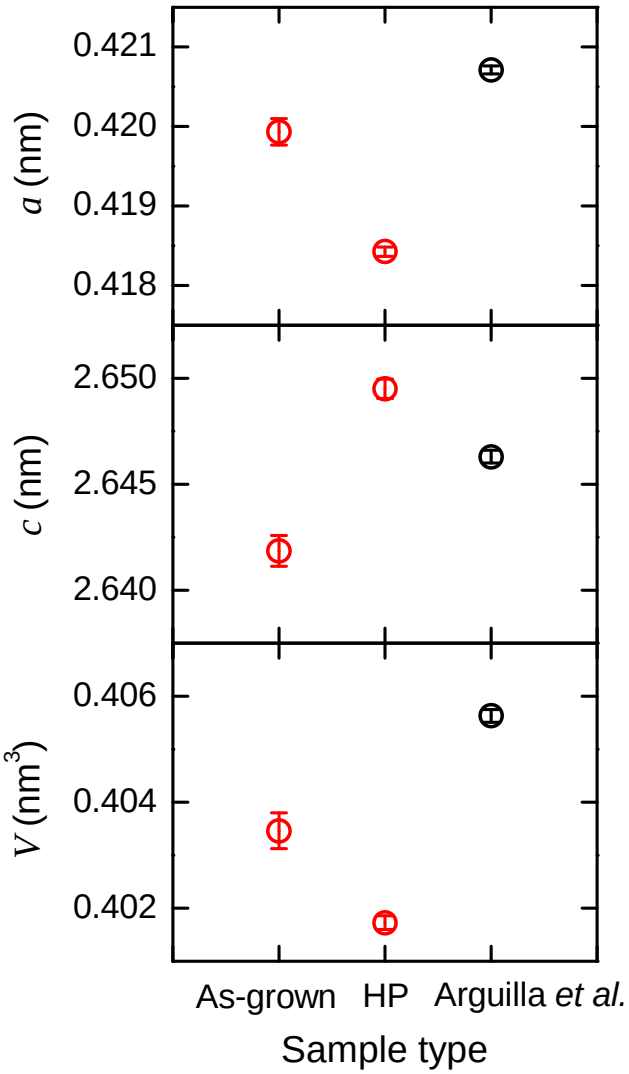

Fig. 4.3.3 Lattice constants (a and c) and lattice volumes (V) for hexagonal coordinate system for present polycrystalline $EuSn_2As_2$, including the sample of as-grown $EuSn_2As_2$, the HP-$EuSn_2As_2$, and results reported by Arguilla *et al.*

As shown in Fig. 4.3.3, the lattice constant a for the hexagonal coordinate system of HP-$EuSn_2As_2$ sample was smaller than that of sample of as-grown $EuSn_2As_2$, whereas the lattice constant c of HP-$EuSn_2As_2$ was larger than that of as-grown $EuSn_2As_2$. Samples of HP-$EuSn_2As_2$, as-grown $EuSn_2As_2$, and $EuSn_2As_2$ reported by Arguilla *et al.* [7] differ in their lattice constants. Differences in lattice constants indicate slight but finite distinctions between the chemical compositions of the samples or differences in standard reference materials for

Table 4.3.1 Elemental composition ratios computed from the EDX spectrum of the polished specimen of the HP$EuSn_2As_2$ sample as shown in Fig. 4.3.4 (d), assuming that the specimen was composed of only Eu, Sn, As, and O.

Spot	Eu	Sn	As	O
Spot 1 in Fig. 4.3.4 (b)	0.181(9)	0.385(15)	0.379(16)	0.054(3)
Spot 2 in Fig. 4.3.4 (b)	0.40(3)	0.088(4)	0.100(5)	0.415(12)
Spot 3 in Fig. 4.3.4 (c)	0.204(11)	0.144(6)	0.63(3)	0.020(2)

the calibration of the optical axis in X-ray diffractometry [21].

4.3.2 Scanning electron microscopy observations with energy-dispersive X-ray spectroscopy (SEM/EDX)

Figure 4.3.4 shows SEM observations and EDX elemental analyses of a specimen of the HP-$EuSn_2As_2$ sample. The back-scattered electron (BSE) SEM image demonstrates the compositional homogeneity of the specimen on a scale of several tens of thousands of square micrometers (Fig. 4.3.4 (a)). The images shown in Figs. 4.3.4 (b) and 4.3.4 (c) denote the existence of second and third phases with surface areas of several hundred square micrometers. Figure 4.3.4 (d) shows the corresponding EDX spectrum, with vertical bars at the bottom representing the photon energies of certain elements [85]. Spots 1 and 2 in Fig. 4.3.4 (b) and spot 3 in Fig. 4.3.4 (c) all contained Eu, Sn, As, oxygen (O), carbon (C), and nickel (Ni) atoms. C is always detected using this SEM instrument probably because the sample holder are covered by conductive carbon adhesive tape. Spots 1 and 2 in Fig. 4.3.4 (b) consist of iron (Fe). Ni and Fe mainly arise from the tweezers used for handling.

Table 4.3.1 shows EDX elemental analysis for the regions shown in Fig. 4.3.4 (d) on the assumption that the components of the specimen are only Eu, Sn, As, and O. The observed elemental composition ratio of the spot 1 in Fig. 4.3.4 (b) is consistent with the main phase of the specimen: $EuSn_2As_2$. Spot 2 in Fig. 4.3.4 (b) contains >40 vol.% of Eu and O. Thus, the specimen is shown to contain small grains of EuO, Eu_2O_3, or $Eu(OH)_3$, whose volume fractions are too small to be detected in the XRD measurements of the HP-$EuSn_2As_2$ sample. Spot 3 in Fig. 4.3.4 (c) contained >60 vol.% of As and smaller amounts of Eu and Sn. The volume fractions of these subsequent phases correspond to less than $\sim$ 1 vol.% of the specimen.

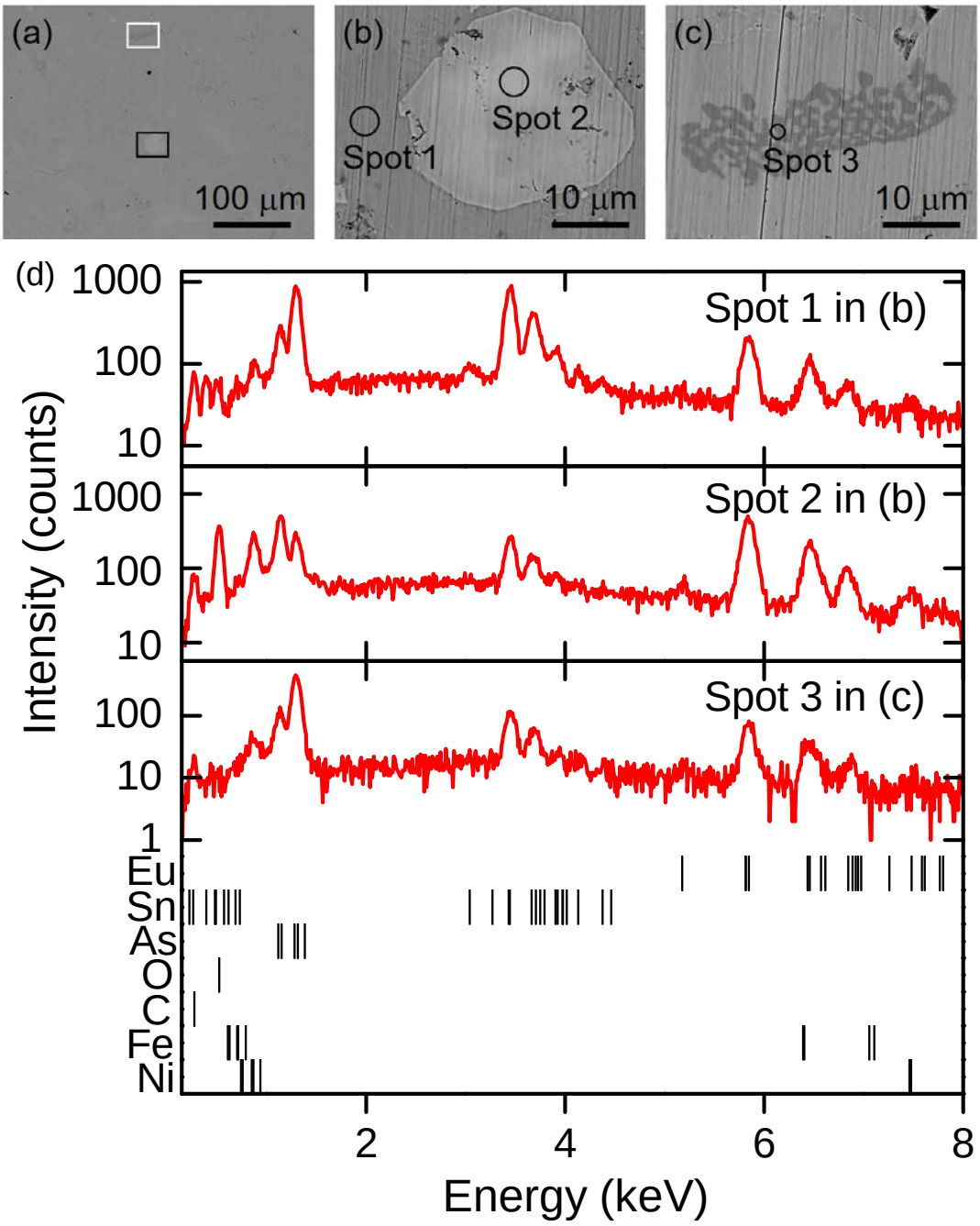

Fig. 4.3.4 Scanning electron microscopy (SEM) observations with energy-dispersive X-ray spectroscopy (EDX) elemental analyses of a polished spicimen of the HP-$EuSn_2As_2$ sample in the $\mathbf{P}_{\parallel}$ direction. (a) Back-scattered electron (BSE) SEM image of the specimen. (b) BSE SEM image of the lower area surrounded by a rectangular balck frame in (a). (d) EDX spectrum for each spot shown in (b) and (c). Spots identification is indicated near the spectrum. The vertcal bars at the bottom represent the photon energies of europium (Eu), Sn, arsenic (As), oxygen (O), carbon (C), iron (Fe), and nickel (Ni) [85].

4.3.3 TE transport properties

Figure caption

This subsubsection describes caption of Fig. 4.3.5. The figure shows TE transport properties of specimens of the HP-$EuSn_2As_2$ sample in the $\mathbf{P}_\perp$ direction as a function of T. (a) Open and closed circles denote values of electrical resistivity (ρ) with increasing T and decreasing T, respectively. The solid line represents a fitted curve based on a mathematical model, i.e., $\rho(T) = 0.164$ mΩ cm + 4.91×10^{-7} mΩ cm $K^{-2.06} \times T^{2.06}$. (b) Open circles denote Seebeck coefficient (S). The solid line represents a fitted line based on a physical model: $S(T) = 0.0750$ μV $K^{-2} \times T$. (c) Open circles, upward-pointing triangles, downward-pointing triangles, and lozenges denote thermal conductivity (κ), electronic thermal conductivity (κ_{el}) with increasing T, κ_{el} with decreasing T, and phonon thermal conductivity (κ_{ph}). The solid line, dashed line, and dashed and dotted line indicate fitted curves of $\kappa(T)$, $\kappa_{el}(T)$, and $\kappa_{ph}(T)$. $\kappa_{ph}(T)$ was defined as: $\kappa_{ph}(T) = 1.69$ kW m^{-1}/T. (d) Open circles denote the power factor (P), which is defined as $P = S^2\rho^{-1}$. Measurements of ρ used are those obtained with increasing T. The solid line represents a fitted curve based on a model as follows: $P(T) = [S(T)]^2[\rho(T)]^{-1}$. (e) Open circles denote the dimensionless figure of merit (ZT), which is defined as $ZT = S^2T\rho^{-1}\kappa^{-1}$. Again, the measurements of ρ used are those obtained with increasing T. The solid line represents a fitted curve based on the following model: $ZT(T) = [S(T)]^2T[\rho(T)]^{-1}[\kappa(T)]^{-1}$.

Main text

Specimens for measurements of TE transport properties had lengths, widths, and thicknesses on the order of 0.8 to 5 mm. Concidering the compositional homogeneity as shown in Fig. 4.3.4 (a), the location dependence of the properties can be neglected in the specimen.

Figure 4.3.5 shows the TE transport properties for HP-$EuSn_2As_2$ as a function of T. Figure 4.3.5 (a) shows ρ in the $\mathbf{P}_\perp$ direction, demonstrating that ρ increases with increasing T. Differences between the measurements of ρ when the T was increased and decreased were smaller than measurement uncertainties: ρ was 0.223(9) mΩ cm at 298(2) K and 0.50(3) mΩ cm at 673(2) K in the comprehensive measurement with increasing and decreasing T. Such ρ values indicate metallic temperature dependence.

Figure 4.3.5 (b) shows the initial measurement of S values of HP-$EuSn_2As_2$ in the $\mathbf{P}_\perp$ direction. S was 28(2) μV K^{-1} at 374(4) K and 50(4) μV K^{-1} at 673(6) K. S is positive and

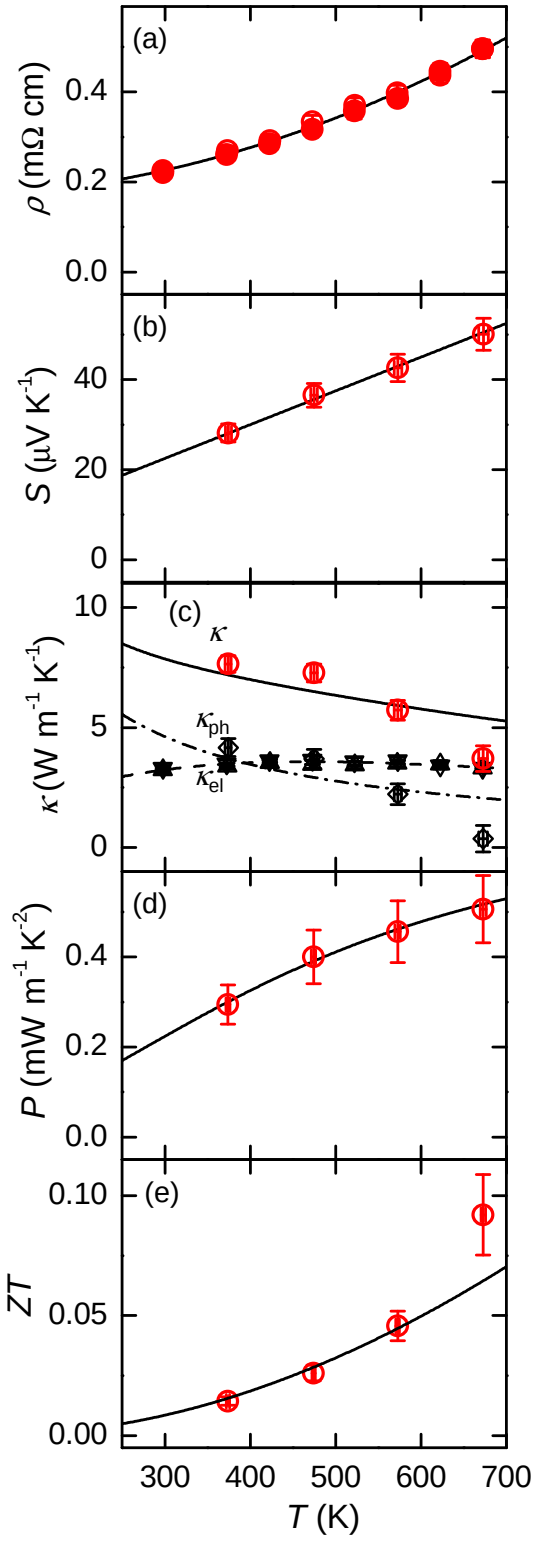

Fig. 4.3.5 TE transport properties of specimens of the HP-$EuSn_2As_2$ sample in the $\mathbf{P}_\perp$ direction as a function of temperature (T).

it increases with increasing T, demonstrating that the carriers have p-type polarity. S was 33(3) μV K^{-1} at 374(5) K after a measurement cycle in T from RT to ~673 K. The S value at 374(5) K after the measurement cycle was ~1.2 times the initial value at 374(4) K. The S value after the measurement cycle was omitted to avoid confusion.

Figure 4.3.5 (c) shows the initial measurement of κ of HP-$EuSn_2As_2$ in the $\mathbf{P}_\perp$ direction. κ was 7.6(4) W m^{-1} K^{-1} at 374(4) K and 3.7(6) W m^{-1} K^{-1} at 673(6) K. κ decreases with increasing T. κ was 5.7(3) W m^{-1} K^{-1} at 374(5) K after the measurement cycle. As noted above, this value was also omitted.

Thermal hysteresis, which was observed for S and κ, was probably derived from the alteration of the specimen in terms of chemical composition and/or hardness, chemical reactions between $EuSn_2As_2$ in the specimen and silver (Ag) in the electrodes, or room temperature fluctuations during the measurements.

4.4 Discussion

4.4.1 Electrical resistivity (ρ)

Using experimental ρ-T data for HP-$EuSn_2As_2$ in the $\mathbf{P}_\perp$ direction, the experimental ρ-T curve was obtained as shown in Fig. 4.3.5 (a). This curve was based on fluctuations mathematical model of $\rho(T)$:

$$\rho(T) = \rho_{r0} + A_r T^r \tag{4.7}$$

with (ρ_{r0}, A_r, r) of (0.164 mΩ cm, 4.91×10^{-7} mΩcm $K^{-2.06}$, 2.06), which were optimized by the least squares method, as shown in Fig. 4.4.1. The curve was shown to be inconsistent with ρ behavior expected from the Bloch–Grüneisen model [86–88], where ρ is proportional to T at higher temperatures than the Debye temperature (Θ) in conventional metals. The $T^{2.06}$ term is probably derived from spectral conductivity (s_c) as a function of energy (ε) relative to the band edge, electron–electron scattering, ionized impurity scattering related to the displacement of participating elements, or intervalley scattering as discussed below.

Comparison between samples of $EuSn_2As_2$

The value of ρ for our specimen of the HP-$EuSn_2As_2$ polycrystalline sample was found to be 0.223(9) mΩ cm at 298(2) K in the $\mathbf{P}_\parallel$ direction. The ρ of a single crystal $EuSn_2As_2$ was reported to be 0.73 mΩ cm at 300 K perpendicular to the c-axis for a hexagonal coordinate system by Arguilla *et al.* [7]. The value of ρ in our HP-$EuSn_2As_2$ was thus less than one

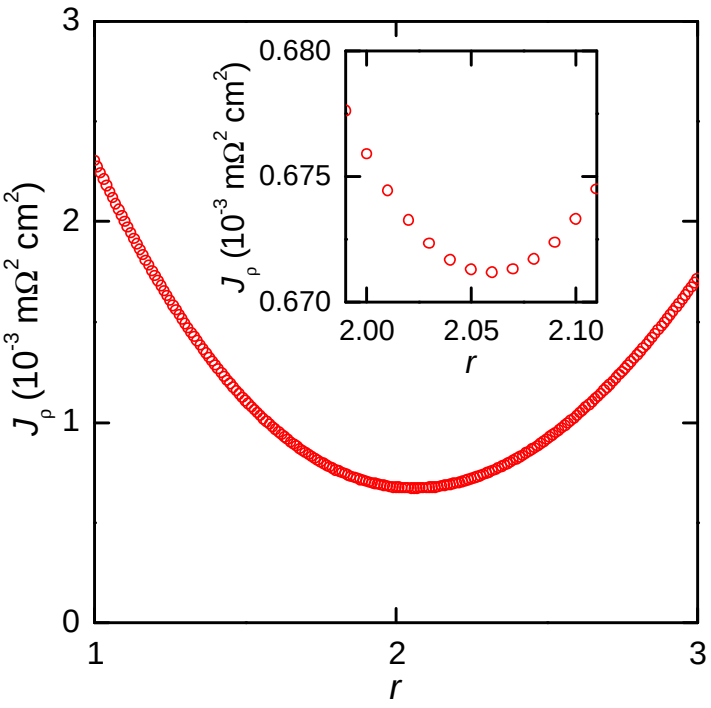

Fig. 4.4.1 An r value dependence of a J_ρ value. The J_ρ is defined as:

$$J_\rho = \sum [\rho - \rho(T)]^2 ,$$

where ρ is the electrical resistivity measurements and $\rho(T)$ is predicted by a mathematical model:

$$\rho(T) = \rho_{r0} + A_r T^r ,$$

where ρ_{r0} and A_r were optimized in order to minimize the J_ρ, regarding the r as fixed.

third of the corresponding value in $EuSn_2As_2$ of Arguilla *et al.* [7]. The reason for this distinction probably reflects a difference in chemical composition, i.e. off-stoichiometry exists in both samples. Indeed, several single crystals intermetallic compounds synthesized via flux methods exhibit off-stoichiometric and inhomogeneous chemical compositions [89, 90].

Semiclassical theory of conduction

For investigations of origin of the power law $T^{2.06}$ in the $\rho(T)$ model, this subsubsection introduces the semiclassical theory of conduction in metals and semimetals, based on band theory, Ferm–Dirac statistics, Boltzmann transport equation, and relaxation time approximation. When the electrical transport properties in isotropic systems are determined by only one

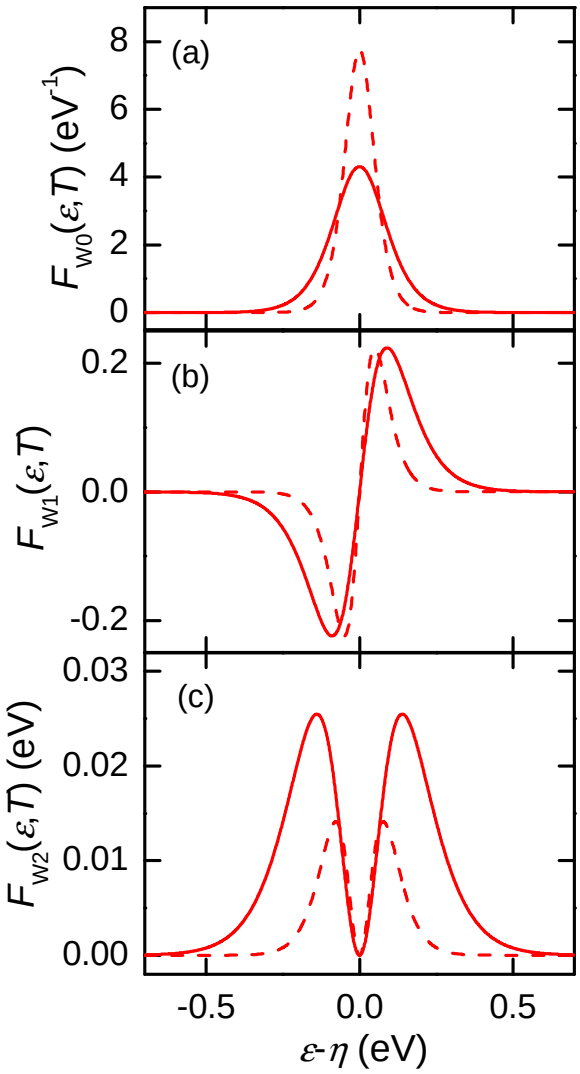

Fig. 4.4.2 Energy (ε) dependences of $F_{Wj}(T)$ (j = 0, 1, and 2) for T = 673 K (solid line) and T = 373 K (dashed line). The $F_{Wj}(T)$ determines TE transport properties. The $F_{Wj}(T)$ are defined as:

$F_{Wj}(\varepsilon, T) = (\varepsilon - \eta)^j(-\partial f_{FD}/\partial\varepsilon)$ where T is temperature, η is chemical potential, and f_{FD} is the Fermi–Dirac distribution function:

$f_{FD} = (\exp((\varepsilon - \eta) / k_B T) + 1)^{-1}$,

where k_B is the Boltzmann constant.

parabolic band near the ε_F, their $s_c(\varepsilon,T)$ is defined as follows:

$$s_c(\varepsilon, T) = \frac{e^2}{3} D(\varepsilon)[v(\varepsilon)]^2 \tau(\varepsilon, T) \tag{4.8}$$

where D, v, and τ represent the electronic density of states (DOSs), magnitude of group velocity of carriers, and relaxation time of carriers, respectively [91–94]. Using the definition of electrical conductivity ($\sigma = \rho^{-1}$), theoretical $\rho(T)$ is calculated as follows:

$$\rho(T) = \left[\int_{-\infty}^{\infty} s_c(\varepsilon, T) F_{W0}(\varepsilon, T) \mathrm{d}\varepsilon \right]^{-1} \tag{4.9}$$

where $F_{W0}(\varepsilon,T)$ is defined as the additive inverse of the derivative of the Fermi–Dirac distribution function (f_{FD}) $F_{Wj}(\varepsilon,T)$ for $j = 0$, 1, or 2 restrict the ε range of integration as window functions [93–95]. As shown in Fig. 4.4.2 (a), $\int_{-\infty}^{\infty} F_{W0}(\varepsilon, T)\mathrm{d}\varepsilon$ is independent of T.

Spectral conduction

The following subsubsection examines candidates for the source of the $T^{2.06}$ term in Eq. 4.7. In metals, relaxation time of carriers for scattering by point imperfection (τ_d) is theoretically expressed as follows:

$$\tau_d = \left[n_c v \int (1 - \cos\theta) I(\theta) d\Omega \right]^{-1} \tag{4.10}$$

where n_c is the concentration of scattering centers, θ is scattering angle, I is the differential scattering cross section, and Ω is a solid angle defined in energy-wave-vector space [96, 97]. On the other hand, the value of relaxation time of carriers for phonon scattering (τ_p) is

$$\tau_p = \left[\frac{2\varepsilon^{3/2}}{\Lambda\Delta} \frac{T}{\Theta} \right]^{-1} \tag{4.11}$$

in metals and

$$\tau_p = \left[\frac{2\varepsilon^{1/2}\Delta}{\Lambda} \frac{T}{\Theta} \right]^{-1} \tag{4.12}$$

in semiconductors, where

$$\Lambda = \left[\frac{3}{4\pi V} \right]^{-\frac{2}{3}} \frac{4m^*}{h^2} \tag{4.13}$$

$$\Delta = \left[\frac{m^*}{2} \right]^{\frac{1}{2}} \left(\frac{3}{4\pi V} \right)^{\frac{1}{3}} \frac{3\pi^2 {C_{sct}}^2 \eta^2}{M k_B \Theta} \tag{4.14}$$

where V is the volume of a unit cell, h is the Planck constant, m^* is an effective mass of carriers, C_{sct} is a scattering-related constant, η is chemical potential, M is the mass of the constituent element, and k_{B} is the Boltzmann constant [97]. The $s_{\mathrm{c}}(\varepsilon, T)$ in Eq. 4.8 is thus rephrased as:

$$s_{\mathrm{c}}(\varepsilon, T) = \left[\frac{1}{s_{\mathrm{c10}}(\varepsilon)} + \frac{1}{s_{\mathrm{c1}}(\varepsilon)} T \right]^{-1} \tag{4.15}$$

for point-imperfection and phonon scattering as described in Eq. 4.10, Eq.4.11, and Eq. 4.12 on the assumption that the reciprocals of the relaxation times are additive [98]. If both $s_{\mathrm{c10}}(\varepsilon)$ and $s_{\mathrm{c1}}(\varepsilon)$ in Eq. 4.15 are independent of ε, ρ is theoretically expressed as follows:

$$\rho(T) = \rho_{10} + A_1 T \tag{4.16}$$

where ρ_{10} and A_1 are constants. Equation 4.16 is, however, inconsistent with the experimental formula Eq. 4.7. Therefore, either $s_{\mathrm{c10}}(\varepsilon)$ or $s_{\mathrm{c1}}(\varepsilon)$ is a function of ε on the assumption that Eq. 4.15 is correct. Indeed, DFT calculations of $EuSn_2As_2$ by Arguilla *et al.* showed multiple edges of the electronic bands in $|\varepsilon - \eta| \leq 0.2$ eV [7]. Such band edges near η can result in ε dependences of $s_{\mathrm{c10}}(\varepsilon)$ and $s_{\mathrm{c1}}(\varepsilon)$. This possibility suggests that if η is changeable for $EuSn_2As_2$-based compounds, B increases at a certain level of η. We term this assumption for $s_{\mathrm{c10}}(\varepsilon)$ and $s_{\mathrm{c1}}(\varepsilon)$ as "spectral conduction".

Electron–electron scattering

The second possible explanation for the $T^{2.06}$ term of HP-$EuSn_2As_2$ is unusually large electron–electron scattering [88, 99]. Baber argued that a relaxation time of carriers for the electron–electron scattering (τ_{e}) of transition metals is theoretically expressed as:

$$\tau_{\mathrm{e}} = \left[\frac{\pi^2}{8} \left(\frac{e^2}{2m_{\mathrm{s}}^*} \right)^2 \left(\frac{m_{\mathrm{s}}^*}{h} \right)^3 \left(\frac{k_{\mathrm{B}} T}{\zeta_{\mathrm{s}}} \right)^2 H \right]^{-1} \tag{4.17}$$

$$H = \frac{8\pi^2 v_{\mathrm{d}}}{\gamma} \frac{{\beta_{\mathrm{r}}}^3 (\beta_{\mathrm{r}} + 1)^3}{\left[(\gamma / v_{\mathrm{d}})^2 + (1 + \beta_{\mathrm{r}})^2 \right]^{3/2}} \int_0^{\pi/2} \frac{\mathrm{d}\phi}{\sqrt{1 - (2\beta_{\mathrm{r}} - 2)(v_{\mathrm{d}}/\gamma)^2 \sin^2 \phi}} \tag{4.18}$$

$$\gamma = \frac{h C_{\mathrm{scr}}}{4\pi} \left(\frac{1}{m_{\mathrm{s}}^*} + \frac{1}{m_{\mathrm{d}}^*} \right) \tag{4.19}$$

$$\beta_{\mathrm{r}} = \frac{m_{\mathrm{d}}^*}{m_{\mathrm{s}}^*} = \frac{v_{\mathrm{s}}}{v_{\mathrm{d}}} \tag{4.20}$$

where m_s^* and m_d^* are the effective masses of the s and d electrons, v_s and v_d are the velocities of the s and d electrons, ζ_s is the width of the s band in eV, and C_{scr} is a screening-related constant [99].The s and d electrons described in Eq. 4.17, Eq.4.18, Eq.4.19 and Eq. 4.20 are probably replaced by other electrons in $EuSn_2As_2$; e.g. Sn $5p$ - As $4p$ covalent electrons and Eu $4f$ electrons, as indicated by the computed partial electronic DOS of $EuSn_2As_2$ by Arguilla *et al.*, although they assumed an antiferromagnetic state [7]. The $s_{\mathrm{c}}(\varepsilon, T)$ in Eq. 4.8 is written as

$$s_{\mathrm{c}}(\varepsilon, T) = \left[\frac{1}{s_{\mathrm{c}20}(\varepsilon)} + \frac{1}{s_{\mathrm{c}2}(\varepsilon)} T^2 \right]^{-1} \tag{4.21}$$

for electron–electron scattering and temperature-independent scattering.

If both $s_{\mathrm{c}20}(\varepsilon)$ and $s_{\mathrm{c}2}(\varepsilon)$ are independent of T, $\rho(T)$ is given by:

$$\rho(T) = \rho_{20} + A_2 T^2 \tag{4.22}$$

where both ρ_{20} and A_2 are constants. A_2 is linked to both the normal and Umklapp components [88]. MacDonald emphasized that a large contribution of phonon-exchange electron-electron scattering to Umklapp components occurs compared with that of Coulomb electron-electron scattering [100]. The fraction of electron-electron scattering of ρ is known to be proportional to T^2 for many Kondo lattices containing cerium (Ce), for example $CeAl_3$ [101], $CeCu_2Si_2$ [102], and CeB_6 [103, 104], as well as for transition-metal compounds such as TiNi [105], TiS_2 [106], $Sr_{0.2}La_{0.8}TiO_3$ [107], and $La_{0.9}Na_{0.1}MnO_{3.0076}$ [108]. Applying experimental ρ-T data from HP-$EuSn_2As_2$ to the $\rho(T)$ model in Eq. 4.22, (ρ_{20}, A_2) are calculated as (0.159 mΩcm, 0.734 nΩ cm K^{-2}) by the least squares method.

The A_2 value for HP-$EuSn_2As_2$ is approximately one twenty-seventh of that for TiS_2, which is 20 nΩ cm K^{-2} according to the data of the ρ-T curve from 10 to 400 K [106]. It has been noted that the crystallographic phase of TiS_2 also contains vdW interaction [109]. Thompson proposed that the increase of ρ at a rate proportional to T^2 for TiS_2 was caused by electron–electron scattering [106]. By analogy with TiS_2, this electron–electron scattering is a candidate for the physical mechanism driving the ρ of HP-$EuSn_2As_2$ above RT. Low-temperature measurements of $EuSn_2As_2$ are required to examine its character as a Kondo lattice.

Ionized impurity scattering

The third candidate for the $T^{2.06}$ term of the HP-$EuSn_2As_2$ is ionized impurity scattering. Based on research by Conwell and Weisskopf, Brooks formulated a relaxation time of carriers for ionized impurity scattering (τ_{i}) of n-type semiconductors as follows:

$$\tau_{\mathrm{i}} = \left\{ \frac{\pi}{m^{*1/2}} \frac{1}{(2\varepsilon)^{3/2}} \frac{e^4(n+n_{\mathrm{A}})}{K^2} \left[\ln(1+b) - \frac{b}{1+b} \right] \right\}^{-1} \tag{4.23}$$

$$b = \frac{8\pi m^* K k_{\mathrm{B}} T \varepsilon}{e^2 h^2} \left[n + \left(1 - \frac{n+n_{\mathrm{A}}}{n_{\mathrm{D}}} \right) (n+n_{\mathrm{A}}) \right]^{-1} \tag{4.24}$$

where K, n, n_{A}, and n_{D} are absolute permittivity, charge carrier concentration, acceptor concentration, and donor concentration, respectively [110, 111]. In Eqs. 4.23 and 4.24, n_{A} and n_{D} are permuted for p-type semiconductors. On the assumption that τ_{i} is regarded as a function of T and that K, n, n_{A}, and n_{D} are independent of T, $[\tau_{\mathrm{i}}(T)]^{-1}$ is an increasing convex downward function for $0 < b < 1$. If τ is equal to τ_{i}, where not only all of K, n, n_{A} and n_{D} are independent of T but also both of $D(\varepsilon)$ and $v(\varepsilon)$ are constant functions near ε_{F}, the theoretical $\rho(T)$ is also an increasing convex downward function for $0 < b < 1$. Under such a situation, the theoretical $\rho(T)$ is qualitatively consistent with the experimental formula Eq. 4.7 in terms of being an increasing, convex downward function with respect to T.

Under RT or higher temperature, HP-$EuSn_2As_2$ produces impurities comprising aggregates of cations and anions of elements at the interstitial positions; this possibly occurs by giant atomic displacement. The shape of the ρ-T curve for HP-$EuSn_2As_2$ in the $\mathbf{P}_{\perp}$ direction is similar to that of As-based intermetallic compound $BaZn_2As_2$ in the $\mathbf{P}_{\parallel}$ direction [33] and BiS_2-based layered compound LaBiSeSO in the $\mathbf{P}_{\perp}$ direction [112]. Such ρ behavior has been observed in layered transition metal compounds, including the low-melting-point metals, such as zinc (Zn) and Bi. The melting points of Zn, Bi, and white Sn are 692.7 K [113], 544.6 K [114], and 505.1 K [113], respectively. Sn atoms in the $EuSn_2As_2$ crystal are expected to result in the large atomic displacement around the melting point of Sn. The cations and anions of elements at the interstitial positions, which occur in association with giant atomic displacement, could potentially function as ionized impurities.

Intervalley scattering

The fourth candidate for the $T^{2.06}$ term of HP-$EuSn_2As_2$ is the intervalley scattering regime. Herring developed models that represent the transport properties of multi-valley semiconductors. [115] In his simplified model, a relaxation time of carriers for intervalley scattering (τ_{v}) by acoustic modes in n-type multi-valley semiconductors is as follows:

$$\tau_{\mathrm{v}} = {C_{\mathrm{inter}}}^{-1} \left\{ \frac{[(\varepsilon/\hbar\omega)+1]^{1/2}}{\exp(\hbar\omega/k_{\mathrm{B}}T)-1} + \frac{[(\varepsilon/\hbar\omega)-1]^{1/2}}{1-\exp(-\hbar\omega/k_{\mathrm{B}}T)} \right\}^{-1} \tag{4.25}$$

where C_{inter} is the coupling constant for intervalley scattering and $\hbar\omega$ is the energy of the acoustic phonon [97, 115]. The first term in the curly bracket { } in Eq. 4.25 corresponds to scattering by phonon absorption and the second term represents scattering by phonon emission; the latter is zero when $\varepsilon \leq \hbar\omega$. For p-type semiconductors, Eq. 4.25 is altered by replacing ε with $-\varepsilon$. Eq. 4.25 shows a radical change of ${\tau_{\text{v}}}^{-1}$ near the band edge. When $\tau(\varepsilon, T)$ is predominantly determined by τ_{v}, the model equation of $\rho(T)$ in Eq. 4.7 is likely to be obtained theoretically for appropriate $D(\varepsilon)$ and $v(\varepsilon)$. It is essential to analyze electronic band dispersion and phonon dispersion for $D(\varepsilon)$, $v(\varepsilon)$, and $h\omega$ before further discussion may be undertaken.

4.4.2 The Seebeck coefficient (S)

As shown in Fig. 4.3.5 (b), T dependence of S in HP-$EuSn_2As_2$ can be represented by an almost straight line from $S = 0$ μV K^{-1} at 0 K. In theory, for p-type metallic conductors, $S(T)$ increases proportionally with T as follows:

$$S(T) = \frac{\pi^2}{3}\frac{k_{\text{B}}}{e}\left(\beta + \frac{3}{2}\right)\frac{k_{\text{B}}T}{\varepsilon_{\text{edge}} - \eta} \tag{4.26}$$

where k_{B} is the Boltzmann constant, e is the elementary charge, β is a positive value, $\varepsilon_{\text{edge}}$ is the edge of the parabolic electronic band that determines electrical conduction, and η is the chemical potential [116]. Equation (4.26) is derived from the Mott relation:

$$S(T) = -\frac{\pi^2}{3}\frac{k_{\text{B}}}{e}k_{\text{B}}T\left.\frac{\partial \ln s_{\text{c}}(\varepsilon, T)}{\partial\varepsilon}\right|_{\varepsilon=\eta} = -\frac{\pi^2}{3}\frac{k_{\text{B}}}{e}\frac{k_{\text{B}}T}{s_{\text{c}}(\eta, T)}\left.\frac{\partial s_{\text{c}}(\varepsilon, T)}{\partial\varepsilon}\right|_{\varepsilon=\eta} \tag{4.27}$$

with the following presumption:

$$\tau \propto |-\varepsilon|^{\beta} \tag{4.28}$$

where τ is the relaxation time of carriers and ε is the energy [91, 116, 117]. The Mott relation shown in Eq. 4.27 is a common property of metallic conductors with simple parabolic electronic bands and strongly correlated electron systems featuring electron-electron interactions [116, 118, 119]. In this regard, the experimental S-T plot of HP-$EuSn_2As_2$ suggests that $EuSn_2As_2$ might be a possible strongly correlated electron system including a Kondo lattice with relatively large S at finite temperatures. Eu $4f$ electrons probably exert limited influence over electrical conduction above RT as demonstrated for $EuFBiS_2$ [120]. It is further noted that the $4f$ electrons do not significantly enhance the S of $EuSn_2As_2$ above RT.

Below, we compare the S value of $EuSn_2As_2$ with that of other TE materials at approximately the same ρ value. The S value of HP-$EuSn_2As_2$ in the $\mathbf{P}_{\perp}$ direction (50(4) μV K^{-1})

at $\rho \sim 0.5$ mΩ cm was roughly one-third of that of a practical TE material $Bi_{0.6}Sb_{1.4}Te_3$ (146 μV K^{-1}), [121] equivalent to that of Sb-based 122 compounds with the $CaAl_2Si_2$ structure-type (40–80 μV K^{-1}) [32, 59] and $BaZn_2Sb_2$ with the α-$BaCu_2S_2$ structure-type (43–78 μV K^{-1}), [74] 1.2–1.7 times of that of $Ba_{1-x}K_xCd_2As_2$ with the α-$BaCu_2S_2$ structure-type (33–37 μV K^{-1}), [77] and 1.5–2.6 times of that of $Ba_{1-x}K_xCd_2As_2$ with the $ThCr_2Si_2$ structure-type (21–36 μV K^{-1}) [33, 77] at $\rho \sim 0.5$ mΩ cm, as shown in Fig. 4.4.5.

4.4.3 Multiband effects on electrical conductivity (σ) and S

The S value of $EuSn_2As_2$ has clearly larger than that of elemental Sn ($S \sim -1$ μV K^{-1} at $T = 280$ K) [122]. On the other hand, Sn-based compound, SnSe exhibits huge S value ($S > 100$ μV K^{-1} at 300 K); one of the causes of its high power factor (P) was reported to be its electronic structure featuring non-parabolic, complex multibands. [123, 124] These previous reports of Sn-based materials suggest that possible multiband electronic structure of $EuSn_2As_2$ should be discussed.

In this subsection, multiband effects [125] on σ and S are described theoretically. For appreciable concentrations of both electrons and holes, the multiband effect is termed the bipolar effect. [126] The whole σ is given as follows:

$$\sigma = \sigma_1 + \sigma_2 \tag{4.29}$$

assuming the presence of two types of carriers, represented by subscripts 1 and 2. [125, 126] Equation (4.29) is equivalent to an expression for the combined conductance of parallel resistors in an electrical circuit. The whole S is given as follows:

$$S = \frac{\sigma_1 S_1 + \sigma_2 S_2}{\sigma_1 + \sigma_2} \tag{4.30}$$

assuming σ as presented in Eq. (4.29). [125, 126] Equation (4.30) indicates that S is calculated as the weighted average of S_1 and S_2 using σ_1 and σ_2 as weights. If σ_1 is much larger than σ_2 ($\sigma_1 \gg \sigma_2$), S is dominantly determined from S_1 ($S \approx S_1$). Equation (4.30) is reminiscent of the Hoashi–Millman theorem in electrical engineering, i.e., the formula for obtaining a voltage at the ends of parallel circuits comprising of voltage sources and resistors in series. [127, 128]

Assuming that ($\sigma_1, \sigma_2, S_1, S_2$) are (3000 Ω^{-1} cm^{-1}, 2000 Ω^{-1} cm^{-1}, 6 μV K^{-1}, 60 μV K^{-1}), the whole (σ, S) are calculated as (5000 Ω^{-1} cm^{-1}, 27.6 μV K^{-1}) accordng to Eqs. (4.29) and (4.30). These values are roughly equivalent to those of HP-$EuSn_2As_2$ in the $\mathbf{P}_\perp$ direction at $T \sim 373$ K.

According to a calculation of electronic band dispesion of $EuSn_2As_2$ for the hexagonal corrdination system in a paramagnetic phase, its Fermi surface is located in six-fold paths, namely, the Γ-M path and the Γ-K path. [11]. The electronic bands of $EuSn_2As_2$ can be six-fold degenerate because the maximum multiplicity of crystallographic sites for Eu, Sn, and As atoms is two whereas the multiplicity of the general position is 12 for the rhombohedral corrdination system (Fig. 4.1.2 (d)). Using expanded Eqs. (4.29) and (4.30), when a single electronic band has (σ_{single}, S_{single}) of (400 Ω^{-1} cm^{-1}, 40 μV K^{-1}) and no interactions between electronic bands occur, the (σ, S) for six-fold degenerated electronic bands are theoretically computed as (2400 Ω^{-1} cm^{-1}, 40 μV K^{-1}). These values are approximately equal to those of HP-$EuSn_2As_2$ in the $\mathbf{P}_\perp$ direction at $T \sim 573$ K.

These simple assumptions indicate that two or more electronic bands (multibands) contribute to the transport properties of $EuSn_2As_2$. Verification of the hypothesis will need direct measurement of electronic band structure of $EuSn_2As_2$ in paramagnetc phase above RT.

4.4.4 The thermal conductivity (κ)

The steady-state thermal conductivity ($^{\mathrm{SS}}\kappa$)

κ_{el} was calculated using the Wiedemann–Franz–Lorenz (WFL) law [129, 130] with the Sommerfeld value [131, 132], which is a variety of Lorenz number [130]. κ_{ph} was obtained by subtracting κ_{el} from κ.

Figure 4.3.5 (c) shows the κ_{ph} of HP-$EuSn_2As_2$ in the $\mathbf{P}_\perp$ direction. κ_{ph} was 4.2(4) W m^{-1} K^{-1} at 374(4) K and 0.4(6) W m^{-1} K^{-1} at 673(6) K. The ratio of κ_{ph} to κ was 0.54(8) at 374(4) K and 0.10(17) at 673(6) K. The κ_{ph} was approximately proportional to $1/T$.

The κ value of HP-$EuSn_2As_2$ in the $\mathbf{P}_\perp$ direction (3.7(6) W m^{-1} K^{-1}) at $\rho \sim 0.5$ mΩ cm was 1.8(3) times higher than that of $Bi_{0.6}Sb_{1.4}Te_3$ (2.08 W m^{-1} K^{-1}) at $\rho \sim 0.5$ mΩ cm [121], as shown in Fig. 4.4.5.

Even though $EuSn_2As_2$ is composed of relatively heavy elements such as Eu and Sn, the κ_{ph} value of HP-$EuSn_2As_2$ in the $\mathbf{P}_\perp$ direction at 374(4) K (4.2(4) W m^{-1} K^{-1}) was relatively high as a TE material. This is probably due to overestimation of κ_{ph}, which was derived from underestimation of κ_{el}. It may be resulted from the multiband effects [125] or the bipolar effects [126, 133] on σ and κ_{el}, which increase the Lorenz number compared to the Sommerfeld value.

Standard uncertainty of κ, as shown in Fig. 4.3.5 (c), was obtained by combining the uncer-

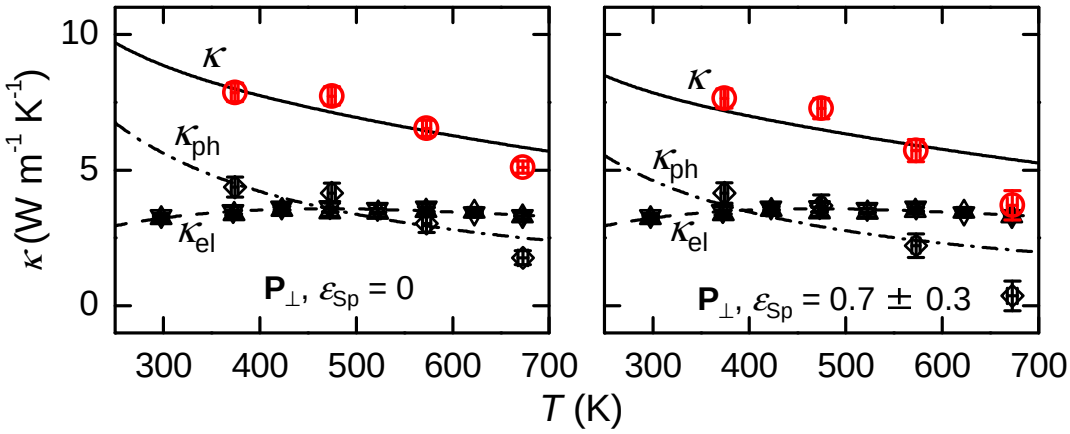

Fig. 4.4.3 T dependence of steady-state thermal conductivity ($^{SS}\kappa$) of HP-$EuSn_2As_2$ in the $\mathbf{P}_\perp$ direction in the cases of emissivity of the specimen (ε_{Sp}) = 0 (left) and ε_{Sp} = 0.7(3) (right).

tainties of the emissivity of the specimen, the distance between the two electrodes, the cross-sectional area of the specimen, and the straight-line approximation of the plots of temperature gradients versus heat fluxes. The relative standard uncertainty of κ due to the uncertainty of emissivity of the specimen (ε_{Sp}) was 1.1% at 374(4) K and 14% at 673(6) K.

The LASER flash thermal conductivity ($^{LF}\kappa$) in the $\mathbf{P}_\perp$ direction.

Figure 4.4.4 shows T dependence of the $^{LF}\kappa$ of HP-$EuSn_2As_2$ in the $\mathbf{P}_\parallel$ direction. $^{LF}\kappa$ was 5.5(6) W m^{-1} K^{-1} at 376.4 K and 4.4(5) W m^{-1} K^{-1} at 673.0 K. The data for $^{LF}\kappa$ during a period of T increase matched the data obtained during a period of T decrease, indicating that there was little change in chemical composition during measurements.

$^{LF}\kappa_{ph}$ was 2.0(6) W m^{-1} K^{-1} at 376.4 K and 1.1(5) W m^{-1} K^{-1} at 673.0 K. $^{LF}\kappa_{ph}$ was calculated by subtracting κ_{el} from $^{LF}\kappa$ under the assumption of isotropy and homogeneity of HP-$EuSn_2As_2$. κ_{el} was obtained from ρ in the $\mathbf{P}_\parallel$ direction, whereas $^{LF}\kappa$ was measured in the $\mathbf{P}_\parallel$ direction. Thus, direction of $^{LF}\kappa_{ph}$ was undefined. Simple comparisons of the values of $^{LF}\kappa_{ph}$ with $^{SS}\kappa_{ph}$ were misleading. Further study is needed to advance this discussion.

Comparisopn between $^{SS}\kappa$ and $^{LF}\kappa$ values

Fig. 4.4.5 (b) indicates the $^{SS}\kappa$ and $^{LF}\kappa$ values of HP-$EuSn_2As_2$ as well as other materials. The differences between the values of $^{SS}\kappa$ and $^{LF}\kappa$ of HP-$EuSn_2As_2$ are greater than the

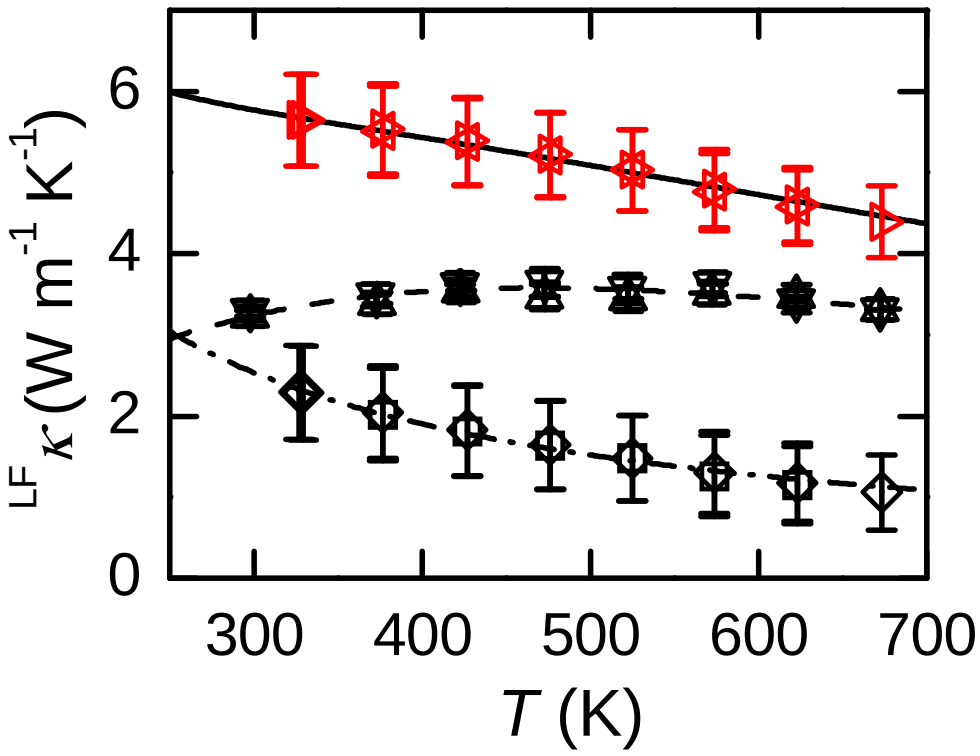

Fig. 4.4.4 T dependence of the LASER flash thermal conductivity ($^{LF}\kappa$) in the $\mathbf{P}_{\parallel}$ direction, κ_{el} in the $\mathbf{P}_{\perp}$ direction, and LASER flash phonon thermal conductivity ($^{LF}\kappa_{ph}$) in the $\mathbf{P}_{\parallel}$ direction of HP-$EuSn_2As_2$. The right-pointing triangles, left-pointing triangles, upward-pointing triangles, downward-pointing triangles, lozenges, and squares denote $^{LF}\kappa$ with increasing T, $^{LF}\kappa$ with decreasing T, κ_{el} with increasing T, κ_{el} with decreasing T, $^{LF}\kappa_{el}$ with increasing T, and $^{LF}\kappa_{el}$ with decreasing T, respectively. The solid line, dashed line, and alternately long and short dashed line indicate fitted curves of $^{LF}\kappa(T)$, $\kappa_{el}(T)$, and $^{LF}\kappa_{el}(T)$. $^{LF}\kappa_{el}(T)$ was defined as: $^{LF}\kappa_{ph}(T) = 0.760\ \mathrm{kW\ m^{-1}} / T$.

uncertainties. The reason for the differences are probably due to anisotropy and/or spatial heterogeneity in HP-$EuSn_2As_2$. Comparison between the values of $^{SS}\kappa$ in the $\mathbf{P}_{\perp}$ direction and $^{LF}\kappa$ in the $\mathbf{P}_{\parallel}$ direction of $EuSn_2As_2$ lead to both underestimation and overestimation of the ZT value.

4.4.5 The power factor (P) and the dimensionless figure of merit (ZT)

As shown in Figs. 4.3.5 (d) and 4.3.5 (e), the P value was 0.51(8) mW m^{-1} K^{-2} at 673(4) K and the ZT value was 0.092(17) at 673(3) K for HP-$EuSn_2As_2$ in the $\mathbf{P}_\perp$ direction.

$EuSn_2As_2$ was reported to exhibit hole concentration of 3.87×10^{20} cm^{-3} at 200 K [20]. This hole concentration value was higher than the optimized carrier concentration of TE materials, which is 10^{18}–10^{19} cm^{-3} [134]. In other words, $EuSn_2As_2$ appears to be over-doped. Electron doping by element substitution with the objective of suppressing the hole concentration should be an effective means of increasing the ZT value of $EuSn_2As_2$-based compounds.

It is noted that the effective masses of carriers in $EuSn_2As_2$ are not reported so far. Based on the result of S as shown in Fig. 4.3.5 (b) and the reported value of carrier concentration at 200 K (3.87×10^{20} cm^{-3}) [20], the effective mass of carriers in $EuSn_2As_2$ at 374(4) K and 673(6) K was estimated to be $5.4(4) \times 10^{-31}$ kg, which was 0.59(5) times heavier than the electron rest mass, on the assumption of the single parabolic band, energy-independent scattering, and S as functions of T, effective mass, and carrier concentration [53, 135]. Microscopic mechanism of the electrical and thermal transport is expected to be revealed from perspective of electronic structure using ARPES and DFT calculations.

4.4.6 TE performance comparison

This paragraph describes caption of Fig. 4.4.5. The figure shows TE transport properties of practical and other TE materials in the trigonal crystal system. The chemical compositions of each compound are expressed as a nominal value. (a) $|S|$ plotted against ρ of HP-$EuSn_2As_2$ in the $\mathbf{P}_\perp$ direction (open circles denoted as "$EuSn_2As_{2\perp}$"), $Bi_{0.4}Sb_{1.6}Te_3$ [121] (open right-pointing triangle), $Bi_{0.5}Sb_{1.5}Te_3$ [121] (open up-pointing triangle), $Bi_{0.5}Sb_{1.5}Te_3$ [126, 137] (open left-pointing triangles denoted as "$Bi_{0.5}Sb_{1.5}Te_3$-G"), $Bi_{0.5}Sb_{1.5}Te_3$ [29, 30] (open left-pointing triangles denoted as "$Bi_{0.5}Sb_{1.5}Te_3$-W"), $EuZn_{1.8}Cd_{0.2}Sb_2$ [31]) (open pentagons), and $Ba_{0.92}K_{0.08}Cd_2As_2$ [76] (open hexagons). The chemical composition of the compounds is expressed as nominal value. The three dashed curves denoted as "10," "1," and "0.1 mW m^{-1}K^{-2}" are the curves of equation of the power factor (P) is equal to these constant values. The data of the $EuSn_2As_2$ were collected from Figs. 4.3.5 (a) and 4.3.5 (b). (b) The steady-state thermal conductivity ($^{SS}\kappa$) plotted against the ρ of the $EuSn_2As_2$ in the $\mathbf{P}_\perp$ direction (open circles denoted as "$^{SS}EuSn_2As_{2\perp}$"), $Bi_{0.56}Sb_{1.44}Te_3$ [136] at 300 K

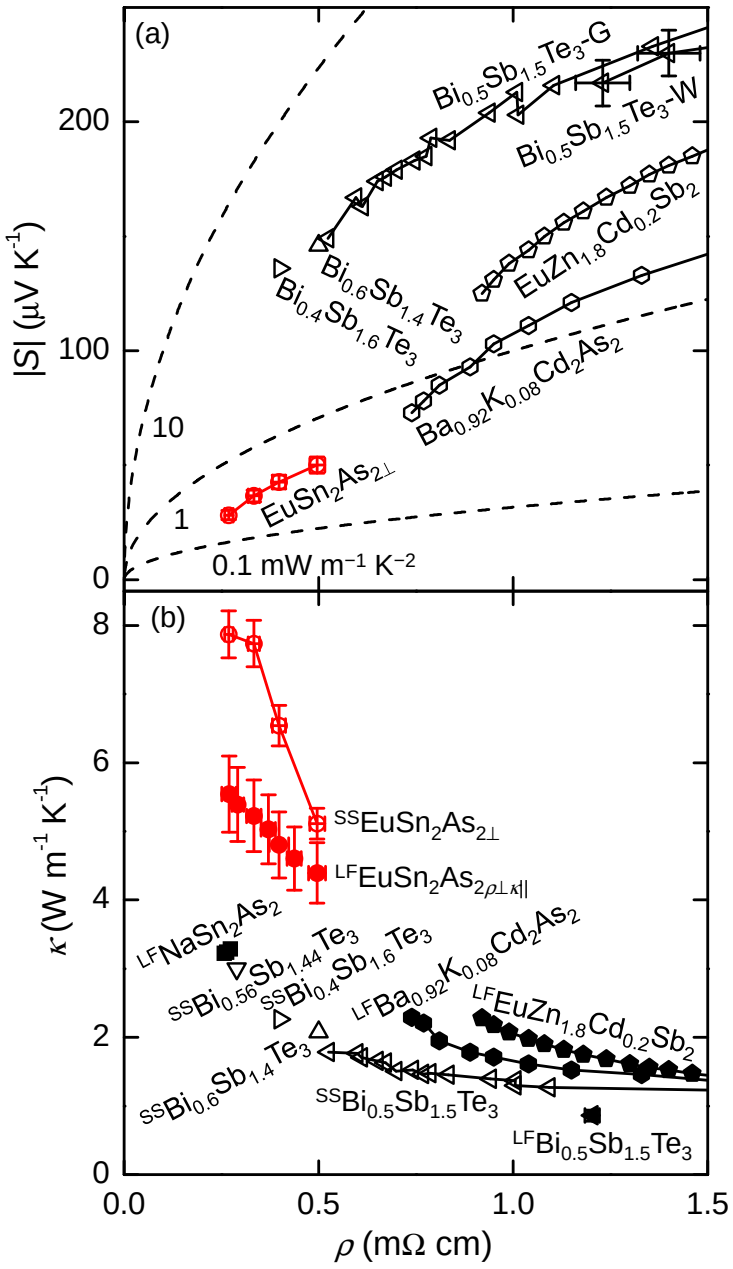

Fig. 4.4.5 TE transport properties of practical and other TE materials in the trigonal crystal system. Details were described in text.

(open down-pointing triangle denoted as $^{SS}Bi_{0.56}Sb_{1.44}Te_3$"), $Bi_{0.4}Sb_{1.6}Te_3$ [121] at 300 K (open right-pointing triangle denoted as "$^{SS}Bi_{0.4}Sb_{1.6}Te_3$"), $Bi_{0.6}Sb_{1.4}Te_3$ [121] at 300 K (open up-pointing triangle denoted as "$^{SS}Bi_{0.6}Sb_{1.4}Te_3$"), $Bi_{0.5}Sb_{1.5}Te_3$ [126, 137] at 20°C (open left-pointing triangle denoted as "$^{SS}Bi_{0.5}Sb_{1.5}Te_3$") and the LASER flash thermal conductivity ($^{LF}\kappa$) plotted against the ρ of the HP polycrystalline sample of $EuSn_2As_2$ (closed circles denoted as "$^{SS}EuSn_2As_{2\|}$"), $NaSn_2As_2$ [104] (closed square denoted as "$^{LF}NaSn_2As_2$), $EuZn_{1.8}Cd_{0.2}Sb_2$ [31] (closed pentagons denoted as "$^{LF}EuZn_{1.8}Cd_{0.2}Sb_2$"), $Ba_{0.92}K_{0.08}Cd_2As_2$ [103] (closed hexagons denoted as "$^{LF}Ba_{0.92}K_{0.08}Cd_2As_2$"), and $Bi_{0.5}Sb_{1.5}Te_3$ [29, 30] at RT (closed left-pointing triangle denoted as "$^{LF}Bi_{0.5}Sb_{1.5}Te_3$"). The chemical composition of the compounds is expressed as nominal value. The data of $EuSn_2As_2$ were collected from Figs. 4.3.5 (a), 4.3.5 (b), and 4.4.4. It is noted that for drawing Fig. 4.4.5 (b) we selected the measurements of the $|S|$ in the $\mathbf{P}_\perp$ direction and the $^{LF}\kappa$ in the $\mathbf{P}_\|$ direction of HP-$EuSn_2As_2$ with increasing T.

Considering the values of (S, $^{SS}\kappa$) at approximately the same ρ for HP-$EuSn_2As_2$ and other TE materials as shown in Fig. 4.4.5, $EuSn_2As_2$-based compounds may be promising new TE materials.

4.5 Short summary

The electrical and thermal transport properties of densified polycrystalline sample of $EuSn_2As_2$ with porosity (ϕ) of 2.4(9) vol.% were measured from RT to ~673 K perpendicular to the pressing direction of hot pressing; i.e. the crystallographic phase of $EuSn_2As_2$ in the sample was weakly oriented to the *a*-*b* plane of the hexagonal coordinate system during our measurements.

The plot of temperature (T) dependence of the electrical resistivity (ρ) shows metallic behavior. The ρ is probably affected by the multiband. The ρ includes T^2 term. The T^2 term is probably derived from spectral conductivity (s_c) as a function of energy (ε) relative to the band edge, electron–electron scattering, ionized impurity scattering related to the displacement of participating elements, and/or intervalley scattering. The plot of T dependence of the Seebeck coefficient (S) shows that the carriers exhibit *p*-type polarity. The measurement values of (ρ, S) was (0.50(3) mΩ cm, 50(4) μV K^{-1}) at $T \sim 673$ K. The power factor (P) was 0.51(8) mW m^{-1} K^{-2} at 673(4) K.

The direct thermal transport measurement reveals that the thermal conductivity (κ) decreases with increasing T. Using the WFL law, the ratio of phonon thermal conductivity (κ_{ph})

to κ, defined as κ_{ph}/κ, was 0.56(8) at T = 374(4) K and 0.35(7) at 673(6) K.

The ZT value was 0.067(8) at T = 673(3) K. $EuSn_2As_2$ seems to be over-doped as a TE material. Suppression of the hole concentration will be a possible route for improving the TE properties of $EuSn_2As_2$-based compounds.

5

Magnetic measurements and Mössbauer spectroscopies of $EuSn_2As_2$

^{151}Eu Mössbauer specroscopies and magnetization measurements of van der Waals-type rhombohedral compound $EuSn_2As_2$ demonstrated both of Eu^{2+} and Eu^3+ components. The Eu^{2+} component indicates magnetic splitting by internal magnetic field (B_{int}) at T = 4.2 K. Sn Mössbauer specroscopies of $EuSn_2As_2$ shows magnetic splitting at 4.2 K, suggesting transferred hyperfine field from Eu^{2+} component.

5.1 Introduction

5.1.1 Purpose

In the present study, we analyze electronic states of $EuSn_2As_2$ below room temperature by using ^{151}Eu and ^{119}Sn Mössbauer spectroscopy and magnetization measurements. ^{151}Eu and ^{119}Sn Mössbauer spectroscopy of $EuSn_2As_2$ observes valences of its Eu and Sn elements and its internal magnetic flux density (B_{int}) as shown in Figs. 5.1.1 and 5.1.2. These obtained results show its chemical-bonding states and are indicators of the randomness of the crystal. These information suggests its magnetic structures with the aid of the results of its magnetization measurements. Because of obtaining these kinds of findings, we propose the usefulness of Mössbauer spectroscopy of topological materials.

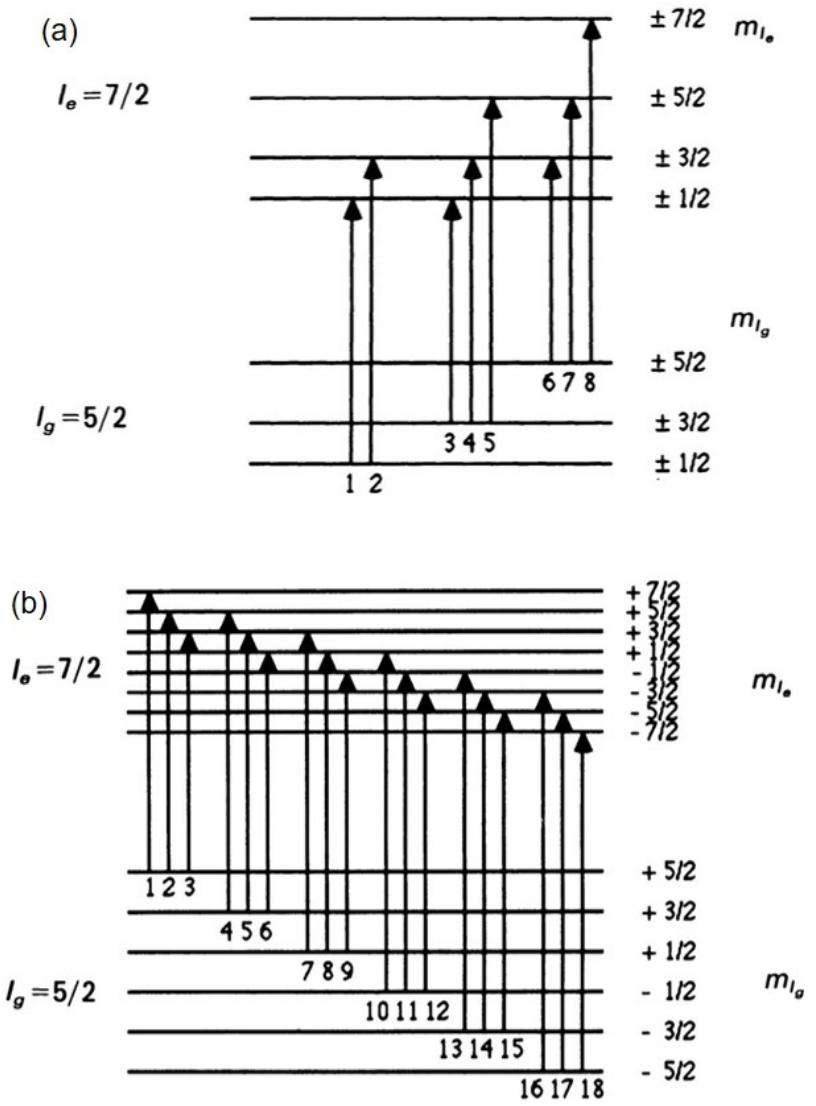

Fig. 5.1.1 Nuclear energy levels for ^{151}Eu in the presence of (a) a quadrupole interaction and (b) a magnetic hyperfine interaction [140].

5.2 Experimental

The polycrystalline sample of $EuSn_2As_2$ was prepared from a Eu ingot and a Sn-As pellet using liquid phase reaction in a carbon crucible inside an evacuated silica tube as described in our previous report [21]. We broke the sample with mortar and pestle to pick up both an oriented crystal and powdered sample.

As shown in Fig. 5.2.1 (a), orientation of the oriented crystal was investigated by a parallel micro beam X-ray diffraction (μXRD; Bruker D8 Discover, Cu Kα radiation, with a two-

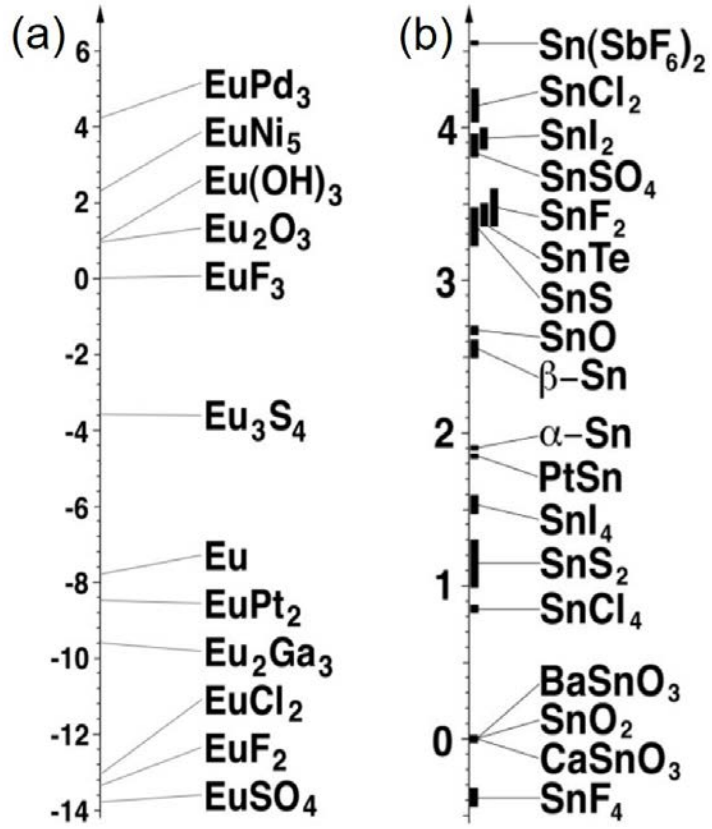

Fig. 5.1.2 Isomer shift (IS) scale for (a) ^{151}Eu and (b) ^{119}Sn. (a) and (b) are reprinted from Mössbauer Effect Data Center [138, 141]

dimentional detector) together with a Göbel mirror for the parallel beam and a collimator and a microslit for 500-μm-diameter beam.

^{151}Eu and ^{119}Sn Mössbauer spectroscopy was carried out in conventional transmission geometry using a ^{151}Sm source (nominal activity of 1.85 GBq, SmF_3 matrix) and a ^{119m}Sn source (nominal activity of 740 MBq, $CaSnO_3$ matrix) (Fig. 5.2.2). To obtain a pellet sample for the Mössbauer spectroscopy, we mixed the powdered sample with powders of BN and polyethylene and then pressed them.

As shown in Fig. 5.2.1 (b)–(h), magnetization was measured on the oriented crystal in directions both perpendicular and parallel to the *c*-axis direction using superconducting quantum interference device (SQUID) magnetometers (Quantum Design MPMS-XL7 EC and MPMS-5 EC) with reciprocating sample option (RSO).

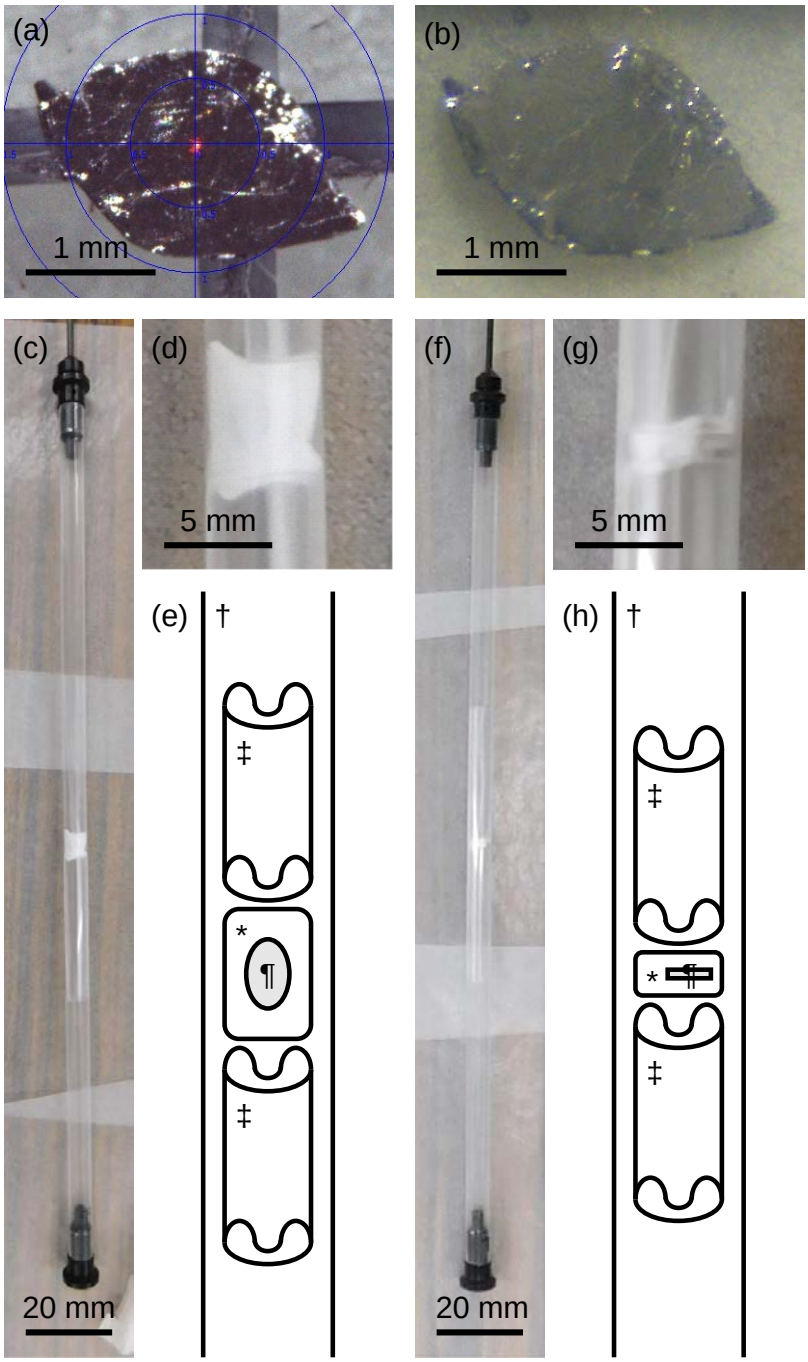

Fig. 5.2.1 (a) $EuSn_2As_2$ oriented crystal for micro beam X-ray diffraction (μXRD) measurements. (b) $EuSn_2As_2$ oriented crystal for magnetization measurement using superconducting quantum interference device (SQUID) magnetometers. (c) The specimen in a capsule of teflon tape inserted in the a straw for magnetization measurements perpendicular to the c-axis ($H \perp c$). (d) Enlarged view of (c). (e) Schematic diagram of (c). (f) The specimen in a capsule of teflon tape inserted in the a straw for magnetization measurements parallel to the c-axis ($H \parallel c$). (g) Enlarged view of (f). (h) Schematic diagram of (f).

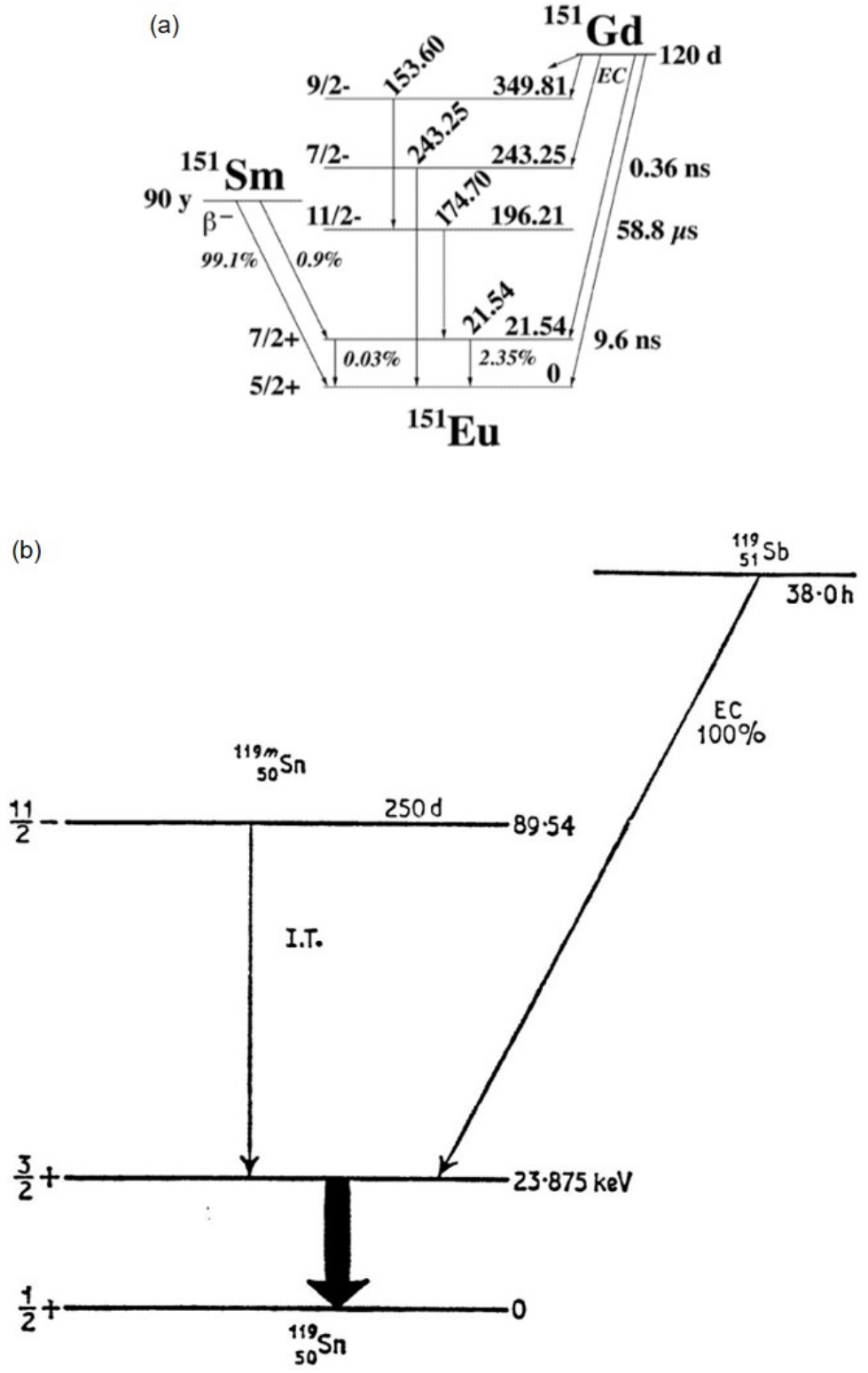

Fig. 5.2.2 The decay diagram for (a) ^{151}Eu and (b) ^{119}Sn. (a) and (b) are reprinted from Mössbauer Effect Data Center [138] and Greenwood and Gibb [139], respectively.

5.3 Results

5.3.1 XRD measurements

Figure 5.3.1 (b) shows μXRD pattern of the oriented crystal. It demonstrates a Laue diffraction pattern. Considering the collimator and the microslit for 500-μm-diameter beam in the μXRD, the oriented crystal contained a crystallite whose diameter of larger than ∼500 μm. Moreover, the *a*-*b* plane of the crystallite faced in a direction of paper surface in Fig. 5.2.1 (a).

5.3.2 ^{151}Eu and ^{119}Sn Mössbauer spectroscopy

Figure 5.3.2 (a) shows ^{151}Eu Mössbauer spectra of the pellet sample. The spectra shows both Eu^{2+} and Eu^3+ components. The Eu^{2+} component indicates magnetic splitting by internal magnetic field (B_{int}) at T = 4.2 K while it consists of singlet at T = 30–297 K. Eu^{3+} component comprises singlet at T = 30–297 K. ^{119}Sn Mössbauer spectra of the pellet sample, as shown in Fig. 5.3.2 (b), magnetic splitting is observed at T = 4.2–297 K.

5.3.3 Magnetization measurements

Figures 5.3.3 and 5.3.4 shows T dependences of M versus $\mu_0 H$ for the $EuSn_2As_2$ oriented crystal. Our sample of $EuSn_2As_2$ showed metamagnetic behaviour. Moreover, easy axis of magnetization was *c* axis.

5.4 Discussion

5.4.1 Electronic structure

As shown in Fig. 5.4.3 (a), we assumed a single internal magnetic field (B_{int}) of Eu^{2+} of 25.7(2) T at T = 4.2 K. This B_{int} value was smaller than that of $EuCo_2As_2$ (29.6(3) T at 4.2 K) and $EuSn_3$ (28.0(8) T at 4.2 K) and was larger than that of EuSn (22.7(7) T at 4.2 K) [143, 144]. The B_{int} value of $EuSn_2As_2$ was reasonable by comparing with Eu compounds [140] as indicated in Fig. 5.4.1.

Figure 5.4.2 shows refined parameters as to the Mössbauer spectroscopy. The isomer shift (IS) indicated that Eu^{2+} component, "(1)", at T = 4.2 K behaves more metallic than at T = 30–297 K. This suggested variation of DOS of Eu *s* electrons at 4.2 K.

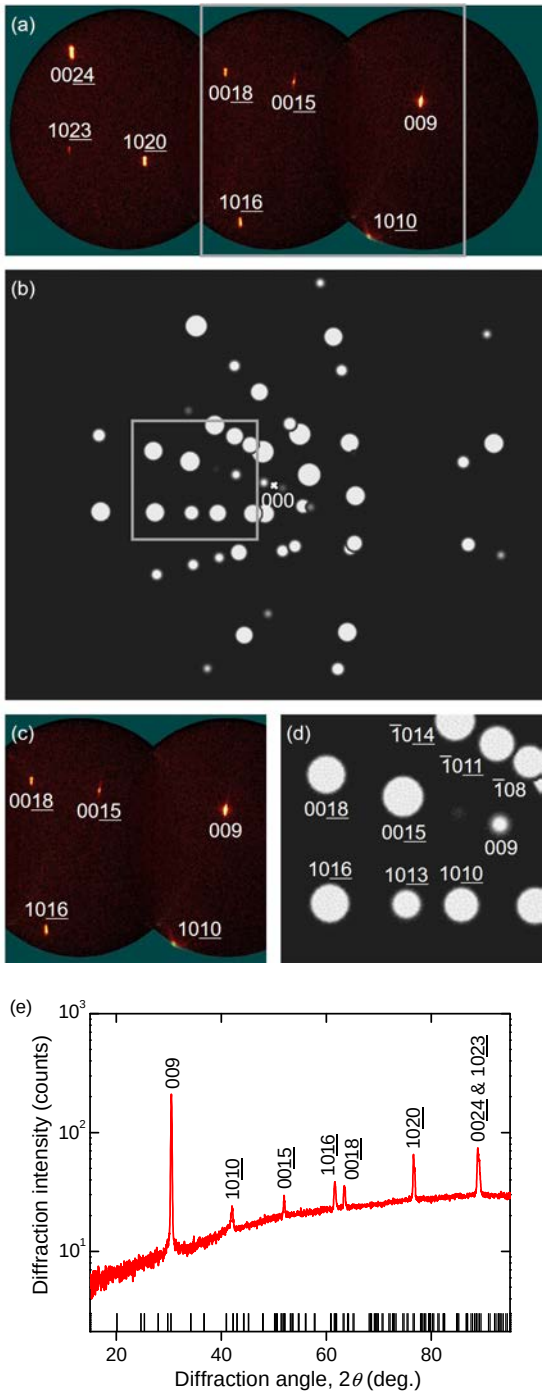

Fig. 5.3.1 (a) μXRD pattern of a $EuSn_2As_2$ oriented crystal. (b) Simulated Laue pattern of $EuSn_2As_2$. (c) The lower area surrounded by a rectangular gray frame in (a). (d) The lower area surrounded by a rectangular gray frame in (b). (e) Integrated pattern of (a).

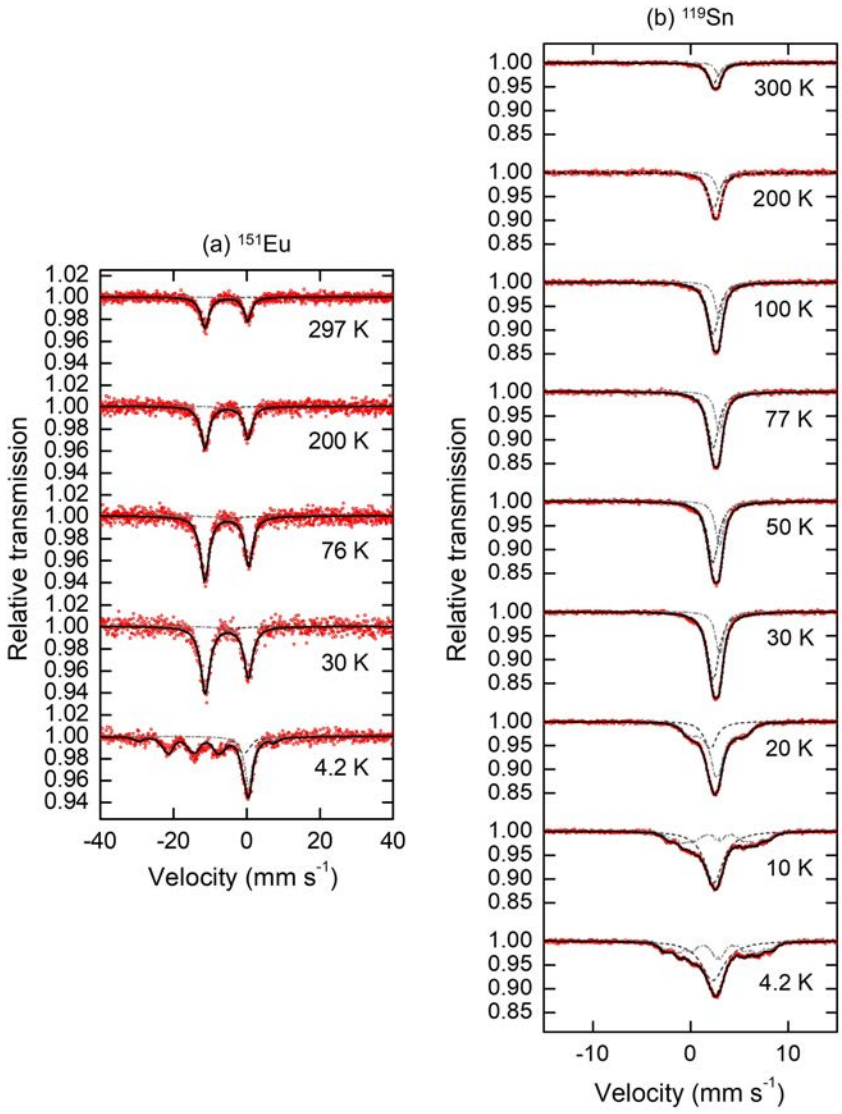

Fig. 5.3.2 (a) ^{151}Eu and (b) ^{119}Sn Mössbauer spectra of a sample of $EuSn_2As_2$. Observed data (open red circles), fitted patterns (solid black lines), a component (dashed dark gray lines) and another component (dashed-and-dotted light gray line) are plotted. Measurement temperatures are denoted near the spectra.

Although you may suppose the number of the electronic states of Sn to be more than two, we found, in terms of the IS, two components of Sn^{2+} cation, "(1)" and "(2)". The component of (1) was covalently bonded[*1] while the component of (2) was between covalently and ionically bonded[*2]. The component of (1) has low IS value as Sn^{2+} at 20 K. This was

[*1] example of electron distribution of metallic Sn^{2+}: $4d^{10}\ 5s^1\ 5p^1$

[*2] electron distribution of ionic Sn^{2+}: $4d^{10}\ 5s^2$

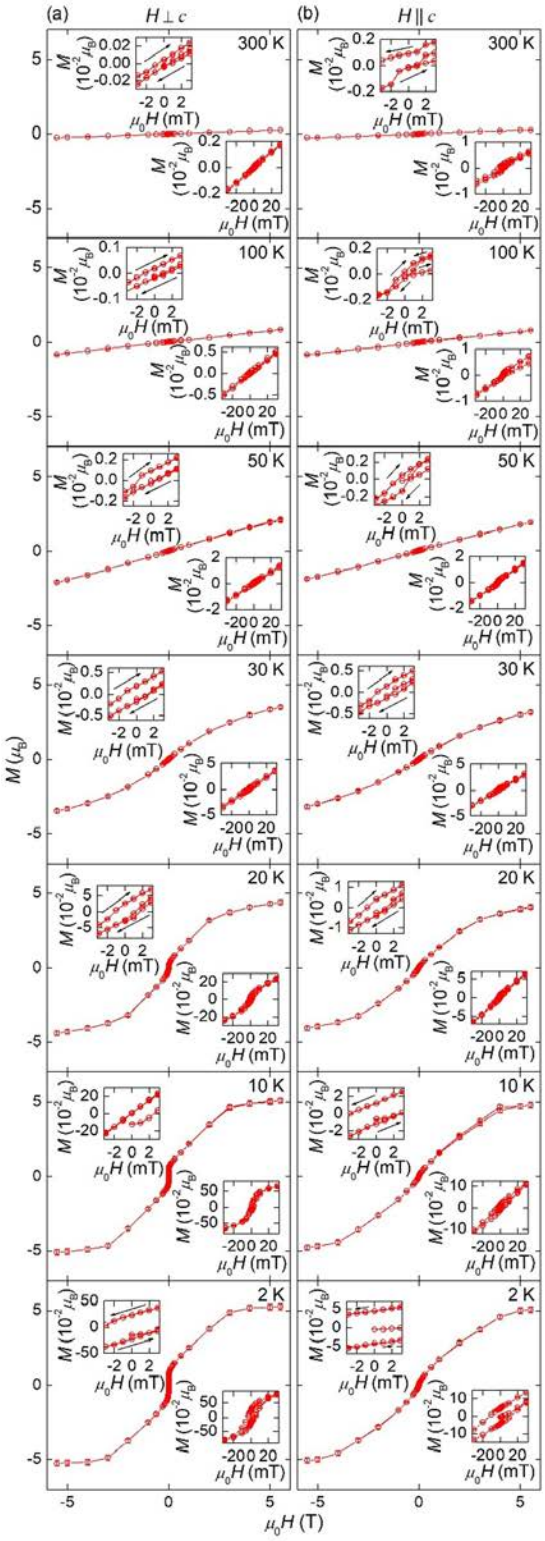

Fig. 5.3.3 Temperature (T) dependences of magnetization (M) versus external magnetic flux density ($\mu_0 H$) for $EuSn_2As_2$ oriented crystal per formula unit (a) in $H \perp c$ and (b) in $H \parallel c$ at various measurement temperatures of 2–300 K.

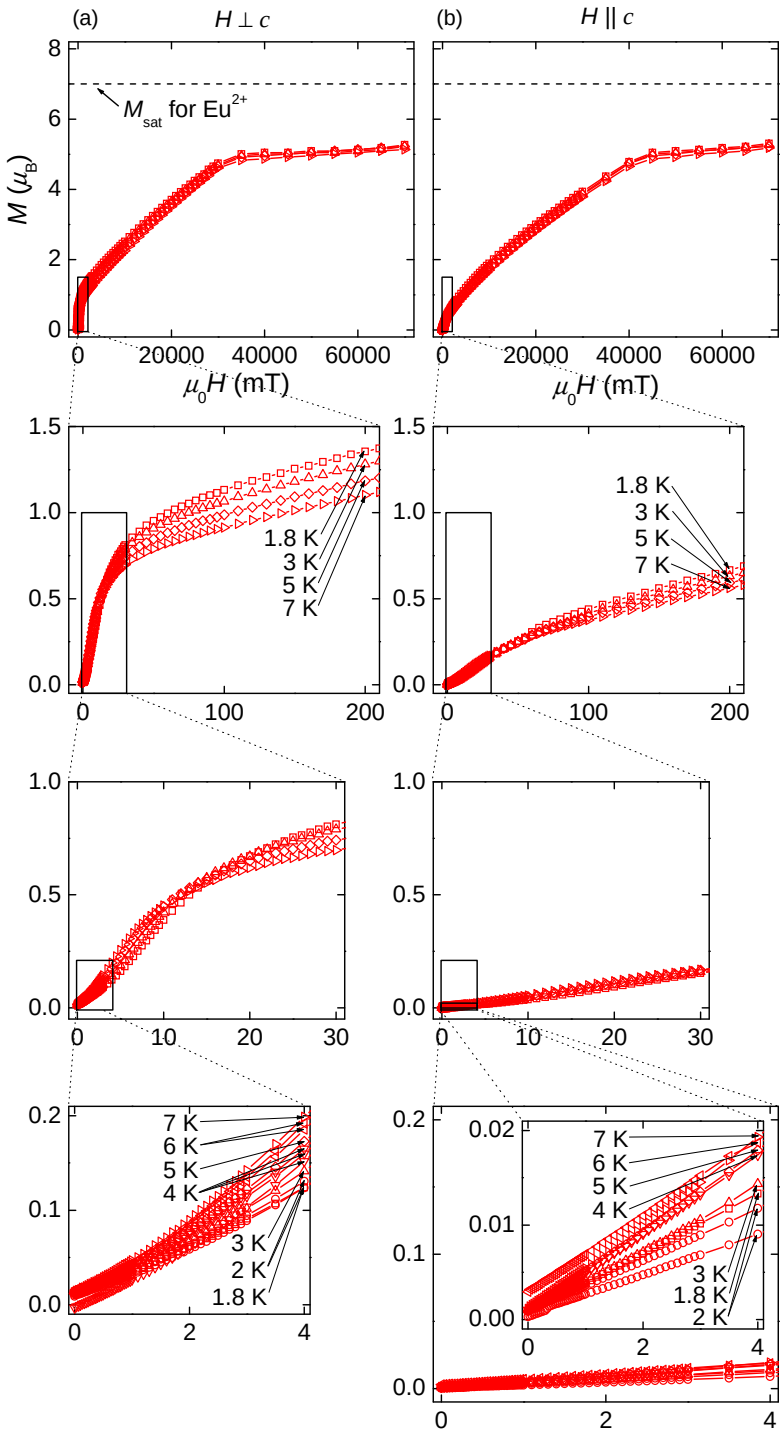

Fig. 5.3.4 T dependences of M versus $\mu_0 H$ for the $EuSn_2As_2$ oriented crystal per formula unit (a) in $H \perp c$ and (b) in $H \parallel c$ at various measurement temperatures of 1.8–7 K. Saturation magnetization (M_{sat}) for Eu^{2+} was written as dotted lines.

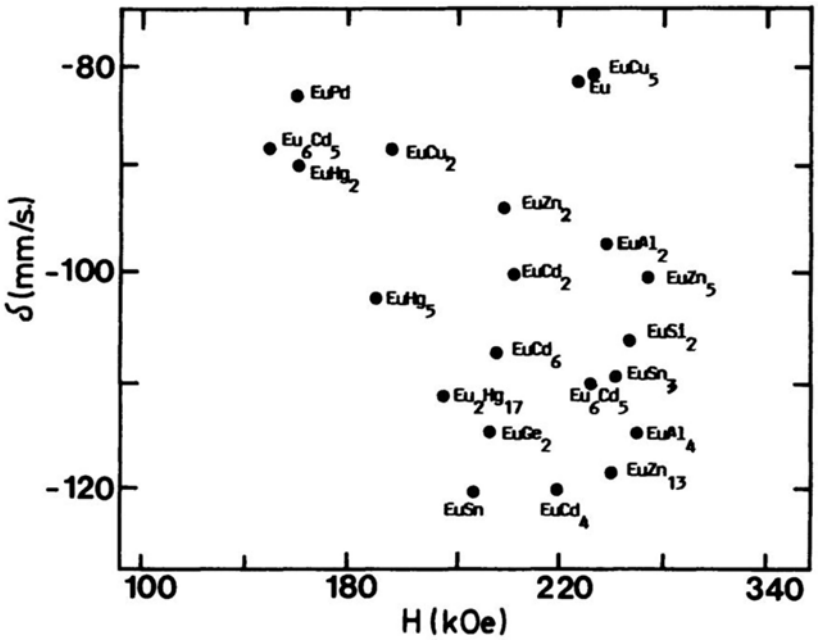

Fig. 5.4.1 IS versus hyperfine field in a series of binary europium-metal compounds [140].

probably derived from magnetic phase transtion. The component of (2) has a peak of the relative amplitude (RA) at T = 20 K. This was also probably involved in the magnetic phase transtion. The component of (2) indicated magnetic splitting. We assumed distribution (W) of B_{int} of the the component of (2) at T = 4.2–20 K as shown in the right bottom part of Fig. 5.4.3. This was interpreted as the transferred hyperfine field because T dependences of magnetic splittings are similar in ^{151}Eu and ^{119}Sn spectra. In other words, B_{int} of Eu^{2+} may be observed in the Sn Mössbauer spectra because of hybridization of Eu and Sn electrons.

Fig. 1.2.5 (a) provides illustrated chemical bonding in $EuSn_2As_2$. For the sake of simplicity, we suppose that Eu atom is bound to six As atoms; Sn atom is bound to three As atoms. There are three As near the Sn atom (labeled as "0" in Fig. 1.2.5 (a)); there are three Eu near the Sn atom. The point is that the Sn atom is close to nine Eu atoms by simple arithmetic and the Sn atom is close to six Eu atoms given the duplication.

The electronic states of Sn cations can be categorized into 16 type on assumptions of the two-type electronic state of Eu cations: Eu^{2+} and Eu^{3+} (Fig. 5.4.4).

5.4.2 Magnetic properties

As shown in Fig. 5.4.5, Arrott plots provides ferromagnetic transition temperature (T_{c}) ~ 20 K in $H \perp c$ and T_{c} ~ 25 K in $H \parallel c$.

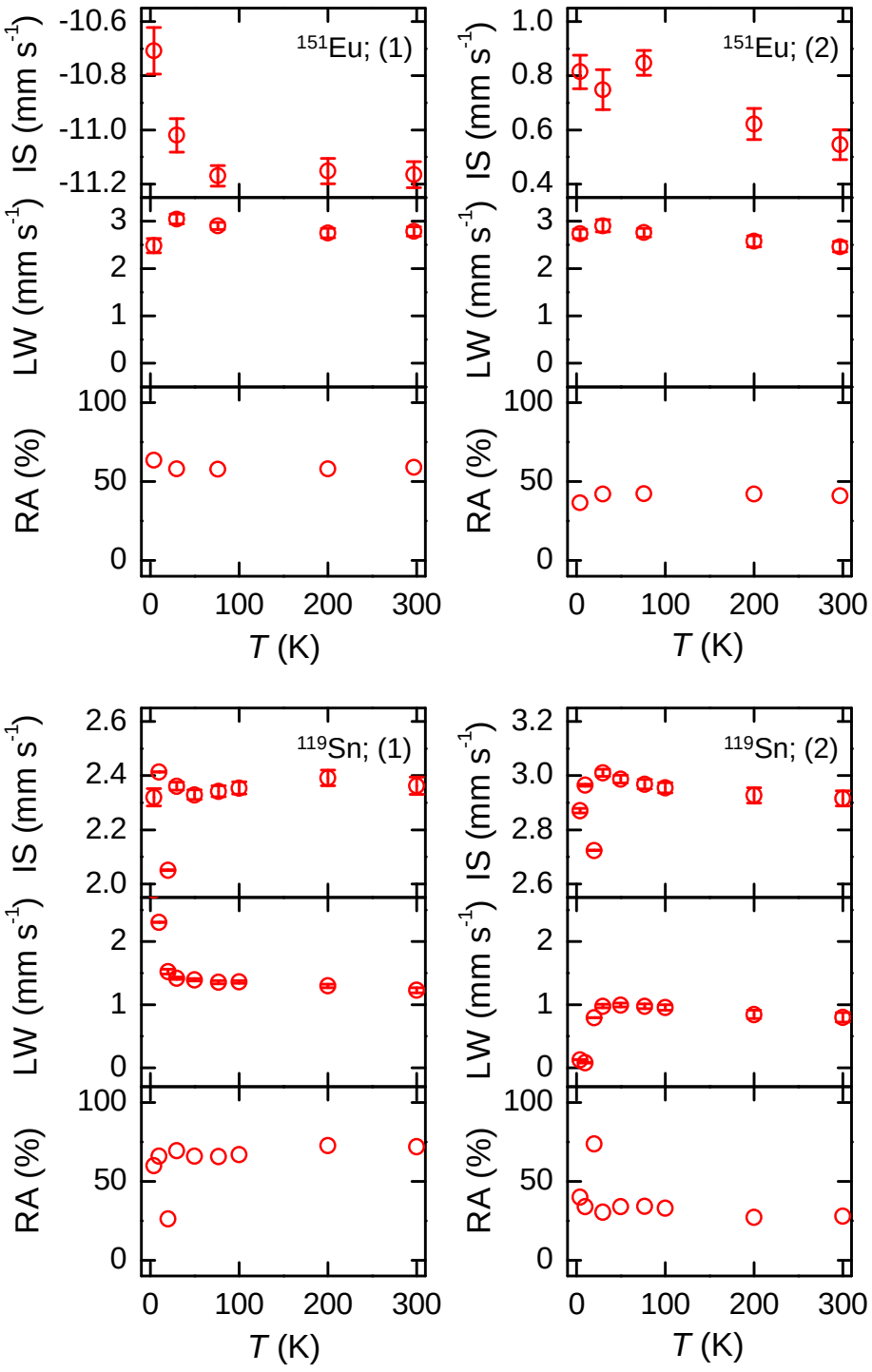

Fig. 5.4.2 Refined parameters of IS, line width (LW), and relative amplitude (RA) for ^{151}Eu and ^{119}Sn Mössbauer spectra of a sample of $EuSn_2As_2$. Mössbauer nuclides and component names are denoted in respective results of IS.

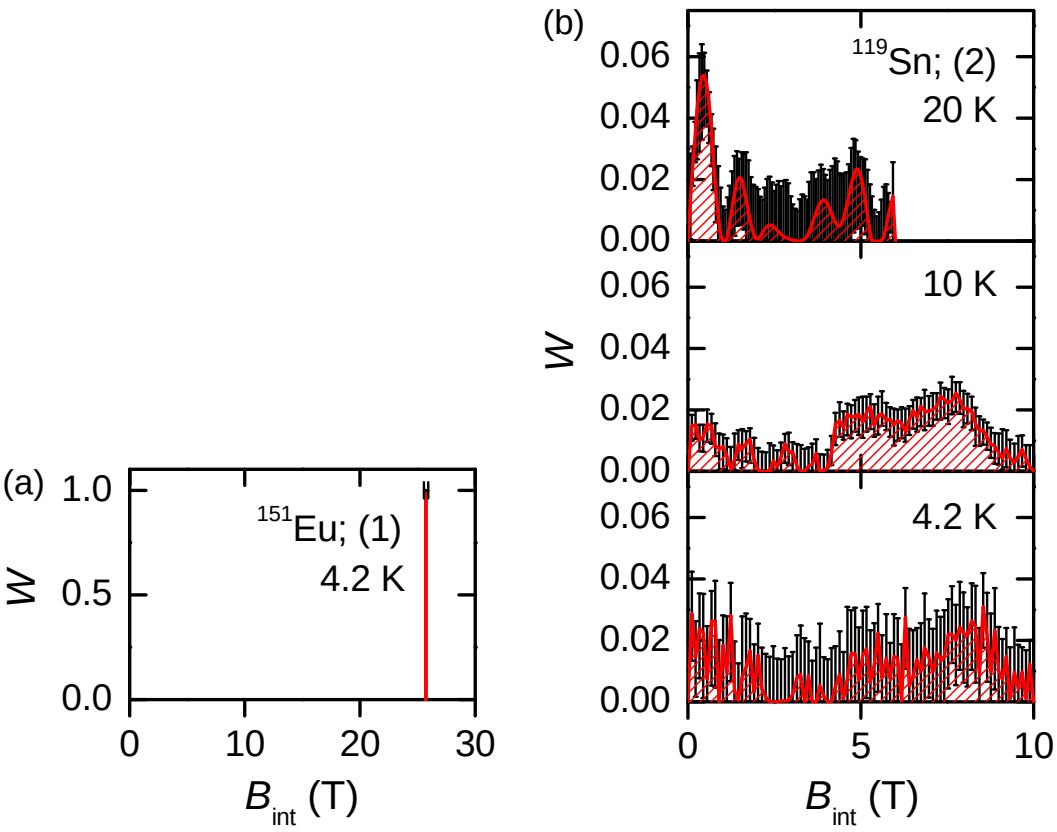

Fig. 5.4.3 Distribution (W) of internal magnetic field (B_{int}) of (a) a component of ^{151}Eu ("^{151}Eu; (1)") at T = 4.2 K and (b) a component of ^{119}Sn ("^{119}Sn; (2)") at T = 4.2–20 K for a sample of $EuSn_2As_2$.

As shown in Fig. 5.4.6, Curie temperature (T_C) for $EuSn_2As_2$ oriented crystal was determined based on T depndence of initial magnetic susceptibility (χ_i). Obtained T_C were 19.3 K in $H \perp c$ and 9.7 K in $H \parallel c$ by using the classical model. T_C were 19.5 K in $H \perp c$ and 17.8 K in $H \parallel c$ by using a model with exponentiation.

5.5 Short summary

Magnetization measurements and Mössbauer spectroscopy for $EuSn_2As_2$ were demonstrated for experimental examination of chemical bonding states and further discussion on the chemical bonding and transport properties. ^{151}Eu Mössbauer spectra indicate both Eu^{2+} and Eu^{3+} components at temperatures from 4.2 to 297 K. This was consistent with measure-

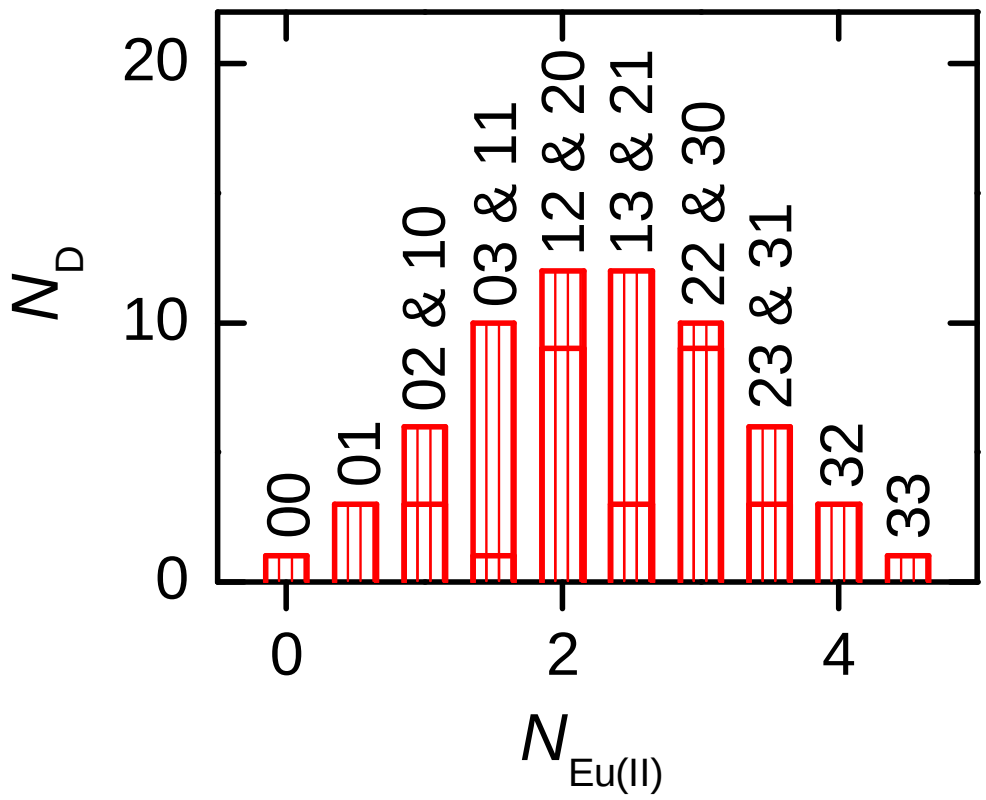

Fig. 5.4.4 The number of the neighbor Eu^{2+} cations ($N_{Eu(II)}$) dependence of the degeneracy (N_D) for Sn cations in $EuSn_2As_2$. The states of Sn cations, ij, have been added. i and j denote the number of those first and second nearest neighbor Eu^{2+} cations, respectively. $N_{Eu(II)}$ and N_D are given as follows:

$N_{Eu(II)} = i + (j / 2)$,

$N_D = {}_3C_i \times {}_3C_j$.

ment values of magnetization of $EuSn_2As_2$ in high magnetic field. The Eu^{2+} component shows magnetic splitting at 4.2 K. ^{119}Sn Mössbauer spectra at 4.2 K also demonstrate magnetic splitting caused by internal magnetic field (B_{int}) of Eu. In $EuSn_2As_2$, Eu atoms are not isolated as cations but rather supply charge carriers to SnAs anionic bilayers. Although this model are not emphasized in previous reports on $EuSn_2As_2$, it will be useful for optimization of charge carrier density in $EuSn_2As_2$-based materials with high thermoelectric properties.

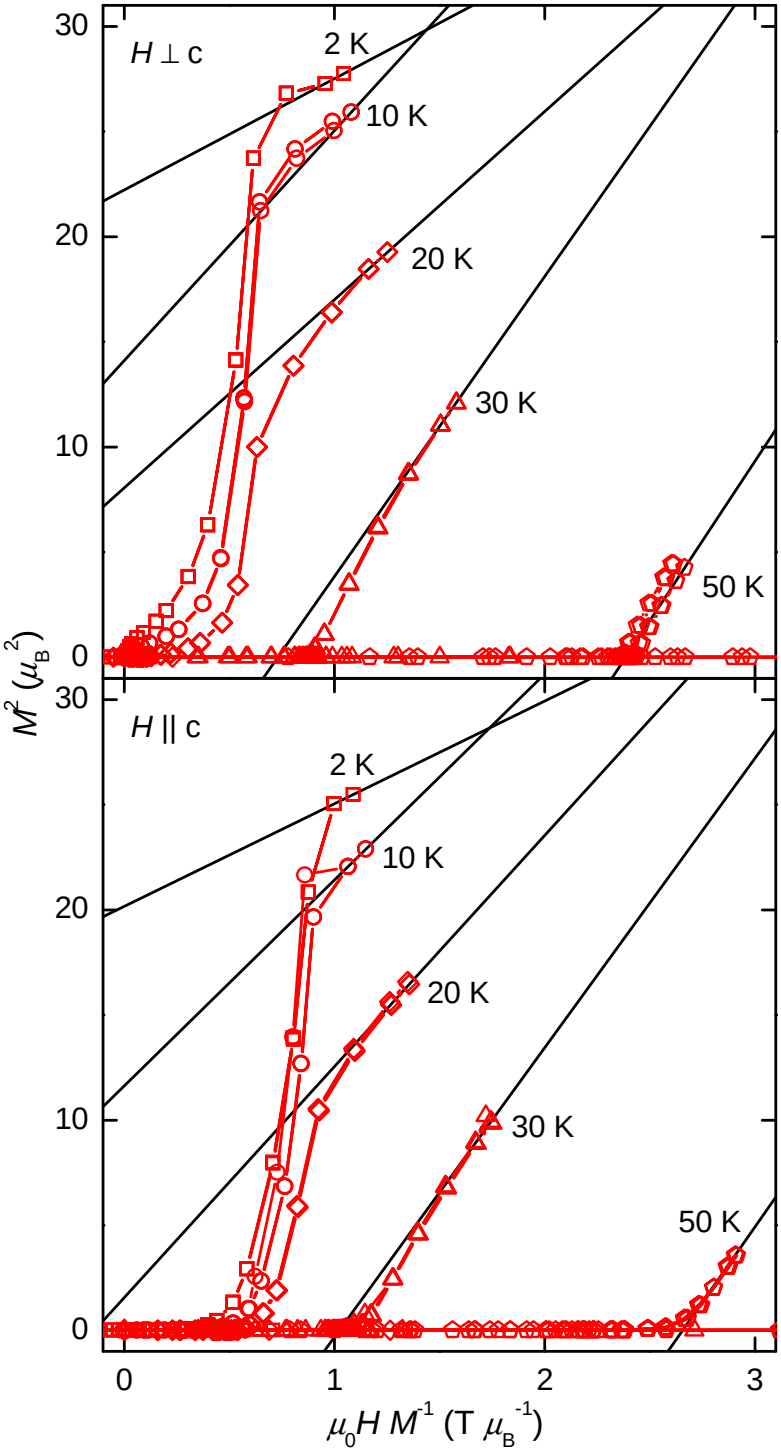

Fig. 5.4.5 Arrott plots for $EuSn_2As_2$ oriented crystal (top) in $H \perp c$ and (bottom) in $H \parallel c$. Measurement temperatures are denoted near the plots. Auxiliary straight lines are drawn for determining the ferromagnetic transition temperature (T_C).

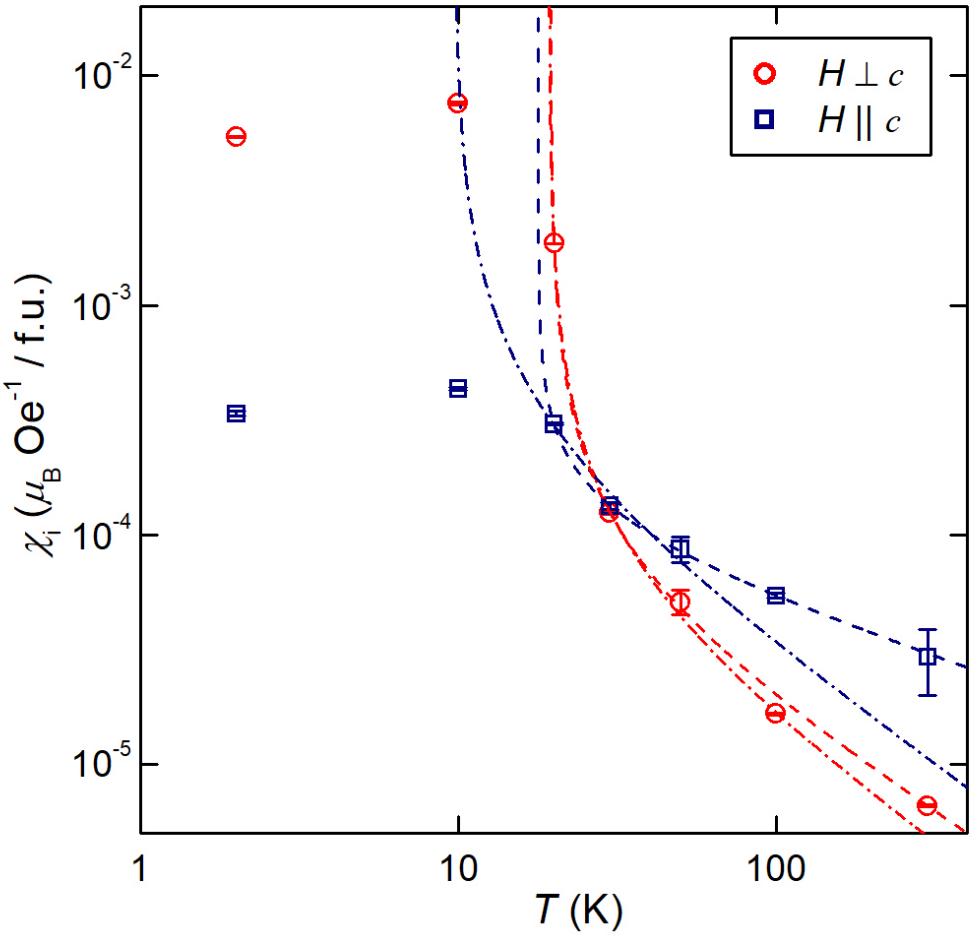

Fig. 5.4.6 χ_i versus T for $EuSn_2As_2$ oriented crystal in $H \perp c$ and in $H \parallel c$. The dashed-and-dotted lines and dashed lines represent fitted curves based on a classical physical model:

$\chi_i(T) = 1 / (T - T_C)$,

and an exponential physical model:

$\chi_i(T) = 1 / (T - T_C)^{\gamma}$,

respectively. T_C and γ are calculated by the least squares method according to plots of $T \geq 20$ K.

6

Electronic states of $EuSn_2As_2$

$EuSn_2As_2$ was reported as "Zintl–Klemm phase" or "Zintl phase" [7]. "Zintl phases" and related compounds[*1] have been said to promising TE materials [57]. This chapter verifies application of $EuSn_2As_2$ to the Zintl–Klemm concept by using electronic state calculations based on DFT.

6.1 Introduction

6.1.1 Backgrounds

Crystallographic structure of $EuSn_2As_2$ on the Zintl–Klemm concept

The Zintl–Klemm concept, which is described in Appendix. A in detail, is applied to $EuSn_2As_2$ in this subsection. The europium (Eu) in $EuSn_2As_2$ may be in a state of mixture of Eu^{2+} and Eu^{3+} cations but we assumed that the Eu is situated in Eu^{2+} cations in this chapter. The Eu atom gives an electron to two Sn atoms one-by-one and becomes a Eu^{2+} cation. The Sn atom is changed into a Sn^- anion with an outer electron configuration of $5s^25p^3$ to form covalent bonds with an As atom with an outer electron configuration of $4s^24p^3$. The Sn^- anion and the As atom, following the octet rule, covalently bond with three Sn^- anions and three As atoms, respectively. Consequently, $[SnAs]^-$ anion layers form a network. Both As atom and Sn^- anion in $EuSn_2As_2$ formally have eight electrons, respectively.

[*1] We refer to these compounds as "Zintl–Klemm cencept compounds"

Possibility of "double" lone s^2 electron pairs (Ls2P) in $EuSn_2As_2$

From the aspect of the application of the Zintl–Klemm concept into $EuSn_2As_2$, both of the Sn^- anion and the As atom have a lone-pair electrons. The $5p^3$ electrons in Sn^- anion and the $4p^3$ electrons in As atoms form the a network of covalent bonds as shown by the lines since the p orbitals are anisotropic while the s orbitals are isotropic, assuming that these orbitals are not hybridized. The $5s^2$ electrons in the Sn^- anion and the $4s^2$ in the As atom, which does not contribute to the covalent bond, are what we called "double" lone s^2 electron pairs (Ls2P) in $EuSn_2As_2$. $NaSn_2As_2$ has less lone electron pairs than $EuSn_2As_2$ from the viewpoint of the Zintl–Klemm concept, reflecting the oxidation state of Na is +1 in $NaSn_2As_2$ while that of Eu is +2 or +3 in $EuSn_2As_2$. In $NaSn_2As_2$, each Sn atom has three covalent bonds and 7.5 electrons whereas each As atom has three covalent bonds and formally eight electrons [34]. The Sn atom has three-quarters lone electron pairs while the As atom has one lone electron pairs in $NaSn_2As_2$. In other words, only 75 % of Sn atoms formally have one lone electron pairs and 25 % of Sn atoms have no lone electron pairs in $NaSn_2As_2$.

Controversial relation between the κ_{ph} and the Ls2P in $EuSn_2As_2$

Lin *et al.* reported that the LASER flash thermal conductivity ($^{LF}\kappa$) at RT of polycrystalline samples of NaSnAs with the porosity (ϕ) of ~4 vol.% and $NaSn_2As_2$ with $\phi \sim 5$ vol.% were 1.70 W m^{-1} K^{-1} and 3.17 W m^{-1} K^{-1}, respectively [34]. The $^{LF}\kappa$ at RT of NaSnAs was nearly equal to the twice of the $^{LF}\kappa$ at RT of $Bi_{0.5}Sb_{1.5}Te_3$ having the measured apparent density (d_{meas}) of 6.77(3) g cm^{-3} [30, 34]. They explained an assumption that the "double" Ls2P reduce the $^{LF}\kappa$ because NaSnAs had far lower $^{LF}\kappa$ than $NaSn_2As_2$ [34]. It is noted that Lin *et al.* compared thermal transport properties of the above-mentioned compounds that have different chemical compositions but these crystallographic structures differ in space group (SG), number of molecules in the unit cell (Z_{uc}), and lattice volume (V) [34]. In contrast, computational physicists determine thermal transport properties of lattice by not only phonon scattering mechanism but also by mass and equilibrium position of the participating elements and computed force constants among the elements [145–147]. Elucidation of the effect of Ls2P on the phonon thermal conductivity (κ_{ph}) should require a comparison between $NaSn_2As_2$ and $EuSn_2As_2$ because they have the same SG and Z_{uc} and almost the same V. $EuSn_2As_2$ have more Ls2P than $NaSn_2As_2$, considering the Zintl–Klemm concept.

Potential of in-plane rattling of Sn atoms in $EuSn_2As_2$

The potential in-plane rattling of Sn atoms in $EuSn_2As_2$ result from the weak chemical bonding of the vdW forces between Sn atoms. The melting point of white Sn is 505.1 K [113], which is lower than the highest temperature in the measurement of the ${}^{SS}\kappa$ and ${}^{LF}\kappa$ of $EuSn_2As_2$. The lowness of melting point of Sn also contributes to the potential rattling in $EuSn_2As_2$. The possible in-plane rattling is expected to lower the κ_{ph} of $EuSn_2As_2$ by analogy with $Cu_{12-x}Zn_x(Sb,As)_4S_{13}$ [148] and LaBi(Se,S)O [149, 150]. The possible "double" Ls2P are also predicted to contribute to the potential rattling in $EuSn_2As_2$ by analogy with $Cu_{12-x}Zn_x(Sb,As)_4S_{13}$ [148].

6.1.2 Aim

This chapter describes electronic states of $EuSn_2As_2$ calculated by *Ab-initio* calculations and evaluates application of Zintl–Klemm concept to $EuSn_2As_2$.

6.2 Method of calculation

Spatial distribution of the charge density difference (CDD; $\Delta\sigma_{ch}$) of $EuSn_2As_2$ was examined using the Vienna *Ab-initio* Simulation Package (VASP) code [151–153] for the DFT calculations with the aid of the Visualization for Electronic and STructual Analysis (VESTA) program [9]. The VASP calculations for charge densities (σ_{ch}) were performed by the plane-wave projector-augmented wave (PAW) method using the Perdew–Burke–Ernzerhof (PBE) functionals [151] as the exchange–correlation functionals. The cuf-off energy was set to 500 eV for plane-wave basis set. The Brillouin zone was sampled by a $24 \times 24 \times 4$ Γ centered grid. Figure 6.2.1 describes the Brillouin zone with the symbol and position of the *k*-points, which was based on the figure obtained by the "Brillouin Zone Viewer" [154].The symbol and position of the *k*-points are in accord with a Brillouin zone of hexagonal lattice produced by Setyawan and Curtarolof [155]. The fractional atomic coordinates of $EuSn_2As_2$ reported by Arguilla *et al.* was adopted. The so-called DFT-D2 method of Grimme [156] was used as description of the van der Waals vdW interactions. The $\Delta\sigma_{ch}$ was obtained by:

$$\Delta\sigma_{ch} = \sigma_{ch}(\text{Compound}) - \sigma_{ch}(\text{Elements}) \tag{6.1}$$

$$\sigma_{ch}(\text{Elements}) = \sum_{i_{el}=1}^{N_{el}} \sigma_{ch}(\text{Element}(i_{el})) \tag{6.2}$$

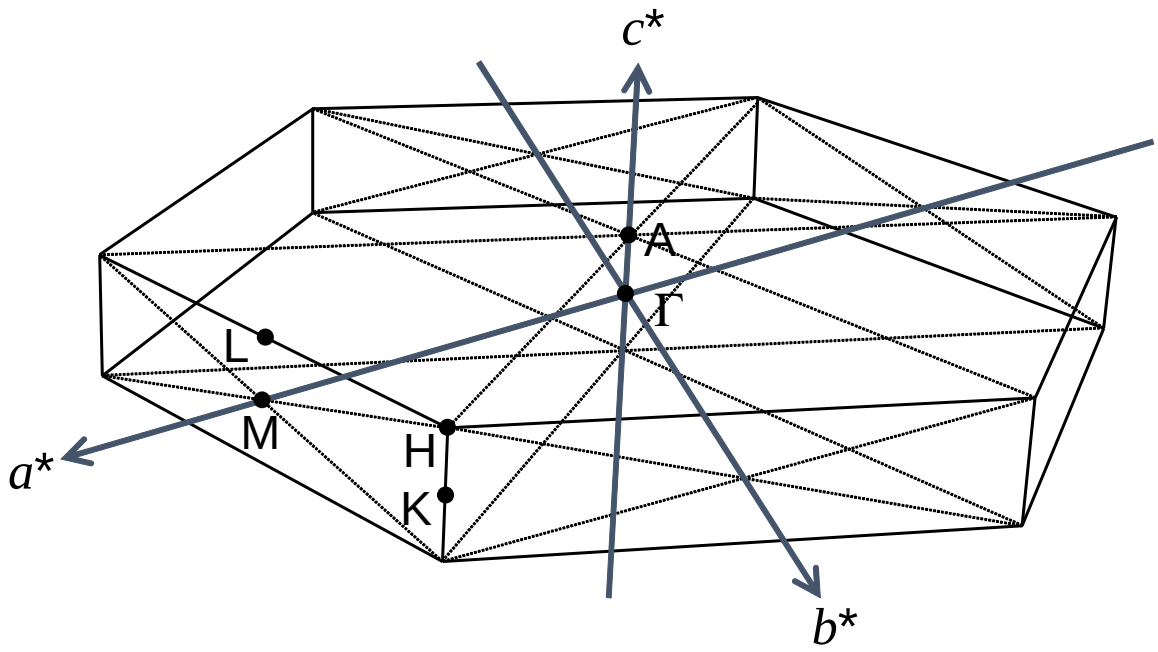

Fig. 6.2.1 A first Brillouin zone of $EuSn_2As_2$ with hexagonal coordinate system with symmetry k-points. The arrows and dotted lines denote the reciprocal vectors and auxiliary lines, respectively. The Brillouin zone was based on the figure by the "Brillouin Zone Viewer" [154]. The symbol and position of the k-points were obtained from the Brillouin zone of hexagonal lattice produced by Setyawan and Curtarolo [155]. The conbinations of the symbols and positions are as follows: Γ (0, 0, 0), A (0, 0, 1/2), H (1/3, 1/3, 1/2), K (1/3, 1/3, 0), L (1/2, 0, 1/2), and M (1/2, 0, 0) [155].

where σ_{ch}(Compound) is the charge density of the compound and σ_{ch}(Element(i_{el})) is the charge density of i_{el}th constituent element in sublattice for the compound. The N_{el} indicates the number of the participating elements of the compound: N_{el} for $EuSn_2As_2$ is equal to three since $EuSn_2As_2$ is composed of Eu, Sn and As. The subtraction in Eq. 6.2 and the summation in Eq. 6.1 were carried out using VESTA. Further details of the calculations were presented in Table 6.2.1.

6.3 Results and discussion

The DFT calculations of $EuSn_2As_2$ to minimize the total free energy (E_{tot}) of the ion-electron system revealed that the optimized hexagonal unit cell volume (V) was 97.4 vol.% compared with that of HP-$EuSn_2As_2$. The reason for the larger value of the experimental

Table 6.2.1 Computational conditions of the density functional theory (DFT) calculation for the charge density difference (CDD; $\Delta\sigma_{ch}$) of $EuSn_2As_2$ using VASP [151–153]. Valency represents the number of electrons obtained by subtracting the number of inner shell electrons from the number of all the electrons in the atom. E_c denotes the default maximum cut-off energy of each pseudopotential. E_{tot} denotes the total free energy of the ion-electron system of $EuSn_2As_2$. Lattice constants are shown for hexagonal coordinate system. Both of on-site Coulomb interaction parameter (U_{os}) and on-site exchange interaction parameter (J_{os}) in europium (Eu) $4f$ electrons are 0 eV.

Pseudopotential	Eu	Title	PAW_PBE Eu_2 06Sep2000
		Valency	8
		E_c (eV)	249.668
	Sn	Title	PAW_PBE Sn_d 06Sep2000
		Valency	14
		E_c (eV)	241.083
	As	Title	PAW_PBE As_d 11Apr2003
		Valency	15
		E_c (eV)	288.651
Lattice	Degrees of freedom	Ions	unmoved
		Cell shape	unchanged
		Cell volume	changed
Others	van der Waals (vdW) interactions		DFT-D2 method of Grimme
	Spin orbit coupling (SOC)		Not taken into account
	Magnetic ordering of Eu		Non spin polarized

lattice constants at RT than the value of the calculated lattice constants for $EuSn_2As_2$ is probably a difficulty for expression of the vdW interactions or a lack of consideration of virtual temperature in the DFT calculations. The vdW interactions are probably difficult to be reproduced by the DFT-D2 method of Grimme in the DFT calculations. Regarding the matter of the virtual temperature, the DFT calculations were performed at absolute zero, where the calculated values of the lattice constants hardly obtain the experimental value at RT. The increasing of the lattice constants at finite temperatures, or thermal expansion, is likely to be caused by an anharmonic term in the phonon. The anharmonic term possibly resulted in not only the giant atomic displacement but also the unusual increasing of the ρ as a function of T.

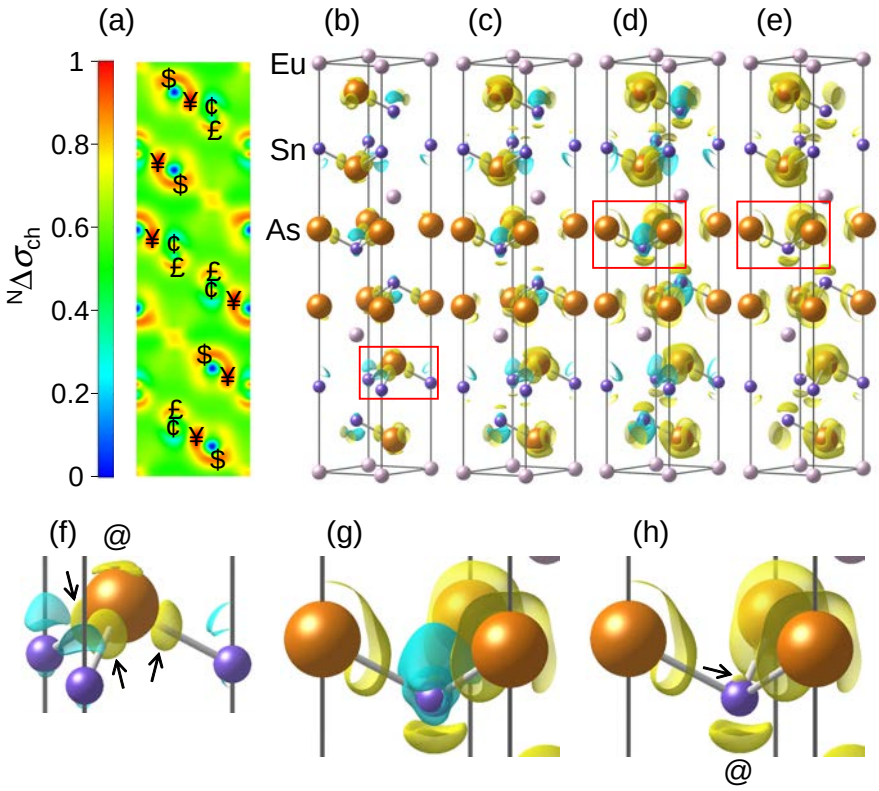

Fig. 6.3.1 Analysis of charge density difference (CDD; $\Delta\sigma$) of $EuSn_2As_2$ with hexagonal coordinate system. (a) Sliced 110 lattice plane. $^{N}\Delta\sigma$ denotes normalized charge density difference defined as:

$$^{N}\Delta\sigma = (\Delta\sigma_{ch} - {}^{Min}\Delta\sigma_{ch}) / ({}^{Max}\Delta\sigma_{ch} - {}^{Min}\Delta\sigma_{ch}),$$

where $^{Max}\Delta\sigma_{ch}$ and $^{Min}\Delta\sigma_{ch}$ is the maximum and minimum $\Delta\sigma_{ch}$ as a function of position in the unit cell, respectively. $^{Max}\Delta\sigma_{ch}$ is equal to $0.0146992{a_B}^{-3}$ and $^{Min}\Delta\sigma_{ch}$ is equal to $-0.0274084{a_B}^{-3}$. a_B is a Bohr radius, whose value is 0.0529177211 nm. $\Delta\sigma$ was calculated by VASP [151–153] and VESTA [9] and visualized using VESTA. Yen signs (¥) mark covalent bonds between the Sn and As atoms. Dollar signs ($) indicate the locations of lone-pair-like electrons near the As site. Cent signs (¢) and pound signs (£) point lone-pair-like electrons near the Sn sites. (b)–(h) Isosurfaces of $\Delta\sigma$. Yellow and blue-green surfaces indicate isosurfaces levels of the electron densities set at (b) $0.010{a_B}^{-3}$ and $-0.010{a_B}^{-3}$, (c) $0.008{a_B}^{-3}$ and $-0.008{a_B}^{-3}$, and (d) $0.006{a_B}^{-3}$ and -$0.006{a_B}^{-3}$, respectively. (e) Yellow surfaces indicate isosurfaces levels of the electron densities set at $0.006{a_B}^{-3}$. (f) Magnified graphics for the area surrounded by a frame in (b). The arrow symbols (←) point covalent bonds between Sn and As atoms. The commercial at sign (@) denotes a lone-pair-like electron cloud surrounding atomic nucleus of As. (g) Magnified graphics for the area surrounded by a frame in (d). (h) Magnified graphics for the area surrounded by a frame in (e). The commercial at sign (@) indicates a lone-pair-like electron cloud surrounding atomic nucleus of Sn. The arrow symbol (←) points an isolated electron cloud surrounding atomic nucleus of Sn.

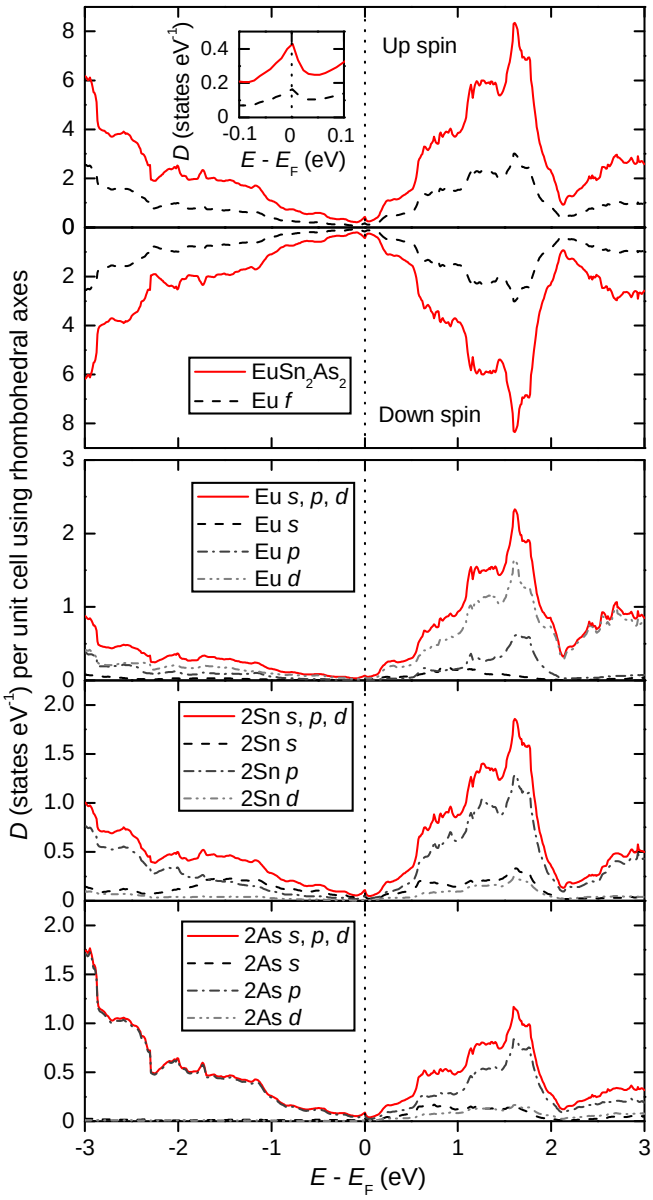

Fig. 6.3.2 Calculated electronic density of states (DOSs) of $EuSn_2As_2$.

Figure 6.3.1 shows computed spatial distribution of the $\Delta\sigma_{ch}$ of $EuSn_2As_2$. Figure 6.3.1 (a) indicated covalent bonds between the Sn and As atoms as shown by yen signs (¥) and lone-pair-like electrons near the As site indicated by dollar signs ($), and near the Sn site indicated by the cent signs (¢) and pound signs (£). There were covalent bonds between Sn and As atoms as shown by three arrow symbols (←) in Fig. 6.3.1 (f).

The As atoms had a lone-pair-like electron cloud surrounding its atomic nucleus as shown

by commercial at sign (@).The Sn atom had an electron cloud in the direction of the enter of the equilateral triangle of As atoms as shown by the arrow symbol (←) in Fig. 6.3.1 (h) and an additional lone-pair-like electron cloud in the opposite direction

The spatial distribution of the $\Delta\sigma_{\mathrm{ch}}$ of $EuSn_2As_2$ suggested the possible existence of the lone-pair electrons near the both Sn and As sites. This interpretation almost corresponded to the chemical bonding in $EuSn_2As_2$ on the Zintl–Klemm concept.The Zintl–Klemm concept, however, unexplained the electron clouds near the Sn site in the direction of the center of the equilateral triangle of As atoms as shown by the arrow symbol (←).

Figure 6.3.2 shows calculated electronic DOSs of $EuSn_2As_2$. The shape of the DOSs suggest covalent-like bonding between Eu, Sn, and As in $EuSn_2As_2$ near the Fermi energy.

6.4 Short summary

Electronic state calculations based on DFT examines application of $EuSn_2As_2$ to the Zintl–Klemm concept. The spatial distribution of the CDD of $EuSn_2As_2$ suggested the possible existence of the lone-pair electrons near the both Sn and As sites. The chemical bonding states of $EuSn_2As_2$ is partly explainable in terms of the Zintl–Klemm concept.

7

Summary and concluding remark

7.1 Summary

Quasi-two-dimensional pnictides are layered compounds that exhibit various functional properties including high thermoelectricity, superconductivity, and topological features. The present study aims application of van der Waals-type quasi-two-dimensional pnictide, $EuSn_2As_2$ to thermoelectric (TE) materials to reveal its transport properties. Furthermore, the present study examines its chemical bonding states by Mössbauer spectroscopy, magnetization measurements, and electrinic state calculations to discuss relations between chemical bonding states and transport properties.

In order to obtain near-single-phase polycrystalline samples of SnAs-based layered compound $EuSn_2As_2$ as a candidate for TE materials, we have established a method of synthesis procedure in which a sample was prepared from Eu ingot and Sn-As pellet in a carbon crucible. As far as our trials were concerned, this synthesis method produced polycrystalline samples free from second phases other than Sn, unlike another syntehsis method in which a sample was prepared from Eu ingot, Sn powder, and As powder in alumina tube. In the method using carbon crucible, 0.8050 g of the 0.9812 g of raw material was recovered. Several trial of this synthesis method will yield an adequate amounts of samples of $EuSn_2As_2$ for TE transport measurements.

Automation of measurements were necessary for experimental competitive development research of the TE materials and superconductors. Automated measurements in our laboratory of electrical resistivity (ρ) above and below room temperature (RT), Seebeck coefficient (S) above RT, and steady-state thermal conductivity ($^{SS}\kappa$) at RT were realized using the Laboratory Virtual Instrument Engineering Workbench (LabVIEW) programs for controlling

electronic test equipments and temperature controllers. Obtained measurement raw data were processed using Python code to obtain physical quantities. Particularly, we established calculation processes for obtaining ${}^{SS}\kappa$ considering loss of thermal radiation. The above-mentioned work will achieve reduction in working hours and also will prevent careless mistakes.

The electrical and thermal transport properties of densified polycrystalline sample of $EuSn_2As_2$ with porosity (ϕ) of 2.4(9) vol.% were measured from RT to ~673 K perpendicular to the pressing direction of hot pressing; i.e. the crystallographic phase of $EuSn_2As_2$ in the sample was weakly oriented to the *a*-*b* plane of the hexagonal coordinate system during our measurements.

The plot of temperature (T) dependence of the electrical resistivity (ρ) shows metallic behavior. The ρ is probably affected by the multiband. The ρ includes T^2 term. The T^2 term is probably derived from spectral conductivity (s_c) as a function of energy (ε) relative to the band edge, electron–electron scattering, ionized impurity scattering related to the displacement of participating elements, and/or intervalley scattering. The plot of T dependence of the Seebeck coefficient (S) shows that the carriers exhibit p-type polarity. The measurement values of (ρ, S) was (0.50(3) mΩ cm, 50(4) μV K^{-1}) at $T \sim 673$ K. The power factor (P) was 0.51(8) mW m^{-1} K^{-2} at 673(4) K. The direct thermal transport measurement reveals that the thermal conductivity (κ) decreases with increasing T. Using the WFL law, the ratio of phonon thermal conductivity (κ_{ph}) to κ, defined as κ_{ph}/κ, was 0.56(8) at $T = 374(4)$ K and 0.35(7) at 673(6) K. The ZT value was 0.067(8) at $T = 673(3)$ K. $EuSn_2As_2$ seems to be over-doped as a TE material. Suppression of the hole concentration will be a possible route for improving the TE properties of $EuSn_2As_2$-based compounds.

Magnetization measurements and Mössbauer spectroscopy for $EuSn_2As_2$ were demonstrated for experimental examination of chemical bonding states and further discussion on the chemical bonding and transport properties. ^{151}Eu Mössbauer spectra indicate both Eu^{2+} and Eu^{3+} components at temperatures from 4.2 to 297 K. This was consistent with measurement values of magnetization of $EuSn_2As_2$ in high magnetic field. The Eu^{2+} component shows magnetic splitting at 4.2 K. ^{119}Sn Mössbauer spectra at 4.2 K also demonstrate magnetic splitting caused by internal magnetic field (B_{int}) of Eu. In $EuSn_2As_2$, Eu atoms are not isolated as cations but rather supply charge carriers to SnAs anionic bilayers. Although this model are not emphasized in previous reports on $EuSn_2As_2$, it will be useful for optimization of charge carrier density in $EuSn_2As_2$-based materials with high thermoelectric properties by means of partial substitution of the Eu atom for other lanthanides.

Electronic state calculations based on density functional theory (DFT) examines applica-

tion of $EuSn_2As_2$ to the Zintl–Klemm concept. The spatial distribution of the charge density difference (CDD; $\Delta\sigma_{ch}$) of $EuSn_2As_2$ suggested the possible existence of the lone-pair electrons near the both Sn and As sites. The chemical bonding states of $EuSn_2As_2$ is partly explainable in terms of the Zintl–Klemm concept.

7.2 Future outlook

Mechanism of T dependence of ρ of $EuSn_2As_2$ at high temperatures needs further discussion. X-ray diffraction (XRD) measurements at high temperatures with the aid of Rietveld refinement will be the key because they will reveal electron-phonon scattering.

$EuSn_2As_2$ seems to be over-doped as a TE material. Suppression of the hole concentration will be a possible route for improving the TE properties of $EuSn_2As_2$-based compounds.

Moreover, Sakuragi *et al.* made a landmark report on anisotropic superconductivity of $EuSn_2As_2$ [12]. The superconductivity was fractional at least; further reports were necessary in order to judge whether or not the supercondutivity occurs in bulk.

Furthermore, chemical bonding states of $EuSn_2As_2$ includng Eu^{3+} cations are needed to uncover.

A

Comments on Zintl–Klemm concept

A.1 Zintl's research of intermetallic compounds

Zintl began research with respect to intermetallic compounds by writing a paper in German in 1929 [157]. This short publication was titled "Salzartige Verbindungen des Natriums und ihr Übergang zu intermetallischen Phasen," whose English translation was "Salt-like Compounds of Sodium and their Transition to Intermetallic Phases" [158].

In 1930s Zintl and co-workers published a series of papers subtitled "Mitteilung über Metalle und Legierungen," whose English version was "Announcement on Metals and Alloys" [159–183]. In these articles, Zintl and colleagues linked the position of the participating elements of the intermetallic compounds in the periodic table to the chemical composition,

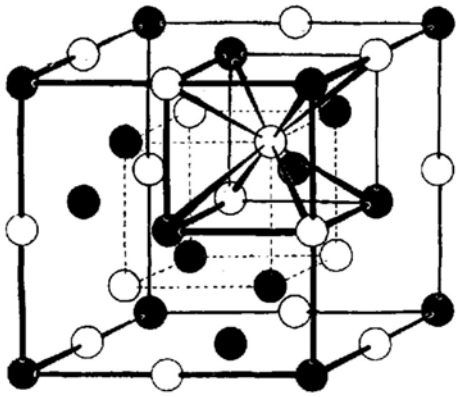

Fig. A.1.1 Crystallographic structure of NaTl. This figure is reprinted from Zintl [184].

Tabelle 6.

NaTl-Strukturen im Periodischen System.

II	III	IV
		C
	LiAl	Si
LiZn	LiGa	Ge
LiCd	LiIn, NaIn	Sn
	NaTl	
rot	weiß	
paramagnetisch?	diamagnetisch?	

Fig. A.1.2 Crystallographic structure of NaTl in the periodic table. This table is reprinted from Zintl [184].

the crystallographic structure, the solubility in ammonia (NH_3), and the valence electron concentration (VEC) of the intermetallic compounds. [159–189]. It is noted that the VEC was defined as the total number of valence electrons per the total number of atoms. [184,187–191].

In 1932, Zintl and Dullenkopf reported the crystallographic structure of NaTl [162]. In 1939, Zintl interpreted a diamond structure of the Tl sublattice in the crystal of NaTl (Fig. A.1.1) [184]. The English version of Zintl's interpretation of NaTl crystal is shown below.

> If one now thinks of the sodium (Na) atoms removed from the NaTl grid, a skeleton is left behind, which is formed from touching thallium (Tl) atoms and has the shape of a diamond lattice. It is known that elements carbon (C), silicon (Si), germanium (Ge) and tin (Sn) crystallize in the diamond grid (Fig. A.1.1). These elements have four valence electrons per atom. aluminum (Al), gallium (Ga), indium (In) and Tl have only three valence electrons, and their atoms do not form a diamond grid on their own. However, they acquire this ability when alloyed with the slightly electron-emitting atoms of lithium (Li) or Na in a ratio of 1 : 1. A total of four valence electrons then meet each Tl atom, and the Tl atoms are arranged into a diamond grid, in whose gaps the hulls of the electron-supplying alkali atoms must be installed. Thus it is explained that the alkali atoms with greatly reduced radii sit in these grids, because the transition of an atom to the positive ion is always associated with a reduction of the particle.
>
> LiZn and LiCd also have the same structure, although there are only three valence electrons on each zinc (Zn) or cadmium (Cd) atom. Here, the electron levels of the dia-

Tabelle 1. Elemente der großen Perioden des Periodischen Systems, welche 1 bis 7 Stellen vor einem Edelgase stehen.

			Anionenbildner				Edelgase
Cu	Zn	Ga	Ge	As	Se	Br	Kr
Ag	Cd	In	Sn	Sb	Te	I	X
Au	Hg	Tl	Pb	Bi			Em

↑ Zintl-Grenze

Fig. A.2.1 Elements of the large periods of the periodic table which lie in less than seven places in front of noble gases. This table is reprinted from Laves [192].

mond binding seem to be incompletely occupied, and this deficiency is also noticeably reflected in the red color of LiZn and LiCd.

The point of view of the electron transfer for NaTl lattice leads to the perspective called Zintl–Klemm concept.

It is noted that in Zintl's paper a table provides physical properties of compounds with NaTl-type crystallographic structure in terms of the position of the participating elements in the periodic table. The table shows that LiZn and LiCd are red and are expected to be paramagnetic while LiAl, LiGa, LiIn, NaIn, and NaTl are white and are anticipated to be diamagnetic.

A.2 Laves' original definition of Zintl phase

In 1941, Laves summarized Zintl's works in an obituary dedicated for Zintl [185, 192]. Laves originally defined a concept of "Zintl-phasen" in German [185, 192]. The following is an English translation and Japanese translation (日本語訳) of Laves' original definition of Zintl phase [192].

■ English translation

Summary of the rules and laws found by Zintl.

If we summarize the above report in brief, the following facts emerge as the core of Zintl's investigations:

1. In the large periods of the periodic system of the elements, elements 1–4 places

in front of a noble gas behave significantly differently in terms of many properties than those elements which stand 5–7 places in front of a noble gas (see Table I[*1]). It was therefore appropriate for this report to draw a line between the elements Ge, Sn, lead (Pb) on the one hand and Ga, In, Tl on the other, which was called the Zintl line.

2. Zintl showed that the elements to the right of the Zintl line can form anions, while those to the left of the line cannot.

3. Zintl also showed that the elements to the right of the Zintl line behave significantly differently from those to the left of the line in their alloy-forming properties. The elements to the right of the line can bind chemically to alkali and alkali earth metals to become components of "valence compounds (valenzlnmäßig zusammengesetzten in German)"[*2], while those to the left of the line cannot.

4. The above-mentioned "valence compounds" containing the elements to the right of the Zintl line are characterized by two important properties, which make it appear appropriate to mark them by the designation of the Zintl-Phases. a) Zintl phases typically crystallize in "non-metallic", salt-like structures such as anti-fluorite, anti-Mn_2O_3, anti-La_2O_3, anti-tysonite, and anti-BiF_3. b) Zintl phases are those alloy systems which contain the largest quantity of alkali or alkali earth metal as components.

5. In addition to the above findings, the structural determination of many alloys including alkali or alkali earth metals, in particular Li and Na, yielded important insights into the binding mechanism of alloys.

■ Japanese translation (日本語訳)

Zintl によって見つかった規則の概要.

上記を簡単に要約して浮かび上がった Zintl の研究の核心は以下のとおりである.

1. 大きな (1 族から 18 族までの) 周期表における, 希ガスから数えて 1–4 周期だけ手前の元素は, 希ガスから数えて 5–7 周期だけ手前の元素よりも, 多くの点で有意に異なる特性を示す (表 I 参照[*3]). したがって, 彼の論文では, Ge, Sn および Pb (の族) と, Ga, In および Tl (の族) との間に, Zintl 境界と呼ばれる線を引くのが適切であった.

2. Zintl は, Zintl 境界の右側の元素はアニオンの形成が可能であるが, 一方で,

[*1] see Fig. A.2.1

[*2] Nowadays, "valence compounds" are understood as compounds intermediate between intermetallic compounds and ionic compounds

[*3] see Fig. A.2.1

Zintl 境界の左側の元素はアニオンの形成が不可能であると示した.

3. Zintl はまた, Zintl 境界の右側の元素と左側の元素とで, 合金形成の特性が大きく異なることを示した. Zintl 境界の右側の元素はアルカリ金属やアルカリ土類金属と化学結合して “価化合物 (ドイツ語で valenzlnmäßig zusammengesetzten)” を作ることが可能であるが, Zintl 境界の左側の元素はこれができない.

4. Zintl 境界の右側の元素を含む, 上で説明した “価化合物” は, (以下で言及する a) と b) の) ふたつの重要な特性により特徴づけられる. これらの特性は (また), Zintl 相という名称 (のもの) を特徴づけると考えるのが適切である.

a) Zintl 相は, 典型的には “非金属的な” 塩, 例を挙げると, 逆蛍石型, 逆 Mn_2O_3 型, 逆 La_2O_3 型, 逆タイソン石型, 逆 BiF_3 型のような結晶構造をとる.

b) Zintl 相は, 上記 (a) で) で述べた合金の中で, アルカリ金属やアルカリ土類金属を構成元素として最大限に含む.

5. 上記に加えて付け加えて言うことには, アルカリ金属やアルカリ土類金属, 特に Li や Na を含む, 多くの合金の結晶構造の決定は, 合金の化学結合のメカニズムに対して, 重要な洞察を与える.

A.3 Establishment of the Zintl–Klemm concept

In 1941, Laves introduced Zintl's interpretation of the valence electronic and crystallographic structure of NaTl crystal as mentioned previously [184, 192]. In 1950s, Klemm and Fricke demonstrated that NaTl showed diamagnetic whereas LiAl, LiIn, NaIn, LiZn, and LiCd exhibited non-magnetic or weakly paramagnetic, which would be explained by making a hypothesis that the magnetic behavior was linked to the difference of the number of electrons per the participating anion, because all the crystallographic structures of these phases are isostructual [193, 194]. Klemm *et al.* generalized Zintl's interpretation of NaTl lattice [185, 193–195]. They argued that the component of electropositive element transfers electrons to the component of electronegative element in the compound and then the resulting outer electronic configuration of the acceptor corresponds to an element with the same number of valence electrons [185–189, 194, 195]. Nowadays researchers tend to refer to the above-mentioned imaginative view as the Zintl–Klemm concept [188, 189].

A.4 Applications of the Zintl–Klemm concept

The Zintl–Klemm concept has been applied to a more wide variety of compounds including ternary compounds and transition metal compounds [185, 186, 196–200]. Some scientists refer to the compounds obeying the Zintl–Klemm concept as Zintl phases [196]. The expanded Zintl phases include layered ternary compound $BaMg_2Si_2$ and $CaNi_2P_2$ [196, 200].From the perspective of the Zintl–Klemm concept, $BaMg_2Si_2$ [201] contains dichalcogenide anions Si^{-}-Si^{-} dumb-bells and $CaNi_2P_2$ [202] consists of $[Ni_2P_2]^{2-}$ anion network layers interspersed with Ca^{2+} cation layers [196, 200]. Kauzlarich and Janka illustrated $BaGe_2As_2$ [203] as a ternary compound obeying the "Zintl concept" [188, 189]. Since the technical words relating to Zintl phase are not unified, today's researchers are required to read "Zintl phase" carefully in recent reports. Scientists who have learned in physical chemistry probably think that phase is closely linked to phase diagram and phase boundary in thermodynamic equilibrium state; i.e. as examples of phase they will mentioned solid phase, crystallographic phase, nematic phase, and ferromagnetic phase. The expanded Zintl phase seems to be not a member of these classical phases but be close to something like a concept.

B

Programs and relevant files for transport measurements

B.1 Laboratory Virtual Instrumentation Engineering Workbench (LabVIEW)

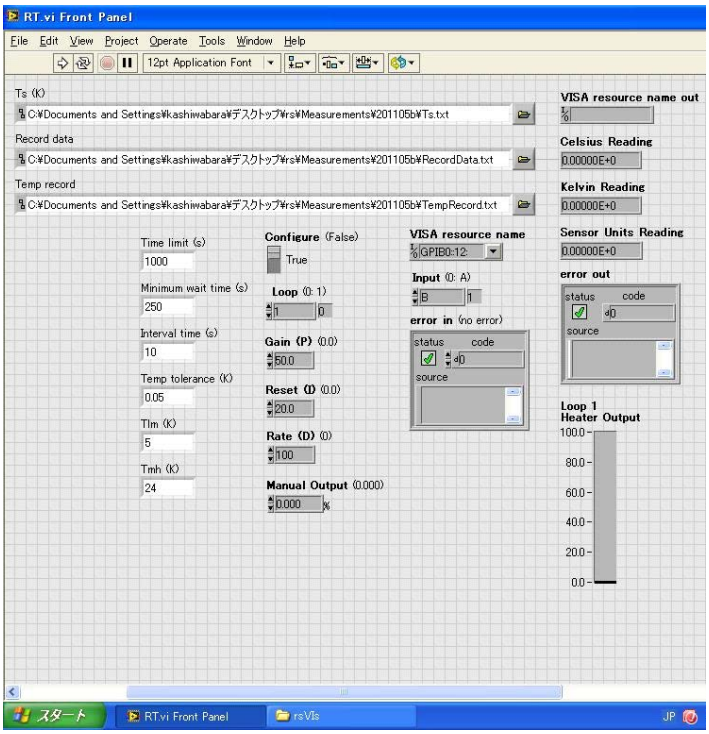

Fig. B.1.1 Left part of the front panel of a LabVIEW virtual instrument (VI) named "RT.vi," which was for measurements of temperature (T) dependence of electrical resistance (R).

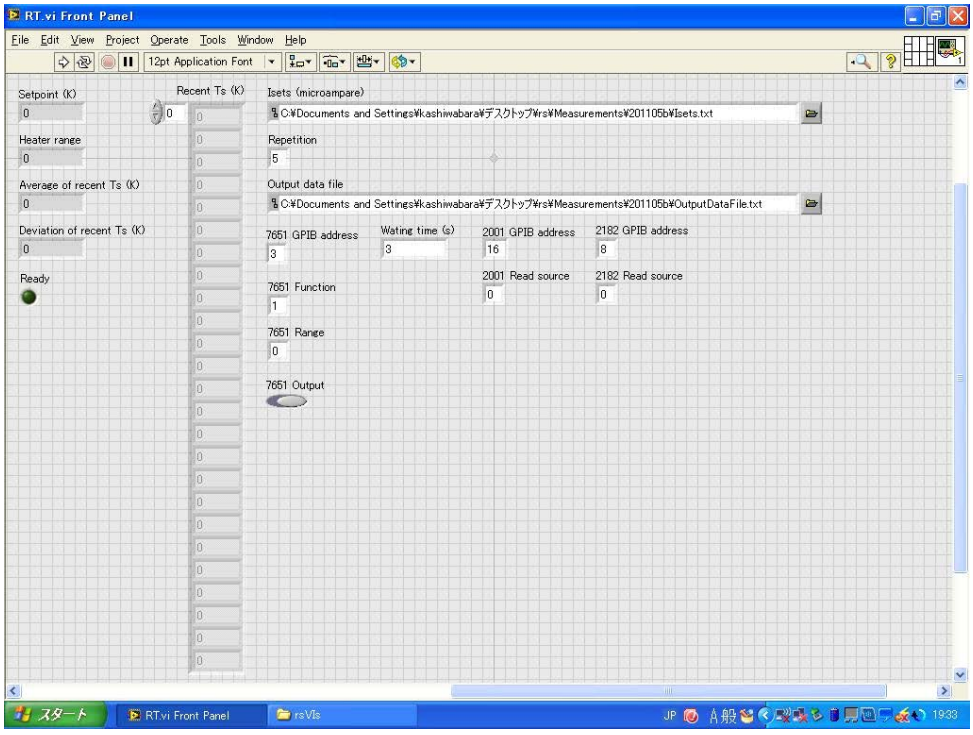

Fig. B.1.2 Right part of the front panel of "RT.vi."

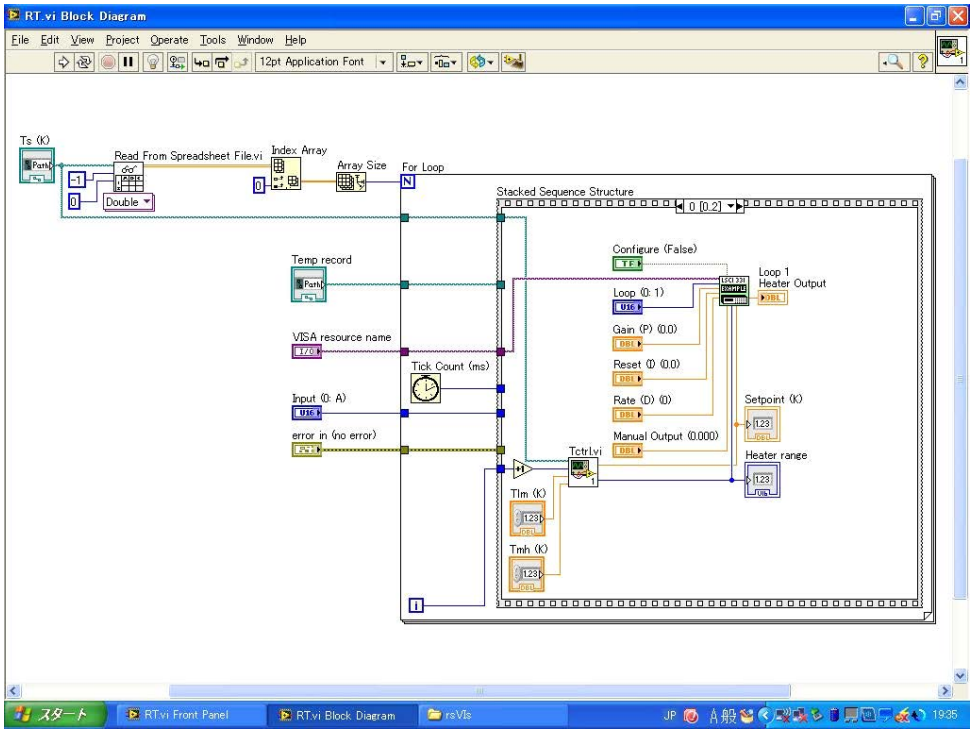

Fig. B.1.3 Block diagram of “RT.vi,” part 0.

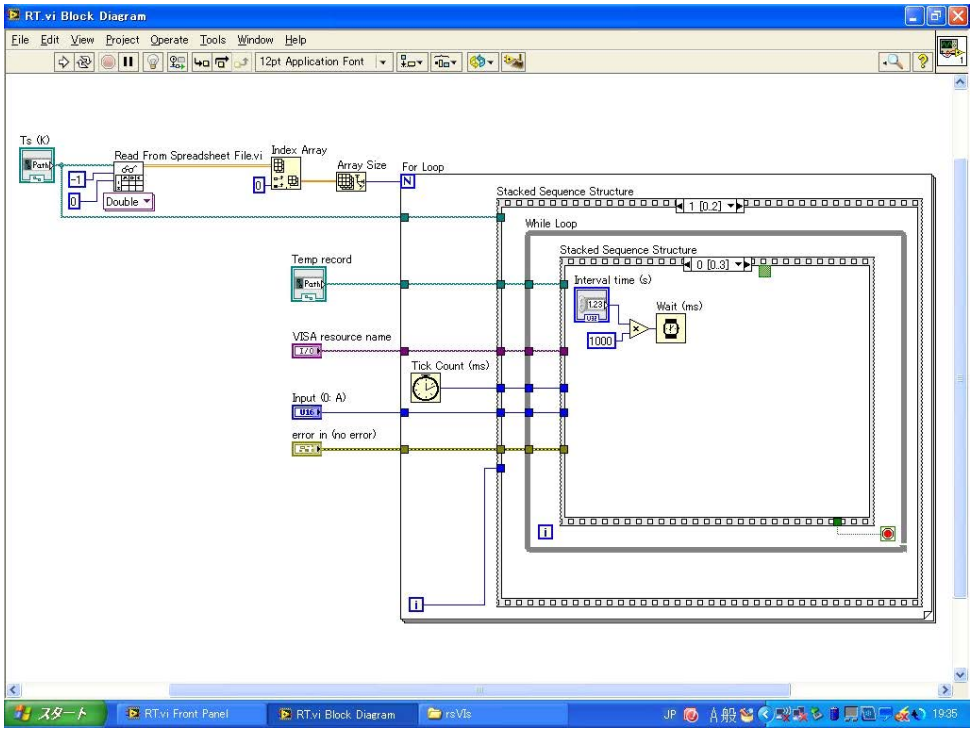

Fig. B.1.4 Block diagram of “RT.vi,” part 1-0.

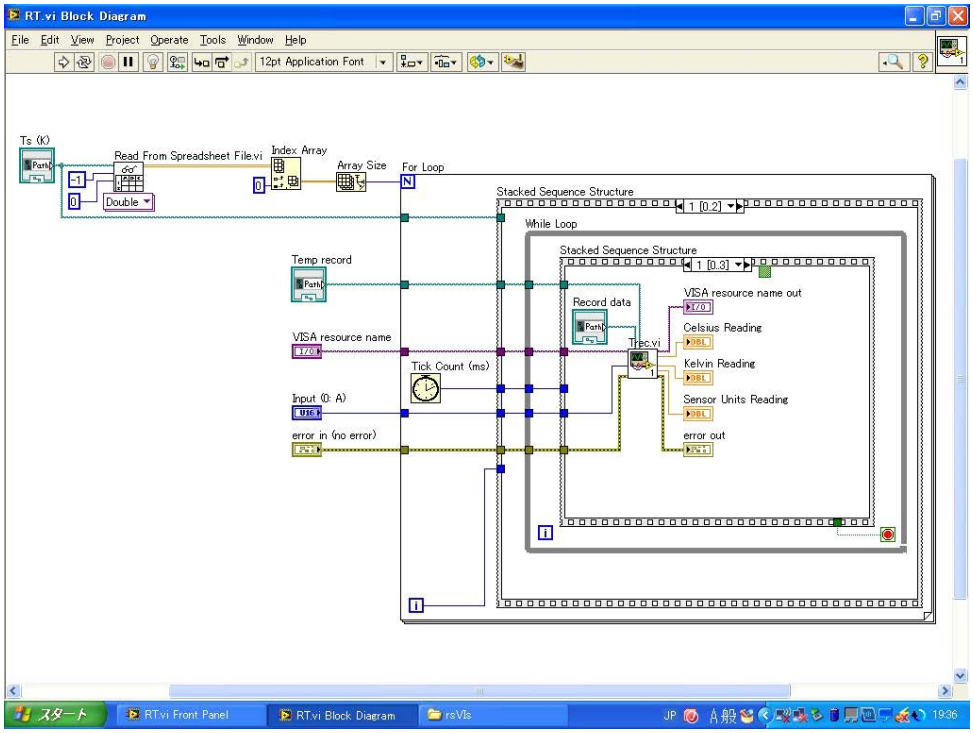

Fig. B.1.5 Block diagram of “RT.vi,” part 1-1.

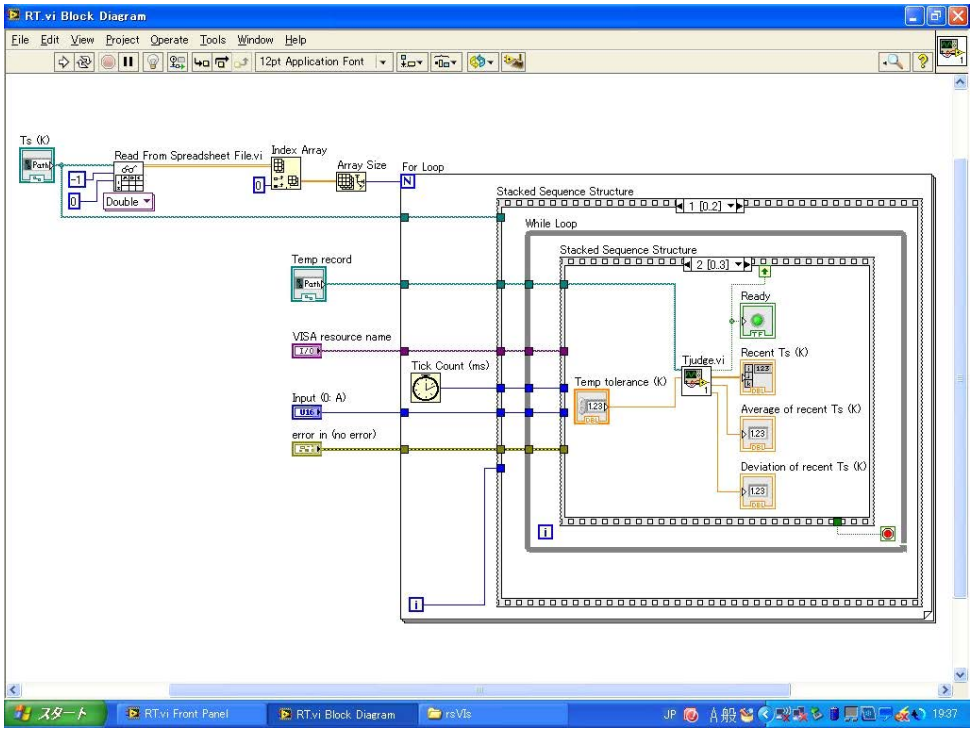

Fig. B.1.6 Block diagram of “RT.vi,” part 1-2.

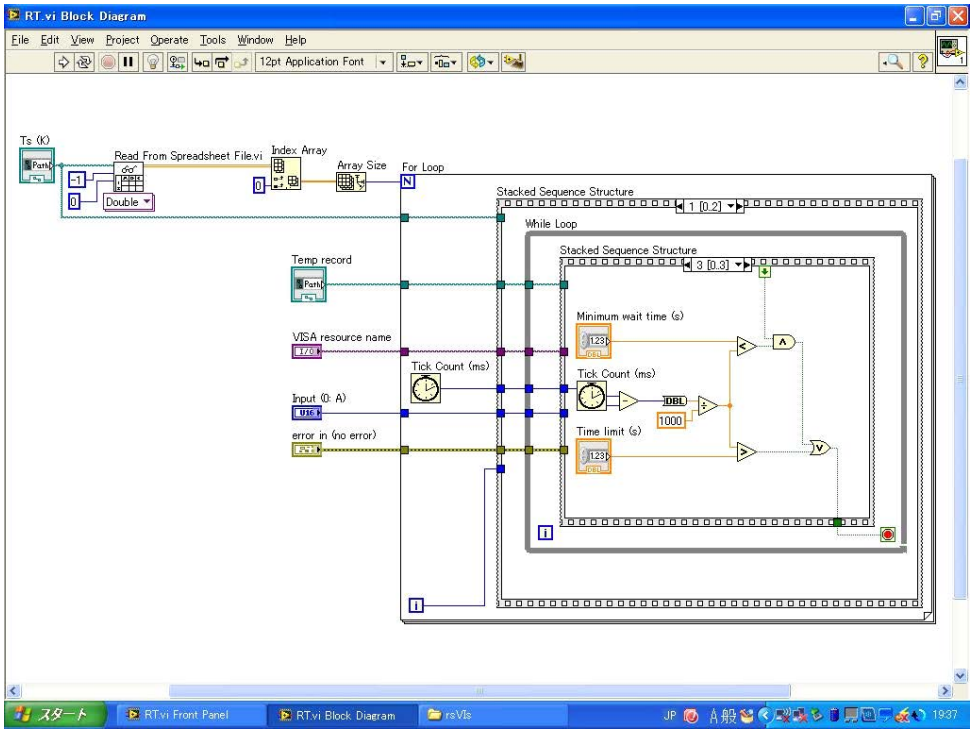

Fig. B.1.7 Block diagram of “RT.vi,” part 1-3.

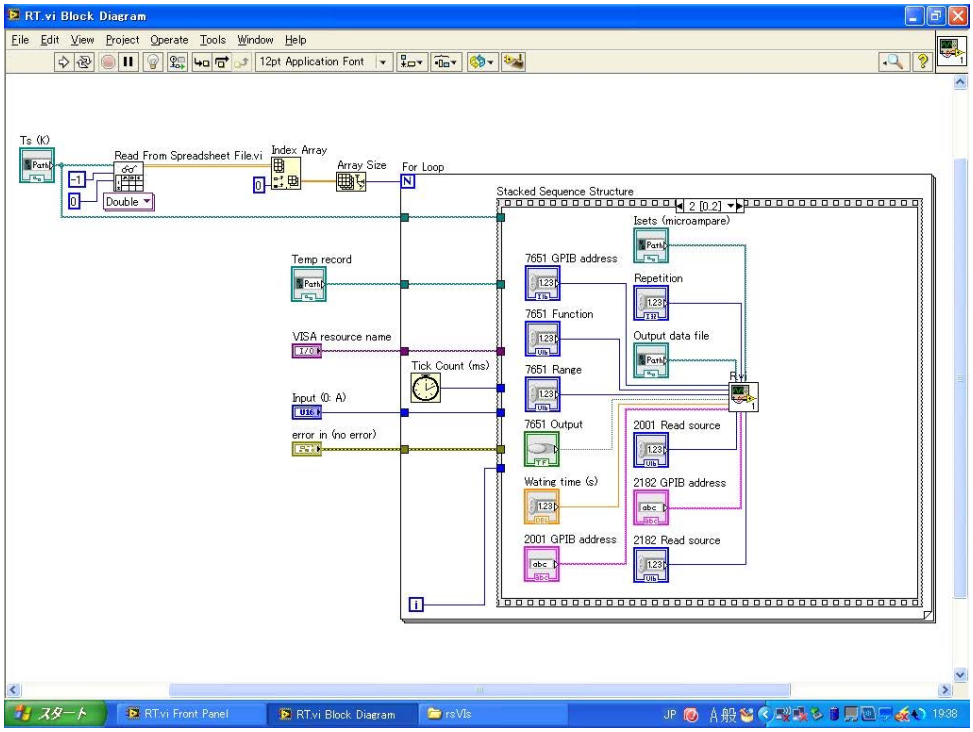

Fig. B.1.8 Block diagram of “RT.vi,” part 2.

(a)
```
-1000↓
-750↓
-500↓
-250↓
0↓
250↓
500↓
750↓
1000↓
```

(b)
```
6↓
8↓
10↓
12↓
14↓
16↓
18↓
20↓
22↓
24↓
26↓
28↓
30↓
31↓
32↓
33↓
34↓
35↓
36↓
37↓
38↓
39↓
40↓
41↓
42↓
43↓
44↓
45↓
46↓
47↓
48↓
49↓
50↓
51↓
52↓
53↓
54↓
55↓
56↓
57↓
58↓
59↓
60↓
62↓
64↓
66↓
68↓
70↓
72↓
74↓
76↓
78↓
80↓
82↓
84↓
86↓
88↓
90↓
95↓
100↓
105↓
110↓
115↓
120↓
130↓
140↓
150↓
160↓
180↓
200↓
220↓
240↓
```

Fig. B.1.9 (a) Isets.txt. (b) Ts.txt.

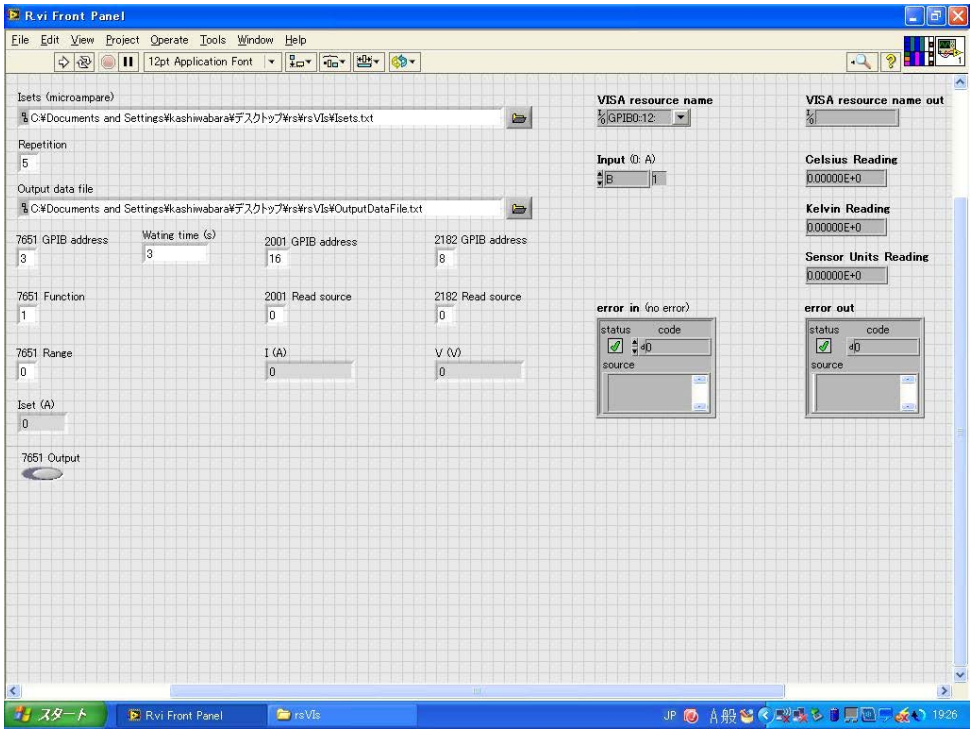

Fig. B.1.10 Front panel of "R.vi," which was for measurements of electrical resistance (R).

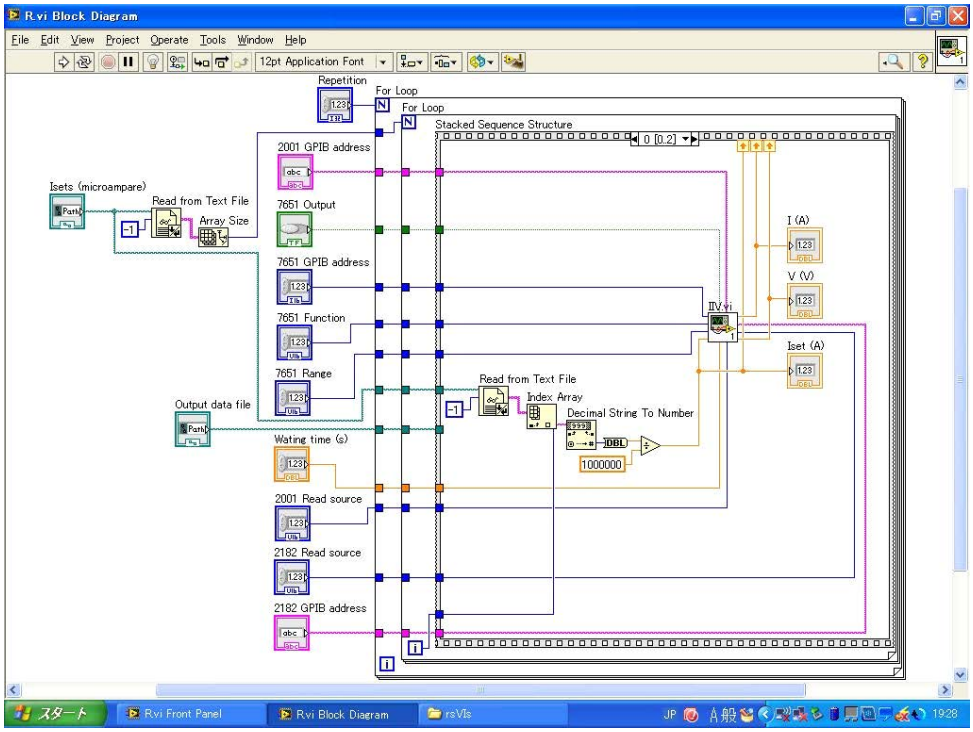

Fig. B.1.11 Block diagram of "R.vi," part 0.

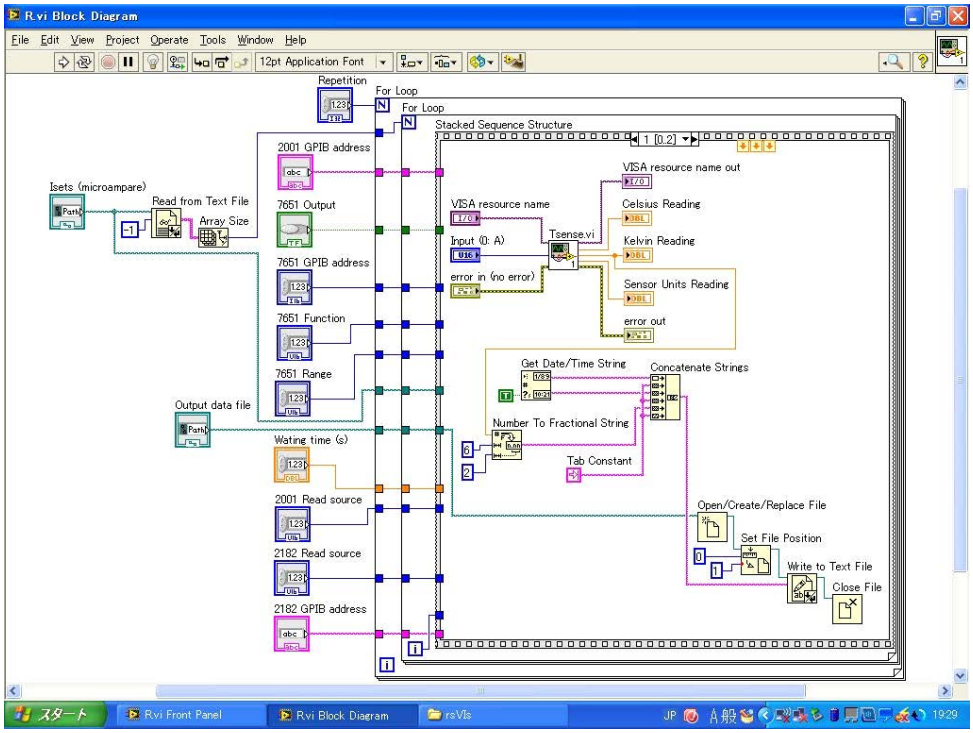

Fig. B.1.12 Block diagram of “R.vi,” part 1.

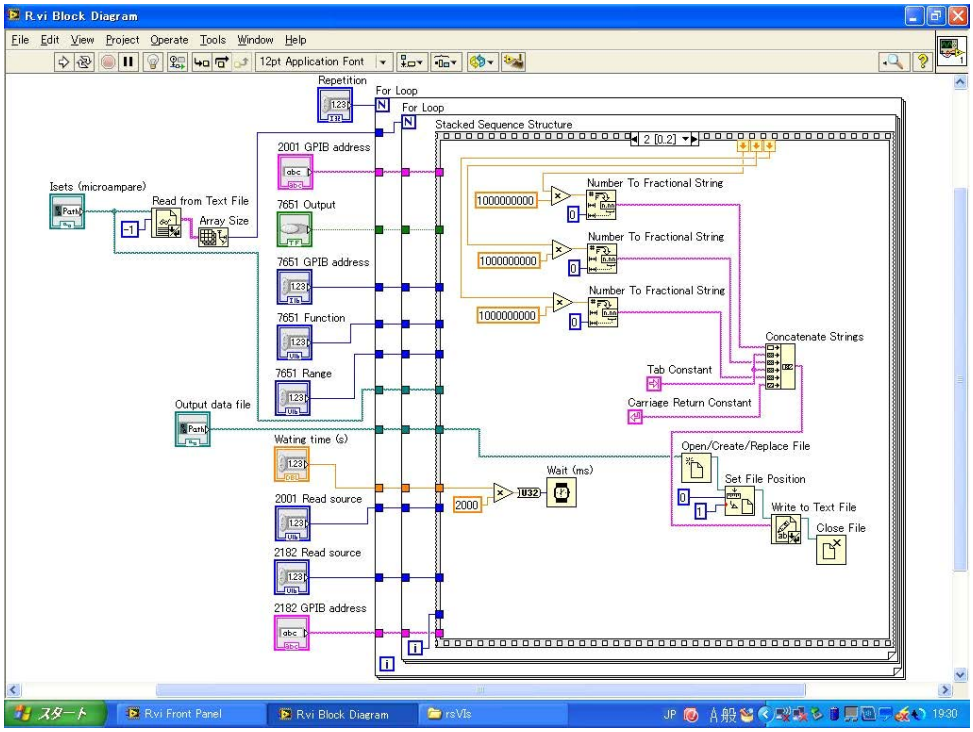

Fig. B.1.13 Block diagram of “R.vi,” part 2.

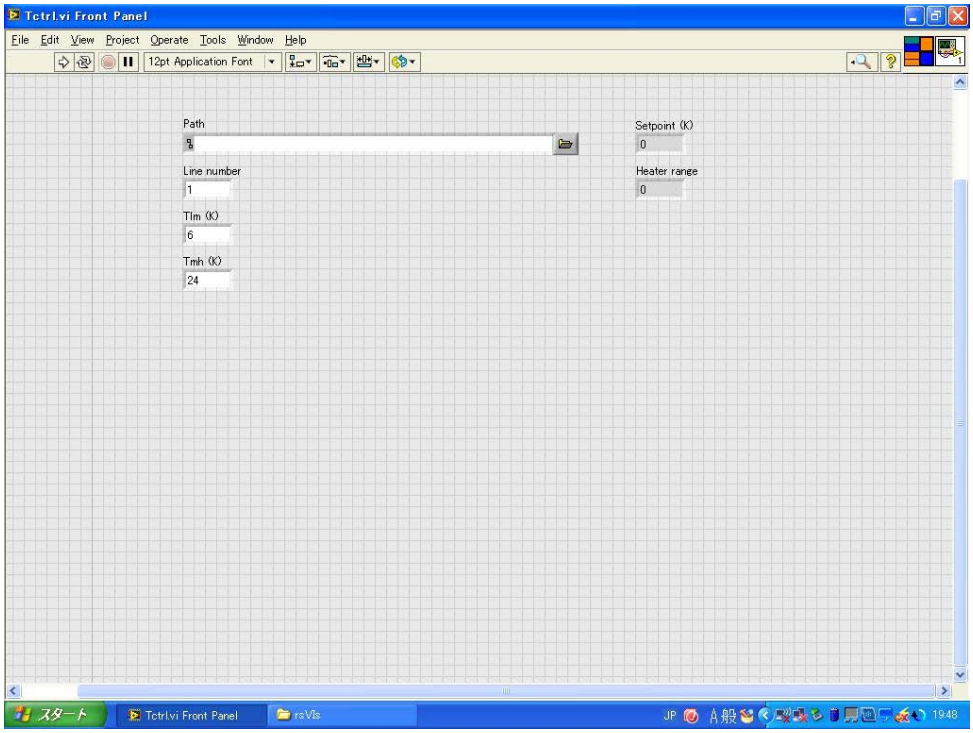

Fig. B.1.14 Front panel of "Tctrl.vi," which was for control of T.

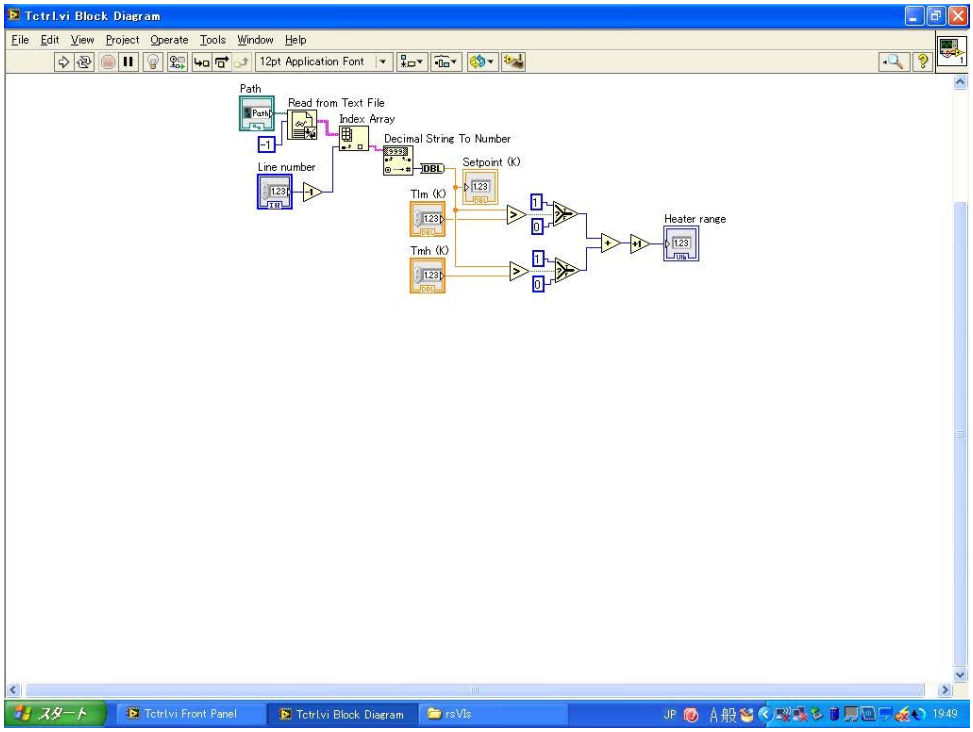

Fig. B.1.15 Block diagram of "Tctrl.vi."

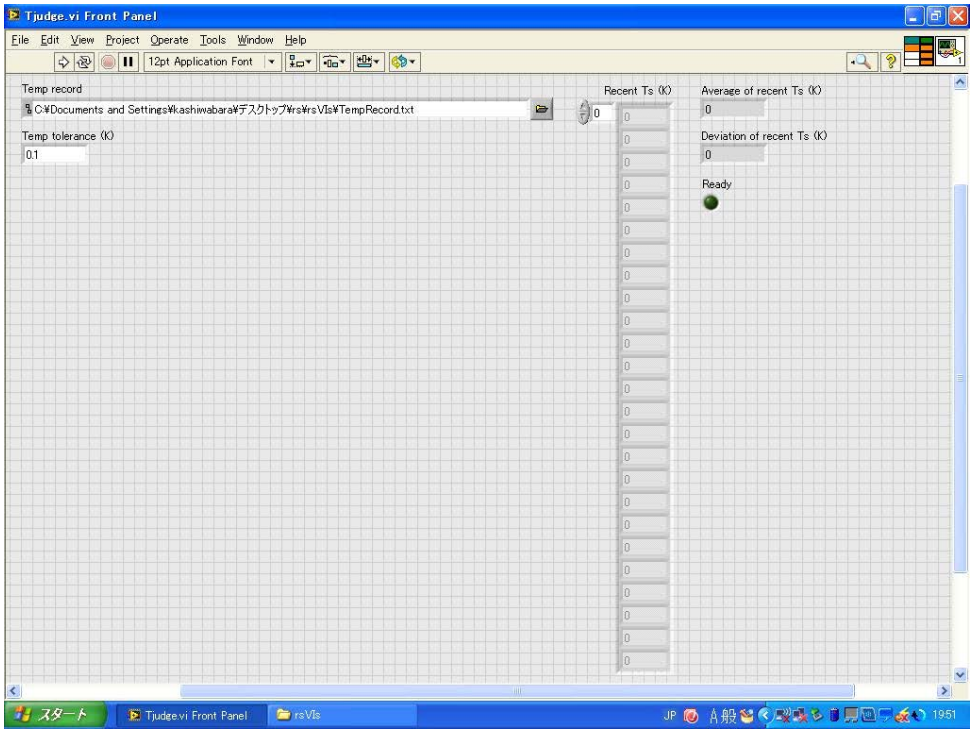

Fig. B.1.16 Front panel of "Tjudge.vi," which was for judgments on whether or not variation in T meets criteria.

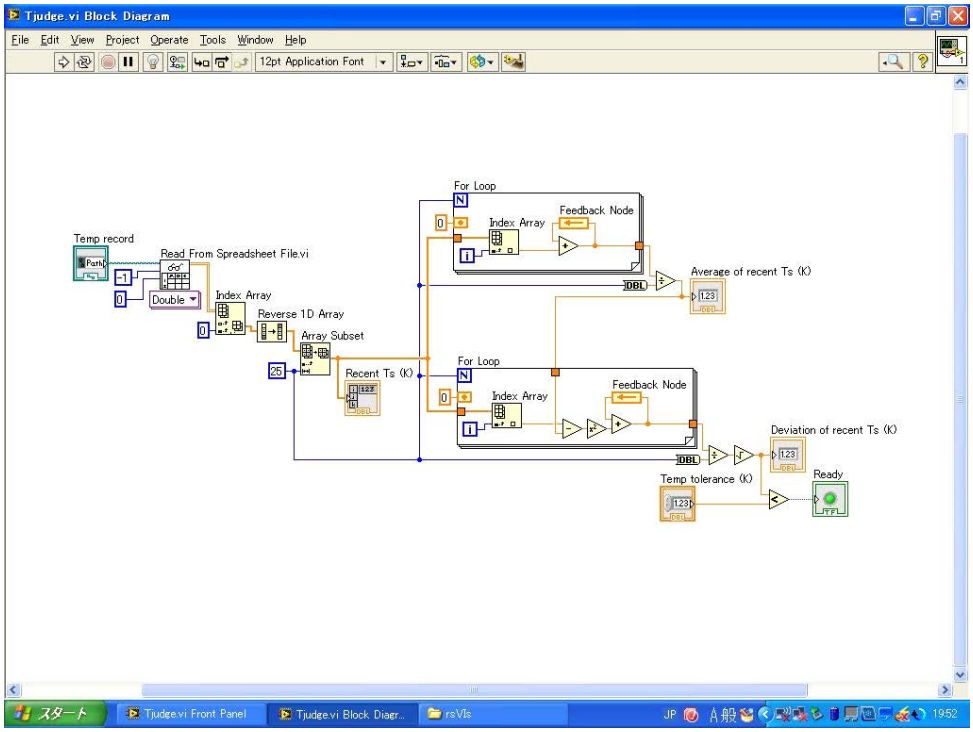

Fig. B.1.17 Block diagram of "Tjudge.vi."

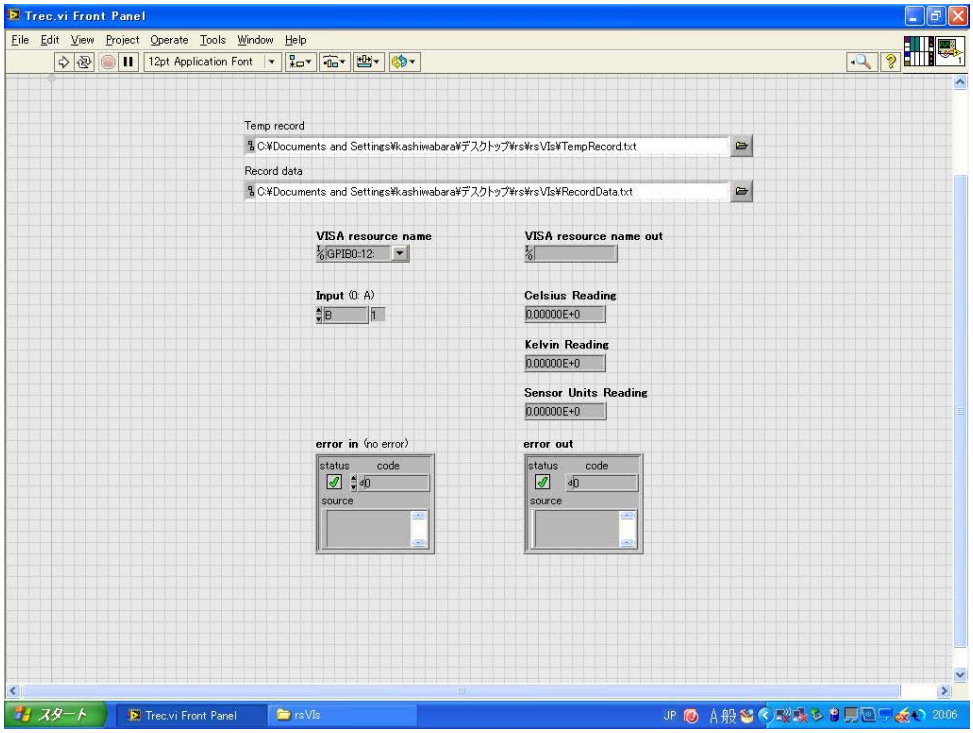

Fig. B.1.18 Front panel of "Trec.vi," which was for record of T.

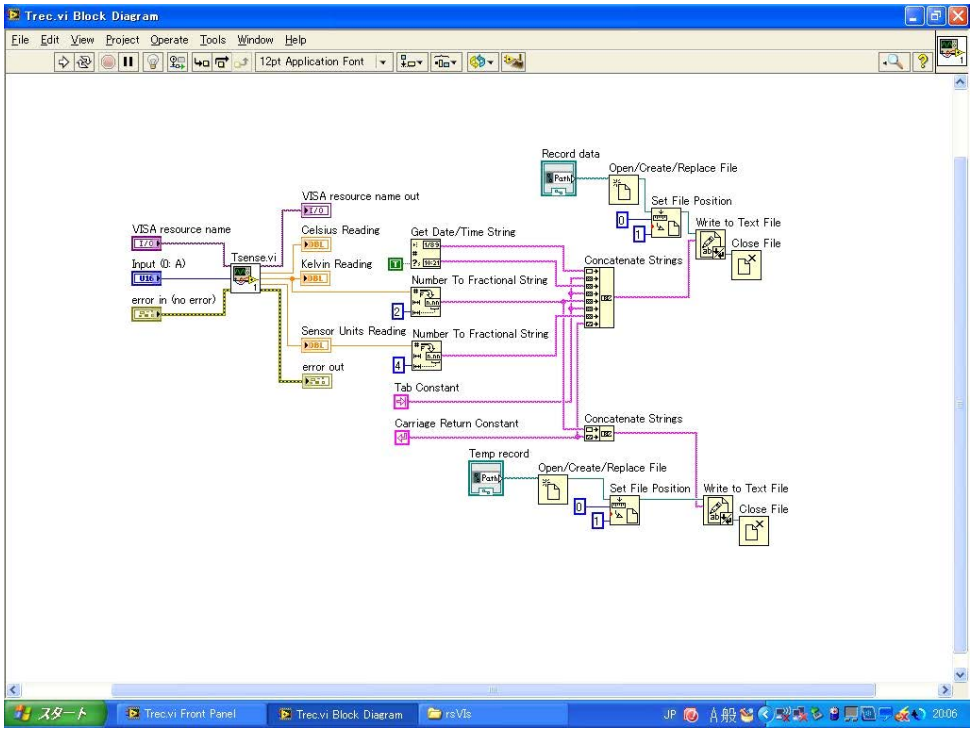

Fig. B.1.19 Block diagram of "Trec.vi."

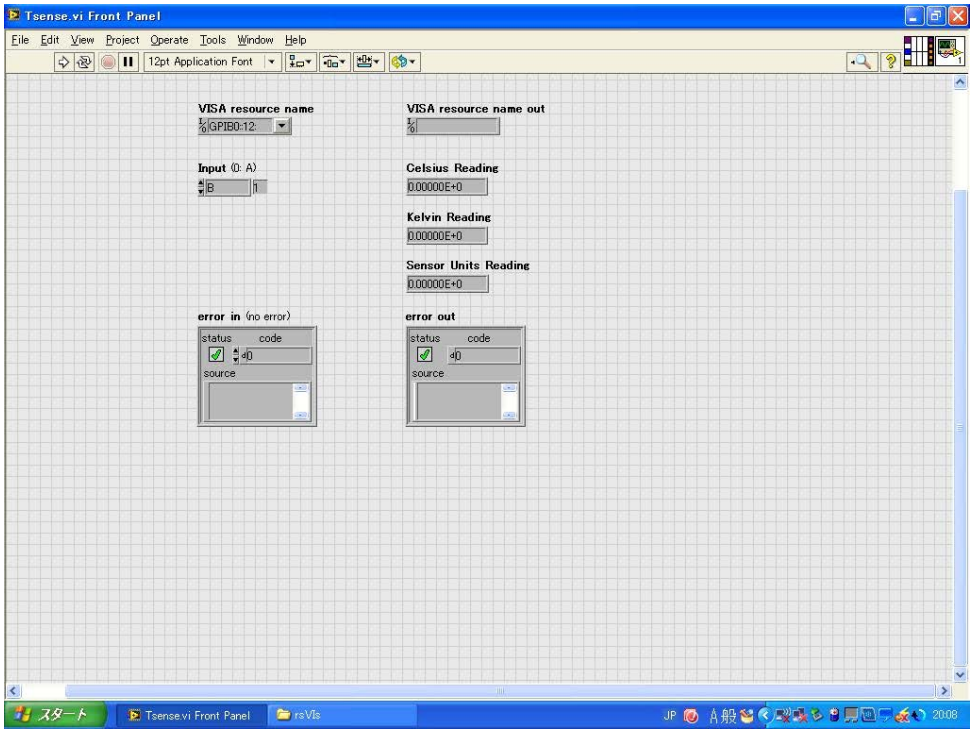

Fig. B.1.20 Front panel of “Tsense.vi,” which was for sensing of T.

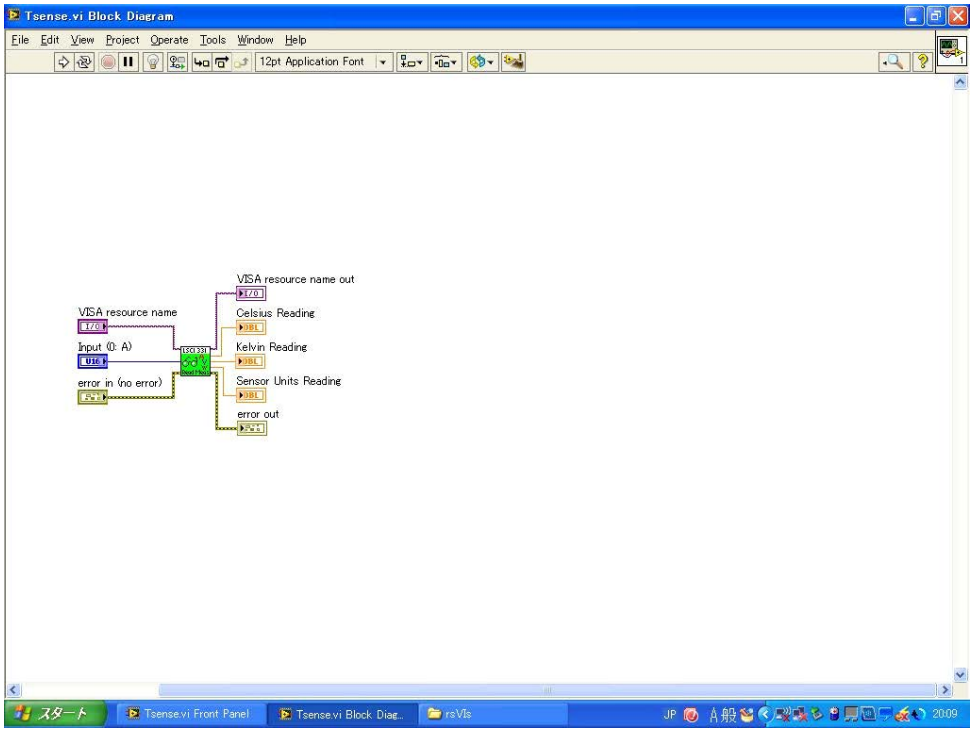

Fig. B.1.21 Block diagram of “Tsense.vi.”

B.2 Python code

Listing B.1 Gd1111-low.txt

```
Date  Time  T (K) Iset (nA) I (nA)  V (nV)
2020/11/6 15:56:39  4 -1000000  -999917 20413
2020/11/6 15:56:48  3.97  -750000 -749931 20444
2020/11/6 15:56:57  3.93  -500000 -499914 20470
2020/11/6 15:57:07  3.91  -250000 -249940 20496
2020/11/6 15:57:16  3.91  0 10  20521
2020/11/6 15:57:25  3.91  250000  249957  20531
2020/11/6 15:57:34  3.93  500000  499928  20543
2020/11/6 15:57:43  4.04  750000  749942  20536
2020/11/6 15:57:52  4.09  1000000 999926  20539
2020/11/6 15:58:01  4.11  -1000000  -999920 20407
2020/11/6 15:58:10  4.07  -750000 -749934 20433
2020/11/6 15:58:19  4.01  -500000 -499915 20455
2020/11/6 15:58:28  3.95  -250000 -249942 20473
2020/11/6 15:58:37  3.92  0 10  20479
2020/11/6 15:58:47  3.9 250000  249957  20486
2020/11/6 15:58:56  3.91  500000  499928  20489
2020/11/6 15:59:05  3.93  750000  749942  20506
2020/11/6 15:59:14  4.01  1000000 999926  20509
2020/11/6 15:59:23  4.08  -1000000  -999920 20377
2020/11/6 15:59:32  4.11  -750000 -749932 20411
2020/11/6 15:59:41  4.06  -500000 -499914 20425
2020/11/6 15:59:50  4.05  -250000 -249942 20450
2020/11/6 15:59:59  3.98  0 10  20468
2020/11/6 16:00:08  3.93  250000  249958  20487
2020/11/6 16:00:18  3.92  500000  499929  20498
2020/11/6 16:00:27  3.9 750000  749943  20486
2020/11/6 16:00:36  3.91  1000000 999926  20502
2020/11/6 16:00:45  3.95  -1000000  -999919 20352
2020/11/6 16:00:54  4.06  -750000 -749931 20412
2020/11/6 16:01:03  4.11  -500000 -499913 20448
2020/11/6 16:01:12  4.08  -250000 -249940 20468
2020/11/6 16:01:21  4.03  0 10  20491
2020/11/6 16:01:30  4 250000  249957  20502
2020/11/6 16:01:39  3.95  500000  499929  20519
2020/11/6 16:01:48  3.92  750000  749941  20531
2020/11/6 16:01:58  3.92  1000000 999927  20523
2020/11/6 16:02:07  3.91  -1000000  -999919 20423
2020/11/6 16:02:16  3.9 -750000 -749934 20458
2020/11/6 16:02:25  3.94  -500000 -499916 20499
2020/11/6 16:02:34  4.05  -250000 -249942 20539
2020/11/6 16:02:43  4.09  0 10  20579
2020/11/6 16:02:52  4.1 250000  249957  20590
2020/11/6 16:03:01  4.05  500000  499928  20614
2020/11/6 16:03:10  3.98  750000  749944  20614
2020/11/6 16:03:19  3.93  1000000 999927  20624
```

Listing B.2 er1.py

```
## Temperature using Si-diode (TSiD) dependence of electrical resistance (R) \
## of the standard reference sample of GdFeAsO0.943F0.057

## Import
import numpy as np
import matplotlib.pyplot as plt
import pandas as pd
import statsmodels.api as sm
from pandas import Series

## Input
nTSiD = 74 # n: number. T: temperature. SiD: silicon diode
nI = 9 # I: electrical current
neI = 2 # e: edge
itr = 5 # iteration

## Read
ML = pd.read_table('C:/python/ER/Gd1111-low.txt') # M: measurand. L: low
MS = pd.read_table('C:/python/ER/Gd1111-scan.txt') # S: scan
MR = pd.read_table('C:/python/ER/Gd1111-room.txt') # R: room
M = pd.concat([ML, MS, MR])
M.reset_index(inplace=True, drop=True)
M.columns = ('date', 'time', 'TSiD', 'Iset', 'I', 'V')

## Determination
L0 = []
for n in range(nTSiD):
    for i in range(itr):
        for l in range(2):
            def Mni(l):
                if l == 0:
                    return M.iloc[n*itr*nI+i*nI : n*itr*nI+i*nI+nI]
                elif l == 1:
                    return M.iloc[n*itr*nI+i*nI+neI : n*itr*nI+i*nI+nI-neI]
            TSiDs = Mni(l)['TSiD']
            Is = Mni(l)['I']
            Vs = Mni(l)['V']
            TSiD = TSiDs.mean()
            uTSiD = TSiDs.std(ddof=1)
            def rep(l):
                if l == 0:
                    return np.repeat(1, nI)
                elif l == 1:
                    return np.repeat(1, nI-2*neI)
            X = np.column_stack((rep(l), Is))
            mod = sm.OLS(Vs, X) # OLS: Ordinary least squares
            res = mod.fit()
            (V0, R) = res.params
            (uV0, uR) = res.bse
            R2 = res.rsquared
            L0.append([n, i, l, TSiD, uTSiD, R, uR, V0, uV0, R2])
D0 = pd.DataFrame([[L0[j][k] for j in range(len(L0))] for k in range(10)], \
    index=['n', 'i', 'l', 'TSiD', 'uTSiD', 'R', 'uR', 'V0','uV0', 'R2'])
D0 = D0.T
D0[['n', 'i', 'l']] = D0[['n', 'i', 'l']].astype('int')
D0 = D0.set_index(['n', 'i', 'l'])

## Statistics
```

```
59  D0mean = D0.mean(level=['n', 'l'])
60  Dmean = D0mean[['TSiD', 'R', 'V0', 'R2']]
61  D0std = D0.std(level=['n', 'l'])
62  Dstd = D0std[['TSiD', 'R', 'V0', 'R2']]
63  Dstd.columns = ['uTSiD', 'uR', 'uV0', 'uR2']
64  D1 = pd.concat([Dmean, Dstd], axis=1)
65
66  ## Selection
67  L1 = []
68  for n in range(nTSiD):
69      def S1():
70          if D1.iloc[2*n]['R2'] >= D1.iloc[2*n+1]['R2']:
71              return D1.iloc[2*n]
72          elif D1.iloc[2*n+1]['R2'] > D1.iloc[2*n]['R2']:
73              return D1.iloc[2*n+1]
74      L1.append(S1())
75  D2 = pd.DataFrame(L1)
76  D2.index.name = ('n', 'l')
77  D2in = D2.query('40 <= TSiD <= 75') # in: inset
78
79  ## Plots
80  plt.close('all')
81  D2N = ['R-TSiD', 'R-TSiD_inset'] # N: name
82  Tmin = [0, 40]
83  Tmax = [300, 75]
84  for d, D in enumerate([D2, D2in]):
85      fig = plt.figure(figsize=(4, 4), dpi=150)
86      ax = fig.add_subplot(1, 1, 1)
87      ax.scatter(D['TSiD'], D['R'], s=5, marker='o', edgecolors='red', \
88          facecolors='none')
89      ax.errorbar(D['TSiD'], D['R'], xerr=D['uTSiD'], yerr=D['uR'], fmt='None', \
90          ecolor='red', elinewidth=1, capsize=0.001)
91      ax.set_xlim(Tmin[d], Tmax[d])
92      ax.set_xlabel('$\it{T}_{\mathrm{SiD}}$ (K)')
93      ax.set_ylabel('$\it{R}$ ($\mathrm{\Omega}$)')
94      ax.tick_params(bottom=True, top= True, left=True, right=True, \
95          direction='in')
96      fig.subplots_adjust(left=0.25, right=0.95, bottom=0.25, top=0.95, \
97          wspace=0.2, hspace=0.2)
98      plt.show(block=False)
99      plt.savefig('C:/python/ER/Gd1111_' + D2N[d] + '.png')
100     plt.savefig('C:/python/ER/Gd1111_' + D2N[d] + '.svg')
101
102 ## Output
103 ofp = 'C:/python/ER/Gd1111_R-TSiD.txt' # ofp: output file path
104 with open(ofp, 'w') as f: # f :file
105     f.write('(n, l)' + '\t' + 'T_{Si-diode} (K)' + '\t' + 'R (Ohm)' + '\t' \
106         + 'V0 (nV)' + '\t' + 'R2' + '\t' + 'uT_{Si-diode} (K)' + '\t' \
107         + 'uR (Ohm)' + '\t' + 'uV0 (nV)' + '\t' + 'uR2' + '\n')
108 D2.to_csv(ofp, sep='\t', header=False, mode='a')
```

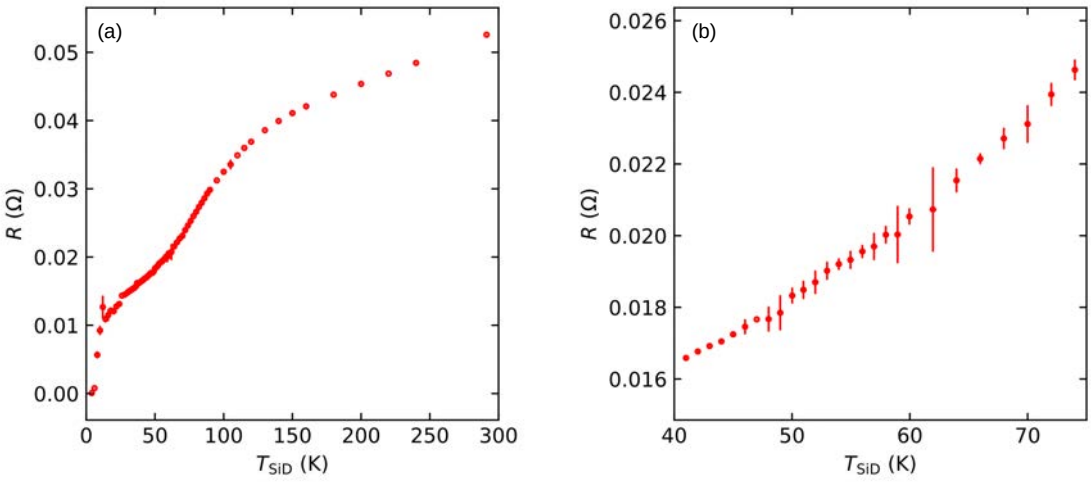

Fig. B.2.1 (a) Electrical resistance (R) of a specimen of $GdFeAsO_{0.943}F_{0.057}$ as a standard reference specimen (Gd1111stn) as a function of observed temperature using Si-diode on the display of a temperature controller (T_{SiD}). (b) Enlarged part of (a) for 40 K $\leq T_{\mathrm{SiD}} \leq$ 75 K.

Listing B.3 er2.py

```
## Temperature using Si-diode (TSiD) dependence of electrical resistance (R) \
## of a sample of nominal SmFeAsO0.84F0.16 for heat treatment temperature \
## (THT) of 950deg.C and holding time (tHld) of 40 h

## Import
import numpy as np
import matplotlib.pyplot as plt
import pandas as pd
import statsmodels.api as sm
from pandas import Series

## Input
nTSiD = 74 # n: number. T: temperature. SiD: siliconn diode
nI = 9 # I: electrical current
neI = 2 # e: edge
itr = 5 # iteration

## Read
ML = pd.read_table('C:/python/ER/Sm1111-low.txt') # M: measurand. L: low
MS = pd.read_table('C:/python/ER/Sm1111-scan.txt') # S: scan
MR = pd.read_table('C:/python/ER/Sm1111-room.txt') # R: room
M = pd.concat([ML, MS, MR])
M.reset_index(inplace=True, drop=True)
M.columns = ('date', 'time', 'TSiD', 'Iset', 'I', 'V')

## Determination
L0 = []
for n in range(nTSiD):
    for i in range(itr):
        for l in range(2):
            def Mni(l):
                if l == 0:
                    return M.iloc[n*itr*nI+i*nI : n*itr*nI+i*nI+nI]
                elif l == 1:
                    return M.iloc[n*itr*nI+i*nI+neI : n*itr*nI+i*nI+nI-neI]
            TSiDs = Mni(l)['TSiD']
            Is = Mni(l)['I']
            Vs = Mni(l)['V']
            TSiD = TSiDs.mean()
            uTSiD = TSiDs.std(ddof=1)
            def rep(l):
                if l == 0:
                    return np.repeat(1, nI)
                elif l == 1:
                    return np.repeat(1, nI-2*neI)
            X = np.column_stack((rep(l), Is))
            mod = sm.OLS(Vs, X) # OLS: Ordinary least squares
            res = mod.fit()
            (V0, R) = res.params
            (uV0, uR) = res.bse
            R2 = res.rsquared
            L0.append([n, i, l, TSiD, uTSiD, R, uR, V0, uV0, R2])
D0 = pd.DataFrame([[L0[j][k] for j in range(len(L0))] for k in range(10)], \
    index=['n', 'i', 'l', 'TSiD', 'uTSiD', 'R', 'uR', 'V0','uV0', 'R2'])
D0 = D0.T
D0[['n', 'i', 'l']] = D0[['n', 'i', 'l']].astype('int')
D0 = D0.set_index(['n', 'i', 'l'])

```

```
59  ## Statistics
60  D0mean = D0.mean(level=['n', 'l'])
61  Dmean = D0mean[['TSiD', 'R', 'V0', 'R2']]
62  D0std = D0.std(level=['n', 'l'])
63  Dstd = D0std[['TSiD', 'R', 'V0', 'R2']]
64  Dstd.columns = ['uTSiD', 'uR', 'uV0', 'uR2']
65  D1 = pd.concat([Dmean, Dstd], axis=1)
66
67  ## Selection
68  L1 = []
69  for n in range(nTSiD):
70      def S1():
71          if D1.iloc[2*n]['R2'] >= D1.iloc[2*n+1]['R2']:
72              return D1.iloc[2*n]
73          elif D1.iloc[2*n+1]['R2'] > D1.iloc[2*n]['R2']:
74              return D1.iloc[2*n+1]
75      L1.append(S1())
76  D2 = pd.DataFrame(L1)
77  D2.index.name = ('n', 'l')
78  D2in = D2.query('40 <= TSiD <= 75') # in: inset
79
80  ## Plots
81  plt.close('all')
82  D2N = ['R-TSiD', 'R-TSiD_inset'] # N: name
83  Tmin = [0, 40]
84  Tmax = [300, 75]
85  for d, D in enumerate([D2, D2in]):
86      fig = plt.figure(figsize=(4, 4), dpi=150)
87      ax = fig.add_subplot(1, 1, 1)
88      ax.scatter(D['TSiD'], D['R'], s=5, marker='o', edgecolors='red', \
89          facecolors='none')
90      ax.errorbar(D['TSiD'], D['R'], xerr=D['uTSiD'], yerr=D['uR'], fmt='None', \
91          ecolor='red', elinewidth=1, capsize=0.001)
92      ax.set_xlim(Tmin[d], Tmax[d])
93      ax.set_xlabel('$\it{T}_{\mathrm{SiD}}$ (K)')
94      ax.set_ylabel('$\it{R}$ ($\mathrm{\Omega}$)')
95      ax.tick_params(bottom=True, top= True, left=True, right=True, \
96          direction='in')
97      fig.subplots_adjust(left=0.25, right=0.95, bottom=0.25, top=0.95, \
98          wspace=0.2, hspace=0.2)
99      plt.show(block=False)
100     plt.savefig('C:/python/ER/Sm1111_' + D2N[d] + '.png')
101     plt.savefig('C:/python/ER/Sm1111_' + D2N[d] + '.svg')
102
103 ## Output
104 ofp = 'C:/python/ER/Sm1111_R-TSiD.txt' # ofp: output file path
105 with open(ofp, 'w') as f: # f :file
106     f.write('(n, l)' + '\t' + 'T_{Si-diode} (K)' + '\t' + 'R (Ohm)' + '\t' \
107         + 'V0 (nV)' + '\t' + 'R2' + '\t' + 'uT_{Si-diode} (K)' + '\t' \
108         + 'uR (Ohm)' + '\t' + 'uV0 (nV)' + '\t' + 'uR2' + '\n')
109 D2.to_csv(ofp, sep='\t', header=False, mode='a')
```

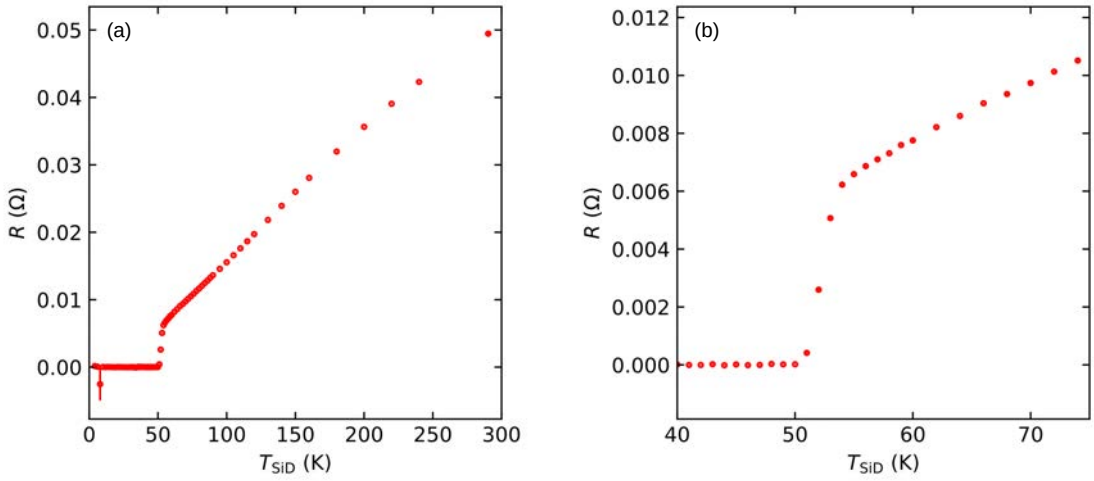

Fig. B.2.2 (a) T_{SiD} dependence of R of a specimen of nominal $SmFeAsO_{1-x}F_x$ (nominal $x = 0.16$) for $(T_{HT}, t_{Hld}) = (950°C, 40\ h)$. (b) Enlarged part of (a) for $40\ K \leq T_{SiD} \leq 75\ K$. The measurements were carried out by Kobayashi [228].

Listing B.4 er3.py

```
## Calibration of temperature in the Automatic Resistivity Measurement System
## (ARMS) using the standard reference sample of GdFeAsO0.943F0.057 (Gd1111)

## Import
import numpy as np
import math
import matplotlib.pyplot as plt
import pandas as pd
from pandas import Series
from scipy import interpolate

## Read
RP = pd.read_table('C:/python/ER/Gd1111_rho-T_PPMS.txt')
    # R: Reference. P: Physical Properties Measurement System (PPMS)
RP.columns = ('T', 'rho')
MA = pd.read_table('C:/python/ER/Gd1111_R-TSiD.txt')
    # M: Measureand. A: Automatic Resistivity Measurement System (ARMS)
MA.columns = (('n', 'l'), 'TSiD', 'R', 'V0', 'R2', 'uTSiD', 'uR', 'uV0', 'uR2')
LOT = MA['TSiD'][0] # L: lowest. O: observed. T: temperature. in K
HOT = MA['TSiD'][len(MA)-1] # H: Highest. in K

## Computational temperatures (CTs)
ICT = 0.01 # I: interval. C: computational. in K
LCTpICT = math.ceil(LOT / ICT) # P: per
HCTpICT = math.floor(HOT / ICT)
NCT = HCTpICT - LCTpICT + 1 # N: number
CTspICT = np.linspace(LCTpICT, HCTpICT, NCT)
CTs = CTspICT * ICT # in K
CTs = pd.Series(CTs)
CTs.rename('CT', inplace=True)

## Conversion from electrical resistance (R) to electrical reietivity (rho)
MARatRT = MA['R'][73]
    # R at T = 291.280667 K using ARMS. in Ohm
RPrhoatRT = RP['rho'][144]
    # rho at T_{Si-diode} = 290.60642 K using PPMS. in milliohm cm
MArhos = (MA['R'] / MARatRT) * RPrhoatRT # in milliohm cm
MArhos.rename('rho', inplace=True)
MAurhos = (MA['uR'] / MA['R']) * MArhos # u: uncertainty. in milliohm cm
MAurhos.rename('urho', inplace=True)
MA = pd.concat([MA, MArhos, MAurhos], axis=1)

## Linear interpolation
RPfunc = interpolate.interp1d(RP['rho'], RP['T'], kind='linear')
    # Input: rho. in milliohm cm
    # Output: T. in K
MAfunc = interpolate.interp1d(MA['TSiD'], MA['rho'], kind='linear')
    # Input: T_{Si-diode}. in K
    # Output: rho. in milliohm cm
MAufunc = interpolate.interp1d(MA['TSiD'], MA['urho'], kind='linear')
    # Input: T_{Si-diode}. in K
    # Output: statistical uncertainty of rho. in milliohm cm

## Calibration of temperature
Tclbs = RPfunc(MAfunc(CTs)) # clb: calibrated. in K
Tclbs = pd.Series(Tclbs)
Tclbs.rename('Tclb', inplace=True)
TclbsmCTs = Tclbs - CTs # in K
```

```
59  TclbsmuTclbms = RPfunc(MAfunc(CTs)-MAufunc(CTs)) # m: minus. in K
60  TclbsmuTclbms = pd.Series(TclbsmuTclbms)
61  uTclbms = Tclbs - TclbsmuTclbms # in K
62  uTclbms.rename('uTclbm', inplace=True)
63  TclbsmCTs.rename('TclbmCT', inplace=True)
64  TclbspuTclbps = RPfunc(MAfunc(CTs)+MAufunc(CTs)) # p: plus. in K
65  TclbspuTclbps = pd.Series(TclbspuTclbps)
66  uTclbps = TclbspuTclbps - Tclbs # in K
67  uTclbps.rename('uTclbp', inplace=True)
68
69  ## Summary
70  D0 = pd.concat([CTs, Tclbs, TclbsmCTs, uTclbms, uTclbps], axis=1)
71  D0in = D0.query('40 <= CT <= 75') # in: inset
72
73  ## Plots
74  plt.close('all')
75  D0TTN = ['T-TSiD', 'T-TSiD_inset'] # N: name
76  D0TmTTN = ['TmTSiD-TSiD', 'TmTSiD-TSiD_inset'] # N: name
77  Tmin = [0, 40]
78  Tmax = [300, 75]
79  for d, D in enumerate([D0, D0in]):
80      fig = plt.figure(figsize=(4, 4), dpi=150)
81      ax = fig.add_subplot(1, 1, 1)
82      ax.plot(D['CT'], D['Tclb']-D['uTclbm'], 'k:')
83      ax.plot(D['CT'], D['Tclb']+D['uTclbp'], 'k:')
84      ax.plot(D['CT'], D['Tclb'], 'r-')
85      ax.set_xlim(Tmin[d], Tmax[d])
86      ax.set_xlabel('$\it{T}_{\mathrm{SiD}}$ (K)')
87      ax.set_ylabel('$\it{T}$ (K)')
88      ax.tick_params(bottom=True, top= True, left=True, right=True, \
89          direction='in')
90      fig.subplots_adjust(left=0.25, right=0.95, bottom=0.25, top=0.95, \
91          wspace=0.2, hspace=0.2)
92      plt.show(block=False)
93      plt.savefig('C:/python/ER/Gd1111' + D0TTN[d] + '.png')
94      plt.savefig('C:/python/ER/Gd1111' + D0TTN[d] + '.svg')
95      fig = plt.figure(figsize=(4, 4), dpi=150)
96      ax = fig.add_subplot(1, 1, 1)
97      ax.plot(D['CT'], D['TclbmCT']-D['uTclbm'], 'k:')
98      ax.plot(D['CT'], D['TclbmCT']+D['uTclbp'], 'k:')
99      ax.plot(D['CT'], D['TclbmCT'], 'r-')
100     ax.set_xlim(Tmin[d], Tmax[d])
101     ax.set_xlabel('$\it{T}_{\mathrm{SiD}}$ (K)')
102     ax.set_ylabel('$\it{T} - \it{T}_{\mathrm{SiD}}$ (K)')
103     ax.tick_params(bottom=True, top= True, left=True, right=True, \
104         direction='in')
105     fig.subplots_adjust(left=0.25, right=0.95, bottom=0.25, top=0.95, \
106         wspace=0.2, hspace=0.2)
107     plt.show(block=False)
108     plt.savefig('C:/python/ER/Gd1111' + D0TmTTN[d] + '.png')
109     plt.savefig('C:/python/ER/Gd1111' + D0TmTTN[d] + '.svg')
110
111 ## Output
112 ofp = 'C:/python/ER/Gd1111_T-TmTSiD-TSiD.txt' # ofp: output file path
113 with open(ofp, 'w') as f: # f: file
114     f.write('z' + '\t' + 'T_{Si-diode} (K)' + '\t' + 'T (K)' + '\t' \
115         + 'T - T_{Si-diode} (K)' + '\t' + 'uTclbp (K)' + '\t' + 'uTclbm (K)' \
116         + '\n')
117 D0.to_csv(ofp, sep='\t', header=False, mode='a')
```

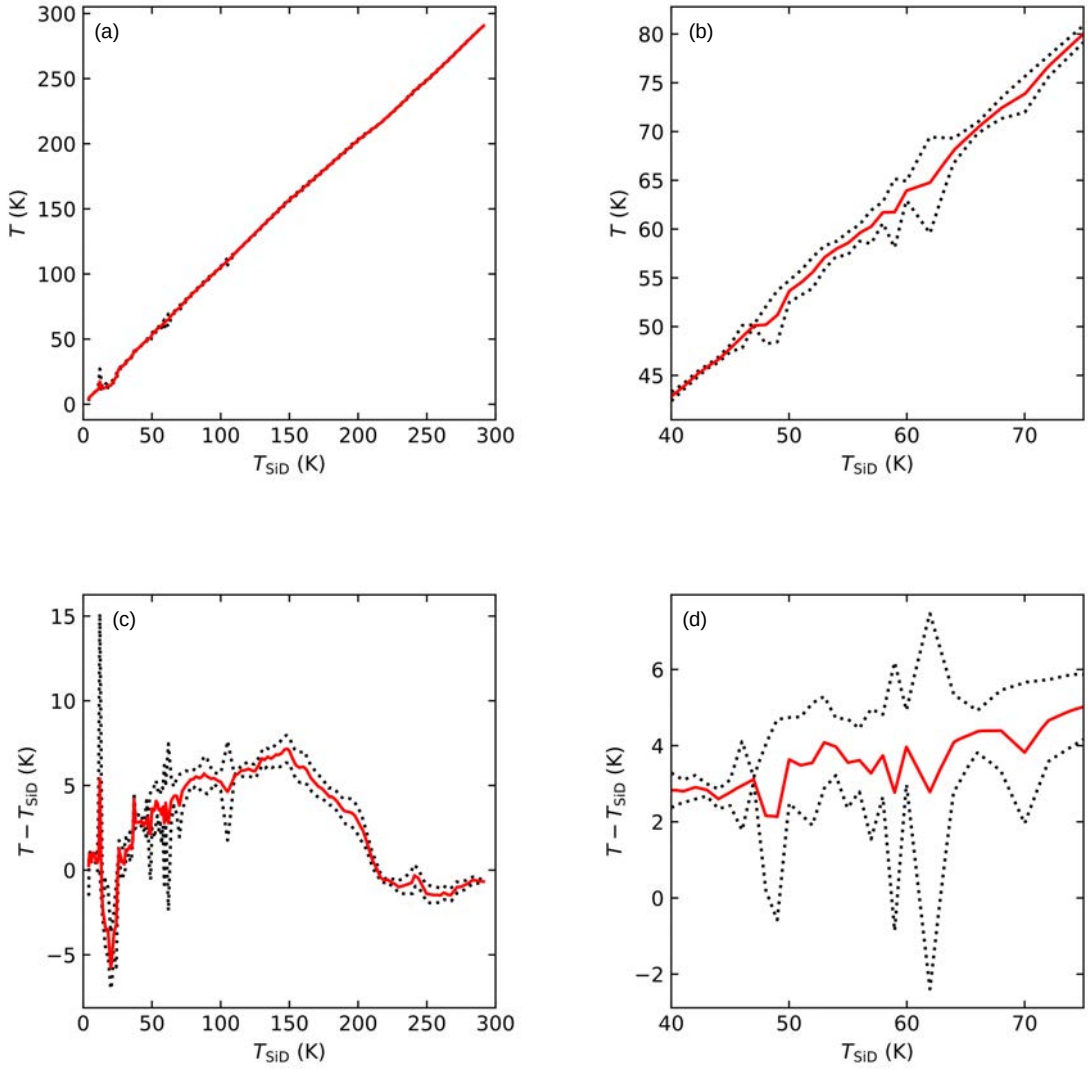

Fig. B.2.3 (a) Temperature (T) versus T_{SiD}. (b) Enlarged part of (a) for 40 K $\leq T_{\mathrm{SiD}} \leq$ 75 K. (c) ($T - T_{\mathrm{SiD}}$) versus T_{SiD}. (d) Enlarged part of (c) for 40 K $\leq T \leq$ 75 K.

Listing B.5 er4.py

```
## Temperature (T) dependence of electrical resistance (R) of a sample of
## nominal SmFeAsO0.84F0.16 for heat treatment temperature (THT) of 950deg.C and
## holding time (tHld) of 40 h

## Import
import numpy as np
import matplotlib.pyplot as plt
import pandas as pd
import statsmodels.api as sm
from pandas import Series

## Input
nT = 73 # n: number. T: temperature
# nT = 74
nI = 9 # I: electrical current
neI = 2 # e: edge
itr = 5 # iteration

## Read
ML = pd.read_table('C:/python/ER/Sm1111-low.txt') # M: measurand. L: low
MS = pd.read_table('C:/python/ER/Sm1111-scan.txt') # S: scan
MR = pd.read_table('C:/python/ER/Sm1111-room.txt') # R: room
M = pd.concat([MS, MR])
# M = pd.concat([ML, MS, MR])
M.reset_index(inplace=True, drop=True)
M.columns = ('date', 'time', 'TSiD', 'Iset', 'I', 'V')
TT = pd.read_table('C:/python/ER/Gd1111_T-TmTSiD-TSiD.txt') # T: temperature
TT.columns = ('z', 'TSiD', 'T', 'TmTSiD', 'uTclbp', 'uTclbm')
TT.set_index('z', inplace=True)

## Calibration of temperature
rT = 0.001 # r: range. T: temperature. in K
L0 = []
for m in range(len(M)):
    S0 = TT[(TT['TSiD']>M['TSiD'][m]-rT)&(TT['TSiD']<M['TSiD'][m]+rT)]
    Tclb = S0['T'].iloc[0]
    uTclbm = S0['uTclbm'].iloc[0]
    uTclbp = S0['uTclbp'].iloc[0]
    L0.append([Tclb, uTclbm, uTclbp])
D0 = pd.DataFrame(L0)
D0.columns = ['T', 'uTm', 'uTp']
M = pd.concat([M, D0], axis=1)

## Determination
L1 = []
for n in range(nT):
    for i in range(itr):
        for l in range(2):
            def Mni(l):
                if l == 0:
                    return M.iloc[n*itr*nI+i*nI : n*itr*nI+i*nI+nI]
                elif l == 1:
                    return M.iloc[n*itr*nI+i*nI+neI : n*itr*nI+i*nI+nI-neI]
            T = Mni(l)['T'].mean()
            uTm = Mni(l)['uTm'].mean()
            uTp = Mni(l)['uTp'].mean()
            Is = Mni(l)['I']
            Vs = Mni(l)['V']
```

```
            def rep(l):
                if l == 0:
                    return np.repeat(1, nI)
                elif l == 1:
                    return np.repeat(1, nI-2*neI)
            X = np.column_stack((rep(l), Is))
            mod = sm.OLS(Vs, X) # OLS: Ordinary least squares
            res = mod.fit()
            (V0, R) = res.params
            (uV0, uR) = res.bse
            R2 = res.rsquared
            L1.append([n, i, l, T, uTm, uTp, R, uR, V0, uV0, R2])
D1 = pd.DataFrame([[L1[j][k] for j in range(len(L1))] for k in range(11)], \
    index=['n', 'i', 'l', 'T', 'uTm', 'uTp', 'R', 'uR', 'V0', 'uV0', 'R2'])
D1 = D1.T
D1[['n', 'i', 'l']] = round(D1[['n', 'i', 'l']]).astype(int)
D1 = D1.set_index(['n', 'i', 'l'])

## Statistics
D1mean = D1.mean(level=['n', 'l'])
Dmean = D1mean[['T', 'uTm', 'uTp', 'R', 'V0', 'R2']]
D1std = D1.std(level=['n', 'l'])
Dstd = D1std[['T', 'R', 'V0', 'R2']]
Dstd.columns = ['uT', 'uR', 'uV0', 'uR2']
cuTm = ((Dstd['uT']**2)+(Dmean['uTm']**2))**(1/2) # c: combined
cuTp = ((Dstd['uT']**2)+(Dmean['uTp']**2))**(1/2)
cuTm.rename('cuTm', inplace=True)
cuTp.rename('cuTp', inplace=True)
D2 = pd.concat([Dmean, Dstd, cuTm, cuTp], axis=1)

## Selection
L2 = []
for n in range(nT):
    def S2():
        if D2.iloc[2*n]['R2'] >= D2.iloc[2*n+1]['R2']:
            return D2.iloc[2*n]
        elif D2.iloc[2*n+1]['R2'] > D2.iloc[2*n]['R2']:
            return D2.iloc[2*n+1]
    L2.append(S2())
D3 = pd.DataFrame(L2)
D3.index.name = ('n', 'l')
D3in = D3.query('40 <= T <= 75') # in: inset

## Plots
plt.close('all')
D3N = ['R-T', 'R-T_inset'] # N: name
Tmin = [0, 40]
Tmax = [300, 75]
for d, D in enumerate([D3, D3in]):
    fig = plt.figure(figsize=(4, 4), dpi=150)
    ax = fig.add_subplot(1, 1, 1)
    ax.scatter(D['T'], D['R'], s=5, marker='o', edgecolors='red', \
        facecolors='none')
    ax.errorbar(D['T'], D['R'], xerr=D['cuTp'], yerr=D['uR'], fmt='None',\
        ecolor='red', elinewidth=1, capsize=0.001, xlolims=True)
    ax.errorbar(D['T'], D['R'], xerr=D['cuTm'], yerr=D['uR'], fmt='None', \
        ecolor='red', elinewidth=1, capsize=0.001, xuplims=True)
    ax.set_xlim(Tmin[d], Tmax[d])
    ax.set_xlabel('$\it{T}$ (K)')
```

```
118     ax.set_ylabel('$\it{R}$ ($\mathrm{\Omega}$)')
119     ax.tick_params(bottom=True, top= True, left=True, right=True, \
120         direction='in')
121     fig.subplots_adjust(left=0.25, right=0.95, bottom=0.25, top=0.95, \
122         wspace=0.2, hspace=0.2)
123     plt.show(block=False)
124     plt.savefig('C:/python/ER/Sm1111_' + D3N[d] + '.png')
125     plt.savefig('C:/python/ER/Sm1111_' + D3N[d] + '.svg')
126 
127 ## Output
128 ofp = 'C:/python/ER/Sm1111_R-T.txt' # ofp: output file path
129 with open(ofp, 'w') as f: # f: file
130     f.write('(n, l)' + '\t' + 'T (K)' + '\t' + 'uTm (K)' + '\t' + 'uTp (K)'\
131         + '\t' + 'R (Ohm)' + '\t' + 'V0 (nV)' + '\t' + 'R2' + '\t' + 'uT (K)' \
132         + '\t' + 'uR (Ohm)' + '\t' + 'uV0 (nV)' + '\t' + 'uR2' + '\t' \
133         + 'cuTm (K)' + '\t' + 'cuTp (K)' + '\n')
134 D3.to_csv(ofp, sep='\t', header=False, mode='a')
```

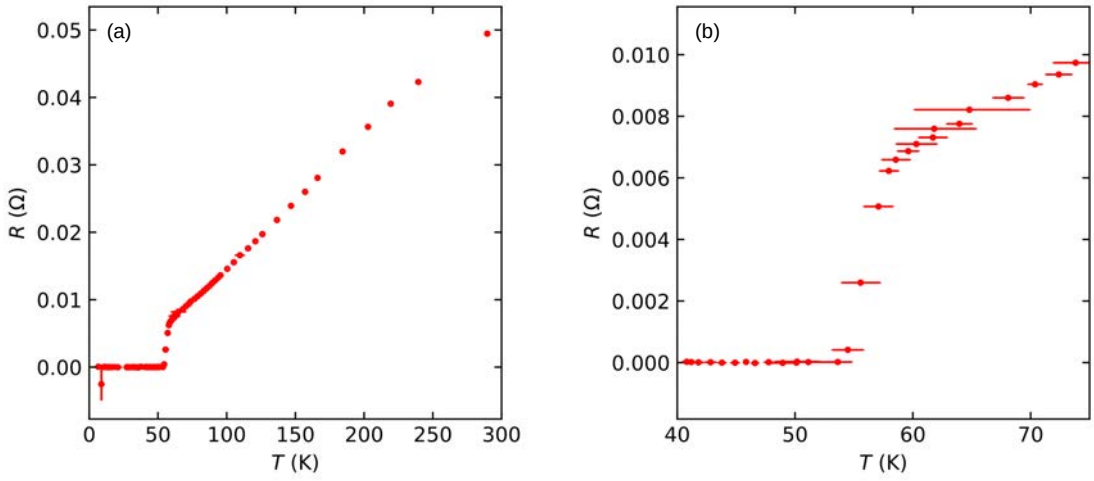

Fig. B.2.4 (a) T dependence of electrical resistance (R) of nominal $SmFeAsO_{1-x}F_x$ (nominal $x = 0.16$) for $(T_{HT}, t_{Hld}) = (950°C, 40\ h)$. (b) Enlarged part of (a) for $40\ K \leq T \leq 75\ K$.

Listing B.6 er5.py

```
## Temperature (T) dependence of electrical resistivity (rho) of a sample of
## nominal SmFeAsO0.84F0.16 for heat treatment temperature (THT) of 950deg.C and
## holding time (tHld) of 40 h

## Import
import numpy as np
import matplotlib.pyplot as plt
import pandas as pd

## Settigs of display
pd.options.display.max_rows = 100

## Input
ds0 = [1.45, 1.40, 1.50, 1.30, 1.20] # d: distances between two terminals in mm
As0 = [1.010959, 0.9941313, 1.101004, 1.127574, 1.030936, \
    1.188785, 1.194492, 1.271252, 1.234053, 1.220473]
    # A: cross-sectional area in mm^{2} reported by Mr. Kobayashi

## Read
D0 = pd.read_table('C:/python/ER/Sm1111_R-T.txt')
    # R: electrical resistance. T: temperature
D0.columns = ('(n, l)', 'T', 'uTm', 'uTp', 'R', 'V0', 'R2', 'uT', 'uR', 'uV0', \
    'uR2', 'cuTm', 'cuTp')
D0.set_index('(n, l)', inplace=True)

## Determination
d = np.mean(ds0)
ud = np.std(ds0, ddof=1) # u: uncertainty
rud = ud / d # ru: relative uncertainty
A = np.mean(As0)
uA = np.std(As0, ddof=1)
ruA = uA / A
D0['ruR'] = D0['uR'] / abs(D0['R'])
D0['rho'] = D0['R'] * (A / d) * (10**2)
    # rho: electrical resistivity in milliohm cm
D0['rurho'] = ((D0['ruR']**2) + (rud**2) + (ruA**2))**(1/2)
D0['urho'] = D0['rurho'] * abs(D0['rho'])
D1all = pd.DataFrame(D0[['T', 'cuTm', 'cuTp', 'R', 'uR', 'ruR', 'rho', 'urho', \
    'rurho']])
D1allin = D1all.query('40 <= T <= 75') # in: inset
D1sel = D1all.query('cuTm < 2 & cuTp < 2') # sel: selected
D1selin = D1sel.query('40 <= T <= 75')

## Plots
D1N = ['rho-T_all', 'rho-T_all_inset', 'rho-T_sel', 'rho-T_sel_inset'] # N: name
Tmin = [0, 40, 0, 40]
Tmax = [300, 75, 300, 75]
plt.close('all')
for d, D1 in enumerate([D1all, D1allin, D1sel, D1selin]):
    fig = plt.figure(figsize=(4, 4), dpi=150)
    ax = fig.add_subplot(1, 1, 1)
    ax.scatter(D1['T'], D1['rho'], s=5, marker='o', edgecolors='red', \
        facecolors='none')
    ax.errorbar(D1['T'], D1['rho'], xerr=D1['cuTp'], yerr=D1['urho'], \
        fmt='None', ecolor='red', elinewidth=1, capsize=0.001)
    ax.errorbar(D1['T'], D1['rho'], xerr=D1['cuTp'], yerr=D1['urho'], \
        fmt='None', ecolor='red', elinewidth=1, capsize=0.001, xuplims=True)
    ax.set_xlim(Tmin[d], Tmax[d])
```

```
59      ax.set_xlabel('$\it{T}$ (K)')
60      ax.set_ylabel(r'$\rho$ (m$\Omega$ cm)')
61      ax.tick_params(bottom=True, top= True, left=True, right=True, \
62          direction='in')
63      fig.subplots_adjust(left=0.25, right=0.95, bottom=0.25, top=0.95, \
64          wspace=0.2, hspace=0.2)
65      plt.show(block=False)
66      plt.savefig('C:/python/ER/Sm1111_' + D1N[d] + '.png')
67      plt.savefig('C:/python/ER/Sm1111_' + D1N[d] + '.svg')
68
69  ## Output
70  ofp0 = 'C:/python/ER/Sm1111_rho-T_all.txt' # ofp: output file path
71  ofp1 = 'C:/python/ER/Sm1111_rho-T_sel.txt'
72  ofps = [ofp0, ofp1]
73  D1s = [D1all, D1sel]
74  for o, ofp in enumerate(ofps):
75      with open(ofp, 'w') as f: # f: file
76          f.write('(n, l)' + '\t' + 'T (K)' + '\t' + 'cuTm (K)' + '\t' \
77              + 'cuTp (K)' + '\t' + 'R (Ohm)' + '\t' + 'uR (Ohm)' + '\t' + 'ruR' \
78              + '\t' + 'rho (milliohm cm)' + '\t' + 'urho (milliohm cm)' + '\t' \
79              +'rurho' + '\n')
80      D1s[o].to_csv(ofp, sep='\t', header=False, mode='a')
```

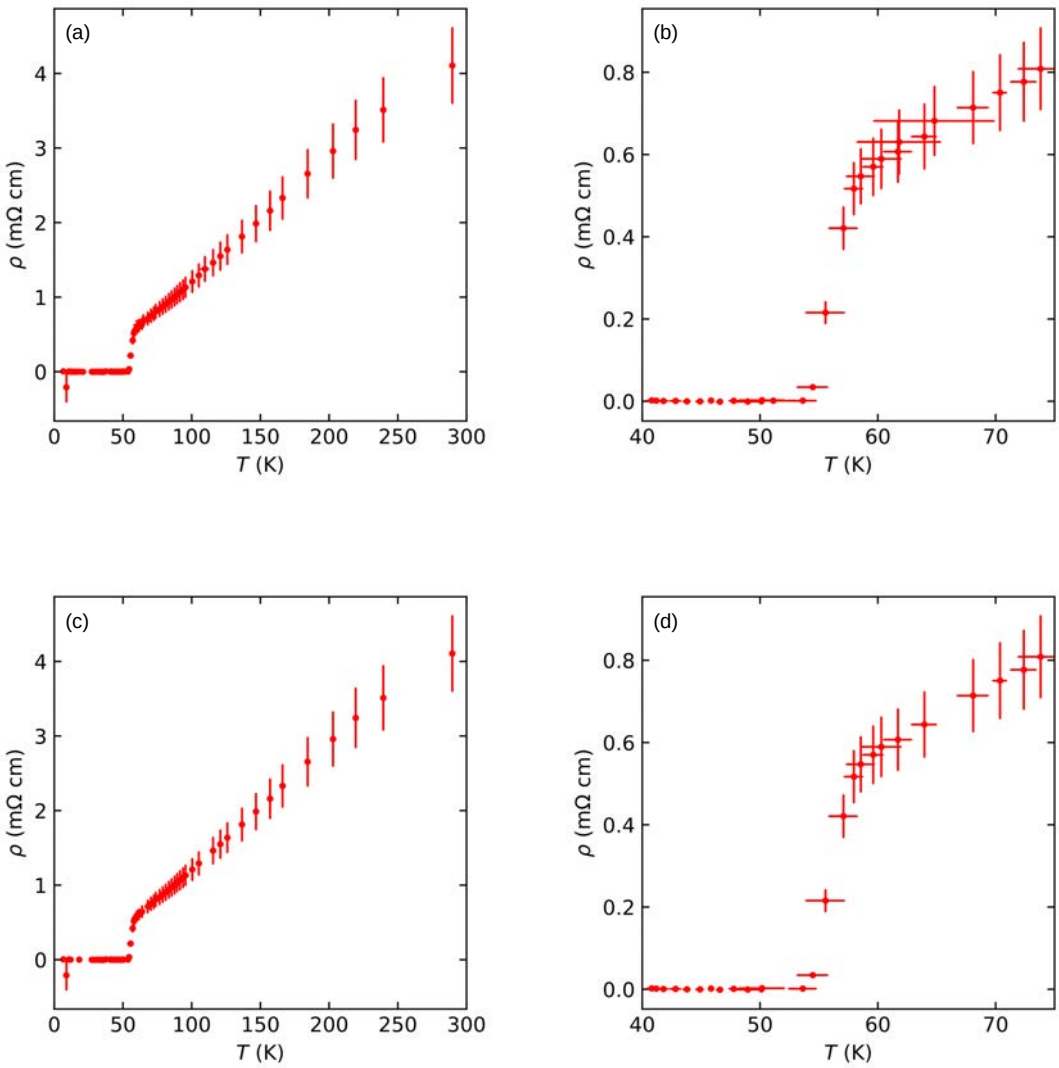

Fig. B.2.5 (a) T dependence of electrical resistivity (ρ) of nominal $SmFeAsO_{1-x}F_x$ (nominal $x = 0.16$) for $(T_{HT}, t_{Hld}) = (950°C, 40\ h)$. (b) Enlarged part of (a) for 40 K $\leq T \leq$ 75 K. (c) (a) for error bar of $T \leq 2$ K. (d) (b) for error bar of $T \leq 2$ K.

B.3 Magnetic property measurement system (MPMS) sequence

Listing B.7 A sequence file for magnetization measurement using MPMS

```
1  MCM MAGMODE 2
2  FLD FIELD 10000.0 2 0
```

```
3  WAI WAITFOR 10 0 0 5.0000 1 0
4  FLD FIELD -9000.0 2 0
5  WAI WAITFOR 10 0 0 5.0000 1 0
6  FLD FIELD 8000.0 2 0
7  WAI WAITFOR 10 0 0 5.0000 1 0
8  FLD FIELD -7000.0 2 0
9  WAI WAITFOR 10 0 0 5.0000 1 0
10 FLD FIELD 6000.0 2 0
11 WAI WAITFOR 10 0 0 5.0000 1 0
12 FLD FIELD -5000.0 2 0
13 WAI WAITFOR 10 0 0 5.0000 1 0
14 FLD FIELD 4000.0 2 0
15 WAI WAITFOR 10 0 0 5.0000 1 0
16 FLD FIELD -3000.0 2 0
17 WAI WAITFOR 10 0 0 5.0000 1 0
18 FLD FIELD 2000.0 2 0
19 WAI WAITFOR 10 0 0 5.0000 1 0
20 FLD FIELD -1000.0 2 0
21 WAI WAITFOR 10 0 0 5.0000 1 0
22 FLD FIELD 500.0 2 0
23 WAI WAITFOR 10 0 0 5.0000 1 0
24 FLD FIELD -250.0 2 0
25 WAI WAITFOR 10 0 0 5.0000 1 0
26 FLD FIELD 125.0 2 0
27 WAI WAITFOR 10 0 0 5.0000 1 0
28 MCM MAGMODE 1
29 FLD FIELD -75.0 1 0
30 WAI WAITFOR 10 0 0 5.0000 1 0
31 FLD FIELD 38.0 1 0
32 WAI WAITFOR 10 0 0 5.0000 1 0
33 FLD FIELD -19.0 1 0
34 WAI WAITFOR 10 0 0 5.0000 1 0
35 FLD FIELD 10.0 1 0
36 WAI WAITFOR 10 0 0 5.0000 1 0
37 FLD FIELD -5.0 1 0
38 WAI WAITFOR 10 0 0 5.0000 1 0
39 FLD FIELD 2.7 1 0
40 WAI WAITFOR 10 0 0 5.0000 1 0
41 FLD FIELD -1.3 1 0
42 WAI WAITFOR 10 0 0 5.0000 1 0
43 FLD FIELD 0.7 1 0
44 WAI WAITFOR 10 0 0 5.0000 1 0
45 FLD FIELD -0.3 1 0
46 WAI WAITFOR 10 0 0 5.0000 1 0
47 MCM MAGMODE 0
48 FLD FIELD 0.0 0 1
49 WAI WAITFOR 10 0 0 5.0000 1 0
50 QUE MAGRESET
51 MCM MAGMODE 1
52 LPB SCANB 0.00 0.00 0 1 1 1
53 MRS MEASURERSO 4.000000 5 3 0 0 1 1 3 3 0 0 1 0 1 1
54 ENB EOS
55 TMP TEMP 40.000 -10.000
56 WAI WAITFOR 10 0 1 299.9507 0 0
57 MCM MAGMODE 1
58 LPB SCANB 0.00 10.00 0 11 1 1
59 MRS MEASURERSO 4.000000 5 3 0 0 1 1 3 3 0 0 1 0 1 1
60 ENB EOS
61 LPB SCANB 14.00 30.00 0 5 1 1
```

```
MRS MEASURERSO 4.000000 5 3 0 0 1 1 3 3 0 0 1 0 1 1
ENB EOS
LPB SCANB 40.00 100.00 0 7 1 1
MRS MEASURERSO 4.000000 5 3 0 0 1 1 3 3 0 0 1 0 1 1
ENB EOS
LPB SCANB 140.00 300.00 0 5 1 1
MRS MEASURERSO 4.000000 5 3 0 0 1 1 3 3 0 0 1 0 1 1
ENB EOS
LPB SCANB 400.00 1000.00 0 7 1 1
MRS MEASURERSO 4.000000 5 3 0 0 1 1 3 3 0 0 1 0 1 1
ENB EOS
LPB SCANB 1400.00 3000.00 0 5 1 1
MRS MEASURERSO 4.000000 5 3 0 0 1 1 3 3 0 0 1 0 1 1
ENB EOS
LPB SCANB 4000.00 10000.00 0 7 1 1
MRS MEASURERSO 4.000000 5 3 0 0 1 1 3 3 0 0 1 0 1 1
ENB EOS
LPB SCANB 14000.00 30000.00 0 5 1 1
MRS MEASURERSO 4.000000 5 3 0 0 1 1 3 3 0 0 1 0 1 1
ENB EOS
LPB SCANB 40000.00 70000.00 0 4 1 1
MRS MEASURERSO 4.000000 5 3 0 0 1 1 3 3 0 0 1 0 1 1
ENB EOS
FLD FIELD 10000.0 2 0
WAI WAITFOR 10 0 0 5.0000 1 0
FLD FIELD -9000.0 2 0
WAI WAITFOR 10 0 0 5.0000 1 0
FLD FIELD 8000.0 2 0
WAI WAITFOR 10 0 0 5.0000 1 0
FLD FIELD -7000.0 2 0
WAI WAITFOR 10 0 0 5.0000 1 0
FLD FIELD 6000.0 2 0
WAI WAITFOR 10 0 0 5.0000 1 0
FLD FIELD -5000.0 2 0
WAI WAITFOR 10 0 0 5.0000 1 0
FLD FIELD 4000.0 2 0
WAI WAITFOR 10 0 0 5.0000 1 0
FLD FIELD -3000.0 2 0
WAI WAITFOR 10 0 0 5.0000 1 0
FLD FIELD 2000.0 2 0
WAI WAITFOR 10 0 0 5.0000 1 0
FLD FIELD -1000.0 2 0
WAI WAITFOR 10 0 0 5.0000 1 0
FLD FIELD 500.0 2 0
WAI WAITFOR 10 0 0 5.0000 1 0
FLD FIELD -250.0 2 0
WAI WAITFOR 10 0 0 5.0000 1 0
FLD FIELD 125.0 2 0
WAI WAITFOR 10 0 0 5.0000 1 0
MCM MAGMODE 1
FLD FIELD -75.0 1 0
WAI WAITFOR 10 0 0 5.0000 1 0
FLD FIELD 38.0 1 0
WAI WAITFOR 10 0 0 5.0000 1 0
FLD FIELD -19.0 1 0
WAI WAITFOR 10 0 0 5.0000 1 0
FLD FIELD 10.0 1 0
WAI WAITFOR 10 0 0 5.0000 1 0
FLD FIELD -5.0 1 0
```

```
121  WAI WAITFOR 10 0 0 5.0000 1 0
122  FLD FIELD 2.7 1 0
123  WAI WAITFOR 10 0 0 5.0000 1 0
124  FLD FIELD -1.3 1 0
125  WAI WAITFOR 10 0 0 5.0000 1 0
126  FLD FIELD 0.7 1 0
127  WAI WAITFOR 10 0 0 5.0000 1 0
128  FLD FIELD -0.3 1 0
129  WAI WAITFOR 10 0 0 5.0000 1 0
130  MCM MAGMODE 0
131  FLD FIELD 0.0 0 1
132  WAI WAITFOR 10 0 0 5.0000 1 0
133  TMP TEMP 300.000 10.000
134  WAI WAITFOR 10 0 1 299.9507 0 0
```

C

Low-temperature synthesis of $SmFeAsO_{1-x}F_x$

C.1 Introduction

Iron-based superconductors [204, 205] exhibit the second highest superconducting transition temperature (T_c) under ambient pressure next to cuprates. Generally, fabrication of superconducting wires and tapes of iron-based superconductors takes lower cost than that of cuprates. The iron-based superconductors were promising as core materials of superconducting wires and tapes. Among iron-based superconductors with clear chemical composition, $SmFeAsO_{1-x}F_x$ [8, 206, 207] exhibited the highest T_c value (onset $T_c \sim 58.1$ K at nominal $x = 0.26$).

$SmFeAsO_{1-x}F_x$ is suitable for the use under a high magnetic flux density ($\mu_0 H$). The irreversible magnetic flux density ($\mu_0 H_{irr}$) of single crystal of $SmFeAsO_{1-x}F_x$ reached a $\mu_0 H$ as high as $\sim$ 40 T at 15 K parallel to the c axis and $\sim$30 T at 39 K perpendicular to the a-b plane [209].

A magneto-optical imaging technique indicated that the intragrain critical current dencity (intra J_c) at 5 K under a low $\mu_0 H$ of polycrystalline $SmFeAsO_{1-x}F_x$ was estimated as $\sim 2 \times 10^5$ A cm^{-2} by using slab model with the size of the supercurrent loop, and was roughly calculated as $\sim 1.1 \times 10^5$ A cm^{-2} from the magnetic induction profile [210]. The intra J_c at 2 K of a polycrystalline with a nominal composition of $SmFeAsO_{1-d}$, whose intrinsic chemical composition should be $SmFeAsO_{1-x}H_x$ [211], was estimated to be as $\sim 7.3 \times 10^6$ A cm^{-2} [212]. This value is higher than practical J_c transport.Superconducting wires or tapes using $SmFeAsO_{1-x}F_x$ have been demonstrated in order to improve the trans-

port critical current density (transport J_c) [213–222]. After enthusiastic trials [218–220], Zhang *et al.* reported that a Sn-doped $SmFeAsO_{1-x}F_x$ tape, which was fabricated by an *ex-situ* powder-in-tube (PIT) technique, exhibited a transport J_c of $\sim 3.95 \times 10^4$ A cm^{-2} at 4.2 K in self-field [221]. Zhang *et al.* also reported a Sn-doped $SmFeAsO_{1-x}F_x$ tape with a too large transport J_c to be measured with a 240 A current source at 4.2 K in a low $\mu_0 H$ and transport J_c of $\sim 1.8 \times 10^4$ A cm^{-2} at 4.2 K in a $\mu_0 H$ of 0.6 T. that was fabricated by post-rolling heating to as low as 300°C for 6 h [222].

As seen above, transport J_c value in wires or tapes has been lower than intra transport J_c value in $SmFeAsO_{1-x}F_x$ so far. The cause of that is so-called weak links in the boundaries of grain of $SmFeAsO_{1-x}F_x$ and the loss of fluorine (F) in the crystallographic phase of $SmFeAsO_{1-x}F_x$ [217, 218, 223–225]. It is noted that the amounts of secondary crystallographic phases in the polycrystalline bulk samples of $SmFeAsO_{1-x}F_x$ start to increase tremendously at nominal $x = 0.16$ [207]. Any single-phase polycrystalline bulk samples of $SmFeAsO_{1-x}F_x$ have not been reported before 2020, although single-phase polycrystalline samples will be required for fabrication of high-quality superconducting wires and tapes.

The present study was carried out to reveal the lowest temperature at which growth of a polycrystalline SmFeAsO phase occurs. This knowledge will be useful for decision of the post-rolling heat treatment temperature in *ex-situ* PIT techniques for fabrication of $SmFeAsO_{1-x}F_x$ superconducting wires or tapes with a higher value of transport J_c.

C.2 Experimental

Samples of nominal $SmFeAsO_{1-x}F_x$ (nominal $x = 0.16$) were synthesized by a two-step solid-state reaction. Figure C.2.2 shows a flowchart of the synthesis procedures of the samples. Sm powders were obtained by powdering Sm (Nilaco; 99.9 wt.%) ingot using metal file. As powders were obtained by As (Ko-jundo Chemical Laboratory; 99.9999 wt.%) by pulverizing using agate mortar and pestle. Precursors, namely "133" and "233" powders, were obtained by heating under the conditions shown in Fig. C.2.3 (b) and (c) in evacuated silica (SiO_2) tubes from mixtures of powders of Sm, Fe (Ko-jundo Chemical Laboratory; >99.9 wt.%), and As in a stoichiometic ratio of 1 : 3 : 3 and 2 : 3 : 3, respectively.

The final 133 powder was obtained by mixing the first 133 powder (namely "133-α") and the second 133 powder ("133-β"). Then, a commercial Sm_2O_3 (Nippon Yttrium; 99.9999 wt.%) powder was dehydrated by heating in an alumina (Al_2O_3) crucible to 1000°C for 12 h. A starting materials (SMs) was obtained by mixing powders whose nominal mole

ratios are 133 : Sm_2O_3 : 233 : SmF_3 = $(1-x)$: $(1-x)$:x : x (nominal x= 0.16). The powders were pressed using oil hydraulic press to make pellets. The pellet were then heated in an evacuated silica glass tube to obtain samples of nominal $SmFeAsO_{1-x}F_x$ (nominal x= 0.16) The heat treatment temperatures (T_{HT}) were varied from 550°C to 950°C and the holding time (t_{Hld}) of 40 h or 400 h (Fig. C.2.3 (d)).

All procedures except vacuum seal and heat treatment were carried out in an argon-filled golve box (MIWA Mfg; O_2, H_2O < 1 ppm). It is noted that chemical compositions of the yielded precursors powders depend on the procedures, because finite amounts of the powders stick to mortars, pestles, weighing bowls, spatulas, and inner surfaces of SiO_2 tubes.

XRD (Rigaku RINT2500Ultra) measurements at RT using Cu Kα radiation were applied for characterization of the bulk samples, which were polished by a waterproof abraisive paper (Riken Corundum C34P P1000). A silicon (Si) powder (NIST SRM 640d) was used as an external standard reference material. Multiphase Rietveld refinements of the XRD patterns were performed by using the user interface Profex [226] for the program BGMN. Low-vacuum SEM (Hitachi Miniscope TM3030Plus) observations with energy-dispersive X-ray spectroscopy (EDX; Bruker Quantax70) analysis was carried out for the bulk samples, which were polished by a waterproof abraisive paper (Riken Corundum C34P P1000) and lapping film sheets (3M #3,000, #6,000, and #15,000). Then an optical microscope (Olympus BHSM-MU; 0.37 μm resolution) image was also taken with a digital camera (Olympus DP21; 1600 × 1200 pixels).

Electrical resistivity (ρ) of a bulk sample of $SmFeAsO_{1-x}F_x$ (nominal x = 0.16) was measured by the four-probe technique (Fig. C.2.4). The specimen was Au-sputtered. Measurement temperatures was calibrated using a standard reference material. Moreover, magnetic measurement was performed in order to superconductivity of the sample.

C.3 Results and discussion

Figure C.3.1 shows powder XRD patterns of precursor powders. Figure C.3.5 indicated that "133" and "233" powders mainly contain SmAs, Fe_2As, and FeAs. The "233" powder contains unknown crystallographic phases (Fig. C.3.1). Figure C.3.2 shows T_{HT} dependence of XRD patterns of bulk samples of nominal $SmFeAsO_{1-x}F_x$ with the vertical bars at the bottom representing diffractions due to $SmFeAsO_{1-x}F_x$, SmAs [229], Fe_2As [230], FeAs [231], B-type Sm_2O_3 [232], and C-type Sm_2O_3 [233] from above. Figure C.3.6 shows volume fraction of crystallographic phases in the samples of nominal $SmFeAsO_{1-x}F_x$ (nom-

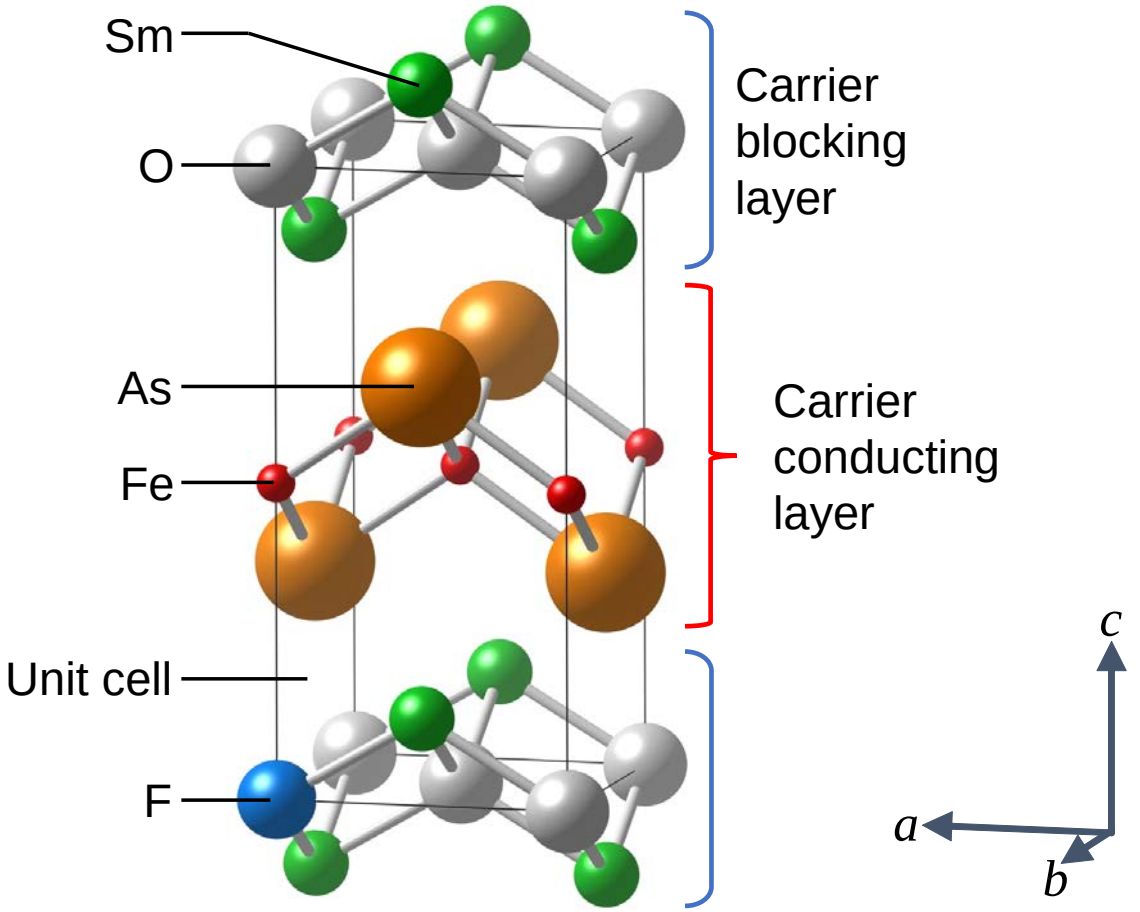

Fig. C.2.1 Crystallographic structure of $SmFeAsO_{1-x}F_x$ (nominal $x = 0.0625$) drawn using VESTA [9].

inal $x = 0.16$). $SmFeAsO_{1-x}F_x$ was a main phase in the samples heated to 650–950°C. In the 650°C sample there were subphases of the reactants: SmAs, Fe_2As, FeAs, B-type Sm_2O_3, and C-type Sm_2O_3. A $SmFeAsO_{1-x}F_x$ phase appeared as a subphase in the sample heated to 575–625°C. Figure C.3.3 shows t_{Hld} dependence of XRD patterns of bulk samples of nominal $SmFeAsO_{1-x}F_x$ with $t_{HT} = 625$°C. The $SmFeAsO_{1-x}F_x$ phase appeared as a subphase in the sample of $t_{Hld} = 40$ h while it appeared as a main phase in a sample of $t_{Hld} = 400$ h. This indicates that $SmFeAsO_{1-x}F_x$ grows at 625°C for hundreds of hours.

Microscopies as shown in Fig. C.3.4 indicates heterogeneous chemical compositions in a scale of hundreds of micrometers in any samples.

Figure C.3.7 shows lattice parameters in $SmFeAsO_{1-x}F_x$ phase of the samples. Introduction of a ratio, f, which is defined as a caption of Fig. C.3.7, enabled change of V to describe.

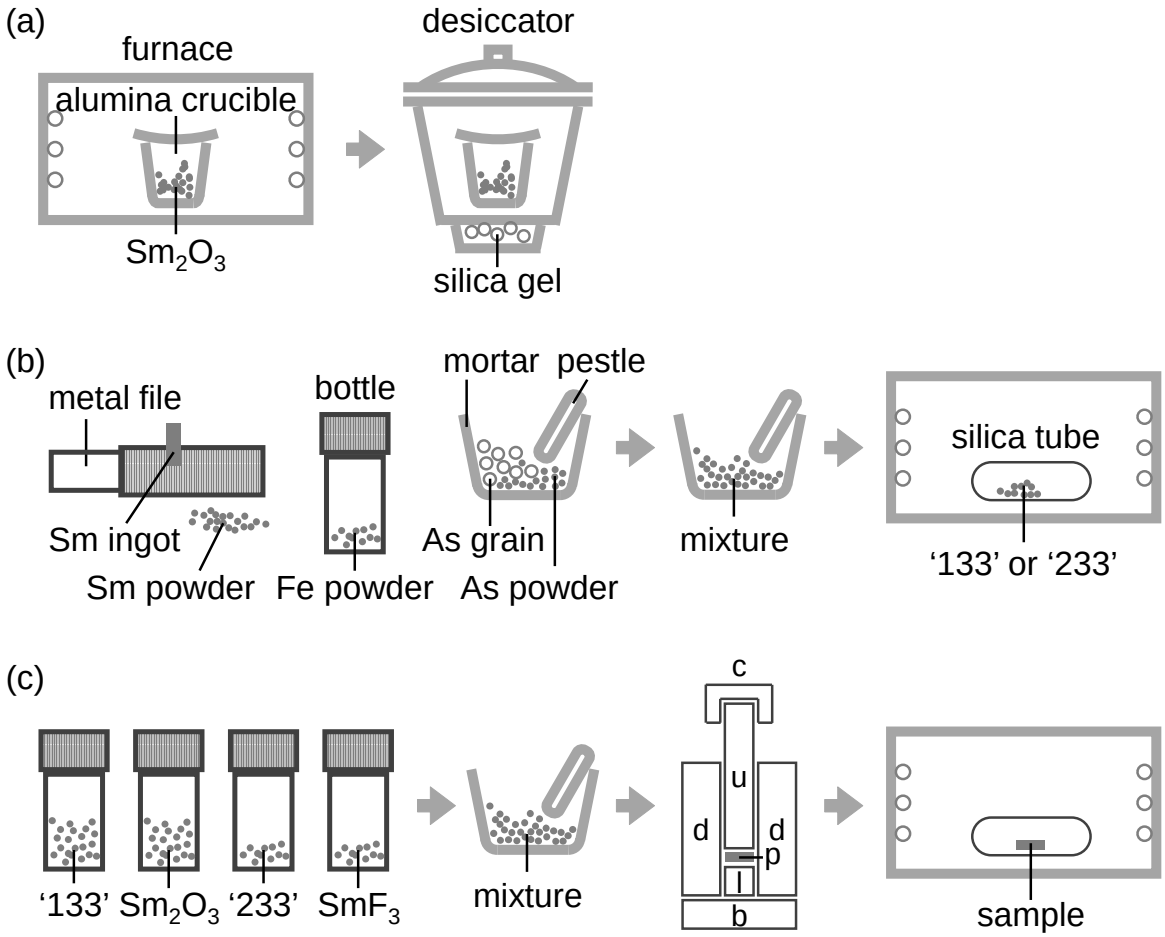

Fig. C.2.2 Flowchart for synthesis procedures of (a) dehydrated powder of Sm_2O_3, (b) precursor powders of "133" and "233," and (c) pellet sample of nominal $SmFeAsO_{1-x}F_x$. It is noted that "133" and "233" denote precursor powders whose mole ratios are Sm : Fe : As = 1 : 3 : 3 and 2 : 3 : 3, respectively. The letters of "c," "u," "d," "p," "l," and "b" in (c) are abbreviations for "cap," "upper punch," "die," "pellet of precursors," "lower punch," and "board," respectively.

Figure C.3.8 shows superconductivity of a sampe of (T_{HT}, t_{Hld}) = (950°C, 40 h) below 50 K.

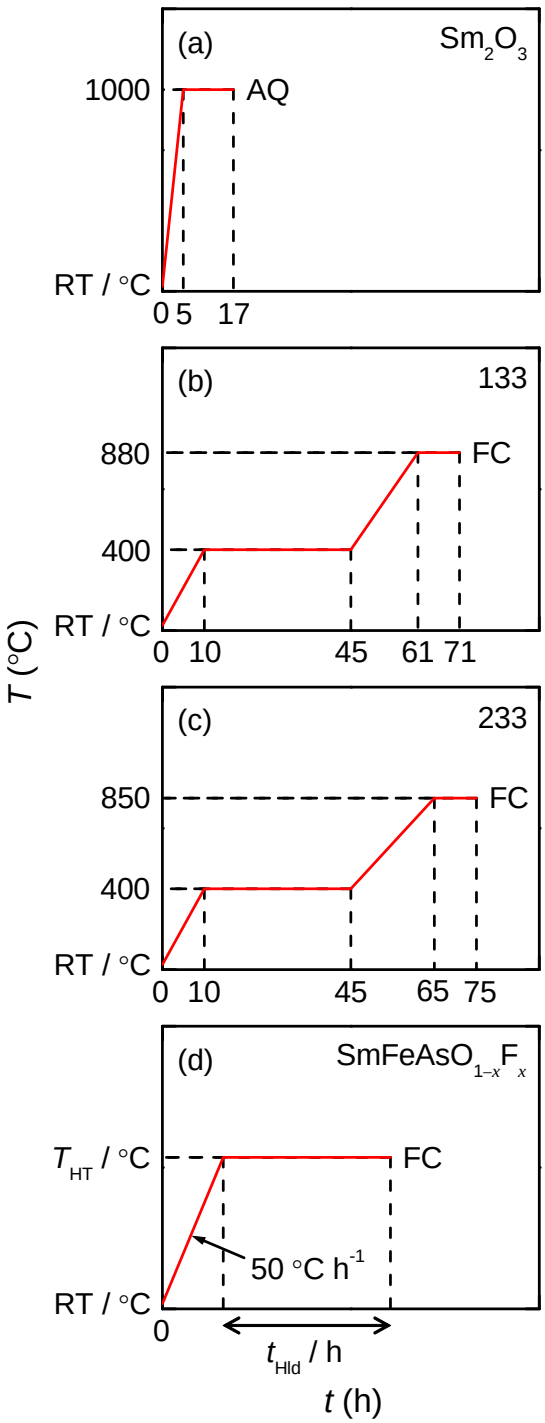

Fig. C.2.3 Heat treatment conditions for synthesis of (a) a dehydrated powder of Sm_2O_3, (b) precursor powders of "133," (c) a precursor powder of "233," and (d) samples of nominal $SmFeAsO_{1-x}F_x$. RT, AQ, FC, T_{HT}, and t_{Hld} represent room temperature, air quenching, furnace cooling, heat treatment temperature, and holding time, respectively. (b) and (c) are reproduced from Fujioka [227].

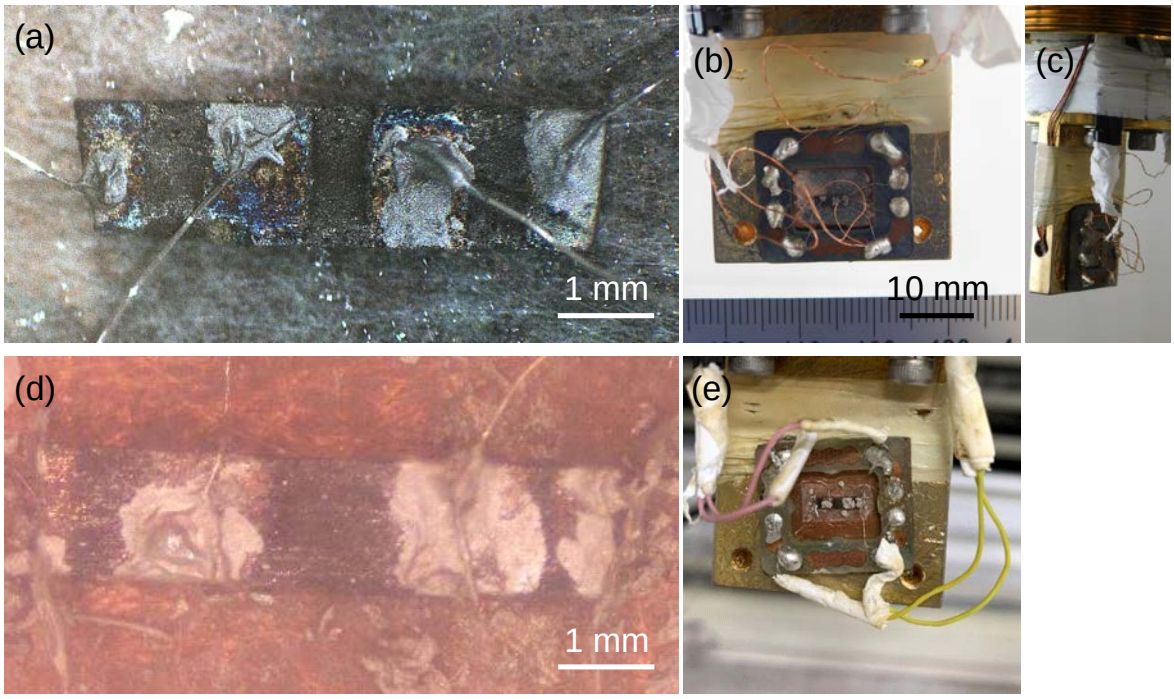

Fig. C.2.4 (a) A specimen of $GdFeAsO_{0.943}F_{0.057}$ as a standard reference specimen (Gd1111stn) with electrodes and wires for measurement of electrical resistivity (ρ). (b) A sample holder on a cold head of a Gifford–McMahon (GM) cryocooler with (a). (c) Side view of (b). (d) A specimen of nominal $SmFeAsO_{1-x}F_x$ (nominal x = 0.16) for (T_{HT}, t_{Hld}) = (950°C, 40 h) with electrodes and wires for measurement of ρ. (e) A sample holder on the cold head of the GM cryocooler with (d). (d) and (e) are reprinted from Kobayashi [228].

C.4 Short summary

During solid-state reaction the lowest temperature at which polycrystalline $SmFeAsO_{1-x}F_x$ grew was 625°C.

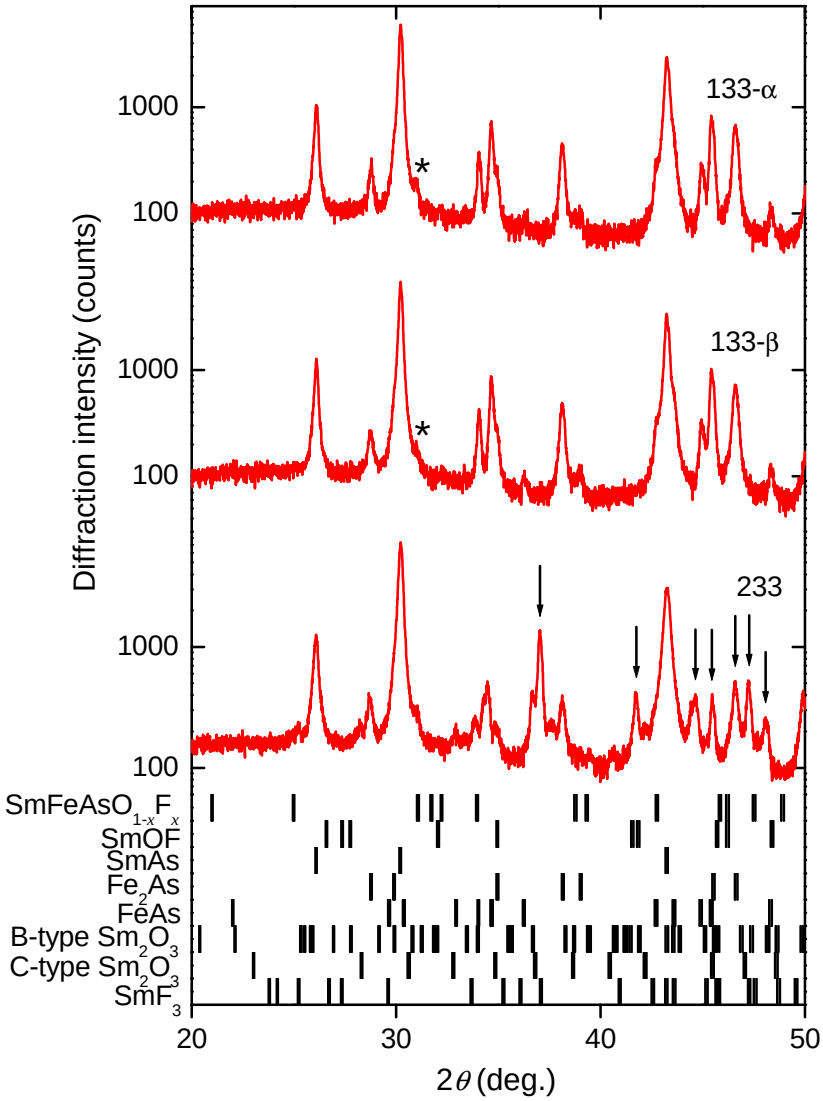

Fig. C.3.1 XRD pattern of precursor powders of "133-α," "133-β," and "233." The names of the powders are denoted near the patterns. The asterisks (*) represent diffractions due to SmFeAsO, little amount of which is contained in both powders of "133-α" and "133-β." The arrows (↓) denote diffractions due to unknown crystallographic phases. The vertical bars at the bottom represent diffractions due to $SmFeAsO_{1-x}F_x$ (ICSD collection code 163840), SmOF (ICSD collection code 81948), SmAs (ICSD collection code 44062), Fe_2As (ICSD collection code 610464), FeAs (ICSD collection code 15009), B-type Sm_2O_3 (ICSD collection code 34291), C-type Sm_2O_3 (ICSD collection code 165779), and SmF_3 (ICSD collection code 9842) from above. The diffractions were calculated by VESTA [9].

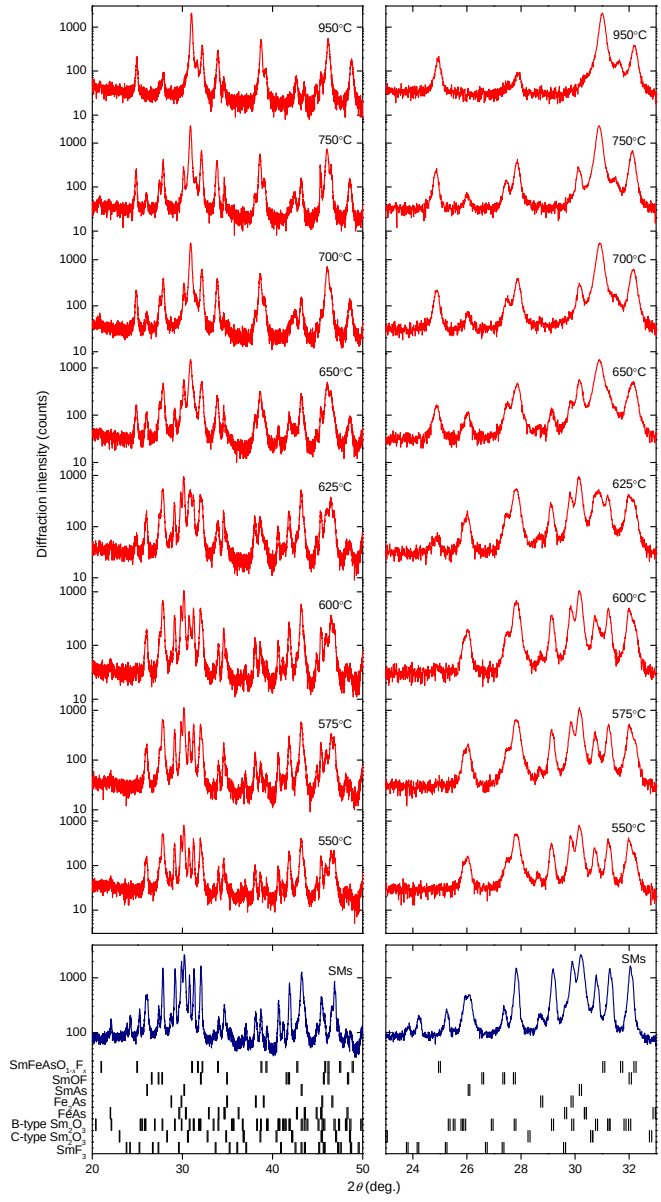

Fig. C.3.2 T_{HT} dependence of XRD pattern of bulk samples of $SmFeAsO_{1-x}F_x$ (nominal $x = 0.16$). T_{HT} or t_{Hld} are denoted near the patterns. The samples were prepared by heating for t_{Hld} of 40 h. Powder XRD pattern of the starting materials (SMs) is added. The vertical bars at the bottom represent diffractions due to $SmFeAsO_{1-x}F_x$ (ICSD collection code 163840), SmOF (ICSD collection code 81948), SmAs (ICSD collection code 44062), Fe_2As (ICSD collection code 610464), FeAs (ICSD collection code 15009), B-type Sm_2O_3 (ICSD collection code 34291), C-type Sm_2O_3 (ICSD collection code 165779), and SmF_3 (ICSD collection code 9842) from above. The diffractions were calculated by VESTA [9]. Left panel: the patterns and diffractions for the range of diffraction angle (2θ) from 20° to 50°. Right panel: the patterns and diffractions for $23° \leq 2\theta \leq 33°$.

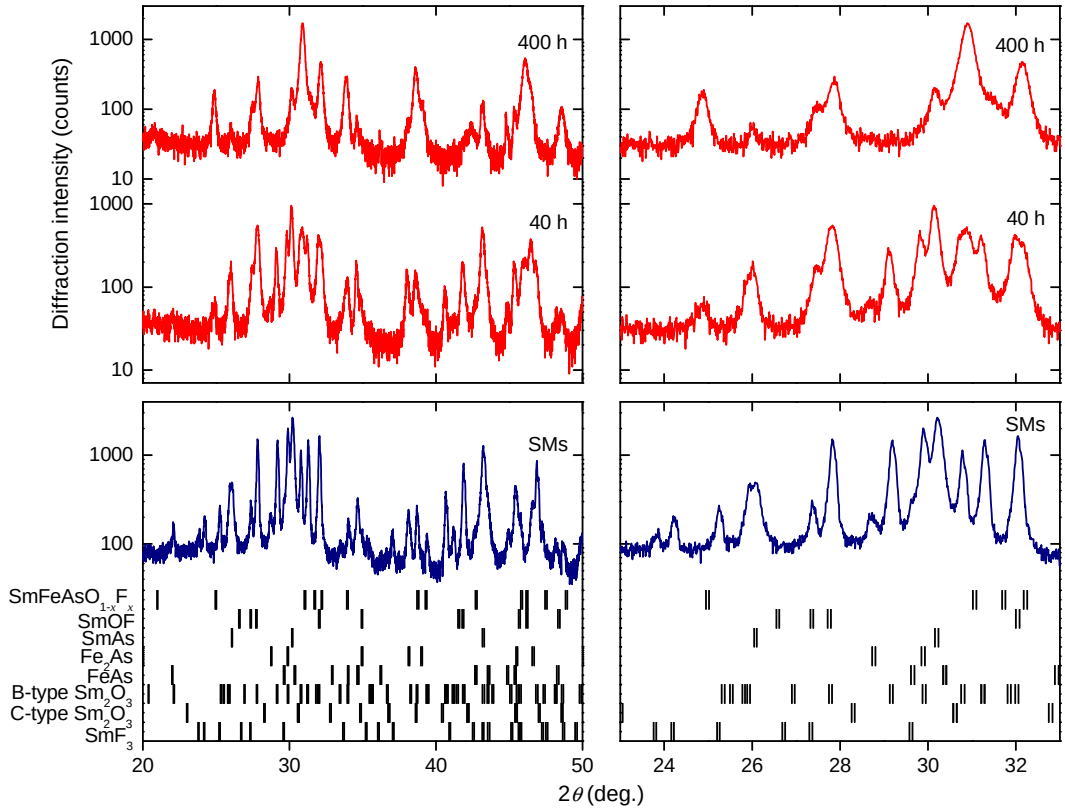

Fig. C.3.3 t_{Hld} dependences of XRD pattern of bulk samples of $SmFeAsO_{1-x}F_x$ (nominal $x = 0.16$). The samples were prepared by heating to T_{HT} of 625°C. t_{Hld} are denoted near the patterns. Powder XRD pattern of the SMs is added. The vertical bars at the bottom represent diffractions due to $SmFeAsO_{1-x}F_x$ (ICSD collection code 163840), SmOF (ICSD collection code 81948), SmAs (ICSD collection code 44062), Fe_2As (ICSD collection code 610464), FeAs (ICSD collection code 15009), B-type Sm_2O_3 (ICSD collection code 34291), C-type Sm_2O_3 (ICSD collection code 165779), and SmF_3 (ICSD collection code 9842) from above. The diffractions were calculated by VESTA [9]. Left panel: the patterns and diffractions for the range of diffraction angle (2θ) from 20° to 50°. Right panel: the patterns and diffractions for $23° \leq 2\theta \leq 33°$.

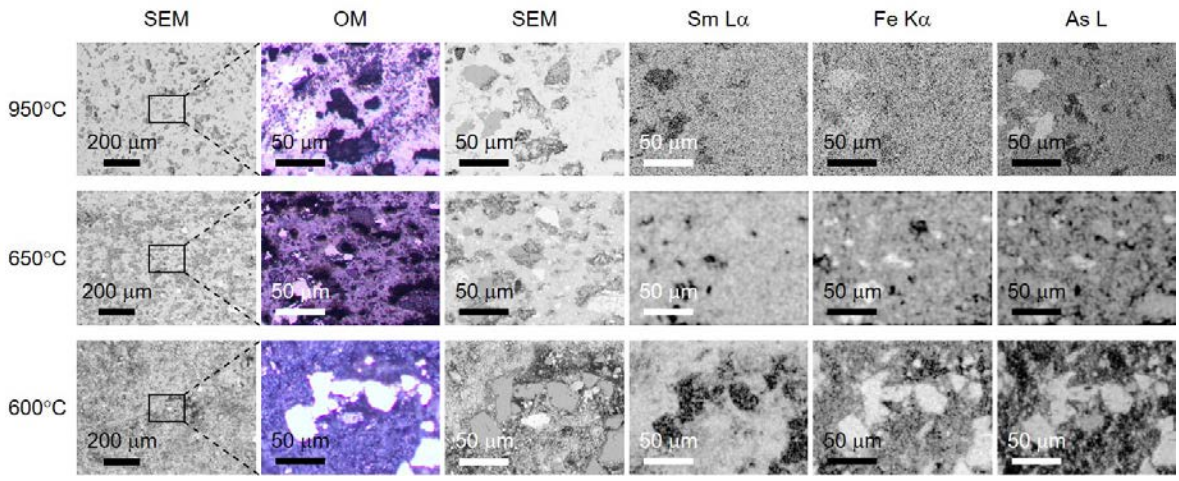

Fig. C.3.4 BSE SEM image, optical microscope (OM) image, and energy-dispersive X-ray spectroscopy (EDX) elemental mappings of samarium (Sm), iron (Fe), and arsenic (As) for bulk samples of $SmFeAsO_{1-x}F_x$ (nominal $x = 0.16$), which were prepared by heating for $t_{Hld} = 40$ h to various T_{HT}. Used lines are denoted next to the elements of the mappings.

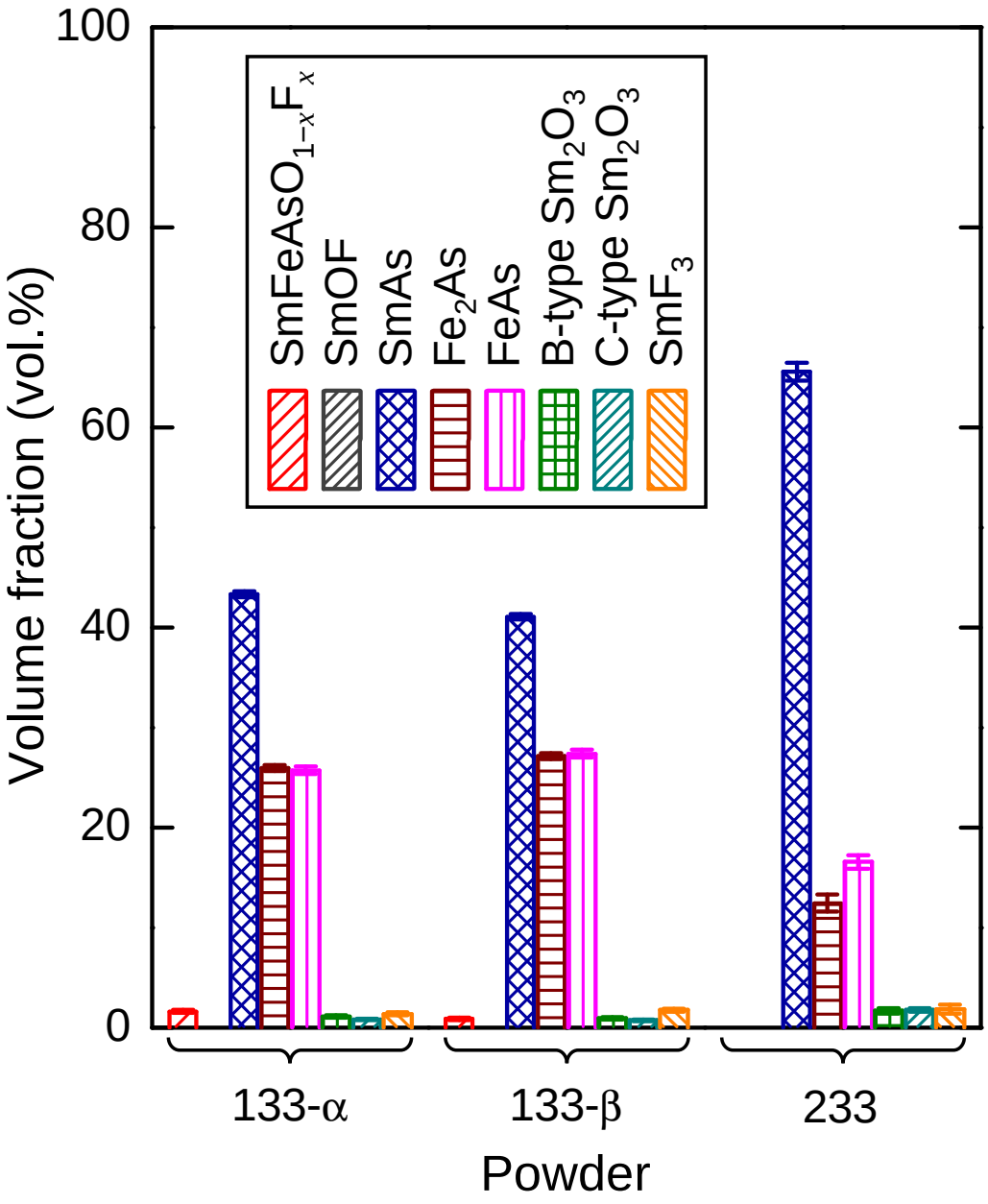

Fig. C.3.5 The volume fraction of crystallographic phases in the precursor powders of "133-a," "133-b," and "233." The volume fraction was calculated by the graphical user interface Profex for the Rietveld refinement program BGMN. The calculations were performed on the assumption that all the powders contains crystallographic phases of only $SmFeAsO_{1-x}F_x$, SmOF, SmAs, Fe_2As, FeAs, B-type Sm_2O_3, C-type Sm_2O_3, and SmF_3.

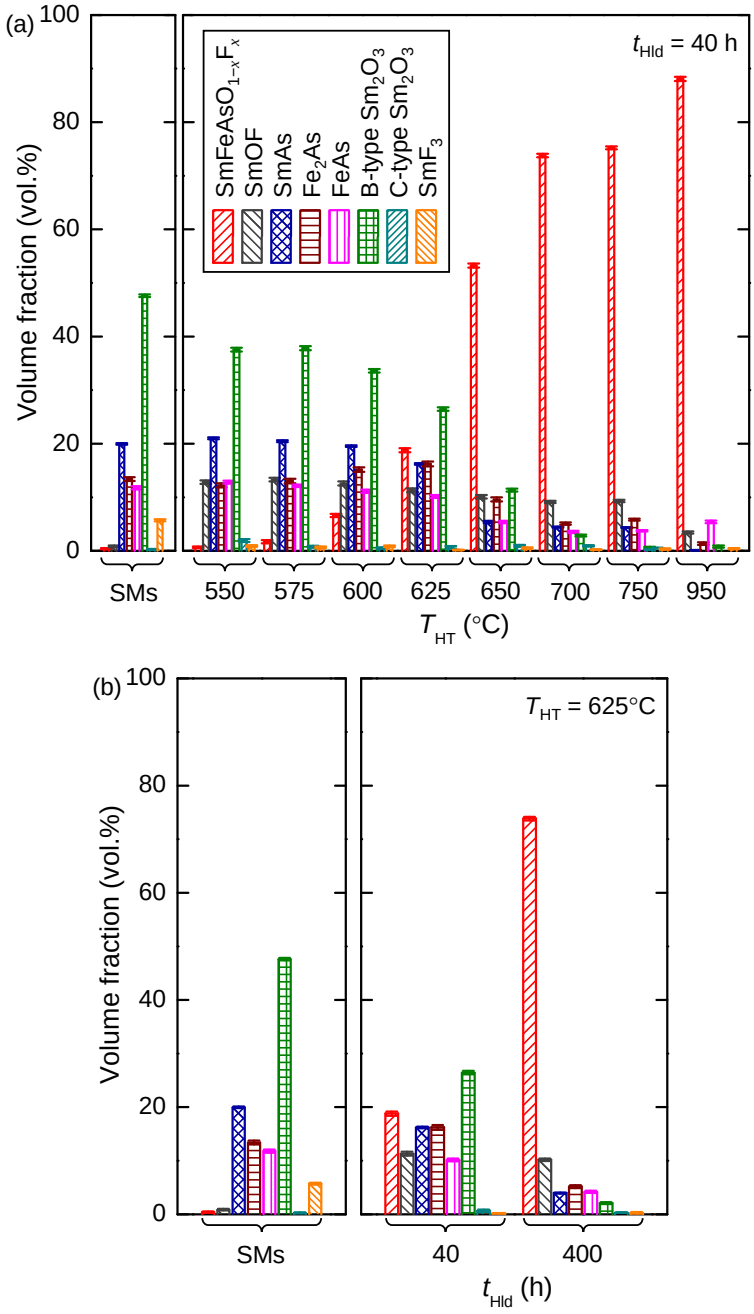

Fig. C.3.6 (a) T_{HT} and (b) t_{Hld} dependences of the volume fraction of crystallographic phases in the samples of nominal $SmFeAsO_{1-x}F_x$ (nominal x = 0.16). The samples were prepared by heating for t_{Hld} = 40 h for (a) and by heating to the T_{HT} = 625°C for (b). Volume fraction of crystallographic phases in the SMs powder is added. The volume fraction was calculated by the graphical user interface Profex for the Rietveld refinement program BGMN.

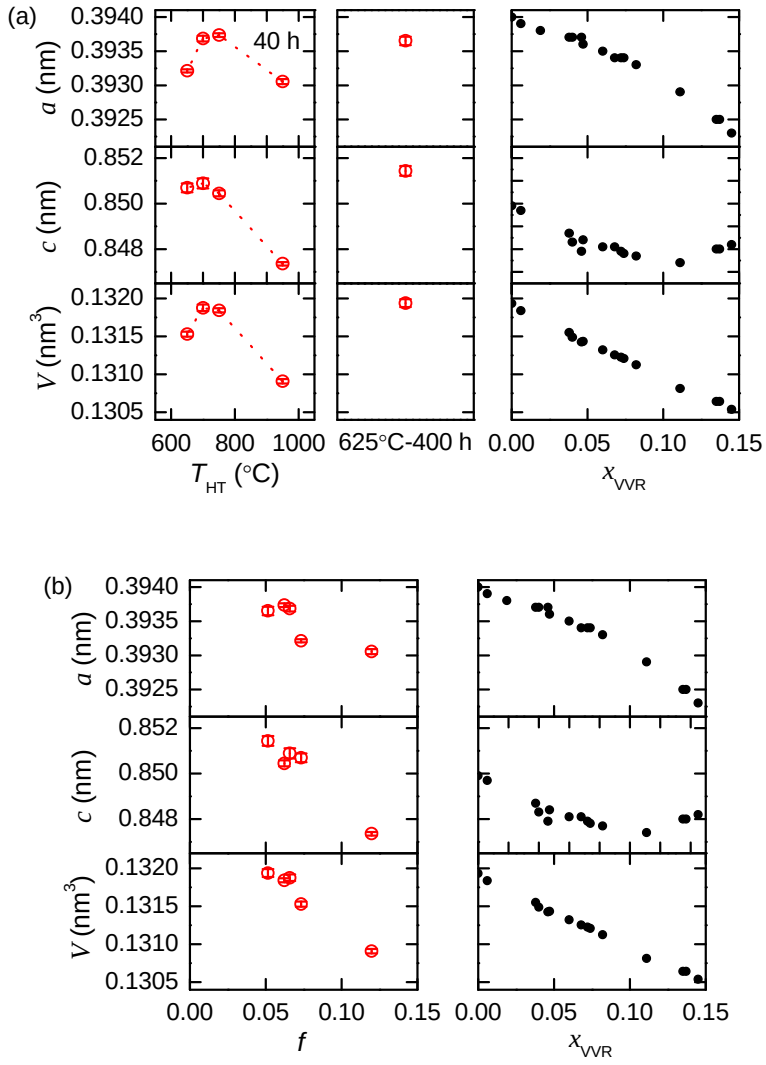

Fig. C.3.7 (a) T_{HT} dependence of lattice constants (a and c) and lattice volumes (V) of pulverized samples of $SmFeAsO_{1-x}F_x$ (nominal x = 0.16) for t_{Hld} = 40 h. The a, c, and V of a sample for (T_{HT}, t_{Hld}) = (625°C, 400 h) are added. The a and c versus the Fluorine (F) content (x_{VVR}), which are reported by Kamihara *et al.* [208], Fujioka [207], and Kamihara and Hosono [206], are also added. The x_{VVR} were determined by the lattice constants using Vegard's volume rule (VVR). (b) The a, c, and V of pulverized samples of $SmFeAsO_{1-x}F_x$ (nominal x = 0.16) as a function of a ratio, f, which is defined as: f = [0.14 − ϕ_{Vol}(SmOF)] / ϕ_{Vol}($SmFeAsO_{1-x}F_x$), where ϕ_{Vol}(SmOF) and ϕ_{Vol}($SmFeAsO_{1-x}F_x$) is volume fractions of SmOF and $SmFeAsO_{1-x}F_x$ (nominal x = 0.16), respectively. They are shown in Fig. 7. The data reported by Kamihara *et al.* [206], Fujioka [207], and Kamihara and Hosono [208] are on the side.

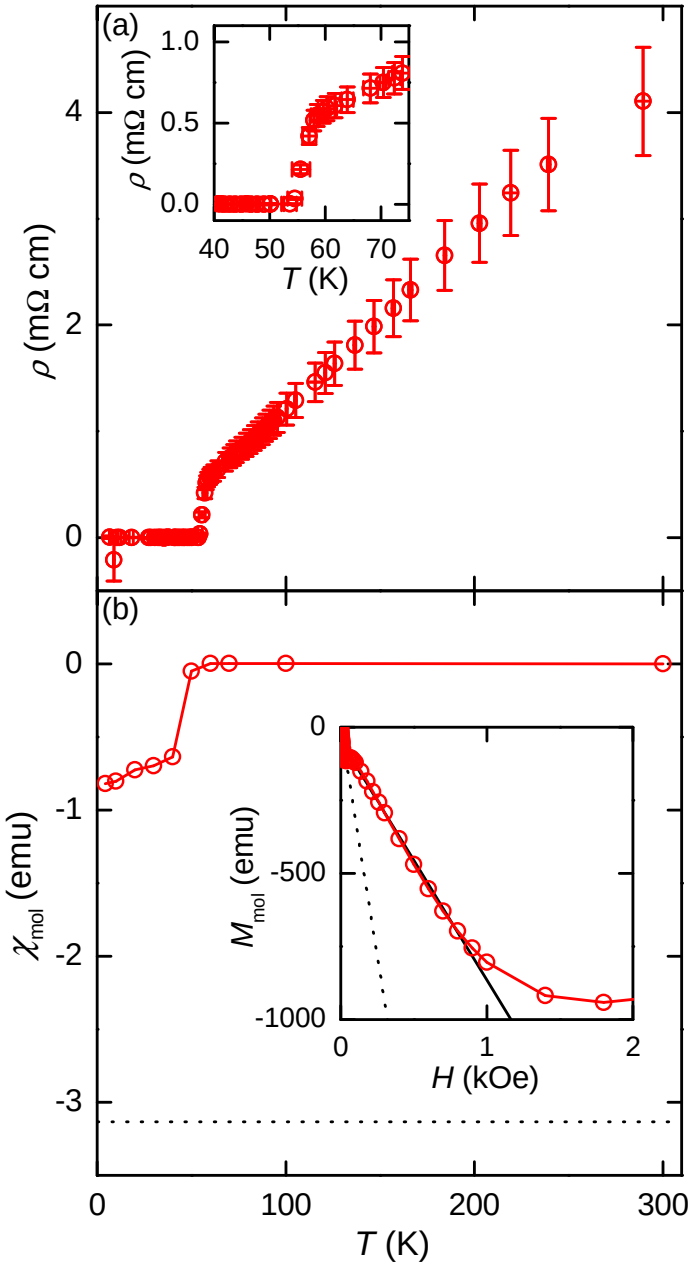

Fig. C.3.8 (a) Temperature (T) dependence of electrical resistivity (ρ) of a sample of nominal $SmFeAsO_{1-x}F_x$ (nominal x = 0.16) for (T_{HT}, t_{Hld}) = (950°C, 40 h). The inset shows enlarged part for 40 K ≤ T ≤ 75 K. (b) T dependence of molar magnetic susceptibility (χ_{mol}) of the sample of nominal $SmFeAsO_{1-x}F_x$ (nominal x = 0.16) for (T_{HT}, t_{Hld}) = (950°C, 40 h). The dotted line denotes the perfect diamagnetism for $SmFeAsO_{0.84}F_{0.16}$. The inset shows molar magnetization (M_{mol}) versus magnetic field (H) of the sample at T = 4.2 K. The solid and dotted lines in the inset represent the slope of a straight-line fit and the perfect diamagnetism for $SmFeAsO_{0.84}F_{0.16}$, respectively.

References

[1] T. H. Geballe and J. K. Hulm, *Bernd Theodor Matthias* (National Academies Press, Washington, D.C., 1996).

[2] H. Hosono, A. Yamamoto, H. Hiramatsu, and Y. Ma, Materials Today **21**, 278 (2017).

[3] M. Wuttig, Phys. Status Soldi B **249**, 1843 (2012).

[4] M. S. Dresselhaus, G. Chen, M. Y. Tang, R.-G. Yang, H. Lee, D.-Z. Wang, Z.-F. Ren, J.-P. Fleurial, and P. Gogna, Adv. Mater. **19**, 1043 (2007).

[5] J.-Y. Raty, M. Schumacher, P. Golub, V. L. Deringer, C. Gatti, and M. Wuttig, Adv. Mater. **31**, 1806280 (2019).

[6] J. B. Taylor, S. L. Bennett, and R. D. Heyding, J. Phys. Chem. Solids **26**, 69 (1965).

[7] M. Q. Arguilla, N. D. Cultrara, Z. J. Baum, S. Jiang, R. D. Ross, and J. E. Goldberger, Inorg. Chem. Front. **4**, 378 (2017).

[8] Z.-A. Ren, W. Lu, J. Yang, W. Yi, X.-L. Shen, Z.-C. Li, G.-C. Che, X.-L. Dong, L.-L. Sun, F. Zhou, and Z.-X. Zhao Chinese Phys. Lett. **25**, 2215 (2008).

[9] K. Momma and F. Izumi, J. Appl. Crystallogr. **44**, 1272 (2011).

[10] Y. Yu, M. Cagnoni, O. C.-Mirédin, and M. Wuttig, Adv. Funct. Mater. **30**, 1904862 (2019).

[11] H. Li, S.-Y. Gao, S.-F. Duan, Y.-F. Xu, K.-J. Zhu, S.-J. Tian, J.-C. Gao, W.-H. Fan, Z.-C. Rao, J.-R. Huang, J.-J. Li, D.-Y. Yan, Z.-T. Liu, W.-L. Liu, Y.-B. Huang, Y.-L. Li, Y. Liu, G.-B. Zhang, P. Zhang, T. Kondo, S. Shin, H.-C. Lei, Y.-G. Shi, W.-T. Zhang, H.-M. Weng, T. Qian, and H. Ding, Phys. Rev. X **9**, 041039 (2019).

[12] S. Sakuragi, S. Sasaki, R. Akashi, R. Sakagami, K. Kuroda, C. Bareille, T. Hashimoto, T. Nagashima, Y. Kinoshita, Y. Hirata, M. Shimozawa, S. Asai, T. Yajima, S. Doi, N. Tsujimoto, S. Kunisada, R. Noguchi, K. Kurokawa, N. Azuma, K. Hirata, Y. Yamasaki, H. Nakao, T. K. Kim, C. Cacho, T. Masuda, M. Tokunaga, H. Wadati, K. Okazaki, S. Shin, Y. Kamihara, M. Yamashita, and T. Kondo, arXiv:2001.07991.

[13] Y. Goto, A. Yamada, T. D. Matusda, Y. Aoki, and Y. Mizuguchi, J. Phys. Soc. Jpn. **86**,

123701 (2017).

[14] K. Ishihara, T. Takenaka, Y. Miao, O. Tanaka, Y. Mizukami, H. Usui, K. Kuroki, M. Konczykowski, Y. Goto, Y. Mizuguchi, and T. Shibaushi, Phys. Rev. B **98**, 020503(R) (2018).

[15] E. J. Cheng, J. M. Ni, F. Q. Meng, T. P. Ying, B. L. Pan, Y. Y. Huang, D. C. Peets, Q. H. Zhang, and S. Y. Li, EPL-Europhys. Lett. **123**, 47004 (2018).

[16] H. Yuwen, Y. Goto, R, Jha, A. Miura, C. Moriyoshi, Y. Kuroiwa, T. D. Matsuda, Y. Aoki, and Y. Mizuguchi, Jpn. J. Appl. Phys. **58**, 083001 (2019).

[17] B. He, Y. Wang, M. Q. Arguilla, N. D. Cultrara, M. R. Scudder, J. E. Goldberger, W. Windl, and J. P. Heremans, Nat. Mater. **18**, 568 (2019).

[18] K. Lee, D. Kaseman, S. Sen, I. Hung, Z. Gan, B. Gerke, R. Pöttgen, M. Feygenson, J. Neuefeind, O.I. Lebedev, K. Kovnir, J. Am. Chem. Soc. **137**, 3622 (2015).

[19] L.-Y. Rong, J.-Z. Ma, S.-M. Nie, Z.-P. Lin, Z.-L. Li, B.-B. Fu, L.-Y. Kong, X.-Z. Zhang, Y.-B. Huang, H.-M. Weng, T. Qian, H. Ding, R.-Z. Tai, Sci. Rep.-UK **7**, 6133 (2017).

[20] H.-C. Chen, Z.-F. Lou, Y.-X. Zhou, Q. Chen, B.-J. Xu, S.-J. Chen, J.-H. Du, J.-H. Yang, H.-D. Wang, and M.-H. Fang, Chinese Phys. Lett. **37**, 047201 (2020).

[21] R. Sakagami, Y. Goto, Y. Mizuguchi, M. Matoba, and Y. Kamihara, Mater. Sci. Tech. Jpn. **55**, 72 (2018) (in Japanese).

[22] T. J. Seebeck, Magnetische Polarisation der Metalle und Erze durch Temperatur-Differenz (Abh. Akad. Wiss., Berlin, 1822) (in German).

[23] H. J. Goldsmid and R. W. Douglas, Brit. J. Appl. Phys. **5**, 386 (1954).

[24] 寺崎一郎, 熱電材料の物質科学—熱力学・物性物理学・ナノ科学 (内田老鶴圃, 東京, 2017); I. Terasaki, *Materials Science of Thermoelectric Materials: Thermodynamics, Condensed Matter Physics and Nanoscience* (Uchida Rokakuho, Tokyo, 2017) (in Japanese).

[25] D. T. Morelli and G. P. Meisner, J. Appl. Phys. **77**, 3777 (1995).

[26] T. Caillat, J.-P. Fleurial, and A. Borshchevsky, Phys. Chem. Solids **58**, 1119 (1997).

[27] G. S. Nolas, J. L. Cohn, G. A. Slack, and S. B. Schujman, Appl. Phys. Lett. **73**, 178 (1998).

[28] G. A. Slack, *New Materials and Performance Limits for Thermoelectric Cooling* in CRC Handbook of Thermoelectrics, edited by D. M. Rowe (CRC, Boca Raton, 1995).

[29] H. Wang, W. D. Porter, H. Böttner, J. König, L. Chen, S. Q. Bai, T. M. Tritt, A. Mayolet, J. Senawiratne, C. Smith, F. Harris, P. Gilbert, J. Sharp, J. Lo, H. Kleinke,

and L. Kiss, J. Electron. Mater. **42**, 654 (2013).

[30] H. Wang, W. D. Porter, H. Böttner, J. König, L. Chen, S. Q. Bai, T. M. Tritt, A. Mayolet, J. Senawiratne, C. Smith, F. Harris, P. Gilbert, J. Sharp, J. Lo, H. Kleinke, and L. Kiss, J. Electron. Mater. **42**, 1073 (2013).

[31] H. Zhang, M. Baitinger, M.-B. Tang, Z.-Y. Man, H.-H. Chen, X.-X. Yang, Y. Liu, L. Chen, Y. Grin, and J.-T. Zhao, Dalton T **39**, 1101 (2010).

[32] F. Gascoin, S. Ottensmann, D. Stark, S. M. Haïle, and G. J. Snyder, Adv. Funct. Mater. **15**, 1860 (2005).

[33] K. Kihou, H. Nishiate, A. Yamamoto, and C.-H. Lee, Inorg. Chem. **56**, 3709 (2017).

[34] Z.-P. Lin, G. Wang, C.-C. Le, H.-Z. Zhao, N. Liu, J.-P. Hu, L.-W. Guo, and X.-L. Chen, Phys Rev. B **95**, 165201 (2017).

[35] A. Palenzona, P. Manfrinetti, and M. L. Fornasini, J. Alloy. Compd. **280**, 211 (1998).

[36] S. Ono, F. L. Hui, J. G. Despault, L. D. Calvert, and J. B. Taylor, J. Less-Common Met. **25**, 287 (1971).

[37] Springer, http://materials.springer.com/isp/phase-diagram/docs/c_0900186 (Accessed June 2017).

[38] E. R. Jette and F. Foote, J. Chem. Phys. **3**, 605 (1935).

[39] アドバンス理工 (旧社名: アルバック理工), 卓上型ランプ加熱装置 MILA-5000 取扱説明書; Advance Riko (its former company name: ULVAC-RIKO), Instrution manual of infrared lamp heating system, MILA-5000 (in Japanese).

[40] N. Cusack, P. Kendall, P. Phys. Soc. **72**, 898 (1958).

[41] M. J. Laubitz, Can. J. Phys. **47**, 2633 (1969).

[42] J. B. J. Fourier, *Théorie Analytique de la Chaleur* (Cambridge University Press, Cambridge, 2009) (Original work published 1822) (in French).

[43] J. B. J. Fourier, *The Analytical Theory of Heat*, translated by A. Freeman (Cambridge University Press, Cambridge, 2009) (Original work published 1822).

[44] R. Sakagami, Y. Goto, H. Karimata, N. Azuma, M. Yamaguchi, S. Iwasaki, M. Nakanishi, I. Kitawaki, Y. Mizuguchi, M. Matoba, and Y. Kamihara, Jpn. J. Appl. Phys. **60**, 035511 (2021).

[45] G. J. Snyder, in Energy Harvesting Technologies, ed. S. Priya and D. J. Inman (Springer, New York, 2009).

[46] K. Hanamura, Proc. 217th Topical Symp. Magnetic Society of Japan, Tokyo, 2018, p. 9 (in Japanese).

[47] J. W. Gibbs, Transactions of the Connecticut Academy of Arts and Sciences **2**, 382

(1873).

[48] J. W. Gibbs, Transactions of the Connecticut Academy of Arts and Sciences **3**, 108 (1874–1878).

[49] J. W. Gibbs, Transactions of the Connecticut Academy of Arts and Sciences **3** , 343 (1874–1878).

[50] H. B. Callen, Thermodynamics and an Introduction to Thermostatistics (Wiley, New York, 1985) 2nd ed.

[51] H. Tasaki, Netsurikigaku: Gendaiteki-na shiten-kara (Baifukan, Tokyo, 2000) Appendix F, pp. 257–259 (in Japanese).

[52] A. F. Ioffe, Semiconductor Thermoelements and Thermoelectric Cooling (Infosearch, London, 1957).

[53] G. J. Snyder and E. S. Toberer, Nat. Mater. **7**, 105 (2008).

[54] K. Guo, Q.-G. Cao, and J.-T. Zhao, J. Rare Earth. **31**, 1029 (2013).

[55] J.-W. Zhang, L.-R. Song, and B.-B. Iversen, npj Comput. Mater. **5**, 76 (2019).

[56] L.-T. Zheng, W. Li, C. Sun, X.-M. Shi, X.-Y. Zhang, and Y.-Z. Pei, J. Alloy. Compd. **821**, 153497 (2020).

[57] E. S. Toberer, A. F. May, B. C. Melot, E. Flage-Larsen, and G. J. Snyder, Dalton T **39**, 1046 (2010).

[58] Q.-G. Cao, H. Zhang, M.-B. Tang, H.-H. Chen, X.-X. Yang, Y. Grin, and J.-T. Zhao, J. Appl. Phys. **107**, 053714 (2010).

[59] X.-J. Wang, M.-B. Tang, H.-H. Chen, X.-X. Yang, J.-T. Zhao, U. Burkhardt, and Y. Grin, Appl. Phys. Lett. **94**, 092106 (2009).

[60] C. Yu, T. J. Zhu, S. N. Zhang, X. B. Zhao, J. He, Z. Su, and T. M. Tritt, J. Appl. Phys. **104**, 013705 (2008).

[61] K. Guo, Q.-G. Cao, X.-J. Feng, M.-B. Tang, H.-H. Chen, X. X. Guo, L. Chen, Y. Grin, and J.-T. Zhao, Eur. J. Inorg. Chem. **26**, 4043 (2011).

[62] C. L. Condron, S. M. Kauzlarich, F. Gascoin, and G. J. Snyder, J. Solid State Chem. **179**, 2252 (2006).

[63] F. Ahmadpour, T. Kolodiazhnyi, and Y. Mozharivskyj, J. Solid State Chem. **180**, 2420 (2007).

[64] S. Kim, C. Kim, Y.-K. Hong, T. Onimaru, K. Suekuni, T. Takabatake, and M.-H. Jung, J. Mater. Chem. A **2**, 12311 (2014).

[65] J. Shuai, Y. Wang, H.-S. Kim, Z. Liu, J. Sun, S. Chen, J. Sui, and Z. Ren, Acta Mater. **93**, 187 (2015).

[66] A. Bhardwaj, A. Rajput, A. K. Shukla, J. J. Pulikkotil, A. K. Srivastava, A. Dhar, G. Gupta, S. Auluck, D. K. Misra, and R. C. Budhani, RSC Adv. **3**, 8504 (2013).

[67] A. Bhardwaj and D. K. Misra, RSC Adv. **4**, 34552 (2014).

[68] H. Tamaki, H. K. Sato, and T. Kanno, Adv. Mater. **28**, 10182 (2016).

[69] J.-W. Zhang, L.-R. Song, S. H. Pedersen, H. Yin, L. T. Hung, and B. B. Iversen, Nat. Commun. **8**, 13901 (2017).

[70] A. F. May, M. A. McGuire, D. J. Singh, J. Ma, O. Delaire, A. Huq, W. Cai, and H. Wang, Phys. Rev. B **85**, 035202 (2012).

[71] J. Shuai, Z.-H. Liu, H. S. Kim, Y.-M. Wang, J. Mao, R. He, J.-H. Sui, and Z.-F. Ren, J. Mater. Chem. A **4**, 4312 (2016).

[72] J. Shuai, H.-Y. Geng, Y.-C. Lan, Z. Zhu, C. Wang, Z.-H. Liu, J.-M. Bao, C.-W. Chu, J-H. Sui, and Z.-F. Ren, P. Natl. Acad. Sci. USA **113**, E4125 (2016).

[73] E. I. Gladyshevskii, P. I. Kripyakevich, and O. I. Bodak, Ukr. Fiz. Zh. **12**, 447 (1967) (in Ukrainian).

[74] X.-J. Wang, M.-B. Tang, J.-T. Zhao, H.-H. Chen, and X.-X. Yang, Appl. Phys. Lett. **90**, 232107 (2007).

[75] J. E. Iglesias, K. E. Pachali, and H. Steinfink, J. Solid State Chem. **9**, 6 (1974).

[76] H. Kunioka, K. Kihou, H. Nishate, A. Yamamoto, H. Usui, K. Kuroki, and C. H. Lee, Dalton T. **47**, 16205 (2018).

[77] H. Kunioka, K. Kihou, D. Kato, H. Usui, T. Iida, H. Nishiate, K. Kuroki, A. Yamamoto, and C. H. Lee, Inorg. Chem. **59**, 5828 (2020).

[78] Z. Ban and M. Sikirica, Acta Crystallogr. **18**, 594 (1965).

[79] D. Harker, Z. Kristallogr. **89**, 175 (1934).

[80] M. Asbrand, B. Eisenmann, and J. Klein, Z. Anorg. Allg. Chem. **621**, 576 (1995) (in German).

[81] Y. Goto, A. Miura, C. Moriyoshi, Y. Kuroiwa, T. D. Mtsuda, Y. Aoki, and Y. Mizuguchi, Sci. Rep.-UK **8**, 12852 (2018).

[82] H. W. Shu, S. Jaulmes, and J. Flahaut, J. Solid State Chem. **74**, 277 (1988).

[83] The International Bureau of Weights and Measures (BIPM), *The International System of Units (SI)* (BIPM, online, 2019).

[84] F. K. Lotgering, J. Inorg. Cucl. Chem. **9**, 113 (1959).

[85] J. A. Bearden, Rev. Mod. Phys. **39**, 78 (1967).

[86] F. Bloch, Z. Phys. **59**, 208 (1930) (in German).

[87] E. Grüneisen, Ann. Phys.-Berlin **16**, 530 (1933) (in German).

[88] J. Bass, W. P. Pratt, Jr, and P. A. Schroeder, Rev. Mod. Phys. **62**, 645 (1990).

[89] J. E. Hoffman, Rep. Prog. Phys. **74**, 124513 (2011).

[90] N. Ni, S. L. Bud'ko, A. Kreyssig, S. Nandi, G. E. Rustan, A. I. Goldman, S. Gupta, J. D. Corbett, A. Kracher, P. C. Canfield, Phys. Rev. B **78**, 014507 (2008).

[91] J. M. Ziman, *Electrons and Phonons: The Theory of Transport Phenomena in Solids* (Clarendon Press, Oxford, 1960).

[92] M. Cutler and N. F. Mott, Phys. Rev. **181**, 1336 (1969).

[93] T. Takeuchi, Mater. Trans. **50**, 2359 (2009).

[94] T. Takeuchi, J. Thermoelectric. Soc. Jpn. **8**, 17 (2011) (in Japanese).

[95] T. Takeuchi, T. Otagiri, H. Sakagami, T. Kondo, U. Mizutani, H. Sato, Phys. Rev. B **70**, 144202 (2004).

[96] R. E. Peierls, *Quantum Theory of Solids* (Clarendon Press, Oxford, 1955).

[97] F. J. Blatt, in: F. Seitz, D. Turnbull (Eds.), Solid State Physics: Advances in Research and Applications, Vol. 4, (Academic Press, New York, 1957).

[98] A. H. Wilson, *The Theory of Metals*, 2nd Edition (Cambridge University Press, Cambridge, 1953).

[99] W. G. Baber, P. R. Soc. A **158**, 383 (1937).

[100] A. H. MacDonald, R. Taylor, and D. J. W. Geldart, Phys. Rev. B **23**, 2718 (1981).

[101] K. Andres, J. E. Graebner, and H. R. Ott, Phys. Rev. Lett. **35**, 1779 (1975).

[102] W. Lieke, U. Rauchschwalbe, C. B. Bredl, F. Steglich, J. Aarts, and F. R. de Boer, J. Appl. Phys. **53**, 2111 (1982).

[103] T. Furuno, N. Sato, S. Kunii, T. Kasuya, W. Sasaki, J. Phys. Soc. Jpn. **54**, 1899 (1985).

[104] N. Sato, A. Sumiyama, S. Kunii, H. Nagano, and T. Kasuya, J. Phys. Soc. Jpn. **54**, 1923 (1985).

[105] J. F. Goff, J. Appl. Phys. **35**, 2919 (1964).

[106] A. H. Thompson, Phys. Rev. Lett. **35**, 1786 (1975).

[107] Y. Tokura, Y. Taguchi, Y. Okada, Y. Fujishima, T. Arima, K. Kumagai, and Y. Iye, Phys. Rev. Lett. **70**, 2126 (1993).

[108] D. Varshney, N. Dodiya, M. W. Shaikh, J. Alloy. Compd. **509**, 7447 (2011).

[109] H. Imai, Y. Shimakawa, and Y. Kubo, Phys. Rev. B **64**, 241104(R) (2001).

[110] E. Conwell and V. F. Weisskopf, Phys. Rev. **77**, 388 (1950).

[111] H. Brooks, Adv. Electron El. Phys. **7**, 85 (1955).

[112] A. Nishida, O. Miura, C.-H. Lee, Y. Mizuguchi, Appl. Phys. Express **8**, 111801 (2015).

[113] H. Preston-Thomas, Metrologia **27**, 3 (1990).

[114] J. Ancsin and E.G. Murdock, Metrologia **27**, 201 (1990).

[115] C. Herring, Bell Syst. Tech. J. **34**, 237 (1955).

[116] N. F. Mott and H. Jones, *The Theory of the Properties of Metals and Alloys* (Clarendon Press, Oxford, 1936).

[117] M. Jonson and G. D. Mahan, Phys. Rev. B **21**, 4223 (1980).

[118] H. Kontani, Phys. Rev. B **67**, 014408 (2003).

[119] J. S. Tse and D. D. Klug, in *Thermoelectrics Handbook: Macro to Nano*, ed. D. M. Rowe (CRC, Boca Raton, 2006).

[120] Y. Goto, J. Kajitani, Y. Mizuguchi, Y. Kamihara, and M. Matoba, J. Phys. Soc. Jpn. **84**, 085003 (2015).

[121] U. Birkholz, Z. Naturforsch. Pt. A **13**, 780 (1958) (in German).

[122] R. E. Fryer, C. C. Lee, V. Rowe, and P. A. Schroeder, Physica **31**, 1491 (1965).

[123] L.-D. Zhao, C. Chang, G. Tan, and M. G. Kanatzidis, Energy Environ. Sci. **9**, 3044 (2016).

[124] T. Nishimura, H. Sakai, H. Mori, K. Akiba, H. Usui, M. Ochi, K. Kuroki, A.Miyake, M. Tokunaga, Y. Uwatoko, K. Katayama, H. Murakawa, and N. Hanasaki, Phys. Rev. Lett. **122**, 226601 (2019).

[125] G. S. Nolas, J. Sharp, and H. J. Goldsmid, *Thermoelectrics* (Springer, Berlin, 2010).

[126] H. J. Goldsmid, *Thermoelectric Refrigeration* (Plenum Press, New York, 1964).

[127] T. Hoashi, J. Inst. Electr. Eng. Jpn. **47**, 595 (1927) (in Japanese).

[128] J. Millman, P. I.R.E. **28**, 413 (1940).

[129] G. Wiedemann and R. Franz, Ann. Phys.-Berlin **165**, 497 (1853) (in German).

[130] L. Lorenz, Ann, Phys.-Berlin **223**, 429 (1872) (in German).

[131] A. Sommerfeld, Naturwissenschaften **15**, 825 (1927) (in German).

[132] A. Sommerfeld, Naturwissenschaften **16**, 374 (1928) (in German).

[133] P. J. Price, Philos. Mag. **46**, 1252 (1955).

[134] G. D. Mahan, Solid State Phys. **51**, 81 (1998).

[135] M. Cutler, J. F. Leavy, and R. L. Fitzpatrick, Phys. Rev. **133**, A1143 (1964).

[136] F. D. Rosi, B. Abeles, and R. V. Jensen, J. Phys. Chem. Solids **10**, 191 (1959).

[137] H. J. Goldsmid, R. T. Delves, G.E.C. Journal **28**, 102 (1961).

[138] Mössbauer Effect Data Center, https://medc.dicp.ac.cn/Resources-isotopes/Resource-Eu.php (Accessed in May 2021).

[139] N. N. Greenwood and T. C. Gibb, Mössbauer Spectroscopy, Tin-119 (1971) pp. 371–432.

[140] F. Grandjean and G. J. Long, Mössbauer Spectroscopy of Europium-Containing Compounds (1989). p. 526

[141] Mössbauer Effect Data Center, https://medc.dicp.ac.cn/Resources-isotopes/Resource-Sn.php (Accessed in May 2021).

[142] I. Nowik, M. Campagna, and G. K. Wertheim, Phys. Rev. Lett. **38**, 43 (1977).

[143] M. Loewenhaupt and S. Hüfner, Phys. Lett. **30A**, 309 (1969).

[144] G. Wortmann, W. Krone, E.V. Sampathkumaran, and G. Kaindl, Hyperfine Interact. **28**, 581 (1986).

[145] G. P. Srivastava, The Physics of Phonons (Taylor & Francis Group, New York, 1990).

[146] L. Chaput, A. Togo, I. Tanaka, and G. Hug, Phys. Rev. B **84**, 094302 (2011).

[147] A. Togo, L. Chaput, and I. Tanaka, Phys. Rev. B **91**, 094306 (2015).

[148] K. Suekuni, C. H. Lee, H. I. Tanaka, E. Nishibori, A. Nakamura, H. Kasai, H. Mori, H. Usui, M. Ochi, T. Hasegawa, M. Nakamura, S. Ohira-Kawamura, T. Kikuchi, K. Kaneko, H. Nishiate, K. Hashikuni, Y. Kosaka, K. Kuroki, and T. Takabatake, Adv. Mater. **30**, 1706230 (2018).

[149] Y. Mizuguchi, A. Miura, A. Nishida, O. Miura, K. Tadanaga, N. Kumada, C. H. Lee, E. Magome, C. Moriyoshi, and Y. Kuroiwa, J. Appl. Phys. **119**, 155103 (2016).

[150] C. H. Lee, A. Nishida, T. Hasegawa, H. Nishiate, H. Kunioka, S. Ohira-Kawamura, M. Nakamura, K. Nakajima, and Y. Mizuguchi, Appl. Phys. Lett. **112**, 023903 (2018).

[151] J. P. Perdew, K. Burke, and M. Ernzerhof, Phys. Rev. Lett. **77**, 3865 (1996).

[152] G. Kresse and J. Fürthmuller, Comp. Mater. Sci. **6**, 15 (1996).

[153] G. Kresse and J. Fürthmuller, Phys. Rev. B **54**, 11169 (1996).

[154] P. Sarangapani, A. G. Akkala, S. Steiger, H.-H. Park, Y. Borga, T. C. Kubis, M. Povolotskyi, and G. Klimeck (2014), "Brillouin Zone Viewer," https://nanohub.org/resources/brillouin (DOI: 10.21981/D3DB7VQ35).

[155] W. Setyawan and S. Curtarolo, Comp. Mater. Sci. **49**, 299 (2010).

[156] S. Grimme, J. Comput. Chem. **27**, 1787 (2006).

[157] R. Kniep, *Eduard Zintl: His Life and Scholarly Work* in Chemistry, Structure, and Bonding of Zintl Phases and Ions edited by S. M. Kauzlarich (VCH, New York, 1996).

[158] E. Zintl, Naturwissenschaften **17**, 782 (1929) (in German).

[159] E. Zintl, J. Goubeau, and W. Dullenkopf, Z. Phys. Chem. A-Chem. T. **154**, 1 (1931) (in German).

[160] E. Zintl and A. Harder, Z. Phys. Chem. A-Chem. T. 154 , 47 (1931) (in German).

[161] E. Zintl and W. Dullenkopf, Z. Phys. Chem. B-Chem. E. **16**, 183 (1932) (in German).

[162] E. Zintl and W. Dullenkopf, Z. Phys. Chem. B-Chem. E. **16**, 195 (1932) (in German).
[163] E. Zintl and A. Harder, Z. Phys. Chem. B-Chem. E. **16**, 206 (1932) (in German).
[164] E. Zintl and H. Kaiser, Z. Anorg. Allg. Chem. **211**, 113 (1933) (in German).
[165] E. Zintl and S. Neumayr, Z. Elktrochem. Angew. P. **39**, 81 (1933) (in German).
[166] E. Zintl and S. Neumayr, Z. Elktrochem. Angew. P. **39**, 84 (1933) (in German).
[167] E. Zintl and S. Neumayr, Z. Elktrochem. Angew. P. **39**, 86 (1933) (in German).
[168] E. Zintl and G. Brauer, Z. Phys. Chem. B-Chem. E. **20**, 245 (1933) (in German).
[169] E. Zintl and S. Neumayr, Z. Phys. Chem. B-Chem. E. **20**, 272 (1933) (in German).
[170] E. Zintl and E. Husemann, Z. Phys. Chem. B-Chem. E. **21**, 138 (1933) (in German).
[171] E. Zintl and A. Schneider, Z. Elktrochem. Angew. P. **41**, 294 (1935) (in German).
[172] E. Zintl and G. Brauer, Z. Elktrochem. Angew. P. **41**, 297 (1935) (in German).
[173] E. Zintl and A. Schneider, Z. Elktrochem. Angew. P. **41**, 764 (1935) (in German).
[174] E. Zintl and A. Harder, Z. Elktrochem. Angew. P. **41**, 767 (1935) (in German).
[175] E. Zintl and A. Schneider, Z. Elktrochem. Angew. P. **41**, 771 (1935) (in German).
[176] E. Zintl and G. Woltersdorf, Z. Elktrochem. Angew. P. **41**, 876 (1935) (in German).
[177] G. Brauer and W. Haucke, Z. Phys. Chem. B-Chem. E. **33**, 304 (1936) (in German).
[178] E. Zintl and O. Treusch, Z. Phys. Chem. B-Chem. E. **34**, 225 (1936) (in German).
[179] E. Zintl and A. Harder, Z. Phys. Chem. B-Chem. E. **34**, 238 (1936) (in German).
[180] E. Zintl, A. Harder, and W. Haucke, Z. Phys. Chem. B-Chem. E. **35**, 354 (1937) (in German).
[181] G. Brauer and E. Zintl, Z. Phys. Chem. B-Chem. E. **37**, 323 (1937) (in German).
[182] W. Haucke, Z. Elktrochem. Angew. P. **43**, 712 (1937) (in German).
[183] E. Zintl and W. Haucke, Z. Elktrochem. Angew. P. **44**, 104 (1938) (in German).
[184] E. Zintl, Angew. Chem.-Ger. Edit. **52**, 1 (1939) (in German).
[185] H. Schäfer, B. Eisenmann, and W. Müller, Angew. Chem. Int. Edit. **12**, 694 (1973).
[186] H. Schäfer, Annu. Rev. Mater. Sci. **15**, 1 (1985).
[187] S. C. Sevov, *Chap. 6* in Intermetallic Compounds: Principles and Practice: Progress, Vol. 3 edited by J. H. Westbrook and R. L. Fleischer (Wiley, Chichester, 2002).
[188] S. M. Kauzlarich, in Encyclopedia of Inorganic Chemistry (Wiley, online, 2006) Zintl compounds.
[189] O. Janka and S. M. Kauzlarich, *Zintl Compounds* in Encyclopedia of Inorganic and Bioinorganic Chemistry (Wiley, online, 2013).
[190] W. Hume-Rothery, J. I. Met. **35**, 295 (1926).
[191] A. Westgren and G. Phragmén, Z. Metallkd. **18**, 279 (1926).

[192] F. Laves, Naturwissenschaften **29**, 244 (1941) (in German).

[193] W. Klemm and H. Fricke, Z. Anorg. Allg. Chem. **282**, 162 (1955) (in German).

[194] W. Klemm, P. Chem. Soc. London **12**, 329 (1958).

[195] W. Klemm and E. Busmann, Z. Anorg. Allg. Chem. **319**, 297 (1963) (in German).

[196] H. Schäfer and B. Eisenmann, Rev. Inorg. Chem. **3**, 29 (1981).

[197] W. Bronger, Pure Appl. Chem. **57**, 1363 (1985).

[198] S. M. Kauzlarich, T. Y. Kuromoto, and M. M. Olmstead, J. Am. Chem. Soc. **111**, 8041 (1989).

[199] S. M. Kauzlarich, Comment. Inorg. Chem. **10**, 75 (1990).

[200] S. M. Kauzlarich, *Transition Metal Zintl Compounds* in Chemistry, Structure, and Bonding of Zintl Phases and Ions edited by S. M. Kauzlarich (VCH, New York, 1996).

[201] B. Eisenmann and H. Schäfer, Z. Anorg. Allg. Chem. **403**, 163 (1974) (in German).

[202] W. Jeitschko and M. Reehuis, J. Phys. Chem. Solids **48**, 667 (1987).

[203] B. Eisenmann and H. Schäfer, Z. Naturforsch. B **36**, 415 (1981) (in German).

[204] Y. Kamihara, H. Hiramatsu, M. Hirano, R. Kawamura, H. Yanagi, T. Kamiya, and H. Hosono, J. Am. Chem. Soc. **128**, 10012 (2006).

[205] Y. Kamihara, T. Watanabe, M. Hirano, and H. Hosono, J. Am. Chem. Soc. **130**, 3296 (2008).

[206] Y. Kamihara, T. Nomura, M. Hirano, J. E. Kim, K. Kato, M. Takata, Y. Kobayashi, S. Kitao, S. Higashitaniguchi, Y. Yoda, M. Seto, and H. Hosono, New J. Phys. **12**, 033005 (2010).

[207] M. Fujioka, S. J. Denholme, T. Ozaki, H. Okazaki, K. Deguchi, S. Demura, H. Hara, T. Watanabe, H. Takeya, T. Yamaguchi, H. Kumakura, and T. Takano, Supercond. Sci. Technol. **26**, 085023 (2013).

[208] Y. Kamihara and H. Hosono, Superconductivity in Iron Oxypnictide Induced by F-Doping Photonic and Electronic Properties of Fluoride Materials: Progress in Fluorine Science Series edited by A. Tressaud and K. Peoppelmeier (Elsevier, Amsterdam, 2016).

[209] P. J. W. Moll, R. Puzniak, F. Balakirev, K. Rogacki, J. Karpinski, N. D. Zhigadlo, and B. Batlogg, Nat. Mater. **9**, 628 (2010).

[210] T. Tamegai, Y. Nakajima, Y. Tsuchiya, A. Iyo, K. Miyazawa, P. M. Shirage, H. Kito, and H. Eisaki, Physica C **469**, 915 (2009).

[211] Y. Muraba, S. Iimura, S. Matsuishi, and H. Hosono, Inorg. Chem. **54**, 11567 (2015).

[212] A. Yamamoto, A. A. Polyanskii, J. Jiang, F. Kametani, C. Tarantini, F. Hunte, J.

Jaroszynski, E. E. Hellstrom, P. J. Lee, A. Gurevich, D. C. Larbalestier, Z. A. Ren, J. Yang, Z. L. Dong, W. Lu, and Z. X. Zhao, Supercond. Sci. Technol. **21**, 095008 (2008).

[213] Z. S. Gao, L. Wang, Y. P. Qi, D. L. Wang, X. P. Zhang, Y. W. Ma, H. Yang, and H. H. Wen, Supercond. Sci. Technol. **21**, 112001 (2008).

[214] Y. W. Ma, Z. S. Gao, Y. P. Qi, X. P. Zhang, L. Wang, Z. Y. Zhang, and D. L. Wang, Physica C **469**, 651 (2009).

[215] L. Wang, Y. P. Qi, D. L. Wang, Z. S. Gao, X. P. Zhang, Z. Y. Zhang, C. L. Wang, and Y. W. Ma, Supercond. Sci. Technol. **23**, 075005 (2010).

[216] Y. W. Ma, L. Wang, Y. P. Qi, Z. S. Gao, D. L. Wang, and X. P. Zhang, IEEE T. Appl. Supercon. **21**, 2878 (2011).

[217] M. Fujioka, T. Kota, M. Matoba, T. Ozaki, Y. Takano, H. Kumakura, and Y. Kamihara, Appl. Phys. Express **4**, 063102 (2011).

[218] Q. J. Zhang, C. L. Wang, C. Yao, H. Lin, X. P. Zhang, D. L. Wang, Y. W. Ma, S. Awaji, and K. Watanabe, J. Appl. Phys. **113** ,123902 (2013).

[219] C.-L. Wang, C. Yao, H. Lin, X.-P. Zhang, Q.-J. Zhang, D.-L. Wang, Y.-W. Ma, S. Awaji, K. Watanabe, Y. Tsuchiya, Y. Sun, and T. Tamegai, Supercond. Sci. Technol. **26**, 075017 (2013).

[220] Q.-J. Zhang, C. Yao, H. Lin, X.-P. Zhang, D.-L. Wang, C.-H. Dong, P.-S. Yuan, S. Tang, Y.-W. Ma, S. Awaji, K. Watanabe, Y. Tsuchiya, amd T. Tamegai, Appl. Phys. Lett. **104**, 172601 (2014).

[221] Q.-J. Zhang, H. Lin, P.-S. Yuan, X.-P. Zhang, C. Yao, D.-L. Wang, C.-H. Dong, Y.-W. Ma, S. Awaji, and K. Watanabe, Supercond. Sci. Technol. **28**, 105005 (2015).

[222] Q.-J. Zhang, X.-P. Zhang, C. Yao, H. Huang, D.-L. Wang, C.-H. Dong, Y.-W Ma, H. Ogino, and S. Awaji, Supercond. Sci. Technol. **30**, 065004 (2017).

[223] C. Senatore, R. Flukiger, M. Cantoni, G. Wu, R.-H. Liu, and X.-H. Chen, Phys. Rev. B **78**, 054514 (2008).

[224] F. Kametani, A. A. Polyanskii, A. Yamamoto, J. Jiang, E. E. Hellstrom, A. Gurevich, D. C. Larbalestier, Z. A. Ren, J. Yang, X. L. Dong, W. Lu, and Z. X. Zhao, Supercond. Sci. Technol. **22**, 015010 (2009).

[225] A. Yamamoto, J. Jiang, F. Kametani, A. Polyanskii, E. Hellstrom, D. Larbalestier, A. Martinelli, A. Palenzona, M. Tropeano, and M. Putti, Supercond. Sci. Technol. **24**, 045010 (2011).

[226] N. Doebelin and R. Kleeberg, J. Appl. Crystallogr. **48**, 1573 (2015).

[227] M. Fujioka, Ph.D thesis (Keio Univ. 2011).

[228] Y. Kobayashi, Graduate thesis (Keio Univ. 2021).

[229] A. Iandelli, Z. Anorg. Allg. Chem. **288**, 81 (1956).

[230] A. Kjekshus and K. E. Skaug, Acta Chem. Scand. **26**, 2554 (1972).

[231] K. Selte and A. Kjekshus, Acta Chem. Scand. **23**, 2047 (1969).

[232] D. T. Cromer, J. Phys. Chem.-US **61**, 753 (1957).

[233] M. Mitric, J. Blanusa, T. Barudzija, Z. Jaglicic, V. Kusigerski, and V. Spasojevic, J. Alloy. Compd. **485**, 473 (2009).

Publications

Papers

Journal papers that are related to this thesis

- 坂上良介, 後藤陽介, 水口佳一, 的場正憲, 神原陽一：「SnAs 層を含む六方晶層状化合物 $EuSn_2As_2$ の多結晶合成」, 材料の科学と工学, **55**, 72 (2018).
  R. Sakagami, Y. Goto, Y. Mizuguchi, M. Matoba, and Y. Kamihara, "Synthesis Method of the SnAs-based Layered Hexagonal Compound, $EuSn_2As_2$," Mater. Sci. Tech. Jpn. **55**, 72 (2018) (in Japanese).
- R. Sakagami, Y. Goto, H. Karimata, N. Azuma, M. Yamaguchi, S. Iwasaki, M. Nakanishi, I. Kitawaki, Y. Mizuguchi, M. Matoba, and Y. Kamihara, "Thermoelectric Transport Properties of the van der Waals-type Layered Rhombohedral SnAs-Based Compound, $EuSn_2As_2$," Jpn. J. Appl. Phys. **60**, 035511 (2021).

The other journal papers

- Y. Goto, A. Miura, R. Sakagami, Y. Kamihara, C. Moriyoshi, Y. Kuroiwa, and Y. Mizuguchi, "Synthesis, Crystal Structure, and Thermoelectric Properties of Layered Antimony Selenides $REOSbSe_2$ (RE = La, Ce)," J. Phys. Soc. Jpn. **87**, 074703 (2018).
- K. Kaneyasu, R. Sakagami, M. Matoba, and Y. Kamihara, "Superconducting properties of a mixed anion layered compound, Ca and F co-doped LaFeAsO with T_c = 31.5 K," Jpn. J. Appl. Phys. **58**, 030911 (2019).
- W. Labban, W. Malaeb, K. Habanjar, M. S. Hassan, R. Sakagami, Y. Kamihara, and R. Awad, "Investigations of Arsenic substitution on the physical, electrical and magnetic properties of Bi-2212 superconductors," Phase Transit. **93**, 1055 (2020).
- 東伸彦, 澤田拓希, 伊藤大平, 坂上良介, 的場正憲, 臼井秀知, 神原陽一：「複合アニオ

ン層状化合物 $LaCu_{1-\delta}S_{0.5}Se_{0.5}O$ ($\delta \sim 0.01$) 多結晶縮退半導体の光学バンドギャップ内構造」, 材料の科学と工学, **58**, 64 (2021).

N. Azuma, H. Sawada, H. Ito, R. Sakagami, M. Matoba, H. Usui, and Y. Kamihara, "In-gap-states of a Mixed Anion Layered Compound, Polycrystalline $LaCu_{1-\delta}S_{0.5}Se_{0.5}O$ ($\delta \sim 0.01$) as a Degenerate Semiconductor," Mater. Sci. Tech. Jpn. **58**, 64 (2021) (in Japanese).

A preprint

- S. Sakuragi, S. Sasaki, R. Akashi, R. Sakagami, K. Kuroda, C. Bareille, T. Hashimoto, T. Nagashima, Y. Kinoshita, Y. Hirata, M. Shimozawa, S. Asai, T. Yajima, S. Doi, N. Tsujimoto, S. Kunisada, R. Noguchi, K. Kurokawa, N. Azuma, K. Hirata, Y. Yamasaki, H. Nakao, T. K. Kim, C. Cacho, T. Masuda, M. Tokunaga, H. Wadati, K. Okazaki, S. Shin, Y. Kamihara, M. Yamashita, and T. Kondo, "Spintronic superconductor in a bulk layered material with natural spin-valve structure" arXiv:2001.07991.

Conferences

The speakers of presentations are underlined below.

Oral presentations in international conferences

- Y. Kamihara, Y. Tojo, S. Iwasaki, R. Sakagami, M. Yamaguchi, S. Hirai, and M. Nakanishi, Electronic Functionality of Superconducting Mixed Anion Layered Compounds (MALCs), International Union of Materials Research Societies – International Conference on Electronic Materials 2018 (IUMRS-ICEM 2018), Daejeon, Korea, August 19–24, 2018.
- R. Sakagami, S. R. Hall, J. Potticary, M. Matoba, and Y. Kamihara, Appearance of SmFeAsO as a mother phase of iron-based superconductor during a solid state reaction in the 580° to 980°C temperature range, International Workshop on the Iron-based Superconductors: advances towards applications (IBS2app), Genoa, Italy, February 12–14, 2020.

Poster presentations in international conferences

- R. Sakagami, H. Karimata, N. Azuma, M. Yamaguchi, S. Iwasaki, Y. Goto, Y. Mizuguchi, M. Matoba, and Y. Kamihara, Transport properties of the layered hexagonal compound, $EuSn_2As_2$, Korea-Japan International Symposium on Materials Science and Technology 2018 (KJMST2018), Yeosu, Korea, November 7–9, 2018.
- R. Sakagami, H. Karimata, Y. Goto, N. Azuma, M. Yamaguchi, S. Iwasaki, M. Nakanishi, I. Kitawaki, Y. Mizuguchi, M. Matoba, and Y. Kamihara, Thermoelectric Properties of the SnAs-based Hexagonal Compound including Europium $4f$ electrons, $EuSn_2As_2$, The Second International Workshop Emergent Condensed-Matter Physics 2019 (ECMP2019), Higashihiroshima, Japan, March 18–20, 2019.
- K. Hirata, R. Sakagami, M. Matoba, and Y. Kamihara, Spontaneous magnetic polarization of a layered hexagonal compound, $EuSn_2As_2$, 6th Japan-Korea International Symposium on Materials Science and Technology 2019 (JKMST2019), Sapporo, Japan, August 25–27, 2019.
- H. Karimata, M. Yamaguchi, S. Iwasaki, R. Sakagami. Y. Goto, Y. Mizuguchi, M. Matoba, and Y. Kamihara, Thermal transport properties of mixed anion layered compound $Sr_2CrFeAsO_{3-\delta}$, 6th Japan-Korea International Symposium on Materials Science and Technology 2019 (JKMST2019), Sapporo, Japan, August 25–27, 2019.
- S. Iwasaki, M. Yamaguchi, R. Sakagami, K. Kihou, C. H. Lee, and Y. Kamihara, Thermoelectric properties of mixed anion layered compound $Sr_2VFeAsO_{3-\delta}$ ($\delta = 0.150$), 6th Japan-Korea International Symposium on Materials Science and Technology 2019 (JKMST2019), Sapporo, Japan, August 25–27, 2019.
- R. Sakagami, S. R. Hall, J. Potticary, M. Matoba, and Y. Kamihara, Synthesis of the Mother Phase of the Iron-Based Superconductor, SmFeAsO via Low-Temperature Heat Treatment, The 32nd International Symposium on Superconductivity (ISS2019), Kyoto, Japan, December 3–5, 2019.
- R. Sakagami, S. R. Hall, J. Potticary, M. Matoba, and Y. Kamihara, Synthesis of the Mother Phase of the Iron-Based Superconductor SmFeAsO at Low Temperatures, Materials Research Meeting 2019 (MRM2019), The Materials Research Society of Japan (MRS-J), Yokohama, Japan, December 10–14, 2019.

Oral presentations in domestic conferences

- R. Sakagami, J. Iihara, I. Chelali, S. R. Hall, M. Matoba, and Y. Kamihara, Diffusion of a binder in policrystalline $SmFeAsO_{1-x}F_x$ synthesized at low temperatures, Heisei-28-Nendo Gakujutsu-Koen-Taikai, Materials Science Society of Japan (MSSJ), Tokyo, Japan, June 29, 2016 (in Japanese).
- I. Chelali, Y. Matsumoto, S. Kawaguchi, R. Sakagami, S. R. Hall, M. Matoba, H. Kaiju, J. Nishii, and Y. Kamihara, Synthesis of transition metal-based High-Tc superconducting micro-wire using bio-polymer., Heisei-28-Nendo Gakujutsu-Koen-Taikai, Materials Science Society of Japan (MSSJ), Tokyo, June 29, 2016.
- K. Kaneyasu, R. Sakagami, M, Matoba, and Y. Kamihara, Synthesis of Ca and F codoped Iron-Based superconductor mother compoound, LaFeAsO, Heisei-29-Nendo Gakujutsu-Koen-Taikai, Materials Science Society of Japan (MSSJ), Yokohama, Japan, June 26, 2017 (in Japanese).
- R. Sakagami, I. Chelali, S. R. Hall, M. Matoba, and Y. Kamihara, Low-temperature syntesis of the mother phase of the iron-based superconductor SmFeAsO, Heisei-29-Nendo Gakujutsu-Koen-Taikai, Materials Science Society of Japan (MSSJ), Yokohama, Japan, June 26, 2017 (in Japanese).
- R. Sakagami, Y. Mizuguchi, Y. Goto, M. Matoba, and Y. Kamihara, Synthesis procedure of the SnAs-based layered $EuSn_2As_2$, Spintronics Research Network of Japan (Spin-RNJ) Symposium 2017, Tokyo, Japan, March 1, 2018 (in Japanese).
- 坂上良介, 後藤陽介, 水口佳一, 的場正憲, 神原陽一, 六方晶層状化合物 $EuSn_2As_2$ の輸送特性, 日本材料科学会主催 平成 30 年度学術講演大会, 横浜, 2018 年 5 月 31 日.
  R. Sakagami, Y. Goto, Y. Mizuguchi, M. Matoba, and Y. Kamihara, Transport properties of the layered hexagonal compound, $EuSn_2As_2$, Heisei-30-Nendo Gakujutsu-Koen-Taikai, Materials Science Society of Japan (MSSJ), Yokohama, Japan, May 31, 2018 (in Japanese).
- R. Sakagami, S. R. Hall, M. Matoba, and Y. Kamihara, Low-temperature synthesis of the mother phase of the iron-based superconductor, SmFeAsO, Tetsu-kei ko-on choden-do hakken 10-shu-nen ki-nen go-do symposium, Tokyo, Japan, June 27, 2018 (in Japanese).
- R. Sakagami. H. Karimata, N. Azuma, S. Iwasaki, Y. Goto, Y. Mizuguchi, and Y. Kamihara, Research on $EuSn_2As_2$ as a thermoelectric material, 4th Workshop for

Materials-Informatics Classic, Materials Science Society of Japan (MSSJ) with 3rd Workshop on Novel Superconducting materials and biomimetic processes 2018, Sapporo, Japan, September 2–3, 2018 (in Japanese).

- Y. Kamihara, J. Potticary, R. Sakagami, M. Murata, T. Iwatake, S. R. Hall, The Effects of Heat Treatment Conditions and Potassium Incorporation on Morphologies of $YBa_2Cu_3O_{7-\delta}$ Micro-wires, 4th Workshop for Materials-Informatics Classic, Materials Science Society of Japan (MSSJ) with 3rd Workshop on Novel Superconducting materials and biomimetic processes 2018, Sapporo, Japan, September 2–3, 2018.
- R. Sakagami, H. Karimata, Y. Goto, K. Hirata, N. Azuma, M. Yamaguchis, S. Iwasaki, M. Nakanishi, I. Kitawaki, Y. Mizuguchi, M. Matoba, and Y. Kamihara, Thermoelectric Transport Properties of a Ferromagnetic Kondo Lattice, $EuSn_2As_2$, Spintronics Research Network of Japan (Spin-RNJ) Symposium 2018, Sendai, Japan, February 20, 2019 (in Japanese).
- S. Sakuragi, R. Sakagami, K. Kuroda, C. Bareille, N. Azuma, T. Iwatake, S. Sasaki, S. Doi, N. Tsujimoto, R. Akashi, S. Kunisada, R. Noguchi, K. Kurokawa, T. K. Kim, C. Cacho, S. Shin, Y. Kamihara, and T. Kondo, Observation of magnetically combined two-dimensional electronic states in a bulk layered antiferromagnet $EuSn_2As_2$, 74th Annual Meeting, The Physical Society of Japan, Fukuoka, Japan, March 14–17, 2019 (in Japanese).
- S. Sakuragi, S. Sasaki, R. Akashi, R. Sakagami, K. Kuroda, C. Bareille, T. Hashimoto, T. Nagashima, Y. Kinoshita, Y. Hirata, M. Shimozawa, S. Doi, N. Tsujimoto, S. Kunisada, R. Noguchi, K. Kurokawa, N. Azuma, K. Hirata, T. K. Kim, C. Cacho, M. Tokunaga, H. Wadati, K. Okazaki, S. Shin, Y. Kamihara, M. Yamashita, and T. Kondo, Unconventional anisotropic superconductivity in bulk layered magnet, Autumn Meeting 2019 (Condensed Matter Physics and Other Fields), The Physical Society of Japan, Gifu, Japan, Septemper 10–13, 2019 (in Japanese).
- Y. Hirata, S. Sakuragi, K. Ikeda, H. Nakao, Y. Yamasaki, R. Sakagami, Y. Kamihara, T. Kondo, H. Wadati, Magnetic structure of Eu-based layered magnet unraveled by resonant soft x-ray scattering, Autumn Meeting 2019 (Condensed Matter Physics and Other Fields), The Physical Society of Japan, Gifu, Japan, Septemper 10–13, 2019 (in Japanese).
- K. Hirata, R. Sakagami, M. Matoba, and Y. Kamihara, Spontaneous polarization of layered hexagonal compound,$EuSn_2As_2$, The 43rd Annual Conference on Magnetics in Japan, The Magnetics Society of Japan, Kyoto, Japan, September 25–27, 2019 (in

Japanese).

- R. Sakagami, H. Karimata, Y. Goto, N. Azuma, K. Hirata, M. Nakanishi, S. Iwasaki, M. Yamaguchi, I. Kitawaki, Y. Mizuguchi, M. Matoba, and Y. Kamihara, Thermoelectric Properties of Two-Dimensional Kondo Lattice, $EuSn_2As_2$, The 43rd Annual Conference on Magnetics in Japan, The Magnetics Society of Japan, Kyoto, Japan, September 25–27, 2019 (in Japanese).
- R. Sakagami, Y. Goto, H. Karimata, N. Azuma, M. Yamaguchi, S. Iwasaki, M. Nakanishi, I. Kitawaki, Y. Mizuguchi, M. Matoba, and Y. Kamihara, Thermoelectric Trnasport of Kondo Lattice, $EuSn_2As_2$, Online Meeting of Spintronics Research Network of Japan (Spin-RNJ) for Young Researchers, online, June 3–4, 2020 (in Japanese).
- H. Sato, R. Sakagami, T. Kawashima, Y. Kamihara, and M. Matoba, Electronic structures of metal hydrides exhibiting superconducting phases under high pressure at temperatures above 200 K, Online Meeting of Spintronics Research Network of Japan (Spin-RNJ) for Young Researchers, online, June 3–4, 2020 (in Japanese).
- R. Sakagami, S. Kitao, M. Seto, and Y. Kamihara, Magnetic splitting of ^{151}Eu and ^{119}Sn Mössbauer spectra of a rhombohedral Kondo lattice, $EuSn_2As_2$, JPS 2020 Autumn Meeting, The Physical Society of Japan, online, September 8–11 and 14–17, 2020 (in Japanese).
- H. Sato, R. Sakagami, T. Kawashima, Y. Kamihara, and M. Matoba, Electronic structures of metal hydrides exhibiting superconducting phases under high pressure at temperatures above 200 K, 2020-Nendo Gakujutsu-Koen-Taikai, Materials Science Society of Japan (MSSJ), online, July 16, 2020 (in Japanese).
- R. Sakagami, Y. Goto, Y. Mizuguchi, M. Matoba, and Y. Kamihara, The Effects of Leakage of Radiation Heat in Steady-State Thermal Conductivity Measurement, 17th Annual Meeting of the Thermoelectrics Society of Japan (TSJ2020), online, September 28–30, 2020 (in Japansese).
- Yoichi Kamihara, Nobuhiko Azuma, Ryosuke Sakagami, and Hidetomo Usui, 複合アニオン層状化合物 LaCu1-δS0.5Se0.5O (δ=0–0.02) 多結晶の絶縁体-縮退半導体-絶縁体転移, The 68th Japan Society of Applied Physics (JSAP) Spring Meeting 2021, online, March 16–19, 2021 (in Japanese).
- R. Sakagami, M. Matoba, Y. Goto, Y. Mizuguchi, S. Kitao, M. Seto, and Y. Kamihara, 擬二次元結晶構造化合物 $EuSn_2As_2$ の磁性と熱電性能, 2020-Nendo Nenji-Hokokukai, Spintronics Research Network of Japan (Spin-RNJ), online, March 9, 2021 (in Japanese).

- Y. Kobayashi, Y. Kamihara, and R. Sakagami, Measurement of transport properties of $SmFeAsO_{0.84}F_{0.16}$ (nominal x = 0.16), 2021-Nendo Gakujutsu-Koen-Taikai, Materials Science Society of Japan (MSSJ), Yokohama, Japan, May 20–21, 2021 (in Japanese).